

## TABLE OF CONTENTS

	Page
INTRODUCTION .....	27
CHAPITRE 1 LITERATURE REVIEW .....	36
1.1 Introduction.....	36
1.2 Definition and Role of Standalone and Hybrid Standalone Power Generation Systems .....	36
1.3 Principal Elements of Hybrid Standalone Power Generation Systems .....	37
1.3.1 Renewable Energy Sources.....	37
1.3.1.1 Wind Turbine Conversion System.....	38
1.3.1.2 Hydro Power System .....	41
1.3.1.3 Solar Photovoltaic (PV) System .....	42
1.3.1.4 Diesel Generator .....	43
1.3.2 Dump loads .....	46
1.3.3 Battery Energy Storage System .....	47
1.3.4 Power Electronics Device.....	48
1.4 Integrated Configurations for Hybrid Standalone Power Generation System.....	48
1.4.1 DC microgrid Configuration for Hybrid Standalone Power Generation Systems .....	49
1.4.2 AC Microgrid Configuration for Hybrid Standalone Power Generation Systems .....	50
1.4.3 Hybrid AC/DC Microgrid Configuration for Hybrid Standalone Power Generation Systems .....	51
1.5 System Control for Energy Flow Management in Hybrid Standalone Power Generation Systems .....	52
1.5.1 Centralized Control Scheme for Hybrid Standalone Power Generation Systems .....	52
1.5.2 Distributed Control Scheme for Hybrid Standalone Power Generation Systems .....	53
1.5.3 Hybrid centralized and distributed control scheme for HSPGS .....	54
1.6 Problematic .....	54
1.6.1 Problems Related to the Intermittence of the Renewable Energy Sources.....	55
1.6.2 Maximization of the Generated Power from Renewable energy sources.....	55
1.6.3 Fuel Consumption Minimisation for DG.....	57
1.6.4 Underutilization of Power Electronics Devices Rating .....	57
1.6.5 Synchronization issues between ESs and PCC.....	57
1.6.5.1 AC Voltage Regulation.....	58
1.6.5.2 System Frequency Regulation .....	58
1.6.5.3 Power Quality Requirement.....	58
1.7 Objectives .....	59

1.8	Methodology .....	59
<b>CHAPITRE 2 MODELING OF THE ELEMENTS OF STANDALONE POWER GENERATION SYSTEMS.....65</b>		
2.1	Introduction.....	65
2.2	Modeling of the Wind Turbine .....	65
2.2.1	Aerodynamic conversion .....	65
2.2.2	Rotor Optimal Tip Speed Ratio .....	68
2.2.3	Transmission.....	69
2.3	Modeling of the solar PV array.....	70
2.3.1	Mathematical model of PV cell .....	71
2.4	Micro-Hydro power .....	72
2.4.1	Micro-Hydro power and governor model .....	72
2.5	Diesel Generator .....	78
2.5.1	Diesel Prime Mover and Governor .....	78
2.6	Classification and modeling of the electrical machines.....	80
2.6.1	Mathematic model of the induction machines.....	81
2.6.1.1	Mathematical model of the Doubly-Fed induction generator....	81
2.6.1.2	Mathematical model of the squirrel cage induction generator...	87
2.6.2	Mathematic model of synchronous machine .....	88
2.6.3	Mathematical model of permanent magnetic synchronous generator .....	96
2.6.4	Mathematical model of Permanent Magnetic Brushless Direct Current Generator.....	100
2.6.5	Mathematical model of Synchronous Reluctance Generator.....	103
2.7	Power Electronics Interface .....	105
2.7.1	Modeling of the DC/AC inverter .....	106
2.7.2	Modeling of the DC/DC boost converter.....	109
2.7.3	Modeling of the DC/DC buck boost converter.....	109
2.8	Conclusion .....	110
<b>CHAPITRE 3 STANDALONE POWER GENERATING SYSTEM EMPLOYING SOLAR-PHOTOVOLTAIC POWER .....111</b>		
3.1	Introduction.....	111
3.2	System Description .....	111
3.3	Modeling and Control Strategy.....	112
3.3.1	Modeling of Solar PV Array.....	112
3.3.2	Mathematical Model of the DC/DC Boost Converter .....	113
3.3.3	Maximum Power Tracking Based on Sliding Mode Approach.....	114
3.3.3.1	Choice of Sliding Surface .....	114
3.3.3.2	Determination of the Equivalent Control.....	115
3.3.3.3	System Stability Analysis .....	116
3.3.4	Overvoltage Protection of the BESS.....	118
3.3.5	Mathematical Model of the CC-VSC .....	120
3.3.6	AC Voltage Regulation Based on Sliding Mode Approach .....	121
3.3.6.1	Choice of Sliding Surface .....	121

3.3.6.2	Determination of the Equivalent Control.....	122
3.3.6.3	Stability Analysis.....	124
3.3.7	Selecting the rating of BESS.....	127
3.4	Simulation Results and Discussion.....	128
3.5	Experimental Results and Discussion.....	132
3.6	Conclusion .....	136
CHAPITRE 4	HYBRID STANDALONE POWER GENERATION SYSTEMS EMPLOYING SOLAR PV ARRAY AND DIESEL GENERATOR .....	137
4.1	Introduction.....	137
4.2	Topology Designs for HSPGS based on Solar PV Array and DE Driven Fixed Speed Generators .....	138
4.2.1.1	System Description and Control .....	139
4.3	Topology Designs of Hybrid Standalone Power Generation System based on PV Array and DE Driven Variable Speed Generators.....	153
4.3.1	System Description and Control .....	155
4.3.1.1	Model of the variable speed DG .....	157
4.3.1.2	Control of the Rotor Side Converter.....	158
4.3.1.3	Control of the interfacing DC/AC inverter .....	162
4.4	Simulation Results and Discussion.....	164
4.4.1	Performance of the HSPGS power generation using PV and DG driven fixed speed SG.....	164
4.4.2	Performance of the HSPGS power generation using PV and DG driven variable speed DFIG.....	171
4.5	Conclusion .....	178
CHAPITRE 5	HYBRID STANDALONE POWER GENERATION SYSTEM EMPLOYING SOLAR PV ARRAY AND MHP .....	179
5.1	Introduction.....	179
5.2	Topology designs of hybrid standalone power generation system based on PV array and MHP driven fixed speed generators.....	180
5.2.1.1	Description and control of hybrid standalone power generation system based on PV and MHP driven fixed speed SyRG.....	181
5.2.1.2	Description and control of hybrid standalone power generation system based on PV and MHP driven fixed speed SCIG .....	184
5.3	Simulation results and discussion.....	193
5.3.1	Performance of the hybrid standalone power generation system based on solar PV and MHP driven fixed speed SyRG.....	193
5.3.1.1	Performance analysis under load and solar irradiation change .....	193
5.3.1.2	Performance analysis under balanced and unbalanced nonlinear loads.....	195

5.3.1.3	Performance analysis when the BESS becomes fully charged (SOC%=100%) .....	198
5.3.2	Performance of the hybrid standalone power generation system based on solar PV and MHP driven fixed speed SCIG .....	199
5.3.2.1	Performance analysis under load and solar irradiation change .....	199
5.3.2.2	Performance analysis under unbalanced linear load .....	201
5.3.2.3	Performance analysis under unbalanced nonlinear load .....	202
5.3.2.4	Performance analysis under completely removed load .....	203
5.4	Conclusion .....	204
CHAPITRE 6	HYBRID STANDALONE POWER GENERATION SYSTEM EMPLOYING SOLAR PV ARRAY AND WT .....	205
6.1	Introduction .....	205
6.2	Topology designs of hybrid standalone power generation system based on PV array and WT driven fixed speed generators .....	206
6.2.1.1	Description and control of hybrid standalone power generation system based on solar PV array and WT driven fixed speed SCIG .....	207
6.2.1.2	Control algorithms for solar PV array and WT driven fixed speed SCIG .....	209
6.3	Topology designs of hybrid standalone power generation system based on solar PV array and WT driven variable speed generators .....	211
6.3.1.1	Control algorithms for solar PV array and WT driven variable speed SyRG .....	212
6.3.1.2	Description and control of hybrid standalone power generation system based on solar PV array and WT driven variable speed PMBLDCG .....	219
6.3.2	Control design of the DC/DC Boost Converter for PV side .....	220
6.3.2.1	MPPT Algorithm Based on Sliding Mode Approach for solar PV array .....	221
	Controller gain design .....	226
6.3.3	Control Design for DC-DC Boost Converter for WT side .....	228
6.3.3.1	Maximum Power Tracking Based on Sliding Mode Approach for WT .....	229
6.3.4	Control of CC-VSC .....	235
6.4	Simulation results and discussion .....	239
6.4.1	Performance of HSPGS based on solar PV array and WT driven fixed speed SCIG .....	239
6.4.2	Performance of HSPGS system based on solar PV array and WT driven variable speed SyRG .....	245
6.4.3	Performance of HSPGS based on solar PV array and WT driven variable speed PMBLDCG .....	251
6.4.3.1	Simulation results .....	251
6.4.3.2	Experimental results .....	253

6.5	Conclusion .....	259
<b>CHAPITRE 7 HYBRID STANDALONE POWER GENERATION SYSTEM EMPLOYING WT AND DG .....</b>		
7.1	Introduction.....	261
7.2	Topology designs of HSPGS based on DG and WT driven fixed speed generators.....	262
	7.2.1.1 Description and control of hybrid standalone power generation system based on WT and DG driven fixed speed SG and PMSG.....	263
7.3	Topology designs of hybrid standalone power generation system employing DG and WT driven variable speed generators.....	269
	7.3.1 Description and control of HSPGS employing WT and DG driven variable speed PMBLDCG and PMSG .....	271
7.4	Simulation results and discussion .....	279
	7.4.1 Performance of the HSPGS based on DG and WT driven fixed speed SG and PMSG.....	279
	7.4.2 Performance of the hybrid standalone power generation system based on DG and WT driven variable speed PMSG and PMBLDCG ...	290
7.5	Conclusion .....	296
CONCLUSION.....		297
RECOMMENDATIONS.....		301
APPENDIX I SYSTEMS PARAMETERS.....		303
APPENDIX II LABORATORY SETUP DETAILS.....		308
BIBLIOGRAPHY.....		310

## LIST OF TABLES

	Page
Table 1.1	Classification of ESS based on time frame.....47
Table 1.2	Classification of ESS based on the form of energy storage.....48
Table 2.1	Classification of PMSG and BLDCG .....100
Table 3.1	Signs of the first and the second terms of (3.22) .....117
Table 3.2	Signs of the Terms Given in (3.35).....126
Table 3.3	Signs of the Terms 1,2,3 and 4 of (3.47) .....126
Table 6.1	Characteristic of the PMBLDCG.....232

**Rapport-Gratuit.com**

## LIST OF FIGURES

	Page
Figure 0.1 Mean wind speed in Quebec .....	29
Figure 0.2 Photovoltaic potential in Canada .....	30
Figure 1.1 WT based on fixed speed generators: a) SCIG and b) SG.....	38
Figure 1.2 SPGS based on WT driven variable speed generators.....	40
Figure 1.3 Fixed speed MHP employing: a) SG, b) SCIG, c) PMSG and d) SyRG.....	42
Figure 1.4 SPGS based on solar PV array.....	43
Figure 1.5 DE driven fixed speed SG.....	44
Figure 1.6 DE driven variable speed generators .....	45
Figure 1.7 Model of the ELC Taken from Singh and Murthy (2006).....	46
Figure 1.8 DC microgrid configuration for HSPGS.....	49
Figure 1.9 AC microgrid configuration for HSPGS.....	50
Figure 1.10 Hybrid AC/DC microgrid configuration HSPGS .....	51
Figure 1.11 Centralized control scheme for HSPGS.....	53
Figure 1.12 Distributed control scheme for HSPGS .....	53
Figure 1.13 Hybrid centralized and distributed control scheme for HSPGS .....	54
Figure 1.14 MPPT control methods for WT .....	56
Figure 2.1 Wind speed variation in ideal model of a WT .....	66
Figure 2.2 Power coefficient $C_p$ and the interference parameters $b$ .....	67
Figure 2.3 Power coefficient- Tip speed ratio Characteristic.....	68
Figure 2.4 Transmission for WT .....	69
Figure 2.5 Mathematical model of the WT .....	70

Figure 2.6 Equivalent electrical circuit of the PV cell and the DC-DC boost converter .....70

Figure 2.7 Characteristics I-V and V-P of PV for: a) fixed T and varying G b) fixed G and varying T .....72

Figure 2.8 Simplified schematic of micro hydro power plant.....73

Figure 2.9 Simplified functional block diagram of MHP power plants .....78

Figure 2.10 Simplified block diagram of the DE and its governor .....80

Figure 2.11 Classification of electrical machines .....80

Figure 2.12 Equivalent circuit of DFIG in d-q axis reference frame .....86

Figure 2.13 Equivalent circuit of SCIG in d-q - axis reference frame .....88

Figure 2.14 (a) schematic diagram of SG, (b)circuit of rotor and (c) circuit of stator .....89

Figure 2.15 Representation of : a) SG windings, b) and c) completed d-q axis windings .....95

Figure 2.16 Equivalent circuit of the PMSG: a) d-axis and b) q-axis .....99

Figure 2.17 Phase back EMF waveforms of PMBLDCG and PMSG .....101

Figure 2.18 Equivalent circuit of SyRM : a) d-axis and b) q-axis .....103

Figure 2.19 Power converters for SPGS and HSPGS .....106

Figure 3.1 SPGS based on solar PV array .....112

Figure 3.2 Control of the DC/DC Boost converter .....118

Figure 3.3 P-V characteristic of the solar PV array .....120

Figure 3.4 Control of CC-VSC.....124

Figure 3.5 Simulation results of capacitor currents and load voltage in d-q axis .....127

Figure 3.6 Dynamic performance of the SPGS based on solar PV array under solar insolation and load change.....129

Figure 3.7 I-V Characteristic curve of PV array at T=20°C and G=1000w/m<sup>2</sup> .....130

Figure 3.8 Dynamic performance of SPGS based on solar PV when SOC% of BESS is equal to 100% .....131

Figure 3.9 Experimental hardware configuration.....132

Figure 3.10 Dynamic performance of SPGS based on solar PV array under load variation .....134

Figure 3.11 Dynamic performance of SPGS based on solar PV array under solar irradiation change.....135

Figure 4.1 Classification of HSPGS based on PV array and DG driven fixed and variable speed generators .....137

Figure 4.2 PV-DG HSPGS employing fixed speed generators.....139

Figure 4.3 HSPGS based on solar PV array and DE driven fixed speed SG .....140

Figure 4.4 Flowchart of Perturbation and observation MPPT algorithm.....141

Figure 4.5 Block diagram for DG .....142

Figure 4.6 Model of the analogue AVR .....143

Figure 4.7 Fuel consumption for variable and fixed speed operation of DG .....144

Figure 4.8 Proposed control algorithm for controlled switch .....146

Figure 4.9 Dump load control algorithm.....147

Figure 4.10 Modified instantaneous power theory control algorithm.....149

Figure 4.11 HSPGS based on solar PV array and DE driven variable speed generators.....154

Figure 4.12 HSPGS based on solar PV array and DE driven variable speed DFIG .....155

Figure 4.13 DFIG operation modes; a) super-synchronous mode and.....156

Figure 4.14 Model of the variable speed DE.....157

Figure 4.15 Control algorithm for rotor side converter.....162

Figure 4.16 Control algorithm for the interfacing DC/AC inverter .....164

Figure 4.17 Dynamic response of PV-DG HSPGS based on fixed speed SG when the SOC% of BESS is greater to 50% .....165

Figure 4.18 Zoom 1 of the results shown in Fig 4.17 .....166

Figure 4.19 Zoom 2 of the results shown in Fig 4.17 .....167

Figure 4.20 Zoom 3 of the results shown in Fig 4.17 .....168

Figure 4.21	Dynamic response of PV-DG HSPGS based on fixed speed SG when the SOC% of BESS is less than 50%.....	169
Figure 4.22	Zoom the results shown in Fig 4.21 between t=0.7 s to t= 0.9 s. ....	170
Figure 4.23	Dynamic response of the PV-DG HSPGS based on variable speed DFIG when the SOC% of BESS is less than 100% and greater than 50%.....	172
Figure 4.24	Dynamic performance of PV-DG HSPG based on variable speed DFIG under linear load change and fixed solar irradiation and when the state charge of battery is less than 50%.....	173
Figure 4.25	Dynamic performance of PV-DG HSPG under balanced and unbalanced nonlinear load and fixed solar irradiation and when the state charge of battery is less than 50%.....	175
Figure 4.26	Zoom of the results shown in Fig.4.25 between t= 0.7 s and t= 0.9s .....	176
Figure 4.27	Dynamic performance PV-DG HSPGS based on DFIG when SOC % of BESS is equal to 100%.....	177
Figure 5.1	Classification of HSPGS power generation based on PV array and MHP driven fixed speed generators .....	180
Figure 5.2	HSPGS based on solar PV array and MHP driven fixed speed generators .....	181
Figure 5.3	HSPGS based on solar PV array and MHP driven fixed speed SyRG .....	182
Figure 5.4	Characteristics torque-speed of MHT .....	183
Figure 5.5	Proposed HSPGS based on solar PV array and MHP driven fixed speed SCIG .....	184
Figure 5.6	Perturbation and Observation MPPT Method.....	185
Figure 5.7	Ppv-Vpv Characteristic of the proposed solar PV array .....	186
Figure 5.8	Dump load control algorithm.....	187
Figure 5.9	System Frequency Control Algorithm.....	189
Figure 5.10	Proposed control algorithm for the DC/AC interfacing inverter .....	192
Figure 5.11	Dynamic performance of PV-MHP HSPGS based on fixed speed SyRG during load and solar irradiation change.....	194
Figure 5.12	Zoom of the results shown in Fig 5-11 .....	195

Figure 5.13	Dynamic performance of PV-MHP HSPGS based on fixed speed SyRG.....	196
Figure 5.14	Dynamic performance of PV-MHP HSPGS based on fixed speed SyRG.....	197
Figure 5.15	Dynamic performance of the PV-MHP HSPGS based on fixed speed SyRG when the SOC% of BESS is equal to 100% .....	198
Figure 5.16	Dynamic performance of PV-MHP SPGS based on fixed speed SCIG under solar and load irradiation change .....	200
Figure 5.17	Zoom1 of the results shown in Fig.5.16 between t=0.45s and t= 0.55 s .....	201
Figure 5.18	Zoom2 of the results shown in Fig.5.16 between t=1.05 s and t= 1.15 s .....	202
Figure 5.19	Zoom3 of the results shown in Fig.5.16 between t=1.35 s and t= 1.45 s .....	203
Figure 6.1	Classification of HSPGS based on PV array and WT driven fixed and variable speed generators.....	205
Figure 6.2	HSPGS based on solar PV array and WT driven fixed speed generators.....	207
Figure 6.3	HSPGS based on PV array and WT driven fixed speed SCIG .....	208
Figure 6.4	Turbine power-speed characteristics for $\beta = 0^\circ$ .....	208
Figure 6.5	d-q control algorithm for DC/AC inverter .....	209
Figure 6.6	HSPGS based on solar PV array and WT driven variable speed generators....	211
Figure 6.7	HSPGS based on solar PV array and WT driven variable speed SyRG.....	213
Figure 6.8	Power-speed characteristics .....	214
Figure 6.9	Rotor oriented control (ROC) for SyRG.....	216
Figure 6.10	Control of the DC/AC interfacing inverter .....	218
Figure 6.11	HSPGS based on solar PV array and WT driven variable speed PMBLDCG .....	219
Figure 6.12	Proposed SMC based control algorithm for the DC-DC boost converter 1 for solar PV array side .....	221
Figure 6.13	Dynamic response of the inductor current for different gain control values ....	226
Figure 6.14	Power-voltage characteristic of the solar PV array.....	227

Figure 6.15	Proposed feedback control algorithm for the DC-DC boost converter WT side .....	228
Figure 6.16	Experimental characteristic of $\omega_r=f(i_{WT})$ .....	232
Figure 6.17	QLC based proposed control algorithm of CC-VSC .....	237
Figure 6.18	Dynamic performance of the PV-WT HSPGS based on fixed speed SCIG under weather conditions change.....	240
Figure 6.19	Zoom of the results shown in Fig 6.18 between $t=0.75$ s and $t=0.85$ s .....	241
Figure 6.20	Steady state performance of PV-WT HSPGS employing fixed speed SCIG under balanced nonlinear load .....	242
Figure 6.21	Steady state performance of PV-WT HSPGS employing fixed speed SCIG under unbalanced nonlinear load .....	243
Figure 6.22	Dynamic performance of the PV-WT HSPGS employing fixed speed SCIG when SOC% is equal to 100%.....	244
Figure 6.23	Dynamic performance of PV-WT HSPGS employing variable speed SyRG under weather conditions change .....	246
Figure 6.24	Dynamic performance of PV-WT HSPGS employing variable speed SyRG under balanced and unbalanced linear load .....	248
Figure 6.25	Dynamic performance of PV-WT HSPGS employing variable speed SyRG under balanced and unbalanced nonlinear load .....	249
Figure 6.26	Dynamic performance of PV-WT HSPGS employing variable speed SyRG when SOC% of BESS becomes equal to 100%.....	250
Figure 6.27	Dynamic performance of PV-WT HSPGS under load variation.....	251
Figure 6.28	Dynamic performance of: a) PMPBLDCG under wind speed variation b) solar PV array and solar irradianations change.....	252
Figure 6.29	Experimental hardware configuration .....	253
Figure 6.30	Dynamic performance of the proposed PV-WT HSPGS employing variable speed PMBLDCG under load change.....	255
Figure 6.31	Dynamic performance of the PMBLDCG under wind speed variation.....	256
Figure 6.32	Dynamic performance of PV-WT HSPGS under solar insolation and wind speed change .....	258

Figure 7.1	Classification of HSPGS based on PV array and WT driven fixed and variable speed generators.....	261
Figure 7.2	HSPGS based on WT and DG driven fixed speed generators.....	263
Figure 7.3	HSPGS based on WT and DG driven fixed speed PMSG and SG.....	264
Figure 7.4	Modified SRF control algorithm.....	265
Figure 7.5	HSPGS based on WT and DG driven variable speed generators .....	270
Figure 7.6	HSPGS based on WT and DG driven variable speed PMBLDCG and PMSG.....	271
Figure 7.7	Control of the DG side DC-DC boost converter.....	272
Figure 7.8	Control of the DC-DC WT side boost converter .....	274
Figure 7.9	Positive, Negative and Zero sequence components.....	275
Figure 7.10	Control of the DC/AC inverter .....	278
Figure 7.11	Dynamic performance of WT-DG HSPGS employing fixed speed generators under wind speed and loads change when the SOC% is greater than 50% .....	280
Figure 7.12	Zoom1 of the results shown in Fig.7.11 between $t= 1.48s$ to $t= 1.55 s$ .....	281
Figure 7.13	Zoom2 of the results shown in Fig.7.11 between $t= 2.48 s$ and $t=2.55 s$ .....	282
Figure 7.14	Dynamic performance of WT-DG HSPGS based on fixed speed generators when SOC% is less than 50% .....	283
Figure 7.15	Zoom1 of the results shown in Fig.7.14 between $t=0.98 s$ and $t=1.05 s$ .....	285
Figure 7.16	Zoom2 of simulation results shown in Fig.7.14 between $t =1.48 s$ and $t=1.55s$ .....	286
Figure 7.17	Dynamic performance of interfacing inverter under balanced nonlinear load.....	287
Figure 7.18	Dynamic performance of interfacing inverter under unbalanced nonlinear load.....	288
Figure 7.19	Dynamic performance of WT-DG HSPGS employing fixed speed generators when the SOC% of BESS is equal to 100%.....	289

Figure 7.20 Dynamic response of WT-DG HSPGS based on variable speed generators when the SOC% of BESS is less than 100% and more than 50% .....291

Figure 7.21 Dynamic response of WT-DG HSPGS based on variable speed generators when SOC% of BESS is less than 50%.....292

Figure 7.22 Dynamic performance of the of WT-DG HSPGS based on variable speed generators under unbalanced linear load.....293

Figure 7.23 Dynamic performance of WT-DG HSPGS based on variable speed generators under unbalanced nonlinear load.....294

Figure 7.24 Dynamic performance of WT-DG HSPGS based on variable speed generators when the SOC% of BESS is equal to 100%.....295

## LIST OF ABBREVIATIONS

AC	Alternative Current
AVR	Automatic Voltage Regulation
BESS	Battery Energy Storage System
CC-VSC	Current Control Voltage Source Converter
DFIG	Doubly Fed Induction Generator
DC	Direct Current
DE	Diesel Engine
DG	Diesel Generator
EFM	Energy Flow Management
ES	Energy Source
ELC	Electronic Load Controller
HP	Hydropower
HSPGS	Hybrid Standalone Power Generation System
HCSC	Hill-Climb Search Control
LHP	Large Hydropower
MHP	Medium Hydropower
Mini-HP	Mini Hydropower
Micro-HP	Micro Hydropower
MW	Megawatts
MPPT	Maximum Power Point Tracking
PCC	Point Common Coupling
PSFC	Power Signal Feedback Control
PMBLDCG	Permanent Magnetic Brushless Direct Current Generator
PMSG	Permanent Magnetic Synchronous Generator
PV Solar	Photovoltaics Panel
QLC	Quasi-Linear Controller
RES	Renewable Energy Source
RSC	Rotor Side converter

SG	Synchronous Generator
SCIG	Squirrel Cage Induction Generator
SyRG	Synchronous Reluctance Generator
SHP	Small Hydropower
SSC	Stator Side Converter
SPGS	Standalone Power Generation System
SMC	Sliding Mode Control Approach
TSRC	Tip Speed Ratio Control
WT	Wind Turbine
WESC	Wind Energy System Conversion
SFR	System Frequency Regulation

Rapport-Gratuit.com

## INTRODUCTION

Canada is among the countries that have shown requirement of electrical power in isolated areas such as telecommunications infrastructure (cellular, microwave, optical ...), mining facilities, routing of oil and gas, as well as, isolated residential areas, which are far and not connected to the main grids. For their electricity requirements, the majority of those areas depend on diesel fuel, which is relatively inefficient, very expensive and responsible for emission of large amounts of greenhouse gases emission (GHG).

During the past several years, the oil prices have achieved historic highs, peaking at 147\$/barrel in July, 2008, averaging over 100\$/barrel during 2011, averaging over 110\$/barrel until October 2014, and then it fell to 80\$/barrel. Recently, the oil price is around 30\$/barrel. Despite this considerable drop, the diesel fuel prices are losing only a few cents in some provinces in Canada. According to statistic Canada, in St. John's Newfoundland, the diesel fuel lost only 5.7 ¢/L, and in Whitehorse in Yukon is increased by 3.5 ¢/L and in Yellowknife in Northwest Territories is set to rise up to 9.3 ¢/L in October 2014 compared to 2013. According to Statistics Canada (<http://www5.statcan.gc.ca>), the decline in crude oil prices is not felt at the pump in this region. However, the pump price gasoline only decreased by 11.8¢/L from a high of \$112 per barrel to a low of \$35 per barrel in December 2015. Therefore, the decrease in oil prices has not greatly affected the price of diesel fuel, which implies that the electrical energy produced using only oil as energy source will always remain expensive, at any cost of barrel. According to Hydro Quebec, extending the main grid to these isolated areas will cost around (1 M \$/ km), which is impossible to do with the actual economic crisis. Therefore, it is important to find new solutions based on clean energy sources available locally, such as, sunlight, wind, moving water, and terrestrial heat, which are inexpensive and environmentally friendly.

Recently, developments in the field of power electronics have caused significant impacts on reducing the cost of the kWh produced by the renewable energy sources. According to (U.S Energy Information Administration), the kWh cost is 0.13\$/kWh for the solar PV,

0.08\$/kWh for Hydro and for the wind turbine, the cost vary between 0.08 \$/kWh and 0.20 \$/kWh. Contrary wise, the average price for electricity produced by the DG is approximately equal to 1.3\$/kWh (Renewable Energy Alternatives for Remote Communities in Northern Ontario, Canada). Generally, 1L of diesel fuel provides 3kWh via DG. At current economics of 1.2 \$/L plus an assumed 25% transportation cost added, this results in variable cost of at least 0.5\$/kWh just for fuel cost reduction, which leads that the full cost of kWh provides from diesel generator is typically in the several dollars per kWh range (Arctic web site: [www.wwf.ca/conservation/arctic](http://www.wwf.ca/conservation/arctic), consulted on 01-02-2016). Therefore, diesel-powered generator as energy source in isolated areas is ineffective and costly. To remedy these drawbacks associated to the use of diesel fuel, and ensuring a stable and uninterruptible power supply in remote areas, hybrid standalone power generation system based on various energy sources, is advised. This new technology is effective and cost-efficient. Unfortunately, it requires a complex design, planning, and control optimization methods.

Several countries in the world such as, Canada, USA and Australia have a large surface area and dispersed population which does not have electricity distribution system. Recently, these countries, as well as, other countries are slowly adopting this new technology in order to reduce the fuel consumption by DG and increase the reliability and cost-effectiveness of the kWh in those isolated areas. According to Statistic Canada, there are 292 Canadian remote communities with a total of 194.281 residents (2006 Statistics Canada Census). Among them, 44 isolated sites are located in the province of Québec with a total population exceeding 34729 persons. According to a report (Status of Remote/Off-grid Communities in Canada, 2011), a total of 251 communities in Canada have their own fossil fuel power plants totaling 453.3 MW. Of these, 176 are diesel fueled, two are natural gas powered and 73 are from unknown sources but most likely diesel power plants or gasoline genset in smaller settlements. These statistics concerned only isolated villages that contain residents, but if we take into account other isolated areas that use DG as energy source, such as, underground mine, telecommunications stations, etc., this statistics on electricity consumption will multiply.

According to the Canadian Wind Energy Atlas, as shown in Fig.0.1, several places in Quebec have a strong wind profile, which could be used to drive wind turbine to produce electricity. According to (<http://www.windatlas.ca>), the density of the wind energy varies from 0 to 1000  $W/m^2$  and the wind velocity varies between 3 and 10 m/s, mainly in the island of Madeline.

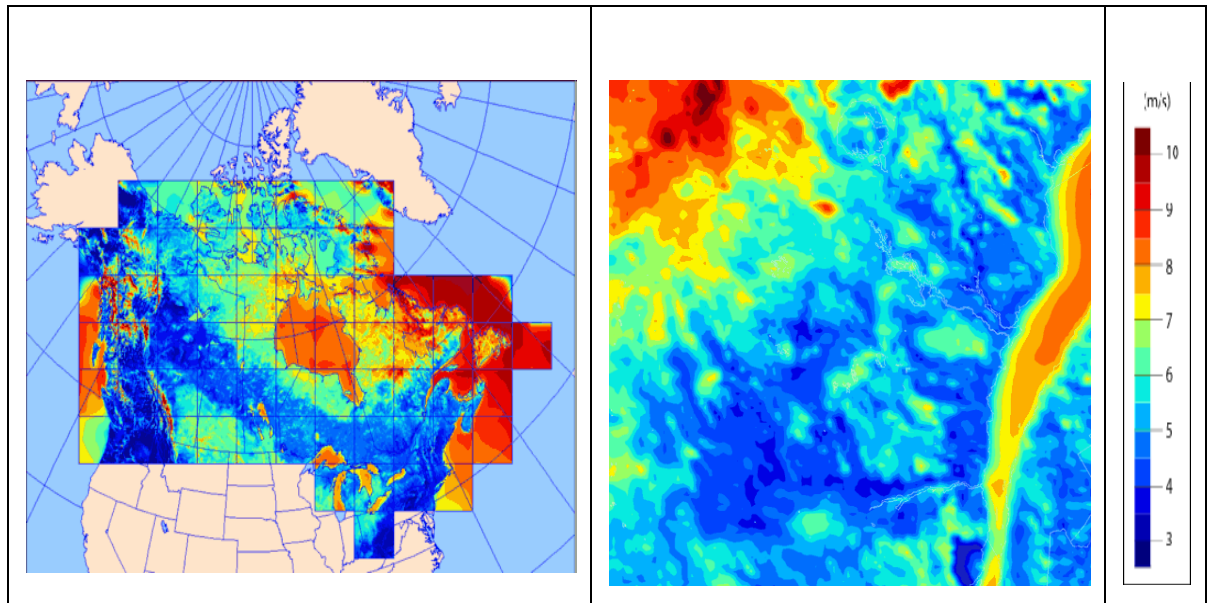


Figure 0.1 Mean wind speed in Quebec  
(<http://www.windatlas.ca>)

The potential for solar in Quebec is also impressive as is shown in Fig.0.2. It is observed that Quebec is a sunny power region whose solar power potential varies from 800 to 1200 kWh/kW.

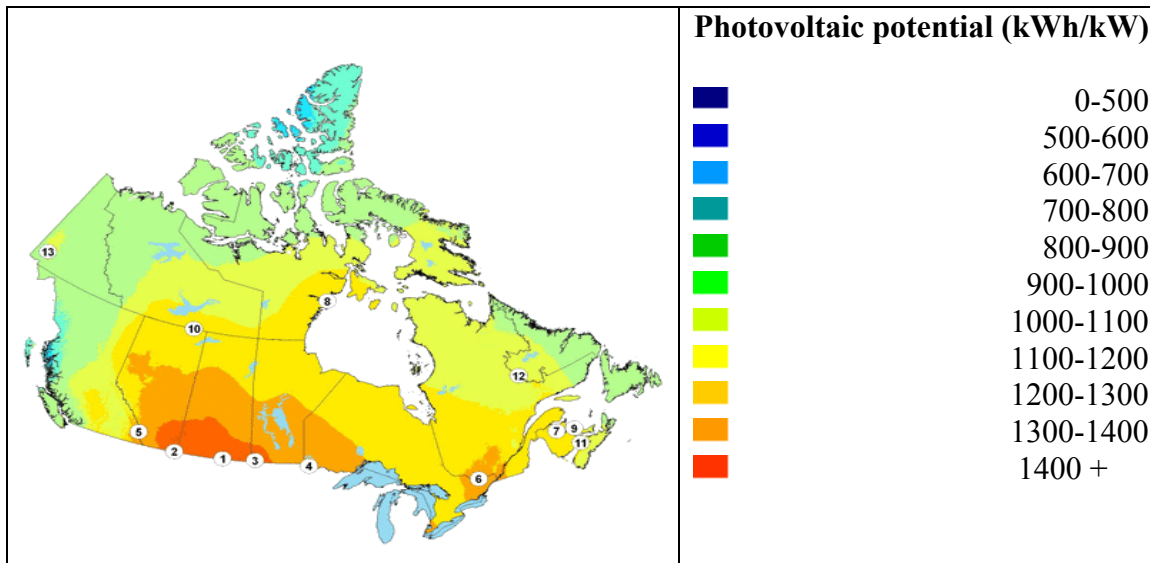


Figure 0.2 Photovoltaic potential in Canada  
(<http://www.nlcpr.com>)

As for storage water or the flow of water in the river, they are available everywhere in the province, as well as in the country. Therefore, use of these renewable energy sources, especially in summer, allows providing to the remote areas permanently a clean energy with reduced cost.

Generally, SPGS contains one or more ESs such as, PVs, WTs, DGs or MHP, and also other elements, such as, batteries, dump loads, power converters, transformers, loads and control system. Usually, these elements are connected through power converters to the AC or DC microgrid, or to the hybrid AC/DC microgrid.

Usually, ESs as, MHP, WT and DE drive electrical generators as, squirrel cage induction generator (SCIG), permanent magnetic synchronous generator (PMSG), rotor wound synchronous generator (SG) or doubly fed induction generator (DFIG). Recently, for low power application, permanent magnet brushless DC generator (PMBLDCG) has taken more attention because of it can operate at low speeds and it possesses high power density compared to the PMSG. Synchronous reluctance generator (SyRG) is better to other

brushless generators due to the advantages it possesses as, magnet-less rotor, no cogging torque and no rotor copper losses. Usually, those energy sources drives electrical generators can operate at fixed speed and at variable speed. Fixed speed operation is considered inefficient but inexpensive compared to the variable speed operation mode because of the absence of the power converters.

Usually, DG is the main electrical energy source in isolated localities, and several of these pollutants ESs have reached their designed life span. Therefore, combination of renewable ESs such as, PV, WT or MHP with DG sets in HSPGS can reduce operating costs, GHG emission and dependence on fossil fuel. Recently, PV-diesel-battery HSPGS for a telecommunication station (microwave radio repeater) as application is installed in the Nahanni Range Mountains, Northwest Territories. Adding PV array into DG in this isolated locality, it is expected that 75% of the electricity needs of this site will be supplied by solar energy. It is unnecessary to run the generators for the most of the summer (Stand-Alone Photovoltaic Applications: Lessons Learned). ENERCON Canada has started deploying wind turbines (WTs) with the existing DGs under the program for integration of the RESs, in some isolated areas, such as, Ross Island, Antarctica and Ascension Islands (ENERCON Canada, consulted on 22-11-2015). The hybridization of ESs, allows saving in the first remote area 463000 L of fuel per year, and reduces 1200 Ton of GHG emission per year. Therefore, in Antarctica and Ascension Islands it allows economy of 700000 \$/year, as well as, reduction in 4500 Ton of GHG.

According to Canadian Solar ([www.canadiansolar.com](http://www.canadiansolar.com), consulted on 05-09-2015), the Deer Lake First Nation is a small Oji-cree community, which is situated in the north of the Red Lake, Ontario, contain in approximately 1,100 resident. It pays close to 2.7 M\$ for diesel fuel every year. Moreover, in coldest days in winter, they are often forced to close their schools and public buildings, due to diesel shortages. Furthermore, existing DGs are not able to meet the rising energy demands of this community. Recently, solar PV array and MHP are added to the existing DGs in this isolated locality. According to Canadian Solar, PV-MHP-DG

HSPGS allows reducing in this locality the bill by 92,000\$/per year, and fuel consumption at least 31,000 liters, as well as, 99 tons of GHG.

It is observed that this new technology, which is based on several ESs, is cost effective and environmentally friendly. However, technically there is still much to do, especially, in improving the performance of DGs and in the synchronization between different energy sources that are being used. This technology is not yet fully natured and not efficient.

Currently, most of existing DGs in remote areas operate at a constant rotational speed due to the restriction of constant frequency at the terminals of the generator. This operating mode causes high fuel consumption, as well as, increases the maintenance costs. To overcome these drawbacks, variable speed DGs are being proposed by (Pena et al., 2008). Compared to the fixed speed DGs, variable speed DGs, are more efficient but costly, due to the use of power converters or mechanical transmission. As regards the RESs, such as, WTs or the PVs, power converters are required to get MPPT and to synchronize its phases and frequency prior to connecting to PCC. Moreover, storage elements, such as, batteries and dump loads are necessary in SPGS to ensure stable uninterruptible power supply for loads, and to protect the BESS from the overcharging. Therefore, to operate optimally RESs and DGs together, selection of the appropriate topology and control algorithms will help to improve the energy efficiency of the whole system by improving the performance and minimize the cost of kWh by reducing the fuel consumption by DG.

Generally, DC RESs such as PVs and BESS are connected to the DC bus through DC/DC converters and to the PCC through DC/AC inverters. For AC ESs, such as, WTs, MHP or DG, back-to-back converters are required to connect them to PCC. Usually schemes, which are based on hybrid AC/DC micro-grid, are more effective and inexpensive because of the reduced number of power converters compared to the installations, which are based on only AC or only DC micro-grid.

To achieve high efficiency from RESs, many MPPT techniques have been proposed in the literature. For the solar PV array; constant voltage method, open circuit voltage method, short

circuit current method, perturbation and observation method, incremental conductance and temperature parametric method are proposed. Each MPPT technique has advantages and disadvantages. Generally, accurate, fast and inexpensive method is preferable. For WT system, tip speed ratio control method, optimal torque control method, power signal feedback control method, adaptive perturbation and observation control method are reported. However, the fastest and sensor-less MPPT methods (information about rotor speed is not required) are more attractive.

There are two types of DGs. The first one consists of a DE running at fixed speed mostly coupled to the SG; this solution has the advantage of simplicity. However, there are some drawbacks, including high level of noise regardless of the power level required by the load, high level of GHG even when load power demand is low and over dimensioning in case of non-linear or unbalanced loads. The second option of DG is with variable speed. In this option DE is coupled with an electrical generator operating at variable speed. This concept is able to reduce the fuel consumption and to increase the profitability of DG (Pena et al., 2008).

Micro hydropower (MHP) system is cost-effective but is limited by characteristics of the isolated areas. Mostly, MHP cannot satisfy the load demand, especially in dry season and when rivers freezes. However, additional ESs, such as, solar PV array with BESS has been suggested to complement power deficiency.

The objective of this thesis is to propose new topology designs and new control algorithms for controlling different proposed SPGS and HSPGS in order to obtained high efficiency from ESs with reduced cost. Many control algorithms were studied, simulated, as well as, validated in real time.

The work presented in this thesis is organized as follows:

**CHAPTER 1** presents a detailed literature review of the different elements contained in SPGS and HSPGS. Problematics, objectives, as well as, the methodology used to achieve the desired objectives are discussed in this chapter.

**CHAPTER 2** discusses in details of mathematical models of different elements that SPGS and HSPGS can have, such as, ESs, electrical machines and power converters.

**CHAPTER 3** presents control and real-time implementation of SPGS based on solar PV array without using dump load. Sliding mode control approach is proposed to get the maximum power point tracking from solar PV array side and to regulate the output AC voltage and system frequency for load side. Mathematical models and stability analysis are well detailed in this chapter.

**CHAPTER 4** is dedicated to the proposed HSPGS topologies based on solar PV array and DG driven fixed and variable speed generators, such as, SG, SCIG, PMSG SyRG, PMBLDCG and DFIG. In addition, for each technology one scheme is selected for study. The topology which is based on solar PV array and DG driven fixed speed generator, SG is selected. For controlling the system parameters and achieve MPPT from solar PV array, modified p-q instantaneous power theory and perturbation & observation technique (P&O) are used. The topology which is based on solar PV array and DG driven variable speed generator, DFIG is selected. Indirect stator flux oriented control technique is used for controlling the rotor of the DFIG and P&O technique is used for MPPT for solar PV array. The AC voltage and the system frequency at the PCC are controlled using modified indirect control. To test the effectiveness of the selected topologies and its developed control algorithms, simulation is carried out using MATLAB/Simulink.

**CHAPTER 5** is dedicated to the proposed HSPGS topologies containing solar PV array and MHP driven fixed speed generators such as, SG, SCIG, PMSG and SyRG. Two different topologies are studied in detail. As for the first one, two-stage inverters are used to tie the solar PV array to the PCC, however, MHP driven fixed speed SyRG is connected directly to

the PCC. To get MPPT from solar PV array, P&O technique is used. For the system frequency and the AC voltage regulation, as well as, power quality improvement at the PCC, modified p-q instantaneous power theory is used. In the second topology, single stage inverter is used to tie the solar PV array to the PCC and MHP driven fixed speed SCIG is connected directly to the PCC. Modified P&O technique and modified Anti-Hebbian control algorithms are used to get MPPT from solar PV array, to regulate the system frequency and the AC voltage and to improve the power quality at the PCC. Simulation is carried out using MATLAB/Simulink to test the effectiveness of the selected topologies and their developed control algorithms.

**CHAPTER 6** presents the topologies based on solar PV array and WT driven fixed and variable speed generators. Topologies based on WT driven fixed speed SCIG, WT driven variable speed SyRG and WT driven variable speed PMBLDCG, are studied in detail. Many control approaches, such as P&O technique, modified p-q control, indirect control, rotor oriented control, as well as, sliding mode approach control are used for controlling different power converters of the proposed HSPGSs to get MPPT from solar PV array and WT, and to regulate the system frequency, AC voltage and power quality improvement at the PCC. To test the effectiveness of the selected schemes and the developed control algorithms, simulations are carried out using MATLAB/Simulink. Moreover, validation in real time by experimental setup of the third scheme is also discussed in this chapter.

**CHAPTER 7** is dedicated to the control of HSPGSs, which are based on DG and WT using fixed and variable speed generators. To regulate the AC voltage and the system frequency, improving the power quality, as well as achieving MPPT from WT, several control algorithms such as, modified SRF control approach and a new approach based on symmetrical components and P&O technique, are used. The effectiveness of proposed HSPGSs and their developed control approaches are validated by simulation using MATLAB/Simulink.

The major conclusion of thesis and future recommendations are also provided. In the end of thesis, list of references and appendices regarding hardware implementations are provided.

## CHAPITRE 1

### LITERATURE REVIEW

#### 1.1 Introduction

Currently, most of the world's remote areas use fossil fuels, such as, coal, oil, and gas as ESs to produce electricity. Unfortunately, these fossil energy sources are exhausting, expensive and polluting. Recently, RESs such as, wind, solar or flow of water have received much attention because of their efficiency, local availability, and renewability, as well as, they are environmentally friendly. Unfortunately, these RES are stochastics and intermittent, implying that they are not able to dispatch energy directly to the loads, especially in SPGS. Therefore, an additional reliable ES, such as DG, or storage elements as BESS are necessary to guarantee an uninterruptible power supply and to compensate the power fluctuations of wind/solar/load. Additional elements such as, power converters, BESS, dump loads and control system are necessary to ensure stable operation of the SPGS. The definition and mission of an SPGS is presented. The focus in this chapter is on the state of the art of different elements of the system. The operational problems, solutions, and objectives, as well as, the methodology are discussed.

#### 1.2 Definition and Role of Standalone and Hybrid Standalone Power Generation Systems

A SPGS, also known as remote area power supply, is an off-the-grid electricity system for locations that are completely independent from any electric utility grid.

Generally, in SPGS, electricity is generated using DG. Typically, HSPGS combines at least two complementary technologies: one or more conventional ESs, such as, DG and one or more RESs, such as solar PV array, WT or MHP. The role of the SPGS or HSPGS is to ensure:

- Stable and uninterruptible power supply to the local loads with high power quality and reduced cost,
- Minimization of GHG,
- Minimize the use of diesel fuel and maximize the energy provided from RESs.

### **1.3 Principal Elements of Hybrid Standalone Power Generation Systems**

As already indicated before that HSPGS contains at least two ESs and additional elements, such as, BESS and dump loads. These elements are connected to the AC or DC bus or hybrid AC/DC bus.

Generally, the sizing of these elements is determined based on meteorological data as solar radiation and wind speed and water flow and the exact load profile of consumers over long periods(Rekioua, Matagne, 2012). Therefore, HSPGS is classified by power range, which is outlined as follow:

- **Low power HSPGS** installation with a capacity between 10 and 250 kW, which is designed especially for isolated installation with a medium consumption such as small isolated village or mining facility.
- **Large power HSPGS** installation with a capacity greater than 500kW, which is designed for large consumption installation such as, large isolated village.

#### **1.3.1 Renewable Energy Sources**

Generally, solar PV array is DC ES and is tied to the DC or AC bus through power converters. As for DG, WT, and MHP, which are driven fixed or variable speed generators, are AC ESs and they are tied to the AC or to the DC bus through power converters. In some applications, the AC ESs are connected directly to the PCC.

### 1.3.1.1 Wind Turbine Conversion System

Usually, WTs convert the kinetic energy in wind into electricity using electrical generator such as, DFIG, SG, PMSG, SCIG, PMBLDCG or SyRG. Usually, the choice of the electrical generator is based on the size of the WT and the operating modes, meaning fixed or variable speed operation (Datta et Ranganathan, 2002). For a fixed speed WT, SCIG as shown in Fig.1.1 (a) or SG Fig.1.1 (b) are preferred, because of their design simplicity, robustness and their low cost compared to other generators. Unfortunately, need of an external supply of reactive power for SCIG, and DC current excitation for SG limits their application as standalone generators. However, additional elements, such as, capacitor bank and DC supply are necessary to operate them at fixed voltage and frequency in SPGS (Madawala et al., 2012);(Mendis et al., 2014).

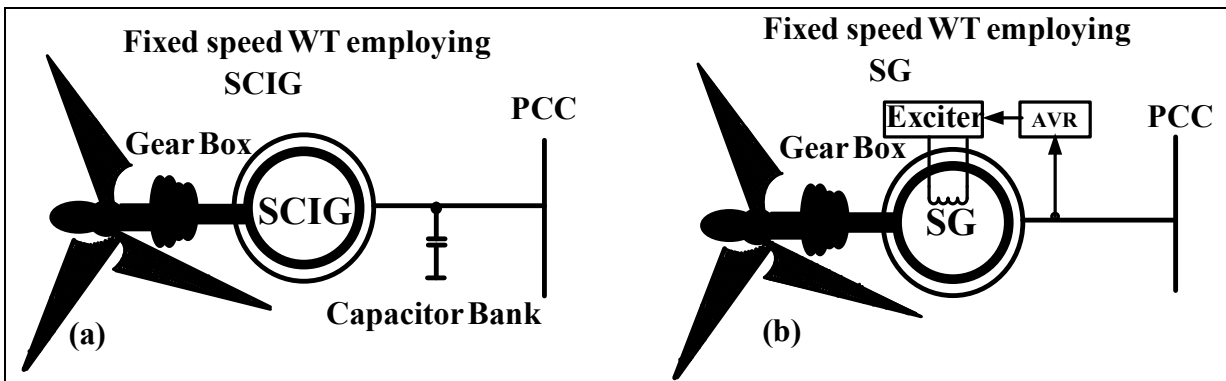


Figure 1.1 WT based on fixed speed generators: a) SCIG and b) SG

Nowadays, a variable speed operation is becoming more attractive from the point of view of efficiency, stability and reduced mechanical stress compared to fixed speed operation. However, this technology is expensive because of the additional elements such as, power converters (Muljadi et Butterfield, 2001); (Schinas, Vovos et Giannakopoulos, 2007) and more complicated of control method (Yang et al., 2014). Furthermore, in SPGS or HSPG, BESS would be absolutely essential to improve the reliability of supply, to minimize load

interruptions in cases of insufficient wind, as well as, to enhance control system flexibility (Sharma et Singh, 2014), which increases significantly the installation cost.

Generally, for variable speed operation, one uses several electrical generators (Chau, Li et Lee, 2012). According to (Blaabjerg et Chen, 2006), one can classify these electrical generators in two groups; with and without rotor windings.

For the first category, which are based on rotor windings we have DFIG. According to (Cardenas et al., 2005), DFIG has many advantages over all other variable speed machines because only a fraction of the mechanical power, typically 25 to 30%, is fed to the PCC through power converter, and the rest of power being fed to the PCC directly from the stator as shown in Fig1.2 (a) (Tremblay, Atayde et Chandra, 2011). Regarding, the second category as shown in Figs. 1.2 (b-f), full-rated power converters are required to connect their stators to the PCC, which make the system more expensive.

According to (Goel et al., 2011), WTs which are driven SCIG or wound rotor SG as shown in Fig.1.2 (b and d) can provide full operating speed range while avoiding the use of slip rings and carbon brushes. Recently, WTs, which drive PMSG as shown in Fig.1.2 (c) become more attractive due to their higher efficiency and power density (Yang et al., 2014).

According to (Sharma et Singh, 2013);(Singh et al., 2014a), PMBLDCG as shown in Fig.1.2 (f), has 15% higher power density compared to PMSG, and because of its trapezoidal EMF, the rectified DC output voltage has reduced ripples.

Recently, SyRG is gaining much attention in wind energy conversion systems due to the following advantages as (Boazzo et al., 2015):

- 1) Simple construction,
- 2) Rugged rotor,
- 3) Low maintenance,
- 4) Ability to operate at high speeds in high-temperature environments,

5) No rotor copper losses.

Therefore, SyRG is more effective compared to SCIG. However, its main challenge is the voltage regulation and the high excitation current. Usually, these requirements can be met with the use of capacitor bank.

Incorporating wind power into SPGS is challenging because of the fluctuation of the wind speed. Thereby, to compensate fluctuation of the wind speed and loads in SPGS, a complementary reliable ESs such as, DG or BESS are suggested (Kassem et Abdelaziz, 2014);(Hirose et Matsuo, 2012), (Bo et al., 2013).

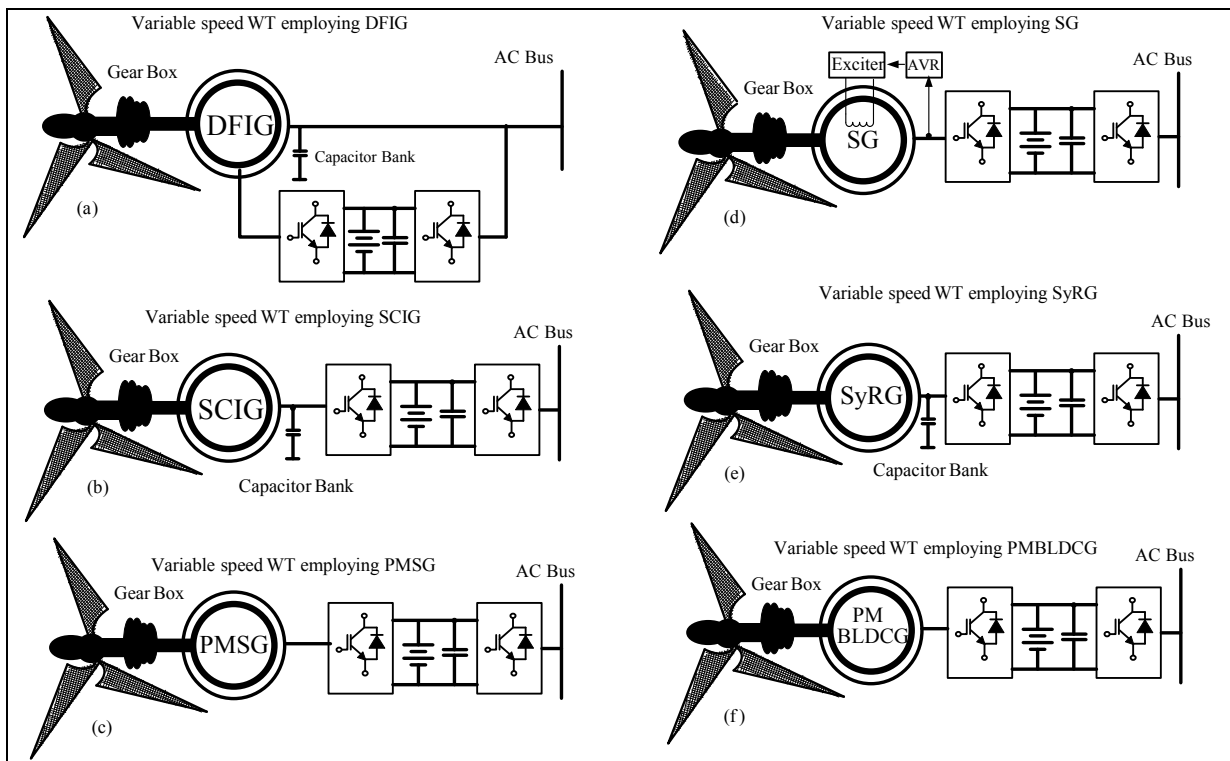


Figure 1.2 SPGS based on WT driven variable speed generators

### 1.3.1.2 Hydro Power System

Usually, HP system uses energy in flowing water to produce mechanical energy. The water flows via channel or penstock to a waterwheel or turbine where it strikes the bucket of the wheel, causing the shaft of the waterwheel or turbine to rotate. The rotating shaft, which is connected to the electrical generator, converts the motion of the shaft into clean electrical energy (Goel et al., 2011).

According to (<https://energypedia.info>); HP installations can be classified by size of power output as:

**Large Hydropower (LHP):** is used to feed a large grid and their capacities is more than 100 MW.

**Medium Hydropower (MHP):** is used to feed a grid and their capacity varies between 15 to 100 MW.

**Small Hydropower (SHP):** is used to feed a grid and their capacity varies between 1 to 15 MW.

**Mini-HP:** it can use to feed a grid and the local grid. Their capacity varies between 100 kW to 1 MW.

**Micro-HP:** their capacity is less than 100 kW. Generally, it is used to provide power for a small local grid.

**Family-HP:** their capacity is less than 1 kW. Generally, it is used to provide power for a small isolated application.

Mostly, MHP is operated at fixed speed employing either SCIG and SG as shown in Fig 1.3 (a and b), because of its lower price, robustness, as well as, the ability to combine high efficiency and low specific cost (Lopes et Borges, 2014).

Recently, authors (Goel et al., 2009), (Borkowski et Wegiel, 2013);(Borkowski et Wegiel, 2013) have proposed PMSG and SyRG as shown in Fig1.3 (c) and (d) for Hydropower system due to certain advantages that they possess.

According to (Goel et al., 2011);(Priolkar et Doolla, 2013), this RES cannot satisfy the load power demand, especially in dry season, therefore, this imbalances in power should be covered by some other ESs, such as DG, WT, solar PV array or BESS.

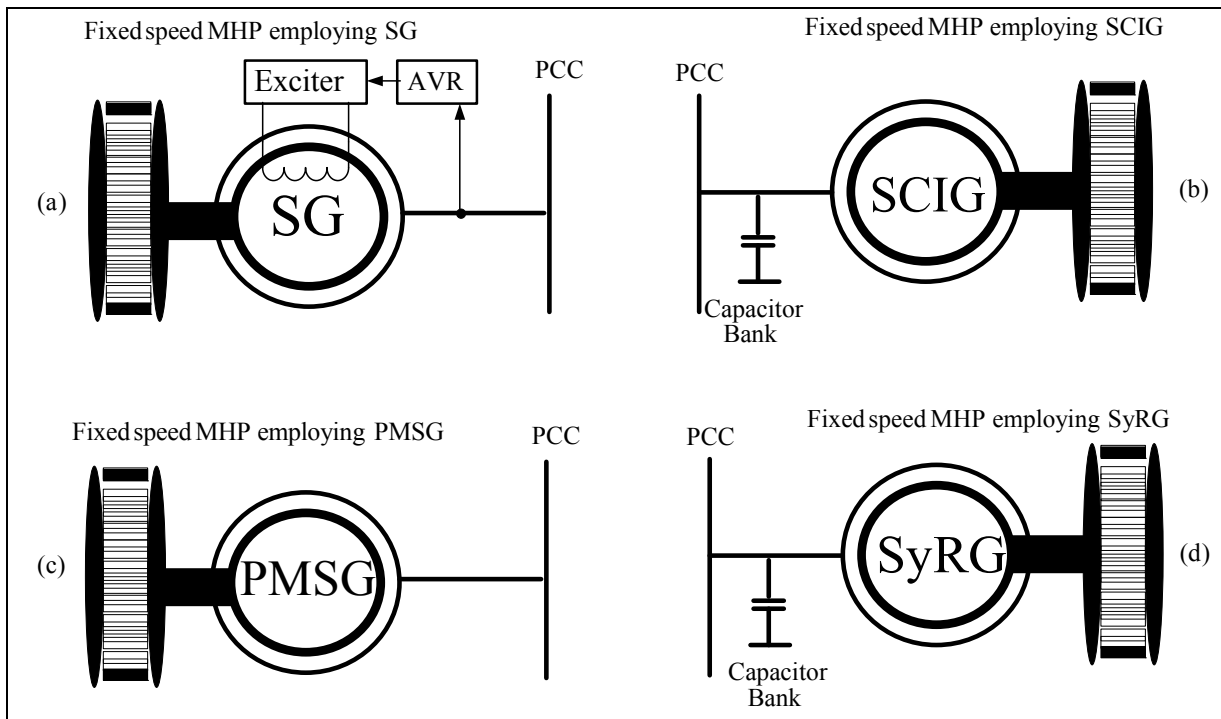


Figure 1.3 Fixed speed MHP employing: a) SG, b) SCIG, c) PMSG and d) SyRG

### 1.3.1.3 Solar Photovoltaic (PV) System

Usually, solar PV array converts sunlight directly into electricity using PV cells. The output of the solar PV array depends on several environmental factors such as, solar irradiance and temperature of the cell (Villalva, Gazoli et Filho, 2009), which makes this RES less reliable solution for SPGS. According to (Elgendy, Zahawi et Atkinson, 2014), (Zhu, Tazvinga et

Xia, 2014) complementary reliable ESs, such as, BESS as shown in Fig1.4 and power converters, as well as dump loads, are required to:

- Ensure continue power supply to the loads by compensating the fluctuation of the power provided by the solar PV array,
- Track the maximum power point (MPP),
- Control the power flow,
- Regulate the AC voltage and the system frequency at the PCC.

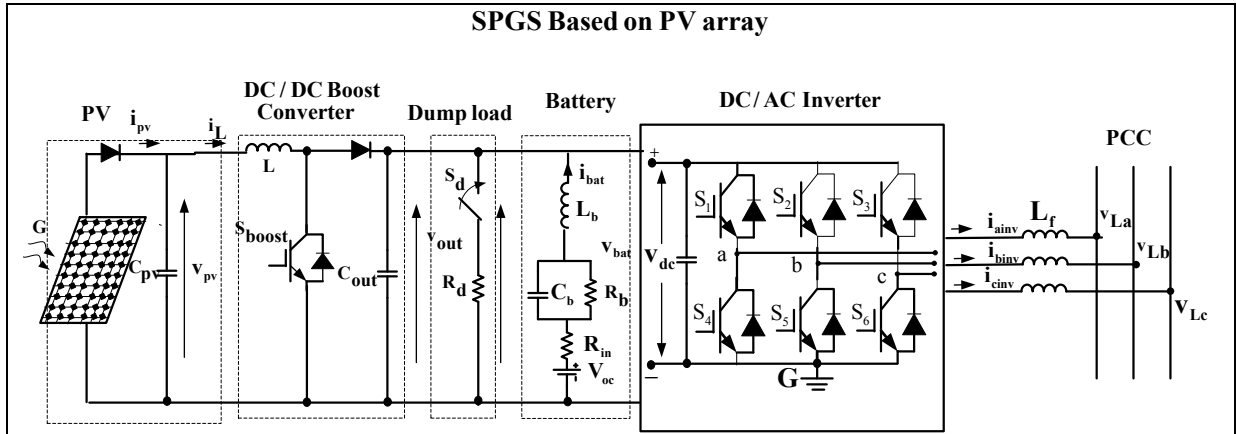


Figure 1.4 SPGS based on solar PV array

#### 1.3.1.4 Diesel Generator

Usually, the conventional DG consists of DE coupled to the electrical generator which is mostly SG (Cidras et Carrillo, 2000). For this ES, the system frequency at the PCC is controlled by adjusting the diesel fuel flow using the speed governor of the DE, as shown in Fig1.5, and the automatic voltage regulator (AVR), is used for AC voltage regulation.

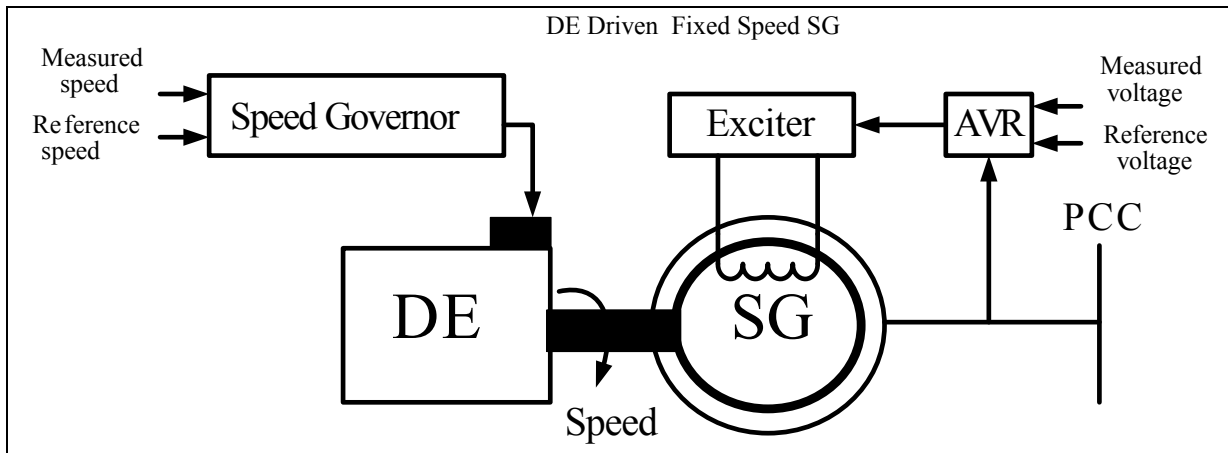


Figure 1.5 DE driven fixed speed SG

Currently, most of the existing DGs installed in isolated localities operate at fixed speed which is between 1500 to 3000 rpm for 50 Hz and between 1800 to 3600 rpm for 60Hz (<http://www.fischerpanda.de/> (Marine Generators with Variable Speed Technology). This ES is reliable but it has some drawbacks as:

- High level of noise regardless of the power level required by the load,
- High level of GHG due to the high engine speed, even when energy demand is low,
- Poor frequency stability and voltage transients in phases,
- Over dimensioning in case of non-linear or unbalanced loads.

To overcome these drawbacks, variable speed DG is proposed by (Pena et al., 2008). Using this proposed technology; the efficiency of the DG is increased by reducing fuel consumption even when DG operates at light load.

Power converters are required to achieve variable speed operation. Authors in (Waris et Nayar, 2008) have proposed DE driven variable speed DFIG in order to reduce the fuel consumption specially at light load and to reduce the cost of the installation by reducing the rating of the power converters used, as shown in Fig.1.6 (a). In (Rahman et al., 1996), (Pathak, Singh et Panigrahi, 2014), (Chunting et al., 2004) as shown in Fig1.6 (b-d), SCIG,

PMSG and SG are proposed as generators and in (Pathak, Singh et Panigrahi, 2014), SyRG and PMBLDCG, as shown in Fig 1.6 (e) and (f) are suggested. These propositions used full rating of the power converter compared to DFIG, which implies that they are expensive.

According to (Hernandez-Aramburo, Green et Mugniot, 2005);(Joon-Hwan, Seung-Hwan et Seung-Ki, 2009), addition of storage system to the variable speed DG can reduce the DE run time, improve the dynamic characteristics of the DE during sudden load change, improve the power quality and reduce the fuel consumption.

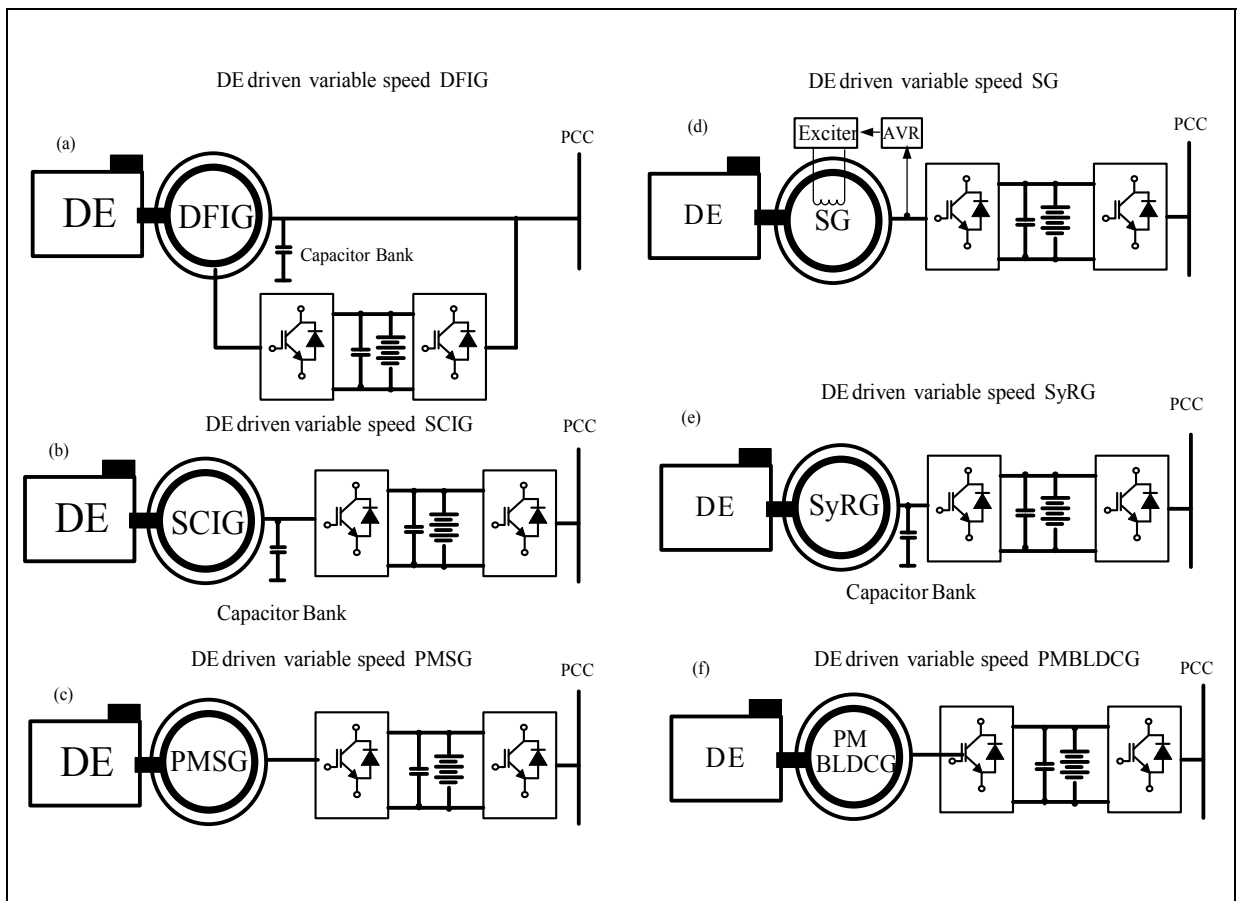


Figure 1.6 DE driven variable speed generators

### 1.3.2 Dump loads

A dump load is simply an electrical device (load) used especially in SPGS for dumping the extra power. Generally, this element is connected in parallel with the consumer load, and consists of rectifier and controlled chopper as shown in Fig1.7 (Singh, Murthy et Gupta, 2006). It has been reported in the literature review there are several types of electronic load controllers (ELCs) such as, binary weighted-switched resistors, phase-controlled thyristor-based load controllers, controlled rectifier feeding dump loads, as well as, uncontrolled rectifier with a controlled chopper.

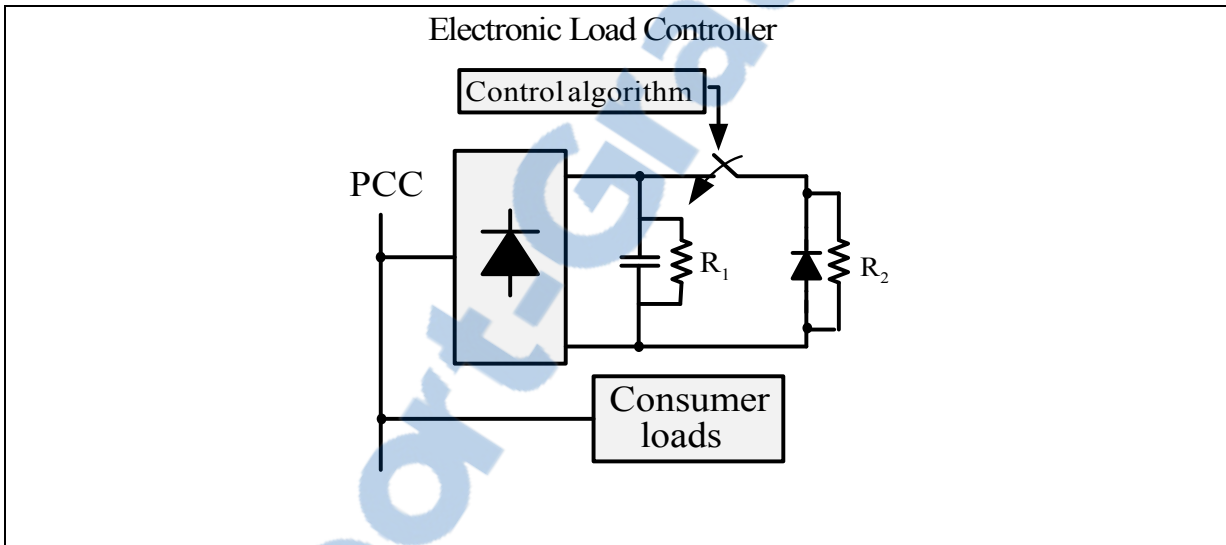


Figure 1.7 Model of the ELC  
Taken from Singh and Murthy (2006)

According to (Singh, Murthy et Gupta, 2006), the binary weighted three-phase switched resistor is less reliable because of the total resistive load, which is divided into a different number of elements where the system is bulky and prone to failure. As for the method, which is based on the phase-controlled thyristor-based load controller is also ineffective and may affect negatively the power quality because of the delay in firing angle, which causes increase in reactive power demands. Consequently, to improve the power quality in the presence of this element, authors (Singh, Kasal et Gairola, 2008) have proposed a new ELC,

which is based on 24-pulse rectifier instead of six-pulse rectifier. With this new concept authors have succeeded to improve the power quality but unfortunately this concept is costly.

### 1.3.3 Battery Energy Storage System

As already indicated that BESS is an important element in SPGS, and it needs to be fully considered in order to ensure stable operation of the whole system (Bo et al., 2013). According to (Chauhan et Saini, 2014), storage technologies are classified on the basis using time frame Table 1-1 or using the form of storage as indicated in Table 1-2 (Chen et al., 2009).

Currently, batteries, such as, lead-acid rechargeable batteries are widely used in SPGS (Bo et al., 2013). These elements are effective and helpful but according to (Wei, Joos et Belanger, 2010) single type of energy storage is not seen to satisfy both power and energy requirements in SPGS. To remedy this drawback authors (Mendis, Muttaqi et Perera, 2014) have proposed hybrid storage system, which consists of battery bank and super-capacitor as solution for SPGS. The obtained results show satisfactory. Therefore, hybrid storage system can offer high energy and power requirements, respectively.

In addition, presence of super-capacitor, as additional storage element help to ensure a healthy operation of the battery storage by preventing it to operate in high depth of discharge regions, as well as to operate at low frequency power regions (Mendis, Muttaqi et Perera, 2014).

Table 1.1 Classification of ESS based on time frame

<b>Duration</b>	<b>Storage technologies</b>
<b>Short term</b>	Capacitors, super-capacitors, flywheel, super conducting magnetic storage
<b>Medium term</b>	Fuel cells, compressed air energy storage, batteries
<b>Long term</b>	Pumped storage

Table 1.2 Classification of ESS based on the form of energy storage

Form of energy storage	Storage technologies
<b>Mechanical energy storage</b>	Pumped hydro storage, compressed air energy storage, flywheels.
<b>Chemical energy storage</b>	Battery energy storage (lead-acid, Ni-Cd, Na-S, Li-ion, metal-air batteries), flow batteries (vanadium redox battery, polysulphide bromide battery, zinc-bromine battery), fuel cells and hydrogen storage.
<b>Electrical energy storage</b>	Superconducting magnetic energy storage and super capacity.

#### 1.3.4 Power Electronics Device

Generally, in SPGS or HSPGS we often find three types of power converters devices; rectifiers, inverters and choppers, which are typically controlled in order to achieve charge/discharge of batteries, to convert the DC current to AC current and vice-versa, to synchronize between different ESs and the PCC. Furthermore, based on these devices one can ensure regulation of the system frequency, AC voltage, improving the power quality at the PCC and maximize the energy provided from RESs.

According to (Singh et Verma, 2008) (Singh et al., 2004), presence of several power electronic converters in SPGS not only increases reactive currents, but also generate harmonics. Therefore, this may increase losses, instability, and voltage distortion which corrupt the power system.

#### 1.4 Integrated Configurations for Hybrid Standalone Power Generation System

Generally, the AC ESs such as, WT, DG, MHP and conventional AC loads are tied to the AC Bus, whereas the DC ESs such as, PVS, ESS and DC loads are tied to the DC Bus.

According to (Xiong, Peng et Poh Chiang, 2011), there are three possible configurations to integrate different elements into SPGS.

#### 1.4.1 DC microgrid Configuration for Hybrid Standalone Power Generation Systems

As shown in Fig.1.8 in DC microgrid configuration, all elements which are AC by nature should be connected to the DC Bus through power converters. The DC loads are served directly from the DC Bus.

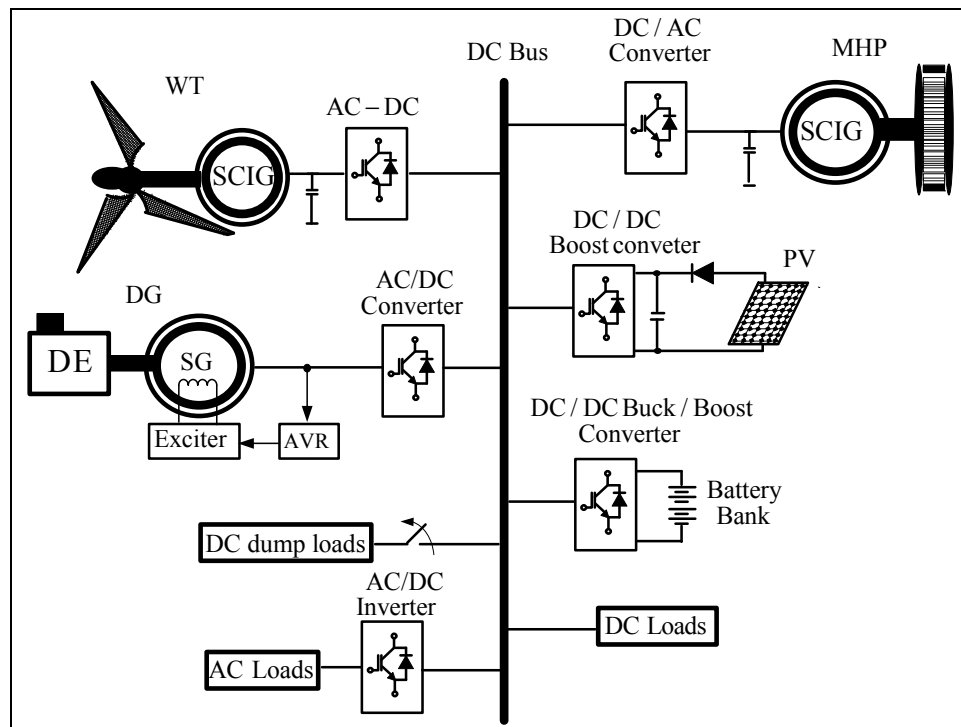


Figure 1.8 DC microgrid configuration for HSPGS

According to (Kakigano, Miura et Ise, 2010), the DC microgrid configuration has the following advantages:

- High efficiency because of less conversion losses,
- Synchronization between ESs is not required,

- Loads are not affected by voltage sag, voltage swell and voltage harmonics,
- Power quality is not affected.
- No need for frequency and phase control.

According to (Kakigano, Miura et Ise, 2010), this type of configurations possess some drawbacks as:

- The protection in DC microgrid is more difficult because there is no zero crossing of voltage,
- Compared to the AC microgrid, DC microgrid is costly,
- No standardization for DC microgrid.

#### 1.4.2 AC Microgrid Configuration for Hybrid Standalone Power Generation Systems

This configuration is the legacy of the traditional distribution system. As shown in Fig 1.9, all AC ESs are tied directly to the AC Bus. On the other side, DC/AC inverters are required for DC ESs.

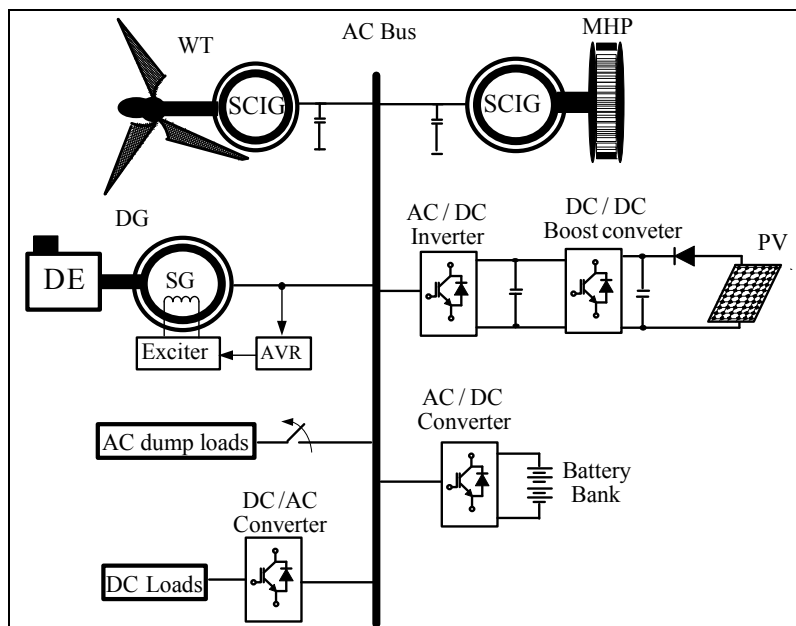


Figure 1.9 AC microgrid configuration for HSPGS

According to (Mariam, Basu et Conlon, 2013), this configuration has the following advantages:

- Utilizing existing AC grid technologies and the shelf products,
- Well established protections and standards.

Of course, there are some drawbacks related to the AC microgrid as indicate by (Jaehong et al., 2011):

- Synchronization between different available ESs and the connected AC Bus,
- Stability problem.

### 1.4.3 Hybrid AC/DC Microgrid Configuration for Hybrid Standalone Power Generation Systems

Several ESs, such as solar PV array, generate power in DC form. Many of the modern electrical loads, as well as ESS, are either internally DC or work equally well with DC power and connect to the AC systems through power converters as shown in Fig.1.10.

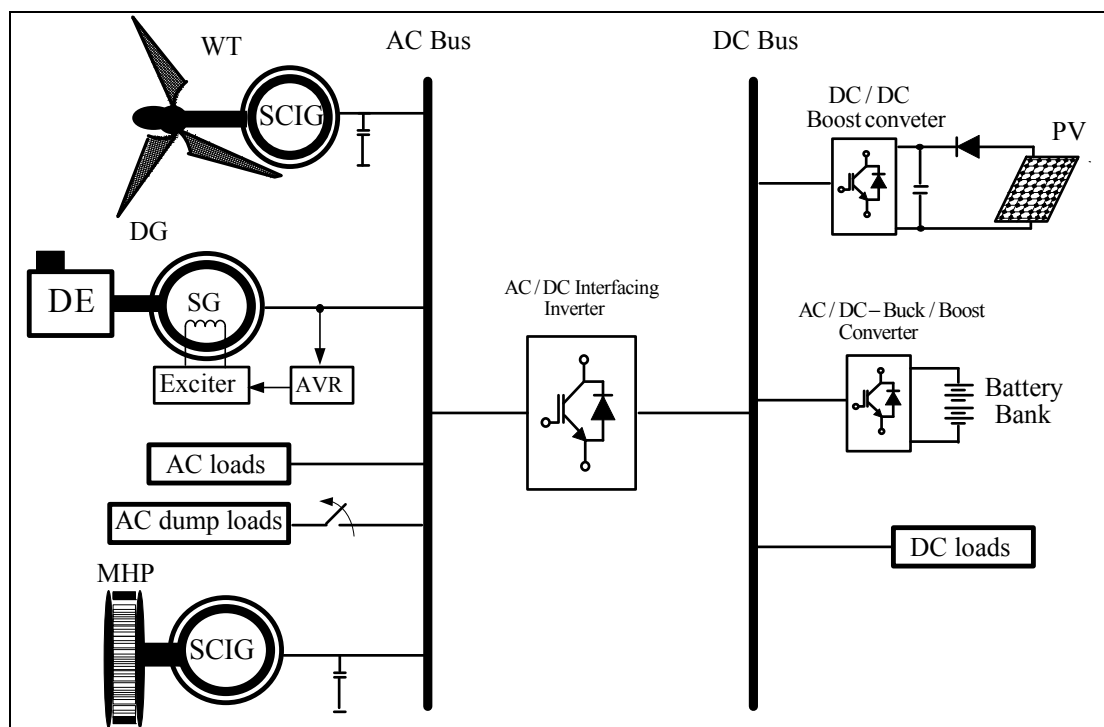


Figure 1.10 Hybrid AC/DC microgrid configuration HSPGS

Thus, application of hybrid AC/DC microgrid configuration allows:

- Elimination of many AC/DC and DC/AC conversion stages, which would in turn result in considerable decrease in component costs and power losses,
- increase in reliability,
- Power quality issues, such as harmonics and unbalances, are not present in this type of configuration.

According to (Peng et al., 2011), AC/DC microgrid configuration has also some drawbacks, which are related to the energy management and control. Furthermore, operation of a hybrid AC/DC microgrid configuration is more complicated compared to AC or DC microgrid configuration.

## **1.5 System Control for Energy Flow Management in Hybrid Standalone Power Generation Systems**

In HSPGS, energy flow management (EFM) is necessary to ensure continuous power supply to the load. According to (Chauhan et Saini, 2014), an optimal energy management strategy ensures a cost effective and reliable integrated energy system with high efficiency. Generally, the control structure in HSPGS for EFM is classified into three categories as:

### **1.5.1 Centralized Control Scheme for Hybrid Standalone Power Generation Systems**

As shown in Fig.1.11, the complete HSPGS contains one master controller and several slave controllers, one for each ESs (Chauhan et Saini, 2014). With this control, sensed data of each ESs are sent to their master controller. Based on this collected data the master controller makes the decision on control action (Valenciaga et Puleston, 2005).

According to (Chauhan et Saini, 2014), this control structure suffers from heavy computation time and sometimes may be subjected to single point failure.

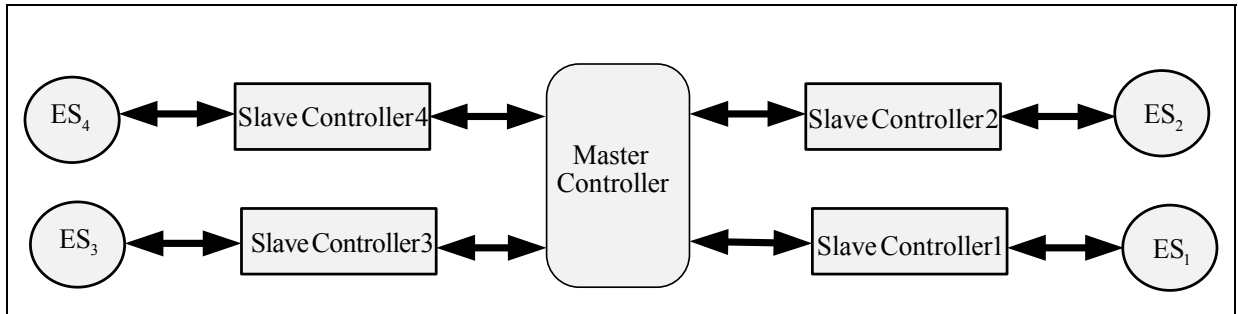


Figure 1.11 Centralized control scheme for HSPGS

### 1.5.2 Distributed Control Scheme for Hybrid Standalone Power Generation Systems

In this control scheme, each ES sends its sensed data to its local controller, and the local controllers communicate with them to take right decision as shown in Fig.1.12 (Chauhan et Saini, 2014).

According to (Lagorse, Simoes et Miraoui, 2009);(Nehrir et al., 2011), for this control arrangement, computation issue is reduced, but communication system among local controller becomes more complicate.

In accordance with (Chauhan et Saini, 2014), artificial algorithms such as, artificial neural network or Multi agent system can solve the problem, which is related to the communication.

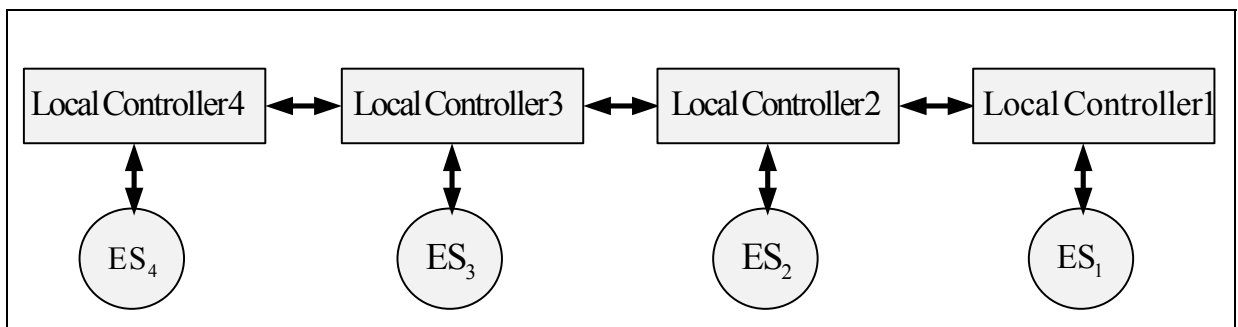


Figure 1.12 Distributed control scheme for HSPGS

### 1.5.3 Hybrid centralized and distributed control scheme for HSPGS

As shown in Fig 1.13, centralized and distributed control schemes are combined together in this proposed control scheme (Chauhan et Saini, 2014) (Hee-Sang et Jatskevich, 2007). All ESs are grouped within integrated system and centralized control is applied within each groupe and distrubited control is used to cordinate each groupe.

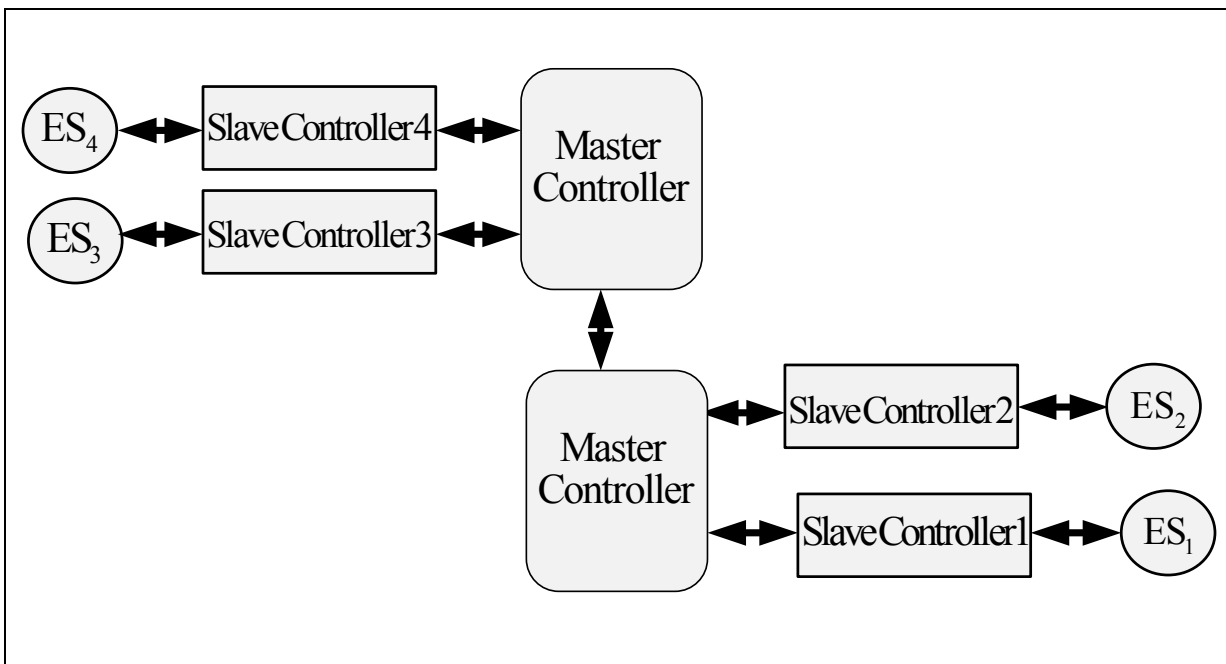


Figure 1.13 Hybrid centralized and distributed control scheme for HSPGS

## 1.6 Problematic

As already indicated that integration of the RESs with the DG in isolated localities have a beneficial impact in terms of cost and availability of energy, as well as, a positive impact on the environment by reducing GHG. On other hand, the intermittency of RESs is one of the major criticisms, which make their integration challenging. Furthermore, to achieve a smooth and successful connection to available local grid, power converters are required, which leads to increased power losses and reduced performance system. Therefore, to make this new

technology more competitive, appropriate designs for SPGS and HSPGS are required. Furthermore, the following issues should also be solved.

### **1.6.1 Problems Related to the Intermittence of the Renewable Energy Sources**

Temperature, humidity, amplitude, topography and atmospheric pressure have impact on the wind speed, implying the power produced by WT is highly dependent on the prediction of wind speed. The generated power from the solar PV array is related to insolation, weather and temperature of the PV cell. Therefore, these RESs are stochastic and intermittent. They are not able to supply continuously power to the connected loads. Seeing that the isolated localities are not connected to the main grid, reliable ESs, such as DG or BESS is suggested to ensure continuous power supply to the load during fluctuation of loads and RESs. Furthermore, start/stop of the DG increase the fuel consumption and decrease the engine life span. With respect to BESS, lead-acid BESS is used in HSPGS, which has a short life cycle and high cost (Bo et al., 2013).

### **1.6.2 Maximization of the Generated Power from Renewable energy sources**

Usually, WTs, solar PV arrays and MHPs are the most used RESs in isolated localities. As for MHP and for economic reason in most of installations, fixed speed generators are employed.

WTs, can operate at variable speed in order to get the maximum power by adjusting the rotor speed optimally. According to (Quincy et Liuchen, 2004); maximum power extraction algorithms can be classified into three main control methods, as shown in Fig 1.14. All these MPPTs control methods are based on rotor position and speed information, which are collected using mechanical sensors. Usually, the use of mechanical sensors leads to increase in cost, hardware complexity and failure rate of the WT (Yue et al., 2013). To reduce this drawback, a variety of optimal position/speed sensorless control strategies have been proposed in the literature (Senjyu et al., 2006); (Xia, Ahmed et Williams, 2011), which are mainly dependent on the mathematical model of the used electrical generators.

According to (Wei, 2012); (Quincy et Liuchen, 2004) these proposed position/speed sensorless control algorithms are unreliable because of simplified computations that use several assumptions, ignorance of parameter variations, as well as, inaccuracy involved with low voltage signal measurement at lower speed.

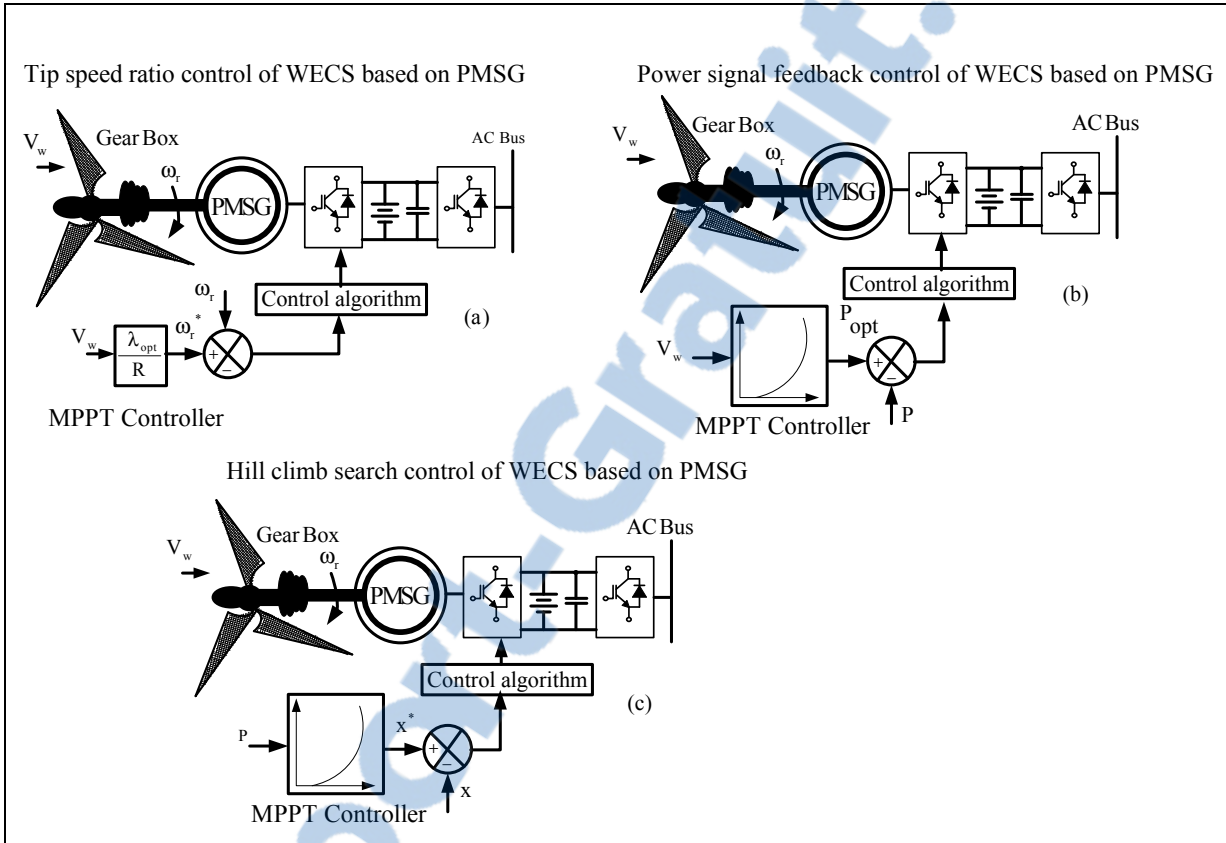


Figure 1.14 MPPT control methods for WT

According to (Logeswaran et SenthilKumar, 2014), the power -voltage characteristic is non-linear and it exhibits multiple peaks including many local peaks and one maximum peak under non-uniform irradiances. Therefore, to track this maximum peak, MPPT is required. To achieve this aim, several MPPT techniques such as, distributed MPPT, Gauss-Newton technique, adaptive perturbation and observation, estimated perturb and perturb, adaptive fuzzy and particle swarm optimization (PSO)-based MPPT are proposed in the literature

(Subudhi et Pradhan, 2013). These proposed are mainly considered complex because of their complexity level on hardware implementation.

### **1.6.3 Fuel Consumption Minimisation for DG**

As already discussed, DE running at fixed speed, which is coupled to the SG has the advantage of simplicity. However, there are some drawbacks, including high level of noise regardless of the power level required by the load, high level of gas emissions even when energy demand is low, poor frequency stability and voltage transients in phases, over dimensioning in case of non-linear or unbalanced loads.

### **1.6.4 Underutilization of Power Electronics Devices Rating**

In HSPGS, several ESs works together, which are tied to the available AC, DC or hybrid AC/DC Bus through power electronics converters, which are rarely utilised up to their rated capacities due to the intermittent nature of wind and solar (Singh et Chandra, 2011). This underutilization of inverter rating effectively increases the cost of power provided by RESs.

### **1.6.5 Synchronization issues between ESs and PCC**

According to the standard *1547.4-2011* (IEEE Guide for Design, Operation, and Integration of Distributed Resource Island Systems with Electric Power Systems, 2011) and (Nikkhajoie et Lasseter, 2009), all ESs must be able to:

- Connect safely to the local grid at the correct frequency and phase,
- Provide power to the connected loads with high quality,
- Disconnect rapidly and safely from the local grid when a fault is detected and reconnect automatically when there is no risk.

### 1.6.5.1 AC Voltage Regulation

Usually, in classical SPGS which uses DG with SG, the AC voltage is regulated by varying the rotor magnetic field using AVR. This method is effective if the DG is the main ES. But, if many ESs are connected to the PCC, reactive power consumption varies continually, implying reactive losses in the system. This full magnitude of the reactive losses cannot be compensated by DG. Therefore, additional equipment is required to regulate the AC voltage at the PCC. Otherwise, this variation will cause serious damage in equipment.

### 1.6.5.2 System Frequency Regulation

Mostly, the system frequency in SPGS, which uses DG is determined by the rotational speed of the generator shaft, and is regulated by keeping the speed of DE constant using its speed governor. However, for MHP driven fixed speed SCIG, ELC is required to regulate the AC voltage and the system frequency. Otherwise, any decrease in local consumer load may accelerate the generator and raise the voltage and frequency, implying large stress at the PCC (Singh, Murthy et Gupta, 2005). Therefore, stable operation of SPGS is dependent on balance between load demand and generation. The difference should be kept equal zero in order to maintain the system frequency constant ( $f=60\text{Hz}$  or  $50\text{Hz}$ ).

### 1.6.5.3 Power Quality Requirement

Usually, the power quality is the major problem in both 'on' and 'off-grid', hence the existing standards in this field are to be applied for both. According to (IEEE Recommended Practices and Requirements for Harmonic Control in Electrical Power Systems, 1993), the injected current in grid should have a total harmonics less than 5%. Otherwise, power quality deterioration many results in increased losses, poor utilization of distribution systems, mal-operation of sensitive equipment and disturbances to nearby consumers, protective devices, and communication systems (Singh, Chandra et Al-Haddad, 2015). Plugging and unplugging RESs and the DG from the SPGS have tendency to create voltage unbalance. Moreover,

continual variation of the loads can also create voltage sag and swell problems (Singh et Chandra, 2011).

## **1.7 Objectives**

Based on the problematics, which are defined in Section 1.6, the main objectives of this research work are;

- Development and design of new topologies based on two energy sources for standalone application, operating at fixed and variable speed using different electrical generators such as, DFIG, SG, SCIG, PMSG, SyRG and PMBLDCG,
- Modeling and control design for the selected HSPGSs topologies,
- Testing the performance of the selected HSPGSs topologies and their developed control algorithms using Matlab/Simulink,
- Implementation in real time of two different topologies.

## **1.8 Methodology**

To achieve the objectives defined in section 1.7, the methodology described below was followed:

Regarding the design of the topologies for HSPGS, several technical and economic aspects were taken into consideration in the proposed topologies to get optimal design, such as, reducing the number of the power converters used, minimisation of the fuel consumption, maximisation of the power provided from RESs, continuous feeding load, stability of the HSPGS during presence of different conditions, protection of the BESS from the overvoltage respecting the *IEEE Std 1547.4-2011* (IEEE Guide for Design, Operation, and Integration of Distributed Resource Island Systems with Electric Power Systems).

As for the SPGS which contain only solar PV array, a detailed modeling and stability analysis are developed. Based on the mathematical models, SMCs are designed to control the DC-DC boost converter in order to get maximum power point tracking (MPPT) from solar PV array and to protect the BESS from overcharging by providing the requested load power demand, and to regulate the output voltage and local grid frequency at the PCC by controlling the CC-VSC. Using MATLAB/Simulink environment, the performance of the proposed scheme and the developed controls algorithms are tested. Furthermore, to validate the simulation results, an experimental scaled prototype is developed in the laboratory.

For HSPGS, which are based on solar PV array and DG, two different topologies are selected for study. The first one uses DE driven fixed speed SG. Dump load and BESS are tied to the DC bus instead of AC side. To get MPPT from solar PV array P&O technique is used. AC voltage and the system frequency regulation, as well as, the power quality improvement at the PCC, are achieved by using the modified instantaneous p-q theory control algorithm. To protect the BESS from the overcharging, dump load is controlled. To optimise fuel consumption by DG and to improve its efficiency, a new controlled switch is added between the PCC and the terminals of DG in order to isolate it from the rest of installation to behave as backup energy source during the day time. The second selected HSPGS uses DE driven variable speed DFIG, the solar PV array is tied to the PCC through two-stage inverters and the rotor of the DFIG is connected to DC bus using AC/DC converter. To achieve MPPT from the solar PV array P&O technique and to regulate the AC voltage and the system frequency, as well as, to improve the power quality at the PCC, indirect control technique is used. To regulate the rotational speed of the DG according to the load power demand, AC/DC converter is controlled using stator flux oriented control technique when the reference DG rotational speed is estimated using reel characteristic of optimal rotational speed of DG versus load curve.

The HSPGS, which are based on solar PV array and MHP, two different topologies are selected for study. The first one uses MHP driven fixed speed SyRG. Dump load and BESS are tied to the DC bus instead of AC side. Solar PV array is tied to the PCC through two-

stage-inverter, which are controlled to achieve MPPT from solar PV array using P&O technique, to regulate the AC voltage and the system frequency, as well as, to improve the power quality at the PCC, respectively using modified instantaneous p-q theory control algorithm. To protect BESS from the overvoltage, dump load is controlled using simple control algorithm which is based on sensing of the DC bus voltage. For the second proposed topology, which consists of MHP driven fixed speed SCIG, solar PV array is tied to the PCC using single stage inverter, which is controlled to achieve MPPT using modified P&O technique. For the AC voltage and power quality improvement at the PCC, Anti-Hebbian learning control algorithm is used. The system frequency is regulated by controlling the DC-DC buck-boost converter.

For HSPGS, which are based on solar PV array and WT, three different architectures are selected for study. The first one uses WT driven fixed speed SCIG. Dump load and BESS are tied to the DC bus instead of the AC side. To achieve MPPT from the solar PV array and to regulate the AC voltage and the system frequency, as well as, improving the power quality at the PCC, DC/DC boost converter and DC/AC inverter are controlled using P&O technique and modified instantaneous p-q theory control algorithm, respectively. To built-up the voltage of SCIG, fixed capacitor Bank is used and the rest of reactive power required to keep the output voltage constant during wind speed change is provided by the DC/AC inverter. The second HSPGS uses WT driven variable speed SyRG. Its stator is connected to the DC bus through AC /DC converter, which is controlled to track the maximum power from WT using rotor oriented control. The MPT from the solar PV array, regulation of the system frequency and the AC voltage, as well as, power quality improvement at the PCC, DC/DC Boost converter and DC/AC inverter are controlled using P&O technique and modified indirect control technique method, respectively. For the BESS protection, dump load is turn on when the BESS becomes fully charged. For the third topology, WT driven variable speed PMBLDCG; detailed mathematical models of HSPGS elements are developed. Based on the mathematical models, SMCs are designed to control the both DC-DC boost converters in order to track maximum power from solar PV array and the WT. To protect BESS from overcharging, new feedback controls are added to the both proposed control algorithms

instead of using dump load. Moreover, a simple and robust nonlinear control using quasi-linear controller (QLC) is proposed to get a fast dynamic tracking response of the AC voltage and the system frequency regulation. Using MATLAB/Simulink environment, the performance of the proposed schemes and the developed control algorithms are tested. Furthermore, to validate the simulation results, an experimental scaled prototype is developed also in laboratory.

Regarding HSPGS, which are based on solar WT array and DG, two different topologies are selected for study. The first one uses WT driven SG and DE driven fixed speed PMSG, BESS and dump load are tied to the PCC through DC/AC inverter, which is controlled using modified SRF control technique to achieve regulation of the AC voltage and system frequency, as well as improving the power quality at the PCC.

DG in this proposed topology used as backup ES, is turn on only if the load power demand is greater than the output WT power. Therefore, to increase its efficiency, it must provide power to the load and charge the BESS, simultaneously. The new proposed topology is based on WT and DE, which are driving variable speed PMBLDCG and PMSG, respectively. They are tied to the DC bus through three-phase diode bridges and DC/DC boost converters and to the PCC through one DC/AC inverter.

The output voltage amplitude and frequency of PMBLDCG are varying under change in the generator speeds caused by wind speed change. Based on the proposed three-phase diode bridge rectifier and boost DC-DC boost converter one convert the variable voltage and variable frequency ac output of PMBLDCG to fixed DC voltage supported by BESS. Therefore, WT based variable speed PMBLDG behaves as solar PV array. However, to achieve MPPT from WT, new technique based on voltage perturbation and change in instantaneous generated power from WT is proposed. Based on this new method, sensing rotor speed of PMBLDG is not required to get the MPPT. For the variable speed DG based on PMSG, to determine the reference electromagnetic torque, the reference rotor speed of the PMSG is estimated using the optimal rotational speed vs load curve characteristic of real DG.

For AC voltage regulation at the PCC, a new control technique based on symmetrical components decomposition of the sensed AC voltages and load currents is used. For the BESS protection from the overcharging, dump load is controlled.



## CHAPITRE 2

### MODELING OF THE ELEMENTS OF STANDALONE POWER GENERATION SYSTEMS

#### 2.1 Introduction

In this chapter modeling of the main elements of SPGS such as, WT, DE and solar PV array, as well as, different electrical generators such as, SCIG, DFIG, PMSG, SG, SyRG and PMBLDCG is discussed. In addition, mathematical models of the power converters are discussed in the end of this chapter.

#### 2.2 Modeling of the Wind Turbine

Usually, WT consists of rotor blades and electrical generator. The rotor blades convert the linear kinetic wind energy into rotational kinetic energy which is converted into electricity using electrical generator. In general, the transmission of power between the hub and the electric generator is realized through a gear box. Therefore, modeling of the WT requires modeling of the wind speed ( $V_{wind}$ ), the aerodynamic behavior of the blades, and mechanical transmission system.

##### 2.2.1 Aerodynamic conversion

Wind turbine rotor is an energy conversion system that converts the kinetic energy of air masses into moving mechanical energy available on the shaft. This kinetic energy is proportional to the mass of air moving at a given speed. Extraction of energy is obtained by slowing the air passing through the rotor, by a force transformation mechanism acting on the blades. Therefore, the power that can be captured is described as follows:

$$P_{wind} = \frac{1}{2} \rho R^2 V_{wind}^3 C_p \quad (2.1)$$

where  $\rho$ ,  $R$ ,  $V_{wind}$ ,  $C_p$  denote the air density, radius of the wind rotor, wind speed and the power coefficient, respectively.

The performance coefficient is dimensionless measure of the efficiency of a WT in extracting the energy content of a wind . According to Betz' Law,  $C_p$  is defined as:

$$C_p = \frac{1}{2}(1+b)(1-(b)^2) \quad (2.2)$$

And

$$b = \frac{V_{wind2}}{V_{wind1}} \quad (2.3)$$

where  $V_{wind1}$  and  $V_{wind2}$  denote wind speed before and after striking the Blade as shown in Fig. 2.1.

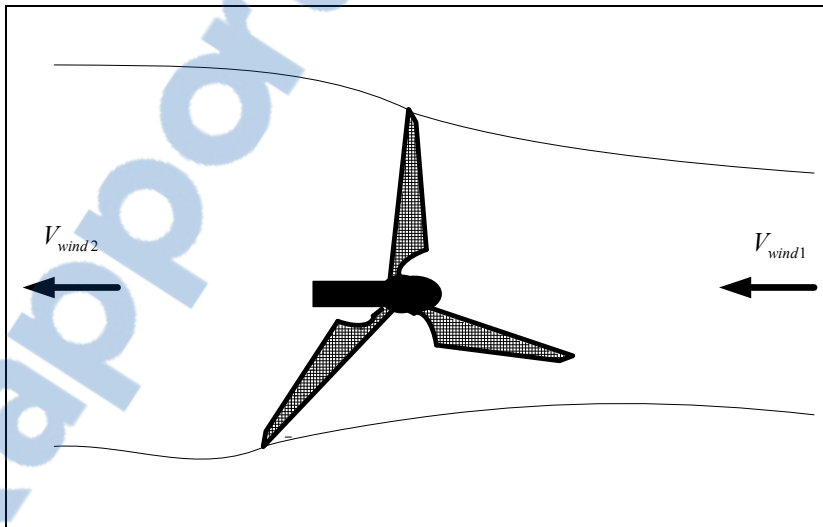


Figure 2.1 Wind speed variation in ideal model of a WT

Therefore, when  $b = 1$ ,  $V_{wind1} = V_{wind2}$  the wind stream is undisturbed, and when  $b=0$ ,  $V_{wind2}=0$ , the turbine stops all the air flow and  $C_p = 0$ , as shown in Fig. 2.2. It is observed that  $C_p$  reaches the maximum around  $b= 0.33$ .

This condition, which is corresponding to the optimal operation, can be obtained also by solving the equation (2.2). Thus, for the maximum, with  $b = 0.33$ , we obtain:

$$C_{p\max} \approx \frac{16}{27} = 0.593 \quad (2.4)$$

This means, the theoretical power fraction that can be extracted from ideal wind stream is equal to 59.3%. Generally, the modern WT's operate at a slight lower practical non-ideal performance coefficient. According to (Fortmann, 2015), the  $C_{Pmax,pract}$  is in the range of;

$$C_{p\max,pract} \approx \frac{2}{5} = 40\% \quad (2.5)$$

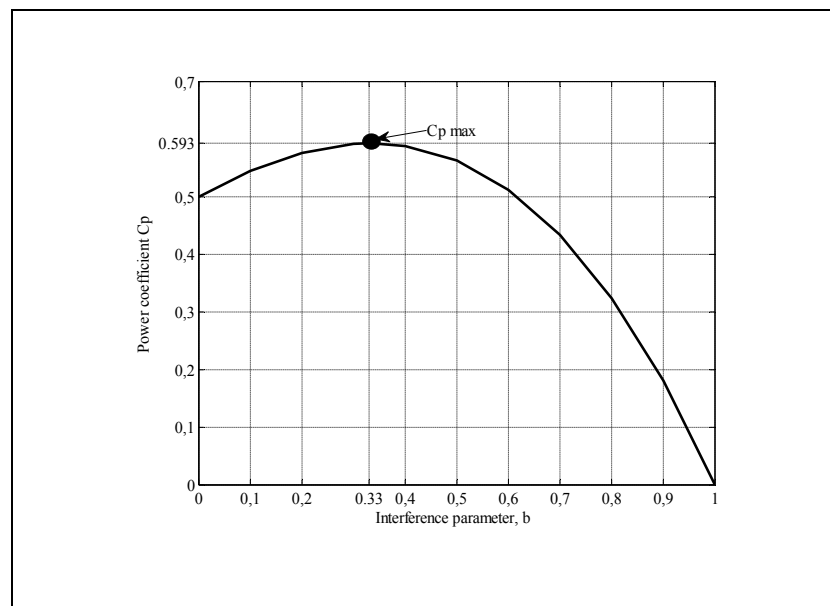


Figure 2.2 Power coefficient  $C_p$  and the interference parameters  $b$

### 2.2.2 Rotor Optimal Tip Speed Ratio

Generally,  $C_p$  is not constant but it depends on the blade pitch angle,  $\beta$ , and the tip speed ratio  $\lambda$ , which is shown in Fig.2.3. The mathematical expression of  $\lambda$  is defined as:

$$TSR = \lambda = \frac{\text{speed of rotor tip}}{\text{wind speed}} = \frac{v}{V_{wind}} = \frac{\omega_R R}{V_{wind}} \quad (2.6)$$

where

$V_{wind}$ : wind speed in (m/sec)

$v = \omega_R R$ : rotor tip speed in (m/s)

$R$ : rotor radius in (m)

$\omega_R = 2\pi f$ : the mechanical angular velocity of the turbine rotor in (rad/s)

$f$ : denote the rotational frequency in Hz, or  $\text{sec}^{-1}$

Therefore, if we consider the turbine aerodynamics, equation (2.1) becomes as follows:

$$P_{wind} = \frac{1}{2} \rho R^2 V_{wind}^3 C_p(\beta, \lambda) \quad (2.7)$$

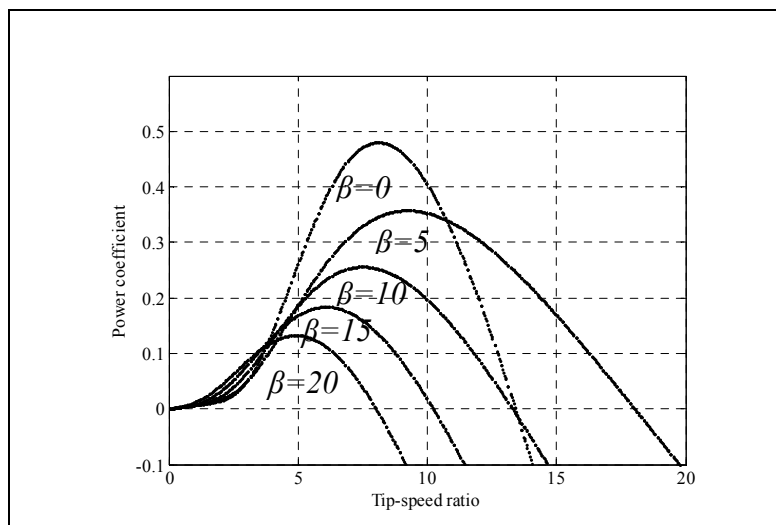


Figure 2.3 Power coefficient- Tip speed ratio Characteristic



It can be observed from Fig.2.3 that to reach the optimal aerodynamic conditions in order to get maximum power out of the wind we must vary the rotor speed. This task is known as Maximum Power Point Tracking (MPPT).

### 2.2.3 Transmission

Usually, the transmission in wind turbine contains slow shaft wind rotor side, gearbox and fast shaft electrical generator side as shown in Fig 2.4. Generally, gearbox is typically used in a wind turbine to increase rotational speed from a low-speed rotor to a higher speed electrical generator. In some applications, WTs have dispensed with a gearbox. In these so-called direct-drive machines, the generator rotor turns at the same speed as the turbine rotor.

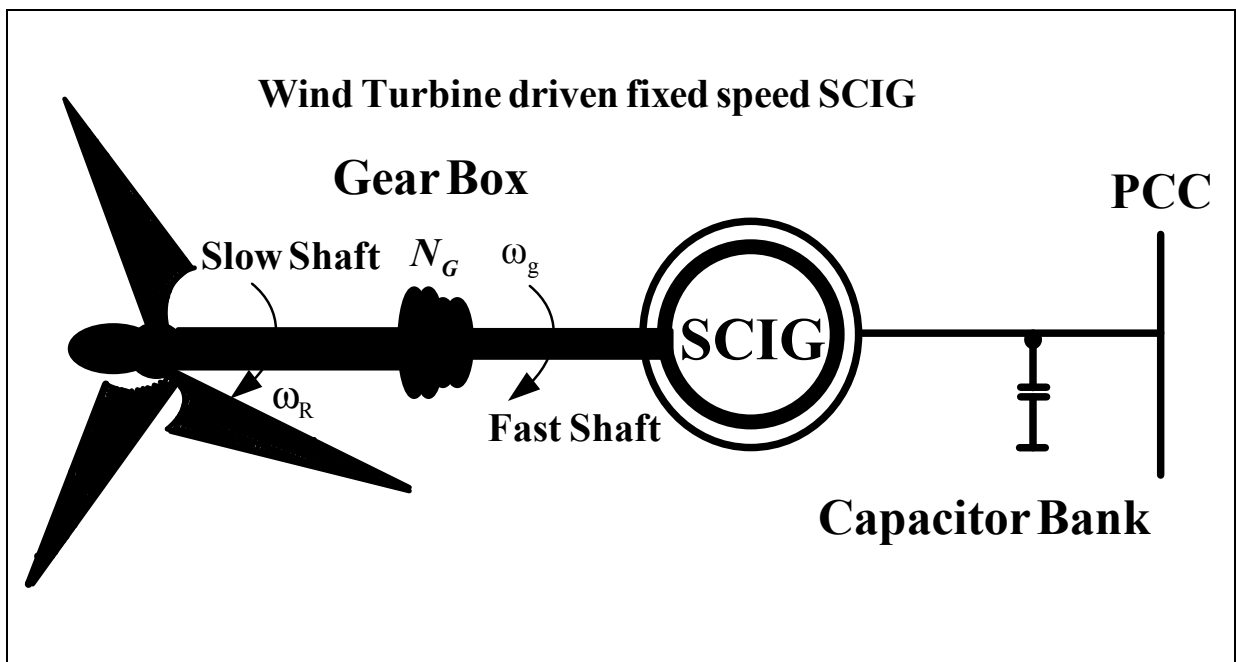


Figure 2.4 Transmission for WT

Finally the detailed mathematical model of the power provided by the WT in the electrical generator side is shown in Fig.2.5.

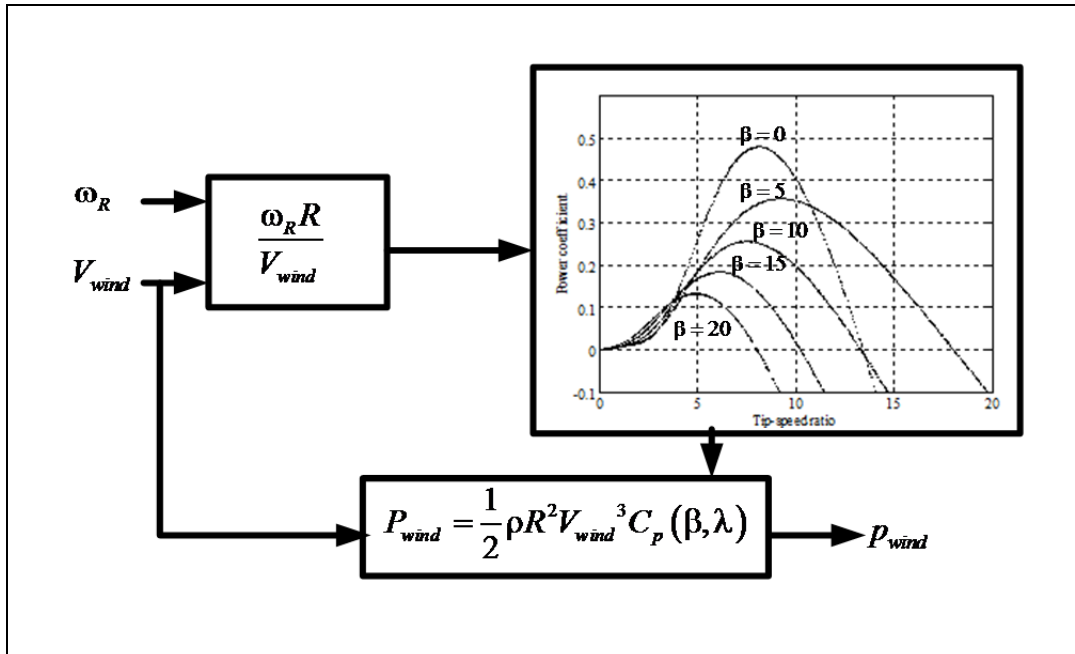


Figure 2.5 Mathematical model of the WT

### 2.3 Modeling of the solar PV array

The photovoltaic conversion system is based on modular blocks as shown in Fig.2.6, which consists of the solar PV array and the DC-DC boost converter.

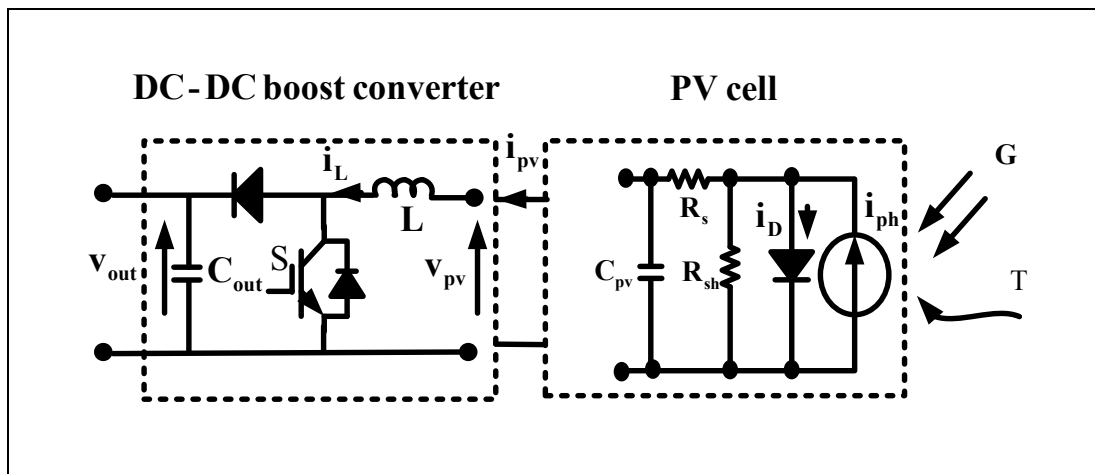


Figure 2.6 Equivalent electrical circuit of the PV cell and the DC-DC boost converter

### 2.3.1 Mathematical model of PV cell

The simplest equivalent circuit of the PV cell consists of the current source in parallel with a diode as shown in Fig.2.6. The current source produces the current  $i_{ph}$ , which depends on impinging radiation  $G$ . Through diode flows the current  $i_D$ , the current  $i_{pv}$ , which flows to load is difference between  $i_{ph}$  and  $i_D$  and it is reduced by the resistance  $R_{sh}$  which represents resistance of cell and connection among cells (Kim et al., 2013; Reis et al., 2015).

$$i_{pv} = i_{ph} - i_D \left[ \text{EXP} \left( \frac{qv_{pv}}{K_b T A} \right) - 1 \right] \quad (2.8)$$

where the light-generated current  $i_{ph}$  and the PV saturation current  $i_D$  are expressed as:

$$i_{ph} = G [i_{scr} + K_i (T - T_r)] \quad (2.9)$$

$$i_D = i_{rr} \left( \frac{T}{T_r} \right)^3 \text{EXP} \left[ \left( \frac{qE_g}{KQA} \right) \left( \frac{1}{T_r} - \frac{1}{T} \right) \right] \quad (2.10)$$

where  $i_{pv}$ ,  $v_{pv}$ ,  $T$ ,  $G$ ,  $T_r$ ,  $i_{rr}$ ,  $i_{scr}$ ,  $K_i$ ,  $q$ ,  $K_b$ ,  $E_g$ ,  $Q$  and  $A$  denote the output current and voltage of PV, cell temperature, radiation, reference temperature, saturation current, short-circuit current, short-circuit temperature coefficient, charge of an electron, Boltzmann's constant, band-gap energy of the material, total electron charge and ideality factor, respectively.

It is observed from Fig.2.7 that the provided power from solar PV array depends on the cell temperature and the insolation. It decreases when the temperature increases, as well as, when insolation decreases. The output PV power (2.11) is based on PV voltage and current. Therefore, to maximize this power, it is necessary to track the maximum power point by controlling the voltage or the current, independently.

$$P_{pv} = v_{pv} i_{pv} \quad (2.11)$$

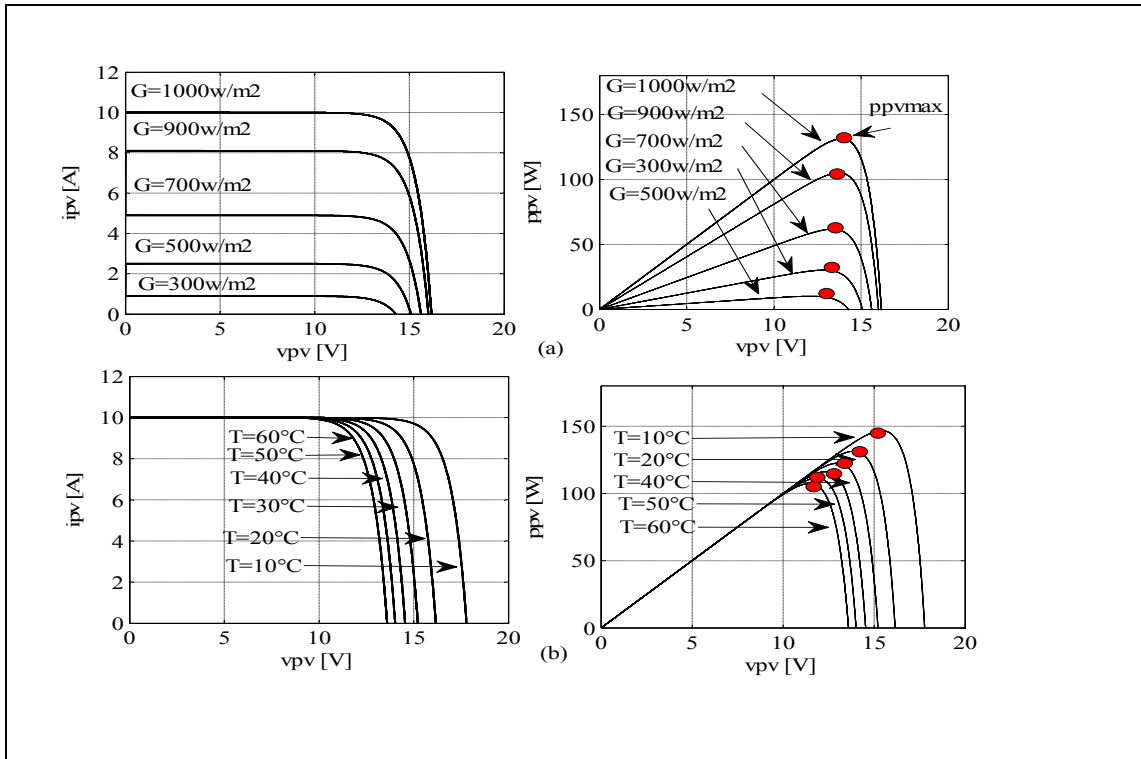


Figure 2.7 Characteristics I-V and V-P of PV for: a) fixed T and varying G  
b) fixed G and varying T

## 2.4 Micro-Hydro power

The power provided by MHP comes from the potential energy of water reservoir driving a water turbine and electrical generator using water column. As shown in Fig.2.8, MHP comprises an intake structure, a penstock, one or more surge tanks and a spiral case (Kishor, Saini et Singh, 2007).

### 2.4.1 Micro-Hydro power and governor model

According to (Kundur, Balu et Lauby, 1994), the turbine and penstock characteristics are determined by three basic equations relating to:

- 1) the velocity of water in the penstock,
- 2) turbine mechanical power,

3) acceleration of water column.

The velocity of the water in the penstock is expressed as:

$$U = K_u G \sqrt{H} \quad (2.12)$$

where  $U$ ,  $G$ ,  $H$  and  $K_u$  denote the water velocity, gate position, hydraulic head at gate and a constant of proportionality, respectively.

A penstock is a sluice or gate or intake structure that controls water flow, or an enclosed pipe that delivers water to hydro turbines and sewerage systems. Penstocks for hydroelectric installations are normally equipped with a gate system and a surge tank. Flow is regulated by turbine operation and is nil when turbines are not in service.

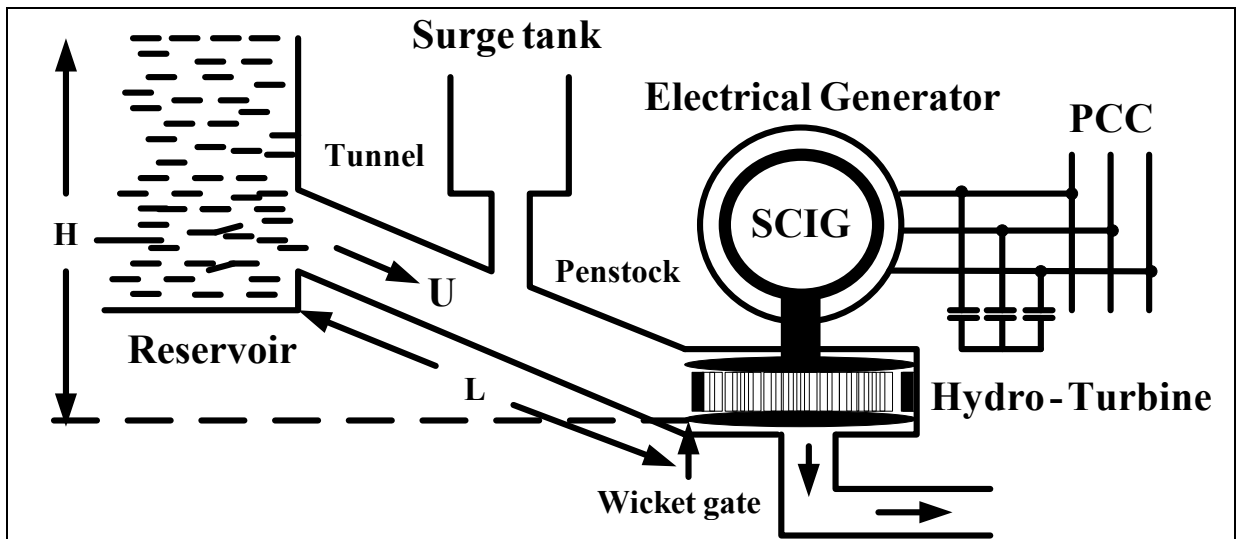


Figure 2.8 Simplified schematic of micro hydro power plant

For small displacement about an operating point, the following expression is obtained:

$$\Delta U = \frac{\partial U}{\partial H} \Delta H + \frac{\partial U}{\partial G} \Delta G \quad (2.13)$$

Replacing the appropriate expressions for the partial derivatives and dividing after by  $U_0 = K_u G_0 \sqrt{H_0}$ , one get the following expression:

$$\frac{\Delta U}{U_0} = \frac{\Delta H}{2H_0} + \frac{\Delta G}{G_0} \quad (2.14)$$

or

$$\Delta \bar{U} = 0.5 \Delta \bar{H} + \Delta \bar{G} \quad (2.15)$$

where the subscript '0' denotes initial steady-state value, 'Δ' represent the small deviation and '–' denotes normalized value based on steady-state operating values.

The turbine mechanical power is of pressure and flow, its expression is written as follows:

$$P_{mH} = K_p H U \quad (2.16)$$

where  $K_p$  is constant of proportionality.

Replacing the appropriate expressions for the partial derivatives and dividing after by  $P_{m0} = K_p H_0 U_0$ , one gets:

$$\frac{\Delta P_{m0}}{P_{m0}} = \frac{\Delta H}{H_0} + \frac{\Delta U}{U_0} \quad (2.17)$$

or

$$\Delta \bar{P}_m = \Delta \bar{H} + \Delta \bar{U} \quad (2.18)$$

Replacing  $\Delta\bar{U}$  by its expression, which is given in (2.15), gives:

$$\Delta\bar{P}_m = 1.5\Delta\bar{H} + \Delta\bar{G} \quad (2.19)$$

And by replacing the expression of  $\Delta\bar{H}$  in (2.19), gives the following expression:

$$\Delta\bar{P}_m = 3\Delta\bar{H} - 2\Delta\bar{G} \quad (2.20)$$

The acceleration of water column depends on Newton's second law of motion and is defined as:

$$(\rho LA) \frac{d\Delta U}{dt} = -A(\rho a_g \Delta H) \quad (2.21)$$

where

$L$ : length of conduit

$A$ : pipe area

$\rho$ : mass density

$a_g$ : acceleration due to the gravity

$\rho LA$ : mass of water in the conduit

$\rho a_g \Delta H$ : incremental change in the pressure at turbine gate.

Dividing the both side of (2.14) by  $A\rho a_g H_0 U_0$ , one obtain the following expression:

$$\frac{LU_0}{a_g H_0} \frac{d}{dt} \left( \frac{\Delta U}{U_0} \right) = -\frac{\Delta H}{H_0} \quad (2.22)$$

or

$$T_w \frac{d\Delta\bar{U}}{dt} = -\Delta\bar{H} \quad (2.23)$$

and

$$T_w = \frac{LU_0}{a_g H_0} \quad (2.24)$$

where  $T_w$  represents the time required for a head  $H_0$  to accelerate the water in the penstock from standstill to velocity  $U_0$ , and it vary with load.

Generally, at full load  $T_w$  is located between 0.5 s and 4.0 s (Kundur, Balu et Lauby, 1994). Replacing (2.15) in (2.23), we obtain:

$$T_w \frac{d\Delta\bar{U}}{dt} = 2(\Delta\bar{G} - \Delta\bar{U}) \quad (2.25)$$

Applying Laplace transformation to (2.25), the following expression is obtained:

$$T_w s \Delta\bar{U} = 2(\Delta\bar{G} - \Delta\bar{U}) \quad (2.26)$$

or

$$\Delta\bar{U} = \frac{\Delta\bar{G}}{1 - \frac{1}{2} T_w s} \quad (2.27)$$

And by Replacing  $\Delta\bar{U}$  given in (2.27) by its expression given in.(2.20) and that of  $\Delta\bar{H}$  given in (2.19) , gives:

$$\frac{\Delta\bar{P}_m}{\Delta\bar{G}} = \frac{1 - T_w s}{1 + \frac{1}{2} T_w s} \quad (2.28)$$

Equation (2.28) represents the transfer function of simplest model of the hydraulic turbine-penstock. It show the output turbine power change in response to a change in gate opening for ideal lossless turbine (Kundur, Balu et Lauby, 1994).

The wicket gate localised at the end of the water column, as shown in Fig. 2.8, is adjustable and pivot open around the periphery of the hydro-turbine, which allows controlling the amount of water admitted to the hydro-turbine.

This gate is adjusted using servo actuator which is controlled by the governor. According to (Kundur, Balu et Lauby, 1994) and (IEEE Guide for the Application of Turbine Governing Systems for Hydroelectric Generating Units, 2011), the modern speed governors for MHP use electro-hydraulic systems. Mostly, the governor is selected to ensure the following tasks:

1. Stable operation during system-islanding conditions or isolated operation,
2. Acceptable speed response for loading and unloading under normal synchronous operation.

As for the stable operation during isolated operation, the optimum choice of the temporary droop  $R_T$  and rest time  $T_R$  is related to the water starting time  $T_w$  and mechanical starting time  $T_M=2H$ .

Where temporary droop  $R_T$  is equal to:

$$R_T = [2.3 - (T_w - 1)0.15] \frac{T_w}{T_M} \quad (2.29)$$

And the rest time is described as:

$$T_R = [5 - (T_w - 1)0.5] T_w \quad (2.30)$$

For loading and unloading during normal interconnection,  $T_R$  should be less than 1.0 s, preferably equal to 0.5s (Kundur, Balu et Lauby, 1994).

The simplified block diagram of the speed-governing system of MHP supplying an isolated load is shown in Fig.2.9, in this representation, the speed governor is consist of transient droop compensation  $G_c(s)$  and main servo time constant  $T_G$ , which is equal to 0.5 s and permanent droop  $R_p$  (Kundur, Balu et Lauby, 1994).

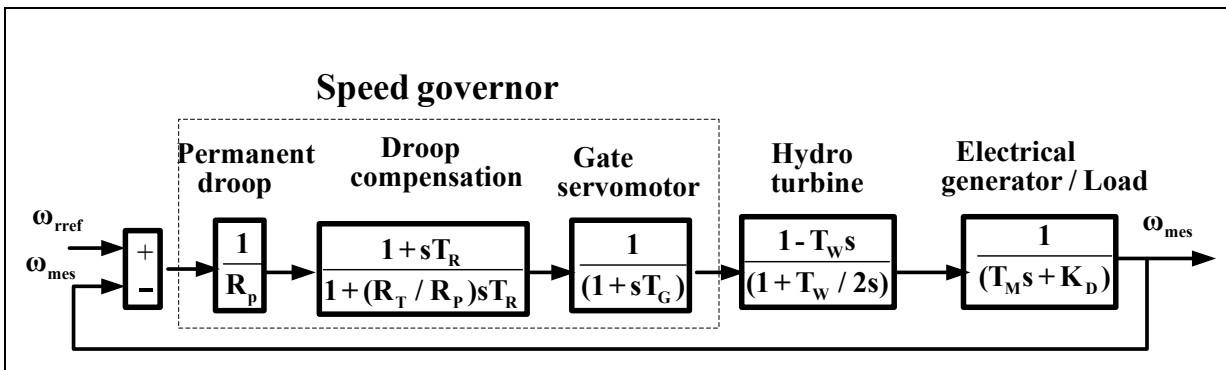


Figure 2.9 Simplified functional block diagram of MHP power plants

## 2.5 Diesel Generator

As already indicate in the previous chapter that DG is consists of electrical generator driven by diesel prime mover, which represents diesel engine (DE).

### 2.5.1 Diesel Prime Mover and Governor

Diesel prime mover is an internal combustion engine; its rotation speed depends on the amount of fuel injected and the load applied to the engine crankshaft. According to (Yeager et Willis, 1993), DE is nonlinear system because it presents dead time and delay, which makes its control complex. The majority of DE models presented in the literature (Leuchter et al., 2009; Pena et al., 2008; Roy, Malik et Hope, 1991) consists of:



1. The fuel inject system,
2. A dead time, which represents the elapsed time until a cylinder produces torque at the engine shaft,
3. Inertia of the rotating parts.

The dynamic of the actuator is represented by a first-order model with a time constant  $\tau_1$  and gain  $K_1$ . Its transfer function is described as follows (Jiang, 1994):

$$\frac{\Phi(s)}{U(s)} = \frac{K_1}{1 + s\tau_1} \quad (2.31)$$

where  $U(s)$  represents the speed error and  $\Phi(s)$  is the amount of fuel injected.

The combustion system is represented as a variable gain  $K_2$ , which depends on the speed and the output power and a dead time  $\tau_2$ . The transfer function of the combustion model is given by:

$$\frac{\Phi(s)}{T_m(s)} = K_2 e^{-s\tau_2} \quad (2.32)$$

where  $T_m(s)$  is the mechanical torque produced by the engine at the common shaft.

The dead time  $\tau_2$  is calculate according to (Pena et al., 2008) as follow:

$$\tau_2 = \frac{60h}{2\Omega n_c} + \frac{60}{4\Omega} \quad (2.33)$$

where  $h=2$  or  $4$  for two or four-stroke engine,  $\Omega$  is the speed in tr/min and  $n_c$  denotes the number of cylinders.

The simplified block diagram of DE and its governor are shown in Fig.2.10.

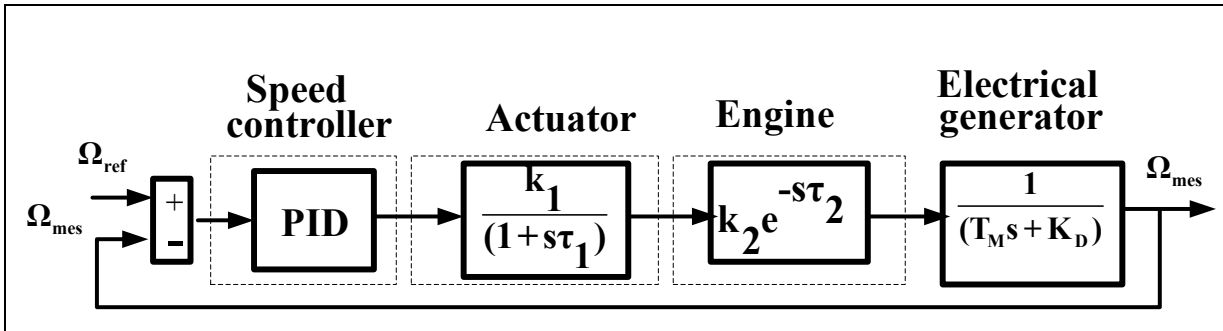


Figure 2.10 Simplified block diagram of the DE and its governor

**2.6 Classification and modeling of the electrical machines**

As already discussed in chapter 1 that ESs such as WT, MHP and DE use electric machines for electricity generation. According to (Chau, Li et Lee, 2012), SG, SCIG, DFIG, and PMSG are the most commonly used generators. Recently, SyRG and PMBLDCG are getting much attention (Singh et Bist, 2015; Singh et Niwas, 2014) because of their high power densities and low costs compared to the conventional electrical machines, for low power applications.

Figure 2.11 shows the proposed classification of the existing electrical machines. The bold types are the electrical machines used in our study.

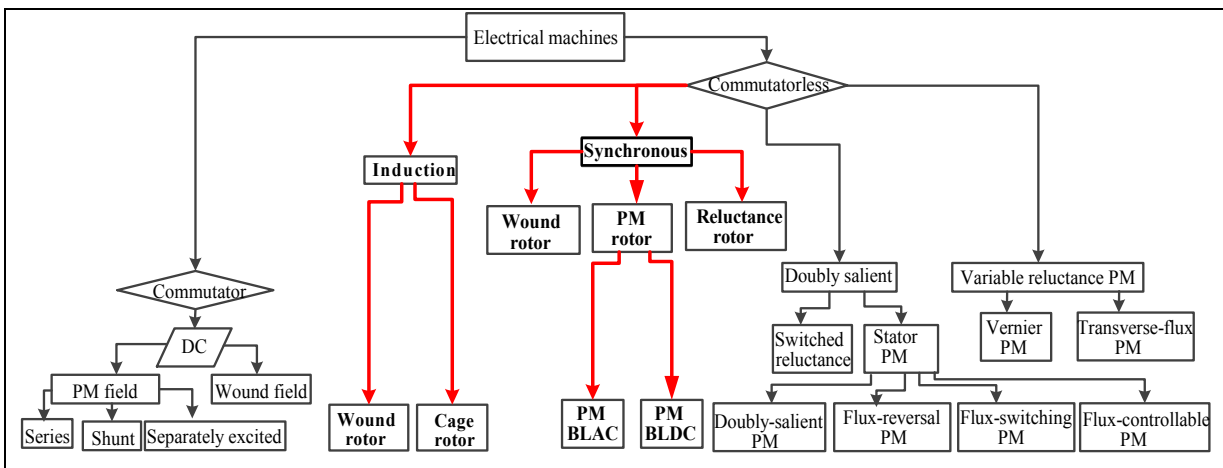


Figure 2.11 Classification of electrical machines

## 2.6.1 Mathematic model of the induction machines

Induction machine has two main parts, a stationary stator which consists of three-phase winding, and rotor. For the rotor, there are two types of rotor windings:

Conventional three-phase windings, which is called wound-rotor, and aluminum bus bars shorted together at the end by two aluminum rings, forming a squirrel-cage shaped circuit.

For steady state analysis the following assumptions are taken (Krause, 1986):

1. The induction machine is linear (no saturation),
2. The stator and rotor windings generate a sinusoidal magnetic field distribution in the gap,
3. Losses in the iron are neglected.

### 2.6.1.1 Mathematical model of the Doubly-Fed induction generator

Using Kirchhoff's and Faraday's laws, the voltage and flux on stator and rotor can be expressed as follows (Krause, 1986):

$$\begin{bmatrix} v_{as} \\ v_{bs} \\ v_{cs} \end{bmatrix} = R_s \begin{bmatrix} i_{as} \\ i_{bs} \\ i_{cs} \end{bmatrix} + \frac{d}{dt} \begin{bmatrix} \lambda_{as} \\ \lambda_{bs} \\ \lambda_{cs} \end{bmatrix} \quad (2.34)$$

And

$$\begin{bmatrix} v_{ar} \\ v_{br} \\ v_{cr} \end{bmatrix} = R_r \begin{bmatrix} i_{ar} \\ i_{br} \\ i_{cr} \end{bmatrix} + \frac{d}{dt} \begin{bmatrix} \lambda_{ar} \\ \lambda_{br} \\ \lambda_{cr} \end{bmatrix} \quad (2.35)$$

where the subscripts «s» and «r» represent the stator and rotor quantities and  $R_s$ ,  $\lambda_s$ ,  $R_r$ ,  $\lambda_r$  denote the resistances and flux linkages of the stator and rotor, respectively.

The flux linkages of the stator and the rotor are defined as:

$$\begin{bmatrix} \lambda_{as} \\ \lambda_{bs} \\ \lambda_{cs} \end{bmatrix} = L_s \begin{bmatrix} i_{as} \\ i_{bs} \\ i_{cs} \end{bmatrix} + L_m \begin{bmatrix} i_{ar} \\ i_{br} \\ i_{cr} \end{bmatrix} \quad (2.36)$$

$$\begin{bmatrix} \lambda_{ar} \\ \lambda_{br} \\ \lambda_{cr} \end{bmatrix} = L_r \begin{bmatrix} i_{ar} \\ i_{br} \\ i_{cr} \end{bmatrix} + L_m^T \begin{bmatrix} i_{as} \\ i_{bs} \\ i_{cs} \end{bmatrix} \quad (2.37)$$

where  $L_s$ ,  $L_r$  and  $L_m$  denote stator, rotor and mutual inductances, which are defined as follows:

$$L_s = \begin{bmatrix} L_{ls} + L_m & -\frac{1}{2}L_m & -\frac{1}{2}L_m \\ -\frac{1}{2}L_m & L_{ls} + L_m & -\frac{1}{2}L_m \\ -\frac{1}{2}L_m & -\frac{1}{2}L_m & L_{ls} + L_m \end{bmatrix} \quad (2.38)$$

$$L_r = \begin{bmatrix} L_{lr} + L_m & -\frac{1}{2}L_m & -\frac{1}{2}L_m \\ -\frac{1}{2}L_m & L_{lr} + L_m & -\frac{1}{2}L_m \\ -\frac{1}{2}L_m & -\frac{1}{2}L_m & L_{lr} + L_m \end{bmatrix} \quad (2.39)$$

$$L_M = L_m \begin{bmatrix} \cos(\theta_r) & \cos\left(\theta_r + \frac{2\pi}{3}\right) & \cos\left(\theta_r - \frac{2\pi}{3}\right) \\ \cos\left(\theta_r - \frac{2\pi}{3}\right) & \cos(\theta_r) & \cos\left(\theta_r + \frac{2\pi}{3}\right) \\ \cos\left(\theta_r + \frac{2\pi}{3}\right) & \cos\left(\theta_r - \frac{2\pi}{3}\right) & \cos(\theta_r) \end{bmatrix} \quad (2.40)$$

where the subscripts « $l$ » and « $m$ » are related to the leakage and the magnetizing inductances,  $L_M$  denotes the mutual inductance between the stator and the rotor and  $\theta_r$  represents the electrical angular displacement, which is expressed as:

$$\theta_r(t) = \int_0^t \omega_r dt + \theta_r(0) \quad (2.41)$$

where  $\theta_r(0)$  represents the position of the rotor at  $t=0$  s.

The torque and rotor speed are related by the following equation:

$$J \frac{d\theta_{rm}}{dt} = T_m - T_e \quad (2.42)$$

where  $J, T_m, T_e$  denote the inertia, the mechanical and the electromagnetic torque of the DFIG and  $\theta_{rm}$  represents the actual angular displacement of the rotor, which is equal to :

$$\theta_r = \left( \frac{2}{P} \right) \theta_{rm} \quad (2.43)$$

where  $P$  is the pole -pair of DFIG.

Usually, the electromagnetic analysis of the electric machines is carried out in a d-q rotating reference frame. Based on this transformation, which is proposed in 1929 by Robert H. Park, three-phase machine can be represented by its equivalent two-phase machine; direct and quadrature axis, which allows elimination of all time-varying inductances. The mathematical model of Park transformation is given as follow:

$$\begin{bmatrix} f_d \\ f_q \\ f_0 \end{bmatrix} = T_{abc \rightarrow dq0} \begin{bmatrix} f_a \\ f_b \\ f_c \end{bmatrix} \quad (2.44)$$

And

$$T_{abc \rightarrow dq0} = \frac{2}{3} \begin{bmatrix} \cos \theta_r & \cos\left(\theta_r - \frac{2\pi}{3}\right) & \cos\left(\theta_r + \frac{2\pi}{3}\right) \\ -\sin \theta_r & -\sin\left(\theta_r - \frac{2\pi}{3}\right) & -\sin\left(\theta_r + \frac{2\pi}{3}\right) \\ \frac{1}{2} & \frac{1}{2} & \frac{1}{2} \end{bmatrix} \quad (2.45)$$

And the inverse Park transformation is given as follow:

$$\begin{bmatrix} f_a \\ f_b \\ f_c \end{bmatrix} = (T_{abc \rightarrow dq0})^{-1} \begin{bmatrix} f_d \\ f_q \\ f_0 \end{bmatrix} \quad (2.46)$$

And

$$(T_{abc \rightarrow dq0})^{-1} = \begin{bmatrix} \cos \theta_r & -\sin \theta_r & 1 \\ \cos\left(\theta_r - \frac{2\pi}{3}\right) & -\sin\left(\theta_r - \frac{2\pi}{3}\right) & 1 \\ \cos\left(\theta_r + \frac{2\pi}{3}\right) & -\sin\left(\theta_r + \frac{2\pi}{3}\right) & 1 \end{bmatrix} \quad (2.47)$$

For balanced system,

$$f_a + f_b + f_c = 0 \quad (2.48)$$

Therefore, the zero-component is equal to zero, which leads that the transformation matrix given in (2.45) and (2.47) can be reduced to:

$$\begin{bmatrix} f_d \\ f_q \end{bmatrix} = T_{abc \rightarrow dq} \begin{bmatrix} f_a \\ f_b \\ f_c \end{bmatrix} = \frac{2}{3} \begin{bmatrix} \cos \theta_r & \cos\left(\theta_r - \frac{2\pi}{3}\right) & \cos\left(\theta_r + \frac{2\pi}{3}\right) \\ -\sin \theta_r & -\sin\left(\theta_r - \frac{2\pi}{3}\right) & -\sin\left(\theta_r + \frac{2\pi}{3}\right) \end{bmatrix} \begin{bmatrix} f_a \\ f_b \\ f_c \end{bmatrix} \quad (2.49)$$

And

$$\begin{bmatrix} f_a \\ f_b \\ f_c \end{bmatrix} = (T_{abc \rightarrow dq0})^{-1} \begin{bmatrix} f_d \\ f_q \end{bmatrix} = \begin{bmatrix} \cos \theta_r & -\sin \theta_r \\ \cos\left(\theta_r - \frac{2\pi}{3}\right) & -\sin\left(\theta_r - \frac{2\pi}{3}\right) \\ \cos\left(\theta_r + \frac{2\pi}{3}\right) & -\sin\left(\theta_r + \frac{2\pi}{3}\right) \end{bmatrix} \begin{bmatrix} f_d \\ f_q \end{bmatrix} \quad (2.50)$$

Applying Park transformation given in (2.49) to stator and rotor voltages equations given in (2.34) and (2.35), one gets:

$$\begin{bmatrix} v_{ds} \\ v_{qs} \end{bmatrix} = R_s \begin{bmatrix} 1 & 0 \\ 0 & 1 \end{bmatrix} \begin{bmatrix} i_{ds} \\ i_{qs} \end{bmatrix} + \omega_s \begin{bmatrix} -1 & 0 \\ 0 & 1 \end{bmatrix} \begin{bmatrix} \lambda_{qs} \\ \lambda_{ds} \end{bmatrix} + \frac{d}{dt} \begin{bmatrix} \lambda_{ds} \\ \lambda_{qs} \end{bmatrix} \quad (2.51)$$

And

$$\begin{bmatrix} v_{dr} \\ v_{qr} \end{bmatrix} = R_r \begin{bmatrix} 1 & 0 \\ 0 & 1 \end{bmatrix} \begin{bmatrix} i_{dr} \\ i_{qr} \end{bmatrix} + (\omega_s - \omega_r) \begin{bmatrix} -1 & 0 \\ 0 & 1 \end{bmatrix} \begin{bmatrix} \lambda_{qr} \\ \lambda_{dr} \end{bmatrix} + \frac{d}{dt} \begin{bmatrix} \lambda_{dr} \\ \lambda_{qr} \end{bmatrix} \quad (2.52)$$

where  $\omega_s$  denote the rotational speed of the synchronous reference and is function of slip  $S$  and the rotor speed. Its expression is given as follows:

$$\omega_s = \frac{\omega_r}{1 - S} \quad (2.53)$$

And by applying Park transformation given in (2.49) to stator and rotor flux linkages equations given in (2.36) and (2.37), one obtains the following expressions:

$$\begin{bmatrix} \lambda_{ds} \\ \lambda_{qs} \end{bmatrix} = \begin{bmatrix} L_{ls} + \frac{3}{2}L_m & 0 \\ 0 & L_{ls} + \frac{3}{2}L_m \end{bmatrix} \begin{bmatrix} i_{ds} \\ i_{qs} \end{bmatrix} + \begin{bmatrix} \frac{3}{2}L_m & 0 \\ 0 & \frac{3}{2}L_m \end{bmatrix} \begin{bmatrix} i_{dr} \\ i_{qr} \end{bmatrix} \quad (2.54)$$

$$\begin{bmatrix} \lambda_{dr} \\ \lambda_{qr} \end{bmatrix} = \begin{bmatrix} L_{lr} + \frac{3}{2}L_m & 0 \\ 0 & L_{lr} + \frac{3}{2}L_m \end{bmatrix} \begin{bmatrix} i_{dr} \\ i_{qr} \end{bmatrix} + \begin{bmatrix} \frac{3}{2}L_m & 0 \\ 0 & \frac{3}{2}L_m \end{bmatrix} \begin{bmatrix} i_{ds} \\ i_{qs} \end{bmatrix} \quad (2.55)$$

The d-axis and q-axis equivalent diagram of the DFIG are shown in the Fig.2.12.

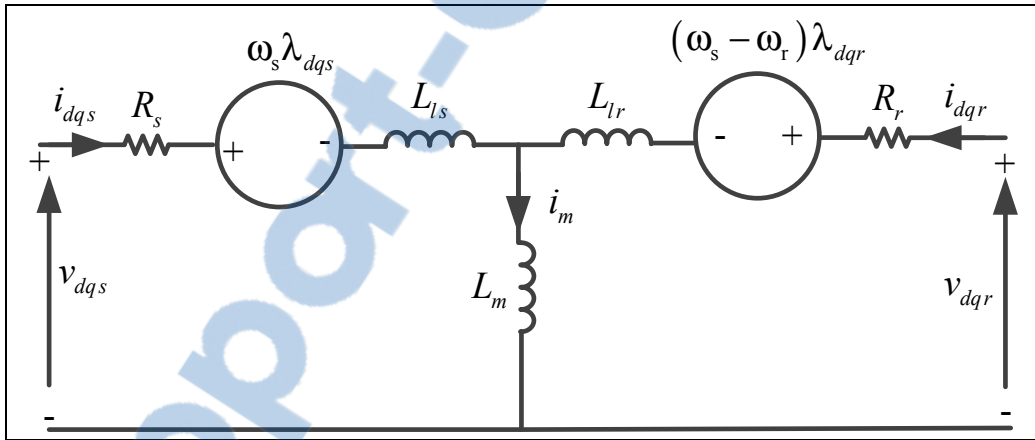


Figure 2.12 Equivalent circuit of DFIG in d-q axis reference frame

The dynamics of the DFIG shaft depends on rotor speed and the electromagnetic torque as given in (2.56):

$$J\left(\frac{2}{P}\right)\frac{d\omega_r}{dt} = T_m - T_e \quad (2.56)$$

where  $P$ ,  $J$ ,  $T_m$  and  $T_e$ , denote, number of pole pairs, inertia, mechanical torque and the electromagnetic torque, respectively:

The electromagnetic torque is expressed as follows:

$$T_e = \left(\frac{3}{2}\right)\left(\frac{P}{2}\right)(\lambda_{dr}i_{qs} - \lambda_{qr}i_{ds}) = \left(\frac{3}{2}\right)\left(\frac{P}{2}\right)(i_{dr}i_{qs} - i_{qr}i_{ds}) \quad (2.57)$$

### 2.6.1.2 Mathematical model of the squirrel cage induction generator

Squirrel cage induction generator (SCIG) has rotor windings short-circuited. Therefore, only stator is connected to the PCC, implying, its rotor voltage is equal to zero. Therefore, its mathematical model is simplified.

The mathematical model used to define the dynamic behavior of SCIG in d-q-axis rotating reference frame is given as follows (Chatelain, 1983):

$$\begin{bmatrix} v_{ds} \\ v_{qs} \end{bmatrix} = R_s \begin{bmatrix} 1 & 0 \\ 0 & 1 \end{bmatrix} \begin{bmatrix} i_{ds} \\ i_{qs} \end{bmatrix} + \omega_s \begin{bmatrix} -1 & 0 \\ 0 & 1 \end{bmatrix} \begin{bmatrix} \lambda_{qs} \\ \lambda_{ds} \end{bmatrix} + \frac{d}{dt} \begin{bmatrix} \lambda_{ds} \\ \lambda_{qs} \end{bmatrix} \quad (2.58)$$

And

$$\begin{bmatrix} v_{dr} \\ v_{qr} \end{bmatrix} = \begin{bmatrix} 0 \\ 0 \end{bmatrix} = R_r \begin{bmatrix} 1 & 0 \\ 0 & 1 \end{bmatrix} \begin{bmatrix} i_{dr} \\ i_{qr} \end{bmatrix} + (\omega_s - \omega_r) \begin{bmatrix} -1 & 0 \\ 0 & 1 \end{bmatrix} \begin{bmatrix} \lambda_{qr} \\ \lambda_{dr} \end{bmatrix} + \frac{d}{dt} \begin{bmatrix} \lambda_{dr} \\ \lambda_{qr} \end{bmatrix} \quad (2.59)$$

The dynamics of the SCIG shaft depends on rotor speed and the electromagnetic torque. Its mathematical model is given as follows:

$$J \left( \frac{2}{P} \right) \frac{d\omega_r}{dt} = T_m - T_e \quad (2.60)$$

where  $P$ ,  $J$ ,  $T_m$  and  $T_e$ , denotes, number of pole, inertia, mechanical torque and the electromagnetic torque, respectively:

The electromagnetic torque is expressed as follows:

$$T_e = \left( \frac{3}{2} \right) \left( \frac{P}{2} \right) (\lambda_{ds} i_{qs} - \lambda_{qs} i_{ds}) \quad (2.61)$$

The d-axis and q-axis equivalent diagram of SCIG are shown in the Fig.2.13.

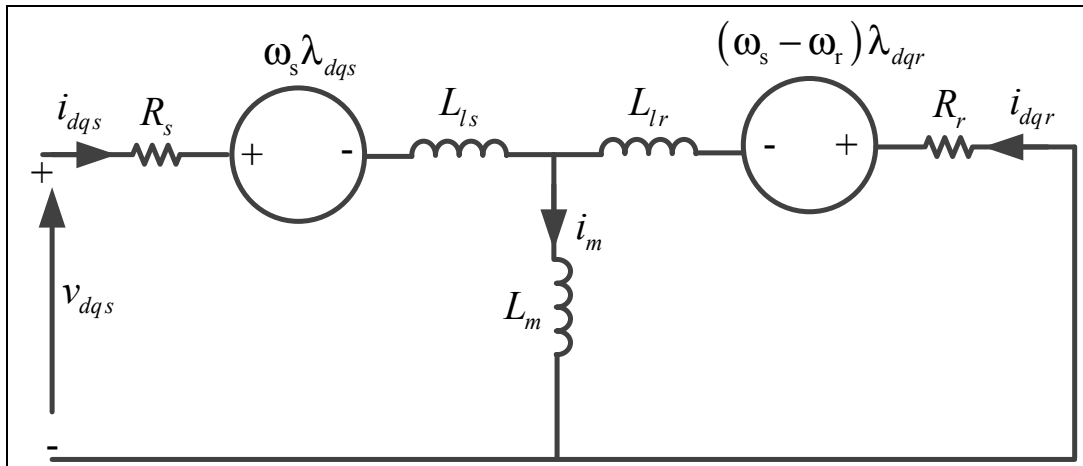


Figure 2.13 Equivalent circuit of SCIG in d-q - axis reference frame

## 2.6.2 Mathematic model of synchronous machine

Mostly, the prime movers as WT, Hydro or DE are connected to the SG. This electrical machine has stationary and mobile parts, which are the stator and rotor respectively as shown in Figs 2.14 (a) and (b). As for the stator circuit, three phase windings a-a', b-b' and c-c' are

distributed in  $120^\circ$ . Regarding, the field winding, which is shown in Fig.2.14 (c), f-f is taken as the direct axis, and the damper windings are permanently short-circuited (Krause et al.).

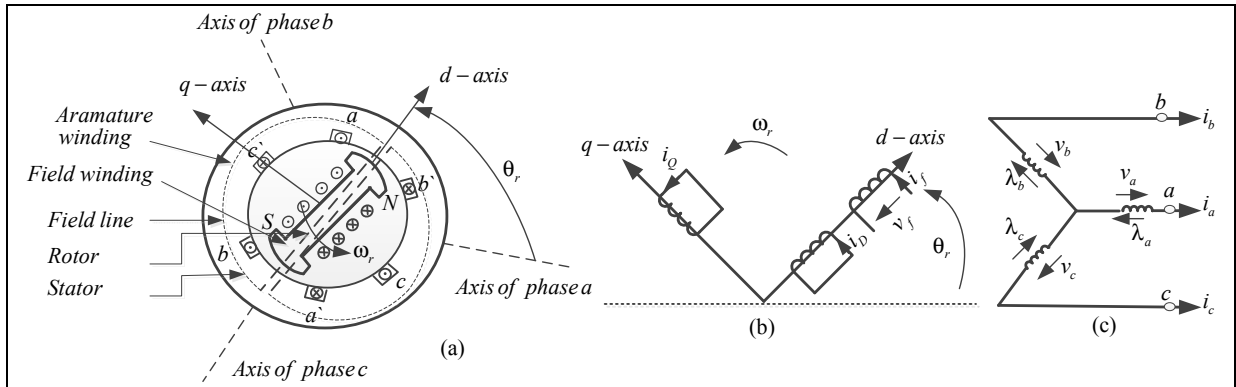


Figure 2.14 (a) schematic diagram of SG, (b) circuit of rotor and (c) circuit of stator

To develop the mathematical model of the SG, one uses the following assumptions, which are given by (Krause et al.):

1. The stator windings are sinusoidally distributed along the air gap,
2. The stator slot has no influence on the rotor inductances,
3. Magnetic hysteresis is negligible,
4. Magnetic saturations are also negligible.

Based on the assumptions given above and by applying Kirchhoff law to the stator, the following equations can be written (Krause et al.):

$$\begin{bmatrix} v_a \\ v_b \\ v_c \end{bmatrix} = \begin{bmatrix} -r_a & & \\ & -r_b & \\ & & -r_c \end{bmatrix} \begin{bmatrix} i_a \\ i_b \\ i_c \end{bmatrix} + \frac{d}{dt} \begin{bmatrix} \lambda_a \\ \lambda_b \\ \lambda_c \end{bmatrix} \quad (2.62)$$

And

$$\begin{bmatrix} v_f \\ 0 \\ 0 \end{bmatrix} = \begin{bmatrix} r_f & & \\ & r_D & \\ & & r_Q \end{bmatrix} \begin{bmatrix} i_f \\ i_D \\ i_Q \end{bmatrix} + \frac{d}{dt} \begin{bmatrix} \lambda_f \\ \lambda_D \\ \lambda_Q \end{bmatrix} \quad (2.63)$$

where  $r_{abc}$ ,  $\lambda_a$ ,  $\lambda_b$  and  $\lambda_c$  denote the resistances and the flux linkages of stator winding of the phases «a, b and c» and  $r_f$ ,  $r_D$ ,  $r_Q$ ,  $\lambda_f$ ,  $\lambda_D$  and  $\lambda_Q$  represent the resistances and the flux linkages of excitation and damper winding, respectively.

The flux linkage in the phase «a» at any instant is expressed as:

$$\lambda_a(t) = -l_{aa}i_a - l_{ab}i_b - l_{ac}i_c + l_{af}i_f + l_{aD}i_D + l_{aQ}i_Q \quad (2.64)$$

The flux linkages of windings of «b» and «c» can be expressed same as (2.64). The stator and the rotor flux linkages of SG are expressed as:

$$\begin{bmatrix} \lambda_a \\ \lambda_b \\ \lambda_c \\ \dots \\ \lambda_f \\ \lambda_D \\ \lambda_Q \end{bmatrix} = \begin{bmatrix} l_{aa} & l_{ab} & l_{ac} & \vdots & l_{af} & l_{aD} & l_{aQ} \\ l_{ba} & l_{bb} & l_{bc} & \vdots & l_{bf} & l_{bD} & l_{bQ} \\ l_{ca} & l_{cb} & l_{cc} & \vdots & l_{cf} & l_{cD} & l_{cQ} \\ \dots & \dots & \dots & \dots & \dots & \dots & \dots \\ l_{fa} & l_{fb} & l_{fc} & \vdots & l_{ff} & l_{fD} & l_{fQ} \\ l_{Da} & l_{Db} & l_{Dc} & \vdots & l_{Df} & l_{DD} & l_{DQ} \\ l_{Qa} & l_{Qb} & l_{Qc} & \vdots & l_{Qf} & l_{QD} & l_{QQ} \end{bmatrix} \begin{bmatrix} -i_a \\ -i_b \\ -i_c \\ \dots \\ i_f \\ i_D \\ i_Q \end{bmatrix} = \begin{bmatrix} \overbrace{L_{SS}}^{Stator} & \vdots & \overbrace{L_{SR}}^{Rotor} \\ \dots & \dots & \dots \\ L_{RS} & \vdots & L_{RR} \end{bmatrix} \begin{bmatrix} -i_a \\ -i_b \\ -i_c \\ \dots \\ i_f \\ i_D \\ i_Q \end{bmatrix} \quad (2.65)$$

The self-inductances  $l_{aa}$ ,  $l_{bb}$  and  $l_{cc}$  due to the air gap magnetic flux are expressed as:

$$l_{aa} = L_{a1} + l_{gaa} = L_{a1} + L_{g0} + L_{aa2} \cos 2(\theta_r) = L_{aa0} + L_{aa2} \cos 2(\theta_r) \quad (2.66)$$

where  $L_{a1}$ ,  $l_{gaa}$  denotes the stator leakage inductance and leakage flux lines, respectively.

In the same manner,  $l_{bb}$  and  $l_{cc}$  are written as follow:

$$l_{bb} = L_{bb0} + L_{bb2} \cos 2\left(\theta_r - \frac{2\pi}{3}\right) \quad (2.67)$$

$$l_{cc} = L_{cc0} + L_{cc2} \cos 2\left(\theta_r + \frac{2\pi}{3}\right) \quad (2.68)$$

Seeing that the windings of the phase «a», «b» and «c» are identical, and with displacement of  $(2\pi/3)$  and  $(-2\pi/3)$ , which leads to:

$$L_{aa0} = L_{bb0} = L_{cc0} \quad \text{and} \quad L_{aa2} = L_{bb2} = L_{cc2}$$

Therefore, (2.67) and (2.68) become as:

$$l_{bb} = L_{aa0} + L_{aa2} \cos 2\left(\theta_r - \frac{2\pi}{3}\right) \quad (2.69)$$

$$l_{cc} = L_{aa0} + L_{aa2} \cos 2\left(\theta_r + \frac{2\pi}{3}\right) \quad (2.70)$$

The variation of stator mutual inductances can be written as follow:

$$l_{ab} = l_{ba} = -L_{ab0} - L_{ab2} \cos\left(2\theta_r + \frac{\pi}{3}\right) \quad (2.71)$$

$$l_{bc} = l_{cb} = -L_{ab0} - L_{ab2} \cos(2\theta_r - \pi) \quad (2.72)$$

$$l_{ca} = l_{ac} = -L_{ab0} - L_{ab2} \cos\left(2\theta_r - \frac{\pi}{3}\right) \quad (2.73)$$

We know also,

$$L_{ab2} = L_{aa2} \text{ and } L_{ab0} \cong \frac{L_{aa2}}{2} \quad (2.74)$$

As for mutual inductance between the stator and the rotor windings are presented as:

$$L_{af} = L_{fa} = L_{md} \cos \theta_r \quad (2.75)$$

$$L_{aD} = L_{Da} = L_{mD} \cos \theta_r \quad (2.76)$$

$$L_{aQ} = L_{Qa} = L_{mQ} \cos \left( \theta_r + \frac{\pi}{2} \right) = -L_{mQ} \sin \theta_r \quad (2.77)$$

The mutual inductances between phase «b» and rotor, as well as, between phase «c» and the rotor are obtained by replacing angle  $\theta_r$  with  $(\theta_r - 2\pi/3)$  and by  $(\theta_r + 2\pi/3)$ .

The rotor self-inductances are constant, and they are represented by following notation:

$$l_{ff} = L_{ff} = L_f$$

$$l_{DD} = L_{DD} = L_D \quad \text{Denote self-inductance of damper windings in the D-axis}$$

$$l_{QQ} = L_{QQ} = L_Q \quad \text{Denote self-inductance of damper windings in the Q-axis}$$

The mutual inductances between the windings in rotor placed on different axes are considered zero. This means,

$$l_{fQ} = l_{Qf} = 0$$

And

$$l_{DQ} = l_{QD} = 0$$

The mutual inductances of the windings in the d-axis (damper D and field f), is equal to;

$$l_{fD} = l_{Df} = L_{fD}$$

Replacing the expression of these inductances into (2.65), one obtained the following matrix:

$$[L_{ss}] = \begin{bmatrix} L_{aa0} + L_{aa2} \cos(2\theta_r) & -L_{ab0} - L_{ab2} \cos\left(2\theta_r + \frac{2\pi}{3}\right) & -L_{ab0} - L_{ab2} \cos\left(2\theta_r - \frac{2\pi}{3}\right) \\ -L_{ab0} - L_{ab2} \cos\left(2\theta_r + \frac{2\pi}{3}\right) & L_{aa} + L_{aa2} \cos\left(2\theta_r - \frac{2\pi}{3}\right) & -L_{ab0} - L_{ab2} \cos(2\theta_r - \pi) \\ -L_{ab0} - L_{ab2} \cos\left(2\theta_r - \frac{2\pi}{3}\right) & -L_{ab0} - L_{ab2} \cos(2\theta_r - \pi) & L_{aa} + L_{aa2} \cos\left(2\theta_r + \frac{2\pi}{3}\right) \end{bmatrix} \quad (2.78)$$

And

$$[L_{sR}] = [L_{SR}]^T = \begin{bmatrix} L_{md} \cos(\theta_r) & L_{mD} \cos(\theta_r) & -L_{mQ} \sin(\theta_r) \\ L_{md} \cos\left(\theta_r - \frac{2\pi}{3}\right) & L_{mD} \cos\left(\theta_r - \frac{2\pi}{3}\right) & -L_{mQ} \sin\left(\theta_r - \frac{2\pi}{3}\right) \\ L_{md} \cos\left(\theta_r + \frac{2\pi}{3}\right) & L_{mD} \cos\left(\theta_r + \frac{2\pi}{3}\right) & -L_{mQ} \sin\left(\theta_r + \frac{2\pi}{3}\right) \end{bmatrix} \quad (2.79)$$

And

$$[L_{RR}] = \begin{bmatrix} L_{ff} & L_{fD} & 0 \\ L_{Df} & L_{DD} & 0 \\ 0 & 0 & -L_{QQ} \end{bmatrix} \quad (2.80)$$

It is observed that expression given in (2.78) and (2.79) depends on the rotor position  $\theta_r$ , which is equal to  $\theta_r = \omega_r t$ , which means that  $L_{SS}(\theta_r)$  and  $L_{SR}(\theta_r)$  are time variable function. Because of this time varying nature of parameters, the study of SG becomes difficult. Therefore, to eliminate all time-varying parameters, one uses Park transformation equation given in (2.49).

Applying Park transformation to (2.62)-(2.63), one obtains the following expressions which represents the stator and rotor voltages of SG in d-q-axis (Krause et al.):

$$\begin{bmatrix} v_d \\ -v_f \\ 0 \end{bmatrix} = - \begin{bmatrix} r & 0 & 0 \\ 0 & r_f & 0 \\ 0 & 0 & r_D \end{bmatrix} \begin{bmatrix} i_d \\ i_f \\ i_D \end{bmatrix} - \begin{bmatrix} \lambda_q \frac{d\theta}{dt} \\ 0 \\ 0 \end{bmatrix} + \begin{bmatrix} \frac{d\lambda_d}{dt} \\ -\frac{d\lambda_f}{dt} \\ \frac{d\lambda_D}{dt} \end{bmatrix} \quad (2.81)$$

And

$$\begin{bmatrix} v_q \\ 0 \end{bmatrix} = \begin{bmatrix} -r & 0 \\ 0 & r_Q \end{bmatrix} \begin{bmatrix} i_q \\ i_Q \end{bmatrix} + \begin{bmatrix} \lambda_d \frac{d\theta_r}{dt} \\ 0 \end{bmatrix} + \begin{bmatrix} \frac{d\lambda_q}{dt} \\ \frac{d\lambda_Q}{dt} \end{bmatrix} \quad (2.82)$$

Where the relationships between flux linkages and currents are expressed as follow:

$$\begin{bmatrix} \lambda_d \\ \lambda_f \\ \lambda_D \end{bmatrix} = \begin{bmatrix} L_d & L_{md} & L_{mD} \\ \frac{3}{2}L_{md} & L_f & L_{fD} \\ \frac{3}{2}L_{mD} & L_{Df} & L_{DD} \end{bmatrix} \begin{bmatrix} i_d \\ i_f \\ i_D \end{bmatrix} \quad (2.83)$$

$$\begin{bmatrix} \lambda_q \\ \lambda_Q \end{bmatrix} = \begin{bmatrix} L_q & L_{mQ} \\ \frac{3}{2}L_{mQ} & L_{QQ} \end{bmatrix} \begin{bmatrix} -i_q \\ i_Q \end{bmatrix} \quad (2.84)$$

The representation of SG windings and its d-q axis equivalent diagrams are shown in Fig.2.15.

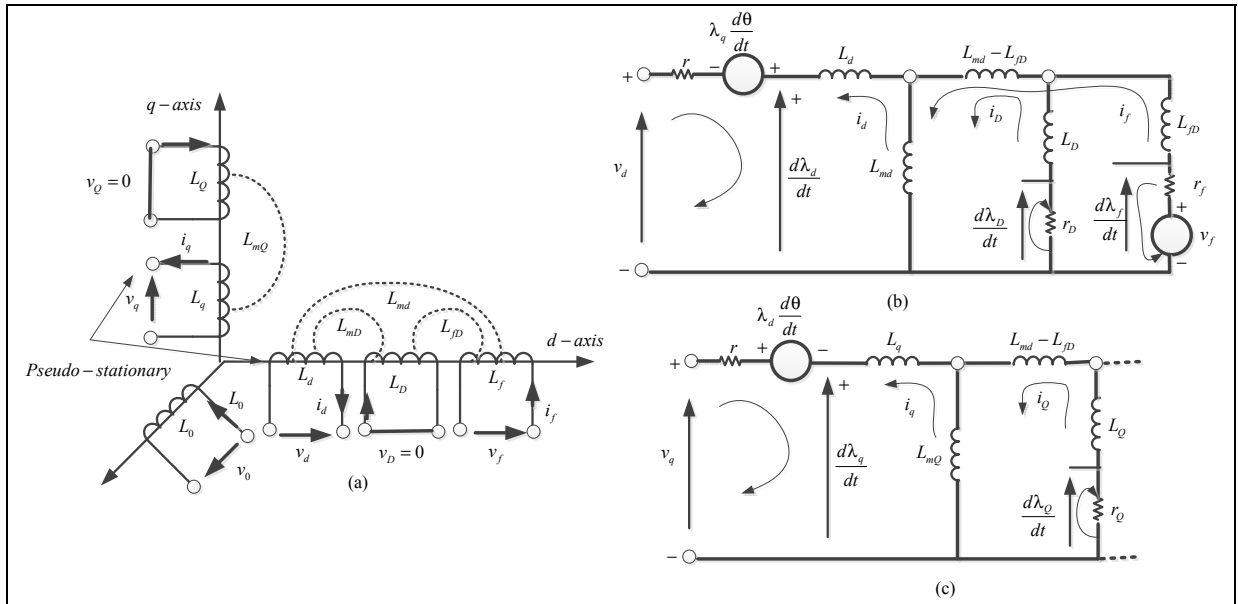


Figure 2.15 Representation of : a) SG windings, b) and c) completed d-q axis windings

The instantaneous three-phase power which is provided by the SG is expressed as:

$$p(t) = v_a i_a + v_b i_b + v_c i_c \quad (2.85)$$

And in d-q-o it is expressed as:

$$p(t) = \frac{3}{2} (v_d i_d + v_q i_q + 2v_o i_o) \quad (2.86)$$

Replacing the voltage component given in (2.81) and (2.82) into (2.86), one obtains:

$$p(t) = \frac{3}{2} \left[ \overbrace{\left( -r i_d - \lambda_q \frac{d\theta_r}{dt} + \frac{d\lambda_d}{dt} \right) i_d}^{\text{Term1}} + \overbrace{\left( -r i_q + \lambda_d \frac{d\theta_r}{dt} + \frac{d\lambda_q}{dt} \right) i_q}^{\text{Term2}} + 2 \overbrace{\left( r i_o + \frac{d\lambda_o}{dt} \right) i_o}^{\text{Term3}} \right] \quad (2.87)$$

And after rearranging of the three terms expressed in (2.87), gives ( Krause et al.):

$$p(t) = \frac{3}{2} \left[ \underbrace{\left( \frac{d\lambda_d}{dt} i_d + \frac{d\lambda_q}{dt} i_q + 2 \frac{d\lambda_o}{dt} i_o \right)}_{\text{Term1}} + \underbrace{\left( \lambda_d i_q - \lambda_q i_d \right) \frac{d\theta_r}{dt}}_{\text{Term2}} - \underbrace{\left( i_d^2 + i_q^2 + 2i_o^2 \right) r}_{\text{Term3}} \right] \quad (2.88)$$

Finally, the electromagnetic torque of the SG is obtained by dividing the second term in (2.88), which represents the power transferred across the air gap by rotor speed ( $\omega_r$ ) as:

$$T_e = \frac{3}{2\omega_r} (\lambda_d i_q - \lambda_q i_d) \frac{d\theta_r}{dt} \quad (2.89)$$

The equation of motion of the SG is given by:

$$J \frac{d^2\theta_r}{dt^2} = T_m - T_e \quad (2.90)$$

where  $J$ ,  $T_m$ ,  $T_e$  and  $\theta_r$  denote the total moment of inertia of the rotor mass in  $\text{kg.m}^2$ , mechanical torque supplied by the prime mover in N.m, electromagnetic torque in N.m and the angular position of the rotor in rad, respectively

### 2.6.3 Mathematical model of permanent magnetic synchronous generator

Permanent magnetic synchronous AC machine is widely used as generator for WT, MHP, as well as, for DE because of the advantages, such as, high power density, reduced copper losses and lower rotor inertia. The only disadvantages of this machine is the possible demagnetization/saturation of magnetic material and parameter variation with passage of time (Singh, 2010).

Its mathematical model is similar to that of SG. Considering the same simplifying assumptions already used to develop the mathematical model of SG, the stator voltage

equations in (abc) stationary reference frame can be expressed in terms of instantaneous currents and stator flux linkages as follows (Krause, Wasynczuk et Sudhoff, 2002b):

$$[v_{abc}] = [r_{abc}][i_{abc}] + \frac{d}{dt}[\lambda_{abc}] \quad (2.91)$$

where  $r_{abc}$  represents the stator resistances and  $\lambda_{abc}$  are the stator flux linkages, which are calculated as :

$$[\lambda_{abc}] = [L][i_{abc}] + [\lambda_{mabc}] \quad (2.92)$$

Where

$$[L] = \begin{bmatrix} \overbrace{L_{ls} + L_{os} + L_{2s} \cos 2\theta_r}^{L_{aa}} & \overbrace{-\frac{L_{os}}{2} + L_{2s} \cos 2\left(\theta_r - \frac{\pi}{3}\right)}^{L_{ab}} & \overbrace{-\frac{L_{os}}{2} + L_{2s} \cos 2\left(\theta_r + \frac{\pi}{3}\right)}^{L_{ac}} \\ \overbrace{-\frac{L_{os}}{2} + L_{2s} \cos 2\left(\theta_r - \frac{\pi}{3}\right)}^{L_{ba}} & \overbrace{L_{ls} + L_{os} + L_{2s} \cos 2\left(\theta_r - \frac{2\pi}{3}\right)}^{L_{bb}} & \overbrace{-\frac{L_{os}}{2} + L_{2s} \cos 2(\theta_r + \pi)}^{L_{bc}} \\ \overbrace{-\frac{L_{os}}{2} + L_{2s} \cos 2\left(\theta_r + \frac{\pi}{3}\right)}^{L_{ca}} & \overbrace{-\frac{L_{os}}{2} + L_{2s} \cos 2(\theta_r + \pi)}^{L_{cb}} & \overbrace{L_{ls} + L_{os} + L_{2s} \cos 2\left(\theta_r + \frac{2\pi}{3}\right)}^{L_{cc}} \end{bmatrix} \quad (2.93)$$

where  $L_{aa}$ ,  $L_{bb}$ ,  $L_{cc}$  represent the stator self-inductance of each phase,  $L_{ls}$ ,  $L_{os}$  and  $L_{2s}$  are the leakage inductances and their magnetizing components, which are function of rotor position  $\theta_r$ .

The mutual inductances ( $\lambda_{mabc}$ ), are described as:

$$[\lambda_{mabc}] = \lambda_m \begin{bmatrix} \cos \theta \\ \cos \left( \theta - \frac{2\pi}{3} \right) \\ \cos \left( \theta - \frac{4\pi}{3} \right) \end{bmatrix} \quad (2.94)$$

It is observed that inductances in (2.93) and (2.94) are a function of time, which complicates the study of this machine. Therefore, to eliminate all time-varying inductances, Park transformation is proposed (Krause, Wasynczuk et Sudhoff, 2002b).

Applying Park transformation given in (2.49) to (2.91) and (2.92), one obtains the following expressions, which represent the stator voltages as function of the stator currents and mutual flux linkage in d-q-0 reference frame.

$$\begin{bmatrix} v_d \\ v_q \\ v_o \end{bmatrix} = \begin{bmatrix} r & 0 & 0 \\ 0 & r & 0 \\ 0 & 0 & r \end{bmatrix} \begin{bmatrix} i_d \\ i_q \\ i_o \end{bmatrix} + \omega_r \begin{bmatrix} 0 & -1 & 0 \\ 1 & 0 & 0 \\ 0 & 0 & 0 \end{bmatrix} \left[ \begin{bmatrix} L_d & 0 & 0 \\ 0 & L_q & 0 \\ 0 & 0 & L_o \end{bmatrix} \begin{bmatrix} i_d \\ i_q \\ i_o \end{bmatrix} + \begin{bmatrix} \lambda_m \\ 0 \\ 0 \end{bmatrix} \right] + \frac{d}{dt} \left[ \begin{bmatrix} L_d & 0 & 0 \\ 0 & L_q & 0 \\ 0 & 0 & L_o \end{bmatrix} \begin{bmatrix} i_d \\ i_q \\ i_o \end{bmatrix} + \begin{bmatrix} \lambda_m \\ 0 \\ 0 \end{bmatrix} \right] \quad (2.95)$$

where  $L_d$ ,  $L_q$ ,  $L_o$  denote direct, in quadrature and homopolar stator inductances, respectively,  $\omega_r$  is the rotor speed in rad/s and  $\lambda_m$  represents mutual inductance.

The stator flux linkage in rotating reference frame is expressed as:

$$\begin{bmatrix} \lambda_d \\ \lambda_q \\ \lambda_o \end{bmatrix} = \begin{bmatrix} L_d & 0 & 0 \\ 0 & L_q & 0 \\ 0 & 0 & L_o \end{bmatrix} \begin{bmatrix} i_d \\ i_q \\ i_o \end{bmatrix} + \begin{bmatrix} \lambda_{dm} \\ \lambda_{qm} \\ \lambda_{om} \end{bmatrix} \quad (2.96)$$

The d-q axis equivalents diagrams of PMSG are shown in Fig 2.16. For this representation, one considers the balanced operation of the PMSG that is why the zero sequence equation is neglected.

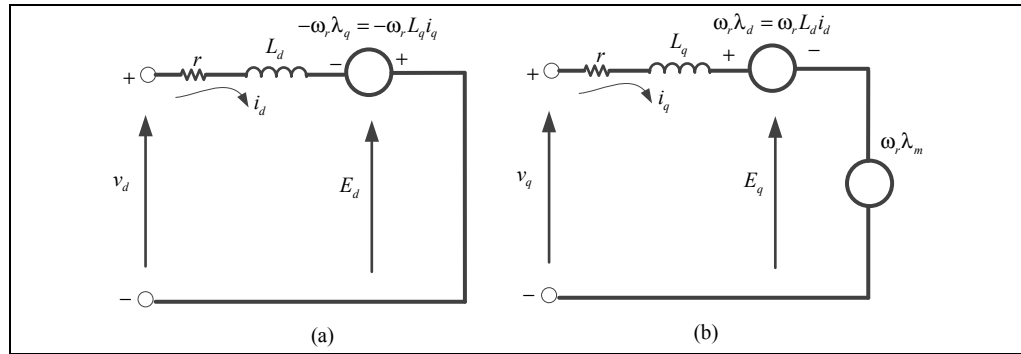


Figure 2.16 Equivalent circuit of the PMSG: a) d-axis and b) q-axis

Finally, the mechanical power developed by the PMSG is expressed as:

$$P_{mec} = \frac{3}{2} (\omega_r \lambda_d i_q - \omega_r \lambda_q i_d) \quad (2.97)$$

And the electromagnetic torque is obtained by dividing (2.97) by the mechanical speed  $\omega_m$  as:

$$T_e = \frac{P_{mec}}{\omega_m} = \frac{P_{mec}}{\omega_r} \left( \frac{P}{2} \right) = \frac{3}{2} \left( \frac{P}{2} \right) (\lambda_d i_q - \lambda_q i_d) \quad (2.98)$$

Replacing (2.96) in (2.98) gives the following expression:

$$T_e = \frac{3}{2} \left( \frac{P}{2} \right) (\lambda_m i_q - (L_q - L_d) i_q i_d) \quad (2.99)$$

The motion expression of the PMSG is described as follows (Krause, Wasynczuk et Sudhoff, 2002b):

$$T_e = J \left( \frac{P}{2} \right) \frac{d}{dt} \omega_r + B \left( \frac{P}{2} \right) \omega_r + T_L \quad (2.100)$$

Where

J: the inertia of the rotor, which is expressed by  $\text{kg.m}^2$

$T_L$ : the torque load is positive when machine is connected as motor and is negative if is working as generator. It has the units N.m.

B: the damping coefficient is constant and it has the units N.m.s/rad According to (Fitzgerald, Kingsley et Umans, 2003), this constant is small and often neglected.

#### 2.6.4 Mathematical model of Permanent Magnetic Brushless Direct Current Generator

Recently, permanent magnet brushless direct current generator (PMBLDCG) is receiving more attention in several applications due to their advantages, such as, (Romerl Martinez et al., 2015):

- 1) High power density,
- 2) High efficiency,
- 3) Simpler winding distribution,
- 4) More fault tolerance.

PMBLDCG is quite similar to PMSG; they have the same structure and the same components. The difference between PMSG and PMBLDCG is indicated in the Table 2-1.

Table 2.1 Classification of PMSG and BLDCG

Property	PMBLDCG	PMSG
Phase current excitation	Trapezoidal	Sinusoidal
Flux density	Square	Sinusoidal
Phase back EMF	Trapezoidal	Sinusoidal
Power and torque	Constant	Constant

Based on the classification given in Table 2-1 and the waveforms, which are shown in Fig.2.17, PMBLDCG is characterized by trapezoidal form of the phase current and the phase back EMF , contrariwise in the PMSG, which are sinusoidal.

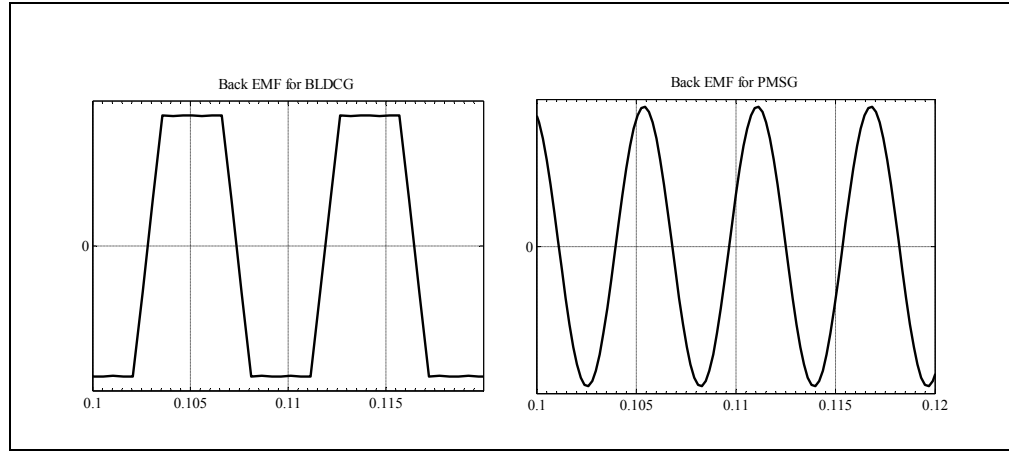


Figure 2.17 Phase back EMF waveforms of PMBLDCG and PMSG

Regarding the mathematical model of the PMBLDCG authors in (Krishnan, 2010; Skvarenina, 2002) say that the transformation of this mathematical model into d-q-axis model is cumbersome, and is not applicable, because of no sinusoidal nature of the back-EMF and current waveforms, as shown in Fig.2.17. Therefore, it is easier to use the phase-variable approach for modeling and simulation.

The standard model of the PMBLDC machine is expressed as follow (Krishnan, 2010):

$$\begin{bmatrix} v_{as} \\ v_{bs} \\ v_{cs} \end{bmatrix} = \begin{bmatrix} R_s & 0 & 0 \\ 0 & R_s & 0 \\ 0 & 0 & R_s \end{bmatrix} \begin{bmatrix} i_{as} \\ i_{bs} \\ i_{cs} \end{bmatrix} + \frac{d}{dt} \begin{bmatrix} L-M & 0 & 0 \\ 0 & L-M & 0 \\ 0 & 0 & L-M \end{bmatrix} \begin{bmatrix} i_{as} \\ i_{bs} \\ i_{cs} \end{bmatrix} + \begin{bmatrix} e_{as} \\ e_{bs} \\ e_{cs} \end{bmatrix} \quad (2.101)$$

where  $v_{abcs}$ ,  $i_{abcs}$ ,  $R_s$ ,  $L$ ,  $M$ ,  $e_{abcs}$  denote phase stator voltages, phase stator currents, stator resistance per phase, which assumed to be equal for all three phases, self-inductance of each

phase, the mutual inductance between any two phases, and the phase back-EMF voltages, which are induced by the kinetics of rotor magnets.

The back-EMF voltages are expressed as:

$$\begin{bmatrix} e_{as} \\ e_{bs} \\ e_{cs} \end{bmatrix} = \frac{d}{dt} \begin{bmatrix} \lambda_{ra} \\ \lambda_{rb} \\ \lambda_{rb} \end{bmatrix} = \omega_m K_e \begin{bmatrix} f_{as}(\theta_r) \\ f_{bs}(\theta_r) \\ f_{cs}(\theta_r) \end{bmatrix} \quad (2.102)$$

Where

$\lambda_{abcr}$ : the linkage magnetic fluxes of the rotor magnets with stator coils,

$K_e$ : the back-EMF coefficient,

$\theta_r$ : the rotor position,

$f_{abcs}(\theta_r)$ : the normalized functions of the back-EMF with a unity peak value.

The electromagnetic torque is expressed as:

$$T_e = [e_{as}i_{as} + e_{bs}i_{bs} + e_{cs}i_{cs}] \frac{1}{\omega_m} = K_e [f_{as}(\theta_r)i_{as} + f_{bs}(\theta_r)i_{bs} + f_{cs}(\theta_r)i_{cs}] \quad (2.103)$$

And the equation of motion is defined as:

$$J \frac{d\omega_m}{dt} + B\omega_m = T_e - T_L \quad (2.104)$$

where  $J, B, T_L$  and  $\omega_m$  denote the inertia, friction coefficient, load torque and mechanical rotor speed, which is given as below:

$$\frac{d\theta_r}{dt} = \frac{P}{2} \omega_m \quad (2.105)$$

where  $P$  is the number of poles.

### 2.6.5 Mathematical model of Synchronous Reluctance Generator

Recently, synchronous reluctance machine (SyRM) has received more attention in certain applications, which requires high speed such as, flywheel energy storage system (Jae-Do, Kalev et Hofmann, 2008). This machine is inexpensive because of the nonexistence of windings and permanent magnets on the rotor. According to (Hofmann et Sanders, 2000), SyRM has following advantages over permanent-magnet machines:

1. There is no concern with demagnetization,
2. This machine has zero spinning losses when the torque is being generated by the machine, which is not the case for the permanent magnet machines with a stator.
3. Is robust compared to squirrel cage induction machine,
4. Less rotor losses than induction machine as rotor rotates at synchronous speed, thus rotor currents are negligible,
5. The output frequency is directly proportional to the speed of the shaft. No slip term
6. Better frequency regulation property than induction generator if is used as generator.

The main challenge of SyRM, is the voltage regulation and the high excitation current. To solve this problem, capacitor bank is required (Abu-Elhaija et Muetze, 2013). Figure 2.18 shows the d and q-axis equivalent circuits of SyRM (Sharaf-Eldin et al., 1999).

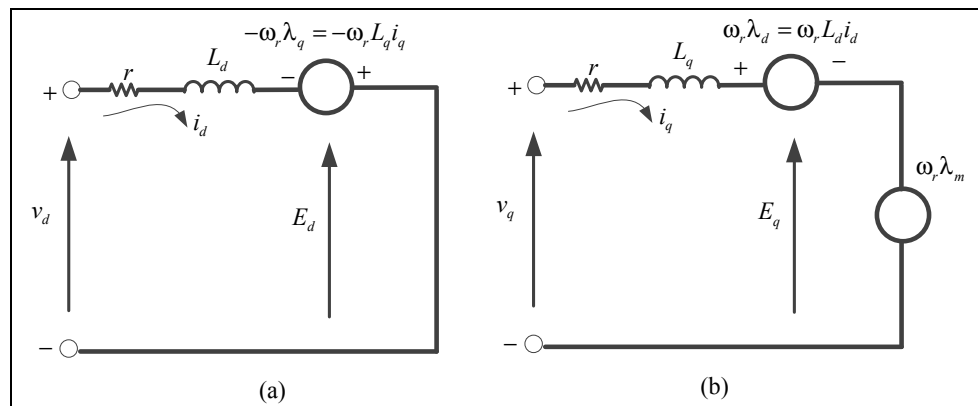


Figure 2.18 Equivalent circuit of SyRM : a) d-axis and b) q-axis

The mathematical model of the SyRM in synchronously rotating reference frame is expressed by the following equations, which ignores the core loss equivalent resistance:

$$v_d = ri_d + \frac{d\lambda_d}{dt} - \omega_r \lambda_q \quad (2.106)$$

$$v_q = ri_q + \frac{d\lambda_q}{dt} + \omega_r \lambda_d \quad (2.107)$$

where  $r$ ,  $i_d$ ,  $i_q$ ,  $\omega_r$ ,  $\lambda_d$  and  $\lambda_q$  denotes the stator resistance, d-axis current, q-axis current, rotor speed, d-axis flux, and q-axis flux, respectively.

If we ignore the core losses and the saturation, the fluxes equations are expressed as follows:

$$\lambda_d = L_{ls}i_d + L_{md}i_d = L_d i_d \quad (2.108)$$

$$\lambda_q = L_{ls}i_q + L_{mq}i_q = L_q i_q \quad (2.109)$$

where  $L_d$  and  $L_q$  denote d-axis and the q-axis inductance.

The electromagnetic torque is expressed as follows:

$$T_e = \frac{3}{2} P i_d i_q (L_d - L_q) \quad (2.110)$$

where  $P$  is the number of pole pairs.

And the motion is defined as:

$$J \frac{d\omega_m}{dt} + B\omega_m = T_e - T_L \quad (2.111)$$

where  $J$ ,  $B$ ,  $T_L$  and  $\omega_m$  denote the inertia, friction coefficient, load torque and mechanical rotor speed.

## 2.7 Power Electronics Interface

As already indicate before, that ESs, such as, WT and solar PV array produce energy only when the wind is blowing and the sun is shining. These sources, they are intermittent; they cannot dispatch energy directly to the load. Therefore, power electronics converters are required to convert the power at the desired voltage and frequency for AC RESs and at the desired DC voltage for the DC RES(Chakraborty, Kramer et Kroposki, 2009).Therefore, selection and design of the power electronics depends on the nature of RESs. Generally, bidirectional DC/AC inverters as shown in Fig.2.19 (a) are the most generic for all RESs (AC and DC).

The configuration shown in Fig. 2.19 (b) is preferred for variable speed generators such as, PMSG, DFIG, SCIG, SG, SyRG and PMBLDCG. The configuration shown in Fig.2.19 (c) is ideal choice for small-scale applications, which use electrical generators such as PMSG or PMBLDCG wherein external rotor excitation is not required. Therefore, only three-phase diode-bridge and DC/DC boost converter can be used to control the rotor speed of these generators, instead of full controlled three-phase converter. Regarding, PV array, DC/DC converter as shown in Fig.2.19 (d) is required to connect the PV array to the DC bus. Usually, this converter is controlled to get the maximum power from solar PV array and to regulate its output DC voltage.

As already indicated, BESS is required in SPGS. This ES is DC by nature, DC/DC buck-boost converter as shown in Fig.2.19 (e) is required to charge and discharge this element and to tie it to the DC bus.

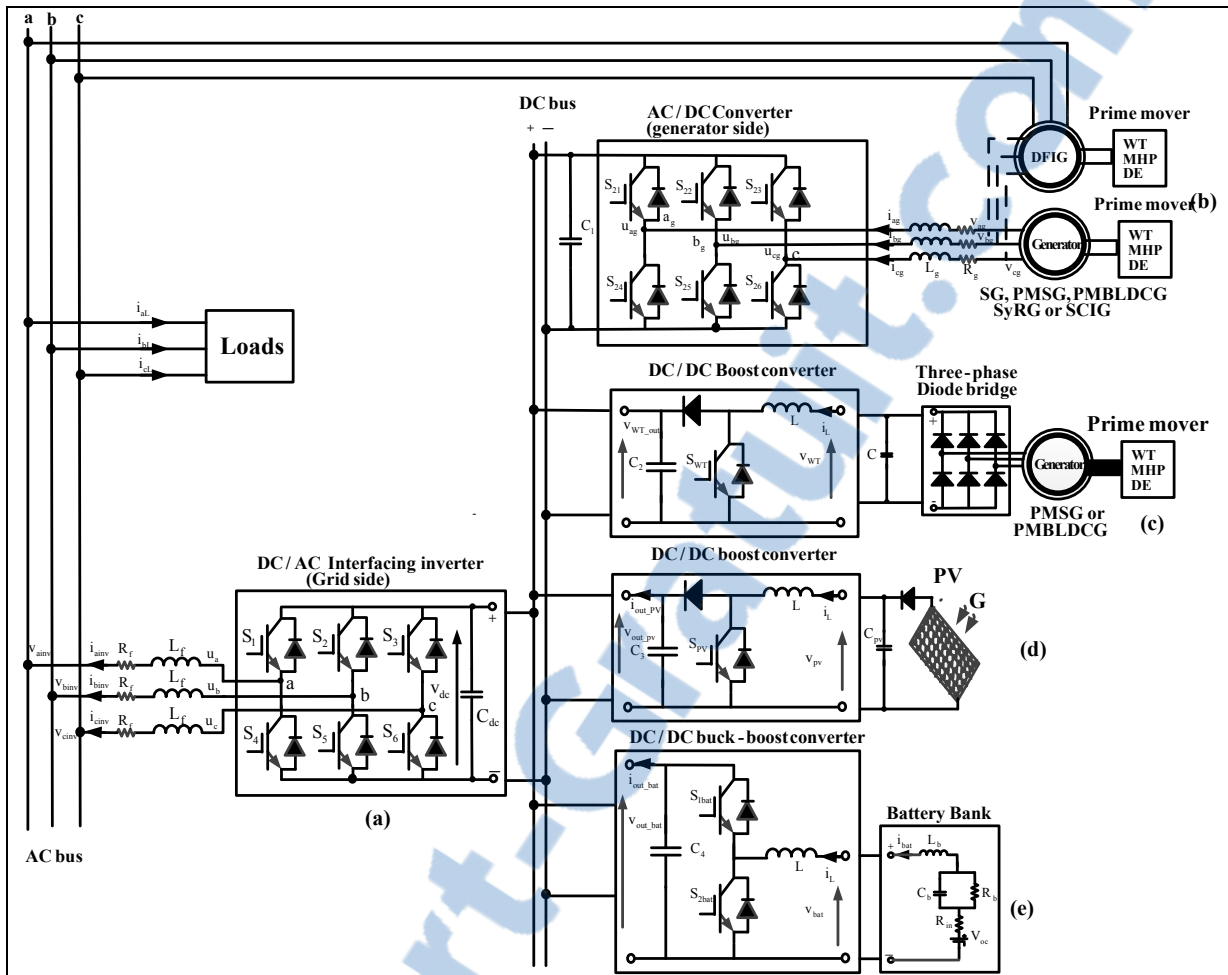


Figure 2.19 Power converters for SPGS and HSPGS

### 2.7.1 Modeling of the DC/AC inverter

The system equations for the DC/AC inverter and for AC/DC converter, which are shown in Figs 2.19 (a) and (b), respectively, are similar. The only difference between both models is the power sign (Alepuz et al., 2006).

Therefore, the voltage equations of the AC side, as shown in Fig.2.19 (a) are expressed as:

$$\begin{bmatrix} v_{ainv} \\ v_{binv} \\ v_{cinv} \end{bmatrix} = \begin{bmatrix} -R_f & 0 & 0 \\ 0 & -R_f & 0 \\ 0 & 0 & -R_f \end{bmatrix} \begin{bmatrix} i_{ainv} \\ i_{binv} \\ i_{cinv} \end{bmatrix} - \begin{bmatrix} L_f & 0 & 0 \\ 0 & L_f & 0 \\ 0 & 0 & L_f \end{bmatrix} \begin{bmatrix} \frac{di_{ainv}}{dt} \\ \frac{di_{binv}}{dt} \\ \frac{di_{cinv}}{dt} \end{bmatrix} + \begin{bmatrix} u_a \\ u_b \\ u_c \end{bmatrix} \quad (2.112)$$

And

$$\begin{bmatrix} u_a \\ u_b \\ u_c \end{bmatrix} = \frac{V_{dc}}{3} \begin{bmatrix} (2S_1 - S_2 - S_3) \\ (2S_2 - S_1 - S_3) \\ (2S_3 - S_1 - S_2) \end{bmatrix} \quad (2.113)$$

where  $S_1, S_2, S_3$  denote the switching positions of each phase for AC side and  $V_{dc}$  represents the DC voltage.

In the same way, the voltage equations for converter generator side, which is shown in Fig.2.19 (b), are expressed as:

$$\begin{bmatrix} v_{ag} \\ v_{bg} \\ v_{cg} \end{bmatrix} = \begin{bmatrix} R_g & 0 & 0 \\ 0 & R_g & 0 \\ 0 & 0 & R_g \end{bmatrix} \begin{bmatrix} i_{ag} \\ i_{bg} \\ i_{cg} \end{bmatrix} + \begin{bmatrix} L_g & 0 & 0 \\ 0 & L_g & 0 \\ 0 & 0 & L_g \end{bmatrix} \begin{bmatrix} \frac{di_{ag}}{dt} \\ \frac{di_{bg}}{dt} \\ \frac{di_{cg}}{dt} \end{bmatrix} + \begin{bmatrix} u_{ag} \\ u_{bg} \\ u_{cg} \end{bmatrix} \quad (2.114)$$

And

$$\begin{bmatrix} u_{ag} \\ u_{bg} \\ u_{cg} \end{bmatrix} = \frac{V_{dc}}{3} \begin{bmatrix} (2S_{21} - S_{22} - S_{23}) \\ (2S_{22} - S_{21} - S_{23}) \\ (2S_{23} - S_{21} - S_{22}) \end{bmatrix} \quad (2.115)$$

where  $S_{21}$ ,  $S_{22}$ ,  $S_{23}$  denote the switching positions of each phase for converter of the generator side.

The system equation of the DC-link capacitor if the both converters (Fig.2-19 (a) and (b)) are connected back-to-back is expressed as:

$$C_{dc} \frac{dV_{dc}}{dt} = S_{21}i_{ag} + S_{22}i_{bg} + S_{23}i_{cg} - (S_{1}i_{af} + S_{2}i_{bf} + S_{3}i_{cf}) \quad (2.116)$$

According to (Asiminoaei, Blaabjerg et Hansen, 2007; Singh, 2010), to develop control algorithms and filter out the noise in the DC signals, as well as, decouple the active and reactive powers independently, one can transform the system equations given in (a-b-c) stationary reference system to rotating d-q reference frame using Park transformation, which is already given in (2.49).

By applying Park transformation to equations (2.112), (2.114), (2.115) and (2.116) by eliminating the zero sequence components, one obtains:

$$\begin{bmatrix} v_{dinv} \\ v_{qinv} \end{bmatrix} = \begin{bmatrix} R_f & 0 \\ 0 & R_f \end{bmatrix} \begin{bmatrix} i_{dinv} \\ i_{qinv} \end{bmatrix} - \begin{bmatrix} \omega_f L_f & 0 \\ 0 & -\omega_f L_f \end{bmatrix} \begin{bmatrix} i_{qinv} \\ i_{dinv} \end{bmatrix} + \begin{bmatrix} L_f & 0 \\ 0 & L_f \end{bmatrix} \begin{bmatrix} \frac{di_{qinv}}{dt} \\ \frac{di_{dinv}}{dt} \end{bmatrix} + \begin{bmatrix} u_d \\ u_q \end{bmatrix} \quad (2.117)$$

As for generator side converter, one obtains:

$$\begin{bmatrix} v_{dg} \\ v_{qg} \end{bmatrix} = \begin{bmatrix} R_g & 0 \\ 0 & R_g \end{bmatrix} \begin{bmatrix} i_{dg} \\ i_{qg} \end{bmatrix} + \begin{bmatrix} L_g & 0 \\ 0 & L_g \end{bmatrix} \begin{bmatrix} \frac{di_{qg}}{dt} \\ \frac{di_{dg}}{dt} \end{bmatrix} + \begin{bmatrix} -\omega_g L_g & 0 \\ 0 & +\omega_g L_g \end{bmatrix} \begin{bmatrix} i_{qg} \\ i_{dg} \end{bmatrix} + \begin{bmatrix} u_{dg} \\ u_{qg} \end{bmatrix} \quad (2.118)$$

The equation of the DC-link capacitor in d-q reference frame is written as:

$$C_{dc} \frac{dV_{dc}}{dt} = \frac{u_{dg}}{V_{dc}} i_{dg} + \frac{u_{qg}}{V_{dc}} i_{qg} - \left( \frac{u_{dimv}}{V_{dc}} i_{dimv} + \frac{u_{qimv}}{V_{dc}} i_{qimv} \right) \quad (2.119)$$

### 2.7.2 Modeling of the DC/DC boost converter

Fig.2.19 (d) shows the circuit of the DC/DC boost converter. It consist of a DC input voltage  $V_{pv}$ , which represents the output PV voltage, a smoothing inductor  $L$ , controlled switch  $S_{pv}$ , freewheeling diode and a filter capacitor  $C_3$ . The mathematical model of the DC/DC boost converter can be easily obtained by applying Kirchhoff's laws in continuous mode.

$$\begin{cases} C_3 \frac{dv_{out\_PV}}{dt} = (1-d)i_L - i_{out\_Pv} \\ L \frac{di_L}{dt} = v_{pv} - (1-d)v_{out\_PV} \end{cases} \quad (2.120)$$

where  $d$  represents the duty-cycle function.

### 2.7.3 Modeling of the DC/DC buck boost converter

Generally, storage elements, such as, Batteries or super-capacity require bidirectional power converter to be connected to the DC-Link. Mostly, DC/DC buck-boost converter is used because it is able to manage the power flow in both directions (Hajizadeh, Golkar et Feliachi, 2010), as shown in Fig.2.19 (e). This converter is slightly more complex compared to DC/DC boost converter, because, it contains one more switch. The average model of this converter is expressed as follows:

$$\begin{cases} \frac{di_L}{dt} = \frac{1}{L}(1-d)v_{out\_bat} + \frac{V_{bat}}{L}d \\ \frac{dv_{out\_bat}}{dt} = (1-d)\frac{1}{C_4}i_L - \frac{i_{out\_bat}}{C_4} \end{cases} \quad (2.121)$$

where  $d$  represents the duty cycle function.

## **2.8 Conclusion**

Modeling of different elements that SPGS or HSPGS can contain has been given in detail in this chapter. These mathematical models will be used in the following chapters as tools in order to develop different control algorithms in order to manage optimally all elements. In the following chapter, we provide design and control of SPGS based on solar PV array.

## **CHAPITRE 3**

### **STANDALONE POWER GENERATING SYSTEM EMPLOYING SOLAR- PHOTOVOLTAIC POWER**

#### **3.1 Introduction**

In this Chapter, solar photovoltaic (PV) array feeding autonomous load, without dump load, is investigated. Two-stage-inverter is controlled to maximize the power from the PV, to protect the battery energy storage system (BESS) from overcharging and to regulate the voltage and frequency at the point of common coupling (PCC). An accurate stability analysis of the system is presented and discussed in this chapter. The effectiveness and the robustness of the developed controllers are validated by simulation and experimental results during the load perturbation and varying climate conditions (Rezkallah et al., 2015a).

#### **3.2 System Description**

As shown in Fig.3.1, the proposed new scheme consists of PV array, BESS, DC-DC boost converter, current control voltage source converter (CC-VSC), inductor capacitor (L-C) low-pass filter and loads. The novelty in this proposition is the removal of dump load usually used to dump the extra power in SPGS. In order to attain a highly efficient system, to regulate the output AC voltage and the system frequency constant at the PCC, sliding mode control approach is proposed to control the DC-DC boost converter and the CC-VSC. In addition, a new feedback current control is added to the proposed control algorithm for the DC-DC boost converter in order to protect the BESS from overcharging instead of dump load, by providing only the required load power demand if the BESS is fully charged.

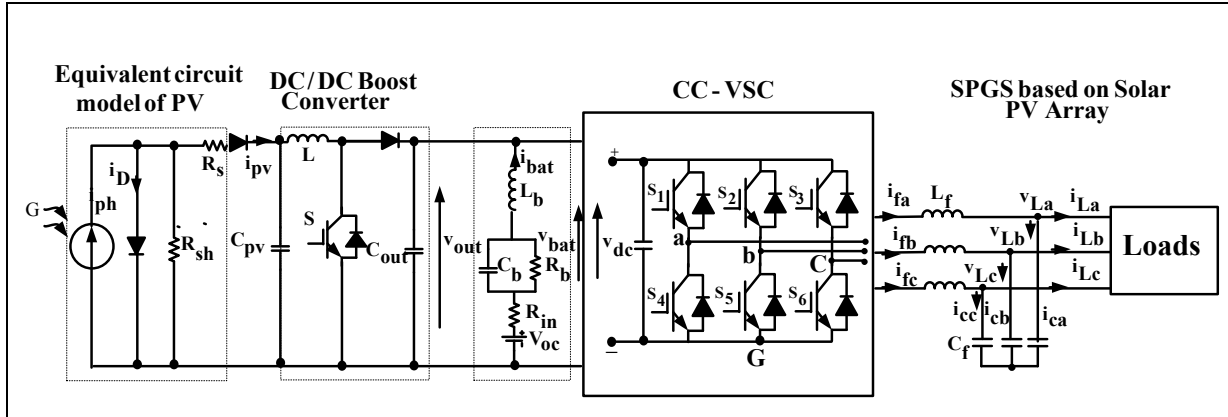


Figure 3.1 SPGS based on solar PV array

### 3.3 Modeling and Control Strategy

The modeling and control algorithms of the proposed SPGS are presented in this section.

#### 3.3.1 Modeling of Solar PV Array

The equivalent circuit model of the PV consists of a light-generated source, diode, series and parallel resistances and capacitors as shown in Fig. 3.1. Its mathematical model is given by the following equations (Villalva, Gazoli et Filho, 2009) as,

$$i_{pv} = i_{ph} - i_D \left[ \text{EXP} \left( \frac{qV_{pv}}{K_b T A} \right) - 1 \right] \quad (3.1)$$

where the light-generated current  $i_{ph}$  and the PV saturation current  $i_D$  are given as,

$$i_{ph} = G \left[ i_{scr} + K_i (T - T_r) \right] \quad (3.2)$$

$$i_D = i_{rr} \left( \frac{T}{T_r} \right)^3 \text{EXP} \left[ \left( \frac{qE_g}{KQA} \right) \left( \frac{1}{T_r} - \frac{1}{T} \right) \right] \quad (3.3)$$

where  $i_{ph}$ ,  $v_{pv}$ ,  $T$ ,  $G$ ,  $T_r$ ,  $i_{rr}$ ,  $i_{scr}$ ,  $K_i$ ,  $q$ ,  $K_b$ ,  $E_g$ ,  $Q$  and  $A$  denote the output current and voltage of PV, cell temperature, solar irradiance, reference temperature, saturation current, short-circuit current, short-circuit temperature coefficient, charge of an electron, Boltzmann's constant, band-gap energy of the material, total electron charge and ideality factor, respectively.

### 3.3.2 Mathematical Model of the DC/DC Boost Converter

The mathematical model of the DC-DC boost converter, as shown in Fig.3.1, is obtained using the Kirchhoff's voltage and current laws. Based on the switching position function ( $S=1$  or  $S=0$ ), the dynamics of the DC-DC boost converter is described by the following set of equations. When the switch position function is set to  $S=1$ , following equations are obtained:

$$L \frac{di_L}{dt} = v_{pv} \quad (3.4)$$

$$C_{out} \frac{dv_{out}}{dt} = -\frac{v_{out}}{R} \quad (3.5)$$

And when the switch position function is set to  $S=0$ , following equations are obtained:

$$L \frac{di_L}{dt} = v_{pv} - v_{out} \quad (3.6)$$

$$C_{out} \frac{dv_{out}}{dt} = i_L - \frac{v_{out}}{R} \quad (3.7)$$

where  $L$ ,  $C_{out}$ ,  $R$  denote the inductance of the input circuit, capacitance of the output filter and the output load resistance, respectively.

From (3.4)-(3.7) one gets the averaging state equations over the duty cycle  $d$  as,

$$\frac{di_L}{dt} = \frac{v_{pv}}{L} - (1-d)\frac{v_{out}}{L} \quad (3.8)$$

$$\frac{dv_{out}}{dt} = \frac{i_L}{C_{out}}(1-d) - \frac{v_{out}}{RC_{out}} \quad (3.9)$$

Where  $d$  is the duty cycle and is limited between  $[0 \ 1]$ . The DC voltage  $v_{out}$  obtained at the output of the boost converters is equal to the battery voltage  $v_{bat}$ ,  $i_L$  is the current flowing through the inductance  $L$  and is equal to the PV current  $i_{pv}$ .

### 3.3.3 Maximum Power Tracking Based on Sliding Mode Approach

The proposed design of the sliding mode control is based on following three steps:

#### 3.3.3.1 Choice of Sliding Surface

The output power of the PV is given as:

$$P_{pv} = v_{pv} i_{pv} \quad (3.10)$$

The maximum power condition is achieved when:

$$\sigma = \frac{\partial P_{pv}}{\partial i_{pv}} = 0 \quad (3.11)$$

In this study, the sliding surface  $\sigma$  is selected from (3.11). With this approach, it can be guaranteed to reach the surface and extract the maximum power.

Substituting (3.11) in (3.10), one gets the following expression is obtained:

$$\sigma = \frac{\partial P_{pv}}{\partial i_{pv}} = \frac{\partial (v_{pv} i_{pv})}{\partial i_{pv}} \quad (3.12)$$

$$\sigma = v_{pv} + i_{pv} \frac{\partial v_{pv}}{\partial i_{pv}} \quad (3.13)$$

where  $v_{pv}$  is the output PV voltage and is varying around an operating point of 50V. The PV current  $i_{pv}$  varies with the variation of the solar irradiation.

### 3.3.3.2 Determination of the Equivalent Control

The equivalent control  $d_{eq}$  shown in Fig. 3.2 is obtained by taking the derivate of equation (3.13) and equating it to zero as:

$$\frac{\partial \sigma}{\partial t} = \left( \frac{\partial \sigma}{\partial i_L} \right) \left( \frac{\partial i_L}{\partial t} \right) = \left( \frac{\partial \sigma}{\partial i_L} \right) \left( \frac{v_{pv}}{L} - (1-d) \frac{v_{out}}{L} \right) = 0 \quad (3.14)$$

The non-trivial solution of (3.14) is as follows:

$$v_{pv} - (1-d_{eq})v_{out} = 0 \quad (3.15)$$

From (3.15), the expression for  $d_{eq}$  is extracted as:

$$d_{eq} = 1 - \frac{v_{pv}}{v_{out}} \quad (3.16)$$

The duty cycle  $d$  takes the values between [0 1]. Thus the real control signal is defined as follows:

$$d = d_{eq} + k \operatorname{sgn}(\sigma) \quad (3.17)$$

And

$$d = \begin{cases} 1 & \text{if } d_{eq} + k \operatorname{sgn}(\sigma) \geq 0 \\ 0 & \text{if } d_{eq} + k \operatorname{sgn}(\sigma) \leq 0 \end{cases} \quad (3.18)$$

### 3.3.3.3 System Stability Analysis

To verify that the system converges to the sliding surface, the Lyapunov function candidate (Leyva et al., 2006) is used as follows:

$$V = \frac{1}{2} \sigma^2 \quad (3.19)$$

The system is globally stable if the derivative of (3.19) is negative.

$$\frac{\partial V}{\partial t} = \sigma \frac{\partial \sigma}{\partial t} < 0 \quad (3.20)$$

Replacing (3.13) and (3.14) in (3.20), the following expression is obtained:

$$\frac{\partial V}{\partial t} = \left( v_{pv} + i_{pv} \frac{\partial v_{pv}}{\partial i_{pv}} \right) \left( \frac{\partial \sigma}{\partial i_L} \right) \left( \frac{v_{pv}}{L} - (1-d) \frac{v_{out}}{L} \right) < 0 \quad (3.21)$$

From Fig.3.1,  $i_L = i_{pv}$ . Therefore, (3.21) can be re-written as follows:

$$\overbrace{\left( v_{pv} + i_L \frac{\partial v_{pv}}{\partial i_L} \right)}^{Term1} \overbrace{\left( 2 \frac{\partial v_{pv}}{\partial i_L} + i_L \frac{\partial^2 v_{pv}}{\partial^2 i_L} \right)}^{Term2} \overbrace{\left( \frac{v_{pv}}{L} - (1-d) \frac{v_{out}}{L} \right)}^{Term3} < 0 \quad (3.22)$$

Equation (3.22) is composed of three terms. Therefore, to verify the stability condition given in (3.20), the sign of each term in (3.22) should be verified independently. The product sign of each term will define the overall sign of (3.22). The first and the second terms in (3.22) contain the derivative of the PV voltage. From (3.1), the expression that defines the PV voltage is as follows:

$$v_{pv} = \frac{K_b TA}{q} \ln \left( \frac{i_{ph} + i_D - i_L}{i_D} \right) \quad (3.23)$$

The first and the second derivative of (23) are given as follows:

$$\frac{\partial v_{pv}}{\partial i_L} = -\frac{K_b TA}{q} \left( \frac{i_D}{i_{ph} + i_D - i_L} \right) \quad (3.24)$$

And

$$\frac{\partial^2 v_{pv}}{\partial^2 i_L} = -\frac{K_b TA}{q} \left( \frac{i_D}{(i_{ph} + i_D - i_L)^2} \right) \quad (3.25)$$

The signs of the first and the second terms in (3.22) are determined by using (3.1)-(3.3), (3.24) and (3.25). The parameters of real PV manufactured by Kyocera Solar Inc. are given in Table A-1 (Chen-Chi et Chieh-Li, 2009) in the Appendix. The obtained results shown in Table 5-1 prove that the sign product of the first and the second terms is negative. Therefore, to verify the condition given in (3.20) the sign of the third term of (3.22) should be positive.

Table 3.1 Signs of the first and the second terms of (3.22)

$v_{pv}$ (V)	$\partial v_{pv} / \partial i_L$	$\partial^2 v_{pv} / \partial^2 i_L$	Term <sub>1</sub>	Term <sub>2</sub>	Total sign
53	-0.0152	-0.0126	52.857	-0.1488	-
52	-0.0152	-0.0190	51.908	-0.1444	-
50.5	-0.0152	-0.0253	50.449	-0.1139	-
49	-0.0152	-0.0379	48.987	-0.0835	-

Replacing (3.16) and (3.17) in the third term of (3.22), the following expression is obtained,

$$\frac{V_{out}}{L} \overbrace{k \operatorname{sgn}(\sigma)}^{\text{term 2}} > 0 \quad (3.26)$$

The sign of the first term in (3.26) is always positive. Therefore, the second term will decide the sign of the third term. To get a positive sign, the second term must fulfill the following conditions,

$$\begin{cases} \text{if } \operatorname{sgn}(\sigma) > 0 & k = 1 \\ \text{if } \operatorname{sgn}(\sigma) < 0 & k = -1 \end{cases} \quad (3.27)$$

where  $k$  is equal to  $\pm 1$ .

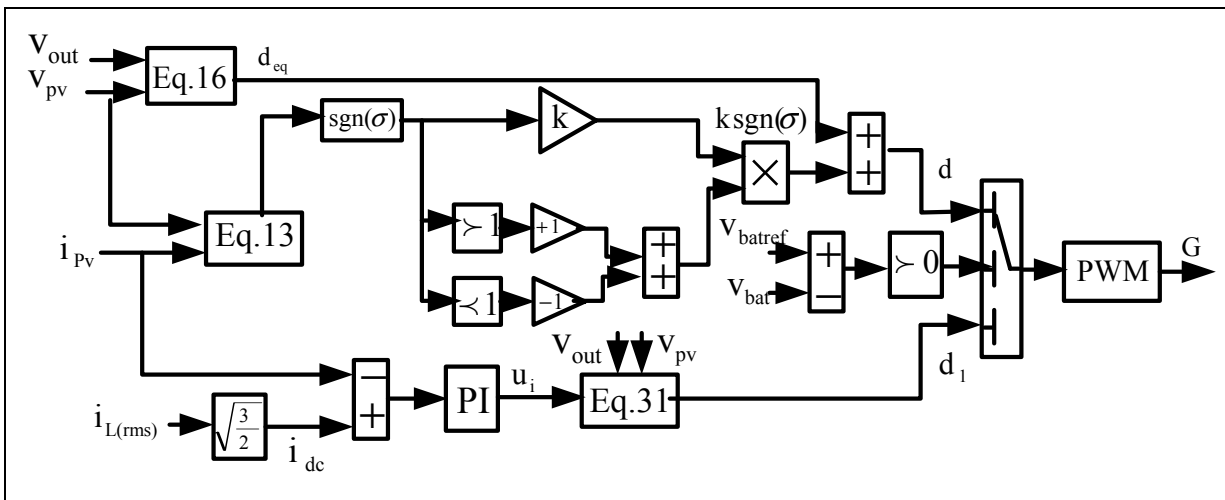


Figure 3.2 Control of the DC/DC Boost converter

### 3.3.4 Overvoltage Protection of the BESS

As shown in Fig.3.1, a dump load is avoided in the proposed system. However, to protect BESS from the overvoltage, the control is as follows. Through the proposed current feedback control, the PV array provides the required load power demand controlled by the DC-DC boost converter. For normal operation, the switch selects the control law defined by  $d$ .

Therefore, the PV array is operated at MPPT ( $P_{max}$ ) shown in Fig. 3.3. In the case to protect the BESS from overvoltage, the switch will select automatically  $d_1$ , as explained below, while maintaining PV array supplying the actual load demand by selecting the points P<sub>1</sub>, P<sub>2</sub> or P<sub>3</sub> on the power-voltage characteristic shown in Fig. 3.3, depending on the load requirement.

The battery voltage error  $\Delta v_{bat}(n)$  is calculated as follows:

$$\Delta v_{bat}(n) = v_{batmax} - v_{bat}(n) \quad (3.28)$$

Where  $v_{batmax}$  is the maximum battery voltage rated by the manufacturer and  $v_{bat}(n)$  is the sensed battery voltage.

Depending on the sign of the  $\Delta v_{bat}(n)$ , the right control is selected. The output of the PI current controller is expressed as:

$$\begin{cases} \text{if } \Delta v_{bat} > 0, d \text{ selected} \\ \text{if } \Delta v_{bat} < 0, d_1 \text{ selected} \end{cases} \quad (3.29)$$

Where,  $d_1$  is the control of the additional current feedback control and is obtained from the dynamic current equation, which is defined as following:

$$u_i = L \frac{di_L}{dt} = v_{pv} - (1 - d_1)v_{out} \quad (3.30)$$

And

$$d_1 = 1 + \frac{u_i - v_{pv}}{v_{out}} \quad (3.31)$$

where,  $u_i$  is the output of the PI current controller.

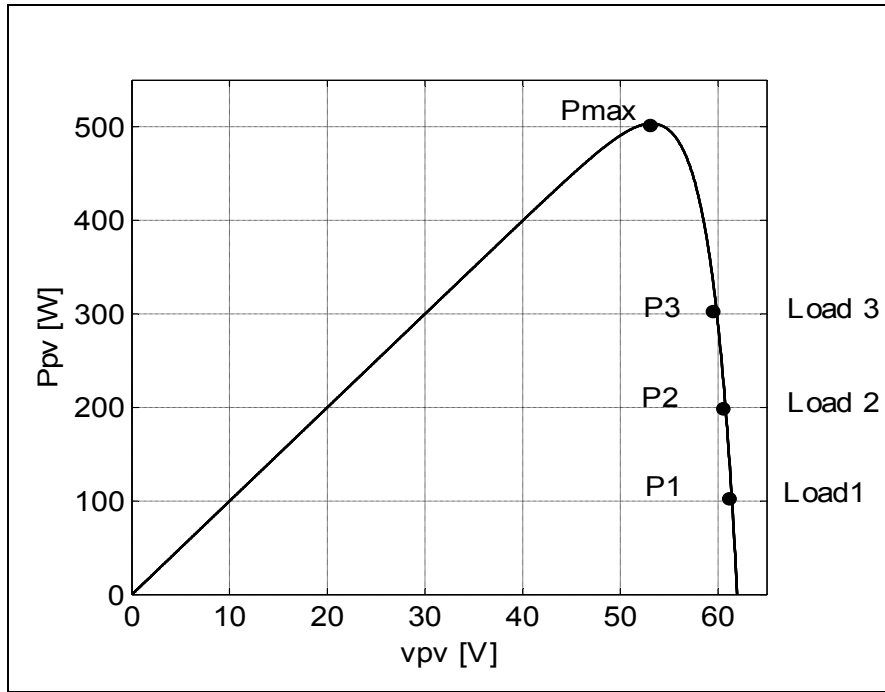


Figure 3.3 P-V characteristic of the solar PV array

### 3.3.5 Mathematical Model of the CC-VSC

Applying Kirchhoff's voltage and current laws to the CC-VSC and the load shown in Fig.3.1, the following output CC-VSC currents and load voltages equations are obtained:

$$\frac{di_{fabc}}{dt} = \frac{1}{L_f} (-v_{Labc} + d_{abc} v_{dc}) \quad (3.32)$$

$$\frac{dv_{Labc}}{dt} = \frac{1}{C_f} (i_{fabc} - i_{Labc}) \quad (3.33)$$

where,  $d_{abc}$ ,  $v_{Labc}$ ,  $i_{fabc}$ ,  $C_f$ ,  $L_f$  denote the controls laws, load voltages, inverter currents, capacitance of the output filter and output CC-VSC inductance, respectively.

Replacing (3.32) in the derivative of (3.33), the following expression is obtained:

$$\frac{d^2 v_{Labc}}{d^2 t} = \frac{1}{C_f} \left( \frac{1}{L_f} (-v_{Labc} + d_{abc} v_{dc}) - \frac{di_{Labc}}{dt} \right) \quad (3.34)$$

The state equation of (3.34) is in the stationary reference frame. It can be transformed in the synchronously rotating d-q reference frame, using Park's transformation already given in (2.49). Using Park's transformation, (3.34) becomes as follow:

$$\begin{cases} \frac{d^2 v_{Ld}}{d^2 t} = \overbrace{\left( -\frac{1}{C_f L_f} + \omega^2 \right)}^{Term1} v_{Ld} + \overbrace{\frac{v_{dc}}{C_f L_f}}^{Term2} d_d - \overbrace{\frac{1}{C_f} \frac{di_{Ld}}{dt}}^{Term3} + \overbrace{2\omega \frac{dv_{Lq}}{dt}}^{Term4} \\ \frac{d^2 v_{Lq}}{d^2 t} = \overbrace{\left( -\frac{1}{C_f L_f} + \omega^2 \right)}^{Term5} v_{Lq} + \overbrace{\frac{v_{dc}}{C_f L_f}}^{Term6} d_q - \overbrace{\frac{1}{C_f} \frac{di_{Lq}}{dt}}^{Term7} - \overbrace{2\omega \frac{dv_{Ld}}{dt}}^{Term8} \end{cases} \quad (3.35)$$

### 3.3.6 AC Voltage Regulation Based on Sliding Mode Approach

The design of the sliding mode control for load voltage regulation is based on following three steps:

#### 3.3.6.1 Choice of Sliding Surface

Sliding surface is defined as(Chan et Gu, 2010):

$$\begin{cases} \sigma_d = \left( \frac{d}{dt} + K_1 \right) \Delta v_{Ld} \\ \sigma_q = \left( \frac{d}{dt} + K_1 \right) \Delta v_{Lq} \end{cases} \quad (3.36)$$

where  $K_1$  is a positive constant and  $\Delta v_{Ld}$  and  $\Delta v_{Lq}$  are the load voltage errors, which are given as follows:

$$\begin{cases} \Delta v_{Ld} = v_{Ld} - v_{Ldref} \\ \Delta v_{Lq} = v_{Lq} - v_{Lqref} \end{cases} \quad (3.37)$$

where  $v_{Ldref}$ ,  $v_{Lqref}$  are respectively the desired load voltage in d-axis and in q-axis.

### 3.3.6.2 Determination of the Equivalent Control

The objective of the proposed control algorithm shown in Fig. 3.4 is to regulate the constant load voltage and frequency in the presence of various conditions. To achieve these objectives, the following conditions are imposed:

$$\begin{cases} v_{Ldref} = v_{LL} \\ v_{Lqref} = 0 \\ \theta = \omega t = 2\pi \cdot f \cdot t \end{cases} \quad (3.38)$$

where  $v_{LL}$  is line-line load voltage and  $f_s$  is the local grid frequency which is equal to 60Hz.

The control input is defined as follows:

$$\begin{cases} d_d = deq_d + k_2 \text{sgn}(\sigma_d) \\ d_q = deq_q + k_2 \text{sgn}(\sigma_q) \end{cases} \quad (3.39)$$

where  $k_2$  is a positive gain.

The equivalent control is obtained from the invariance conditions given as:

$$\begin{cases} \sigma_d = 0 \Rightarrow \frac{d\sigma_d}{dt} = 0 \Rightarrow d_d = deq_d \\ \sigma_q = 0 \Rightarrow \frac{d\sigma_q}{dt} = 0 \Rightarrow d_q = deq_q \end{cases} \quad (3.40)$$

Moreover, the derivative of (3.36) is expressed as follows:

$$\begin{cases} \frac{d\sigma_d}{dt} = \frac{d^2 \Delta v_{Ld}}{d^2 t} + K_1 \frac{d\Delta v_{Ld}}{dt} \\ \frac{d\sigma_q}{dt} = \frac{d^2 \Delta v_{Lq}}{d^2 t} + K_1 \frac{d\Delta v_{Lq}}{dt} \end{cases} \quad (3.41)$$

Applying the conditions given in (3.40) to the obtained equation by replacing (3.37) in (3.41) gives:

$$\begin{cases} 0 = \frac{d^2 (v_{Ld} - v_{Ld \text{ ref}})}{d^2 t} + K_1 \frac{d(v_{Ld} - v_{Ld \text{ ref}})}{dt} \\ 0 = \frac{d^2 (v_{Lq} - v_{Lq \text{ ref}})}{d^2 t} + K_1 \frac{d(v_{Lq} - v_{Lq \text{ ref}})}{dt} \end{cases} \quad (3.42)$$

The derivatives of  $v_{Ld \text{ ref}}$  and  $v_{Lq \text{ ref}}$  in (3.42) are equal to zero. Substituting (3.42) in (3.35), one gets:

$$\begin{cases} 0 = \left( -\frac{1}{C_f L_f} + \omega^2 \right) v_{Ld} + \frac{v_{dc}}{C_f L_f} d_{eqd} - \frac{1}{C_f} \frac{di_{Ld}}{dt} + 2\omega \frac{dv_{Lq}}{dt} + K_1 \frac{d(v_{Ld})}{dt} \\ 0 = \left( -\frac{1}{C_f L_f} + \omega^2 \right) v_{Lq} + \frac{v_{dc}}{C_f L_f} d_{eqq} - \frac{1}{C_f} \frac{di_{Lq}}{dt} - 2\omega \frac{dv_{Ld}}{dt} + K_1 \frac{d(v_{Lq})}{dt} \end{cases} \quad (3.43)$$

Finally, the equivalent controls given below are obtained by arranging (3.43).

$$\begin{cases} d_{eqd} = \frac{C_f L_f}{v_{dc}} \left[ \left( \frac{1}{C_f L_f} - \omega^2 \right) v_{Ld} + \frac{1}{C_f} \frac{di_{Ld}}{dt} - 2\omega \frac{dv_{Lq}}{dt} - K_1 \frac{d(v_{Ld})}{dt} \right] \\ d_{eqq} = \frac{C_f L_f}{v_{dc}} \left[ \left( \frac{1}{C_f L_f} - \omega^2 \right) v_{Lq} + \frac{1}{C_f} \frac{di_{Lq}}{dt} + 2\omega \frac{dv_{Ld}}{dt} - K_1 \frac{d(v_{Lq})}{dt} \right] \end{cases} \quad (3.44)$$

With help of the inverse Park transformation given in (2.47), the obtained control laws  $d_d$  and  $d_q$  are transformed to a-b-c stationary reference frame, and fed to PWM controller with fixed frequency triangular carrier wave of unit amplitude to generate the switching signals to the CC-VSC.

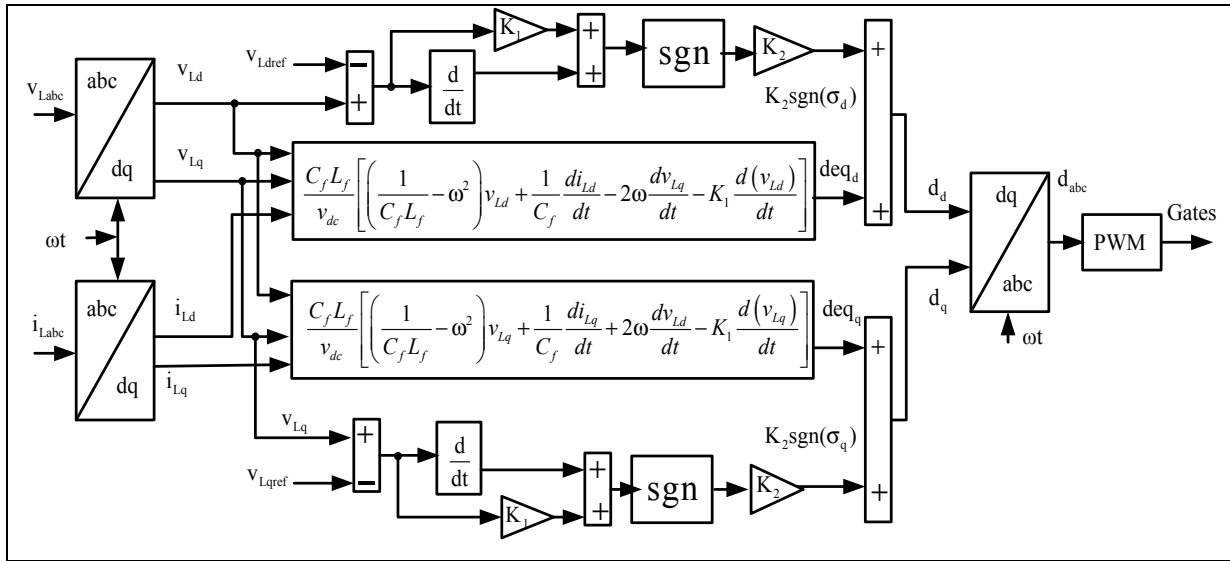


Figure 3.4 Control of CC-VSC

### 3.3.6.3 Stability Analysis

The objective of SMC is to guarantee the convergence of the operation points to predetermine sliding boundary. To verify the stability of the system, Lyapunov function candidate are used,

$$\begin{cases} v_d = \frac{1}{2} \sigma_d^2 \\ v_q = \frac{1}{2} \sigma_q^2 \end{cases} \quad (3.45)$$

The system is globally stable if the derivative of (3.45) is negative.

$$\begin{cases} \frac{dv_d}{dt} = \sigma_d \frac{d\sigma_d}{dt} < 0 \\ \frac{dv_q}{dt} = \sigma_q \frac{d\sigma_q}{dt} < 0 \end{cases} \quad (3.46)$$

Replacing (3.36) and (3.41) in (3.46), one gets:

$$\left\{ \begin{array}{l} \frac{dv_d}{dt} = \left( \overbrace{\frac{d\Delta v_{Ld}}{dt} + K_1 \Delta v_{Ld}}^{\text{Term 1}} \right) \left( \overbrace{\frac{d^2 \Delta v_{Ld}}{d^2 t} + K_1 \frac{d\Delta v_{Ld}}{dt}}^{\text{Term 2}} \right) \langle 0 \\ \frac{dv_q}{dt} = \left( \overbrace{\frac{d\Delta v_{Lq}}{dt} + K_1 \Delta v_{Lq}}^{\text{Term 3}} \right) \left( \overbrace{\frac{d^2 \Delta v_{Lq}}{d^2 t} + K_1 \frac{d\Delta v_{Lq}}{dt}}^{\text{Term 4}} \right) \langle 0 \end{array} \right. \quad (3.47)$$

It is already mentioned before that the derivatives of  $v_{Ldref}$  and  $v_{Lqref}$  are equal to zero. It is observed in (3.47), that the Terms 2 and 4 represents the derivative of the terms 1 and 3. Therefore, it is possible to prove that the signs of  $(dv_d/dt)$  and  $(dv_q/dt)$  are negative by calculate the values of  $(d^2 v_q/dt^2)$  and  $(d^2 v_d/dt^2)$  using (3.35), and the value of the  $(d\Delta v_{Ld}/dt)$  and  $(d\Delta v_{Lq}/dt)$  using the expression of the filter currents  $i_{cdq}$ , which is given as follow:

$$\frac{d\Delta v_{Ldq}}{dt} = \frac{d(v_{Ldq} - v_{Ldqref})}{dt} = \frac{i_{cdq} - (\pm \omega v_{Lqd})}{c_f} \quad (3.48)$$

It is observed in (5.35), that the terms1, 2, 4, 5, 6 and 8, we can easily calculate using the parameters given in Appendix Table A-1 and the simulation results shown in Fig.3.6 and 3.7 except the terms 3 and 7, which contain derivative of the load currents. Therefore, to facilitate this calculation, one use the approximation given by (Mendalek, 2003):

$$\frac{di_{Ldq}}{dt} = \frac{1}{Z} \frac{di_{fdq}}{dt} \quad (3.49)$$

where,  $Z$  represents the equivalent impedance, which is equal to:

$$Z = \frac{Z_L}{Z_f + Z_L} \quad (3.50)$$

where,  $Z_f$  and  $Z_L$  represents impedances of the output inverter and load respectively.

According to (Mendalek, 2003), if the filter compensate adequately,  $Z_L \gg Z_f$ , which implies that  $(d_{i_{Ldq}}/dt) = (d_{i_{fdq}}/dt)$ . Based on this simplification the derivative of the load current is equal to:

$$\frac{d_{i_{Ldq}}}{dt} = \frac{d_{i_{fdq}}}{dt} = \left( \frac{d_{dq}}{L_f} + \frac{v_{Ldq}}{L_f} \mp \omega i_{fdq} \right) \quad (3.51)$$

Now, we can easily determine the signs of terms given in (3.47) using (3.35), (3.48) and (3.51), as well as, the simulation results given in Fig.3.5, and the parameters given in Table 7-1. Based on the results given bellow in Tables 3-2 and 3-3, the signs of the Terms 1 and 3 are always positive and the signs of the terms 2 and 4 are always negative. Therefore, the product of terms 1 and 2 gives negative sign, as well as, the sign of the product of terms 3 and 4 is negative, which satisfies the stability condition given in (3.46).

Table 3.2 Signs of the Terms Given in (3.35)

$d_{dq}$	$d^2v_{Ld}/dt^2$	$d^2v_{Lq}/dt^2$	$dv_{Ld}/dt$	$dv_{Lq}/dt$
0.5	$-1.1746 \cdot 10^9$	$-5.3 \cdot 10^{13}$	26000	$1.13 \cdot 10^9$
0.9	$-1.1746 \cdot 10^9$	$-1.1062 \cdot 10^{14}$	26000	$1.13 \cdot 10^9$

Table 3.3 Signs of the Terms 1,2,3 and 4 of (3.47)

$d_{dq}$	Term <sub>1</sub>	Term <sub>2</sub>	Term <sub>3</sub>	Term <sub>4</sub>
0.5	+26003	$-1.1746 \cdot 10^9$	$+1.13 \cdot 10^9$	$-5.3 \cdot 10^{13}$
0.9	+26003	$-1.1062 \cdot 10^{14}$	$+1.13 \cdot 10^9$	$-1.1062 \cdot 10^{14}$

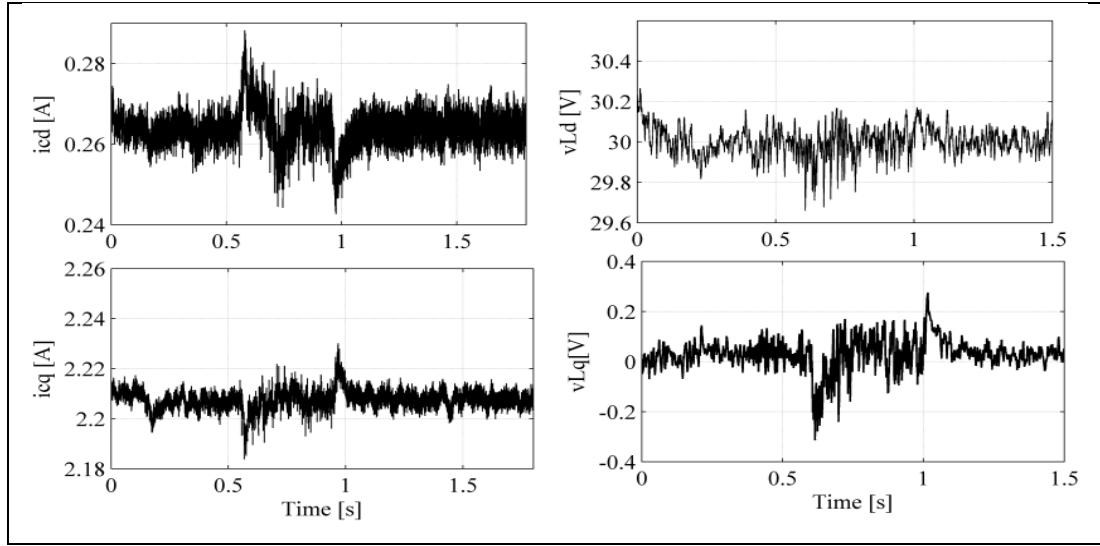


Figure 3.5 Simulation results of capacitor currents and load voltage in d-q axis

### 3.3.7 Selecting the rating of BESS

The Thevenin-based equivalent battery model is used for modeling battery in this study (Kasal et Singh, 2011)(Kasal et Singh, 2011)(Kasal et Singh, 2011) (Kasal et Singh, 2011). This model consists of capacitance  $C_b$ , which is calculated as,

$$C_b = \frac{kWh \times 3600 \times 10^3}{0.5(V_{ocmax}^2 - V_{ocmin}^2)} \quad (3.52)$$

where  $V_{ocmax}$ ,  $V_{ocmin}$ , kWh denote the maximum and minimum open circuit voltage of BESS under fully charged and discharged conditions and energy of the battery respectively.

This model contains also  $R_{in}$ , which represents the equivalent resistance of parallel/series combinations of the battery, its value is smaller. Contrary, the value of  $R_b$  is higher because it represents the self-discharge resistance of battery. The nominal battery voltage  $V_{bat}$  is calculated using the following equation

$$V_{bat} > \left( \frac{2\sqrt{2}}{\sqrt{3} m_a} \right) V_{LL} \quad (3.53)$$

where  $m_a$  and  $V_{LL}$  represents the index of modulation which is taken as 1, and  $V_{LL}$  is the AC line-line rms voltage. For  $V_{LL} = 30V$ , so,  $V_{dc}$  should be greater than 50V, and it is selected 72V. Considering the ability of the proposed system to supply electricity to a load of 500W for 24 h, the design storage capacity of the battery bank is taken as 1500W·h. The commercially available battery bank consists of cells of 12 V. The nominal capacity of each cell is taken as 12 A·h. To achieve a DC-bus voltage of 72V through series connected cells of 12 V, the battery bank should have  $(72/12) = 6$  number of cells in series. Since the storage capacity of this combination is 12 A·h, and the total ampere hour required is  $(1500W/72) = 20.83A·h$ , the number of such sets required to be connected in parallel and would be  $(20.83 A·h/12 A·h) = 2$  (selected). Thus, the battery bank consists of 6 series-connected sets of 2 parallels connected battery cells. Taking the values of  $V_{ocmax} = 78.55V$ ,  $V_{ocmin} = 68.55V$ , and the storage capacity of 1.5 kWh, the value of  $C_b$  obtained using (3.52) is equal to 7346F.

### 3.4 Simulation Results and Discussion

To test the performance of the proposed control algorithms for SS based on PV array, simulations are carried out using MATLAB/Simulink. Fig. 3.6 shows the results in terms of the terminal load voltage and current and their zoomed waveforms for different scenarios as follows, a) sudden linear load variation after completely removed load, b) decreasing of linear load, c) disconnecting of one phase of linear load, d) unbalanced nonlinear load, e) nonlinear load and f) completely removed load. It is observed in (a) that the load is completely removed between  $t = 0$  s to  $t = 0.15$  s and between  $t = 1.2$  s to  $t = 1.5$  s. Linear load is connected to the system at  $t = 0.15$  s and is reduced by 50% at  $t = 0.4$  s.

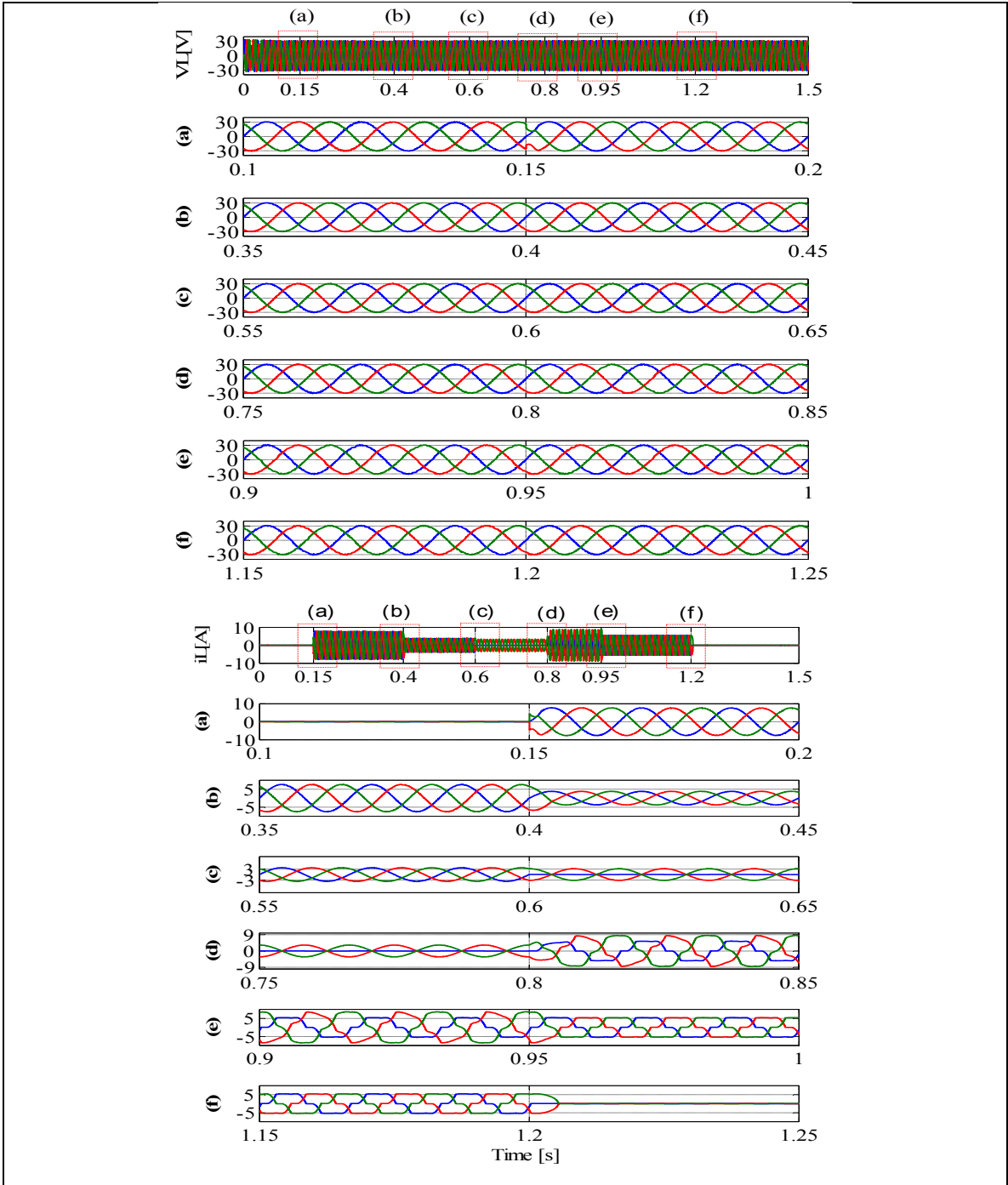


Figure 3.6 Dynamic performance of the SPGS based on solar PV array under solar insolation and load change

At  $t=0.6$  s one phase of linear load is removed and at  $t=0.8$  s unbalanced nonlinear load is connected to system and disconnected at 0.95 s. From  $t=0.95$ s to  $t=1.2$ s only nonlinear load stay connected. From  $t=1.2$ s, no load connected to the system. It is observed that for all tests, the proposed control algorithm based SMC approach confirms the fast dynamic response and zero steady state error in the load voltage, as well as, minimum distortion in the load voltage. It is observed also that the load voltages waveforms are not affected by the load currents harmonics.

Fig.3-7 shows the I-V characteristic curve of the PV at  $T=20^{\circ}\text{C}$  and  $G=1000\text{ w/m}^2$ . It is observed that the output PV current ( $i_{pv}$ ) vary between 0 A and 5A. Therefore, the DC-DC boost converter must extract optimal current corresponding to the maximum power from the PV ( $i_{pvmax}=4.75\text{A}$ ) if the battery is not fully charged. If the battery is fully charged, the exact load current demand ( $i_{pv}=i_{Lrms}=2.4\text{A}$ ) is extracted from the PV array

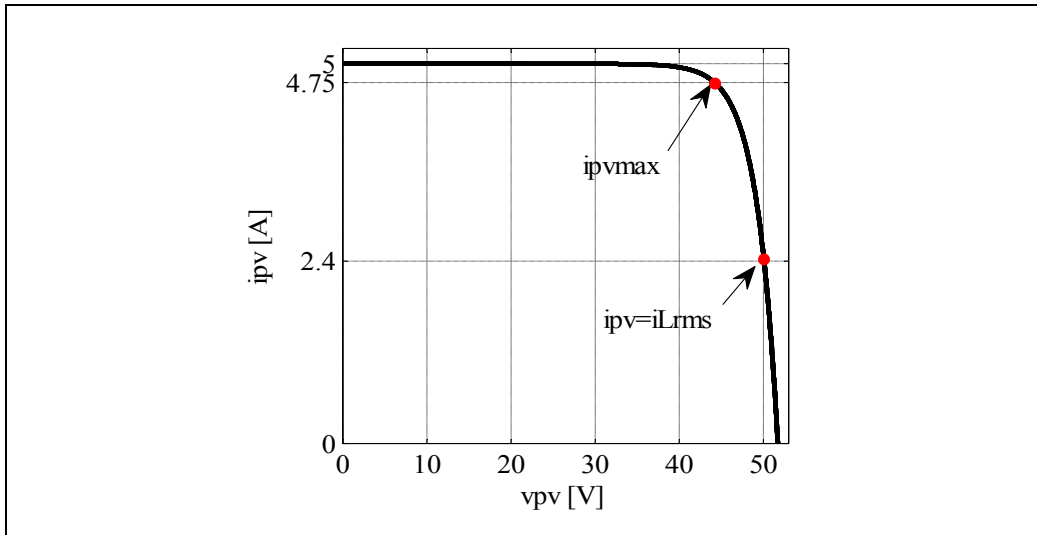


Figure 3.7 I-V Characteristic curve of PV array at  $T=20^{\circ}\text{C}$  and  $G=1000\text{w/m}^2$

Fig.3.8 shows, load voltage ( $v_L$ ), load current ( $i_{Lrms}$ ), battery voltage ( $v_{bat}$ ), state of charge of battery (SOC%), battery current ( $i_{bat}$ ), output PV current ( $i_{pv}$ ) and its reference and the frequency ( $f$ ) at the PCC. It is observed from  $t=0$ s to  $t=0.25$ s, when the SOC% is less than 100%, the MPPT operation takes place. From  $t=0.25$ s, when the SOC% is reaching 100%,

the feedback current control is selected and the PV current of 2.4 A is extracted which corresponds to the required load current. During this time the battery current is equal to zero. At  $t=0.7$ s, the load current is increased to 5A. At this moment, the MPPT control algorithm is selected. As designed, the PV array cannot offer the required load current, the difference is provided by the battery.

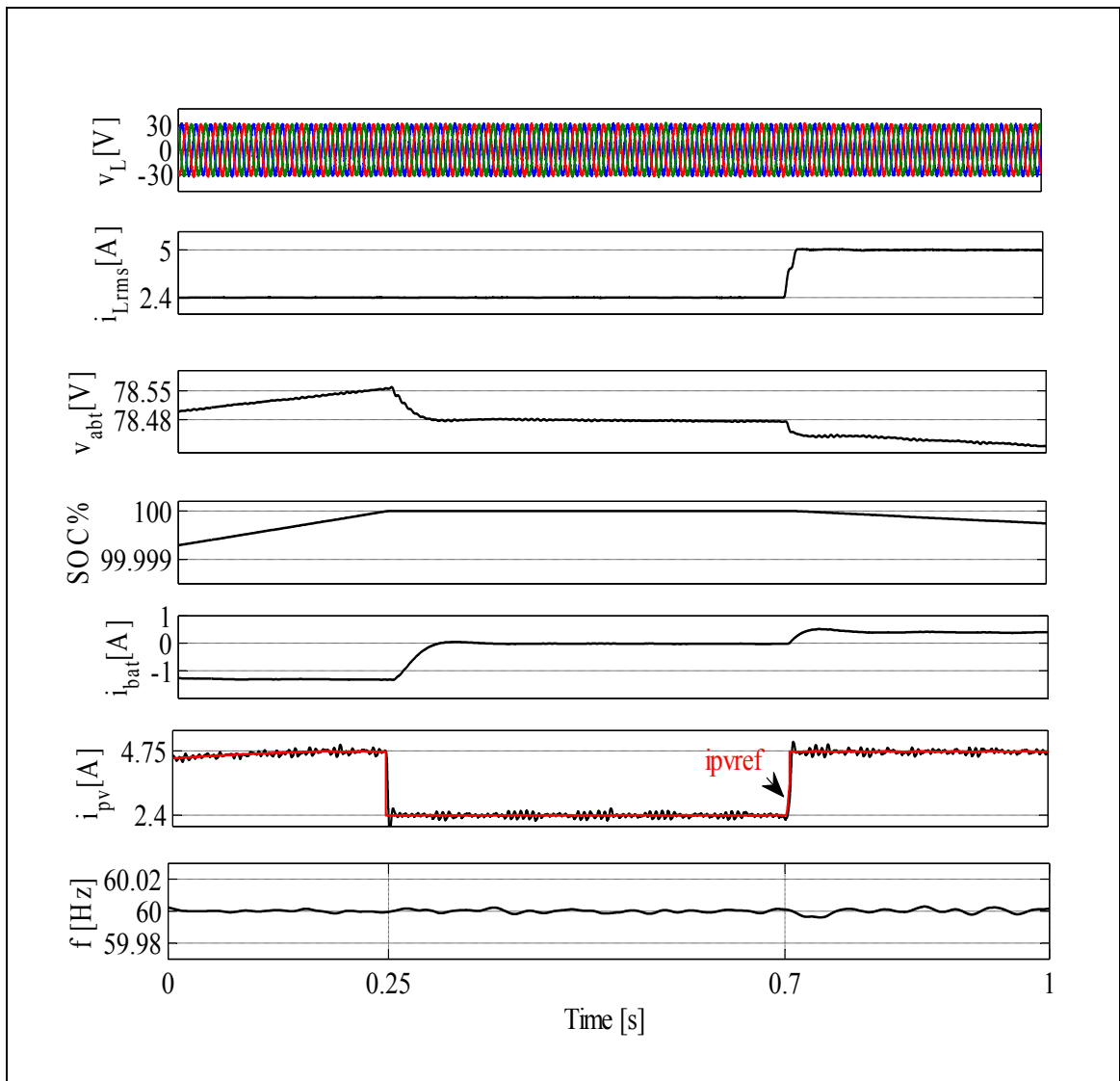
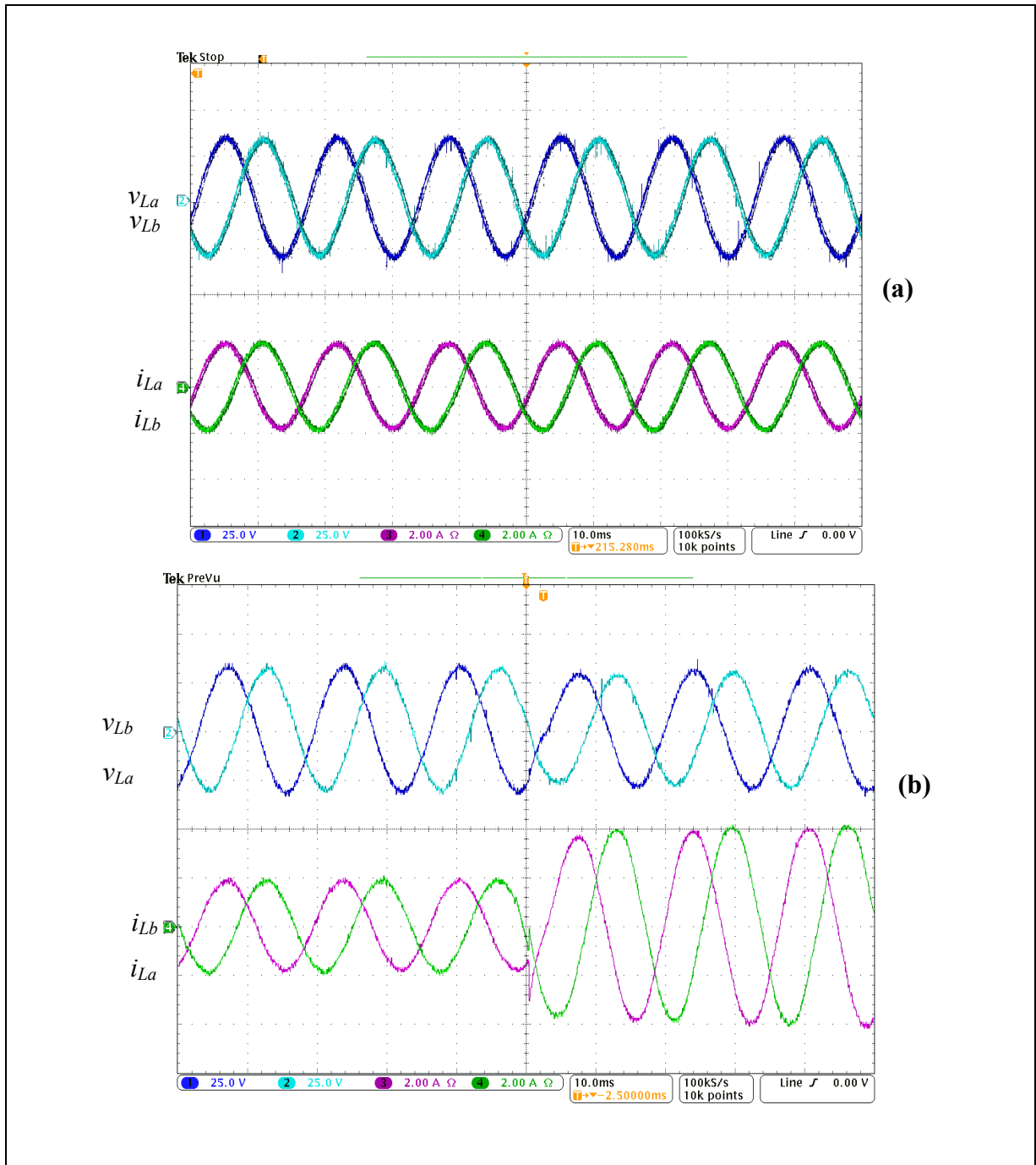


Figure 3.8 Dynamic performance of SPGS based on solar PV when SOC% of BESS is equal to 100%



$t=50\text{ms}$  and d) removal of one phase of linear load from  $t=45\text{ms}$ . It is observed during load variation in (b), (c) and (d) that the load voltages are reaching their desired values within less than three cycles. Therefore, the obtained simulation results are validated experimentally which confirm the effectiveness of the proposed control algorithm.



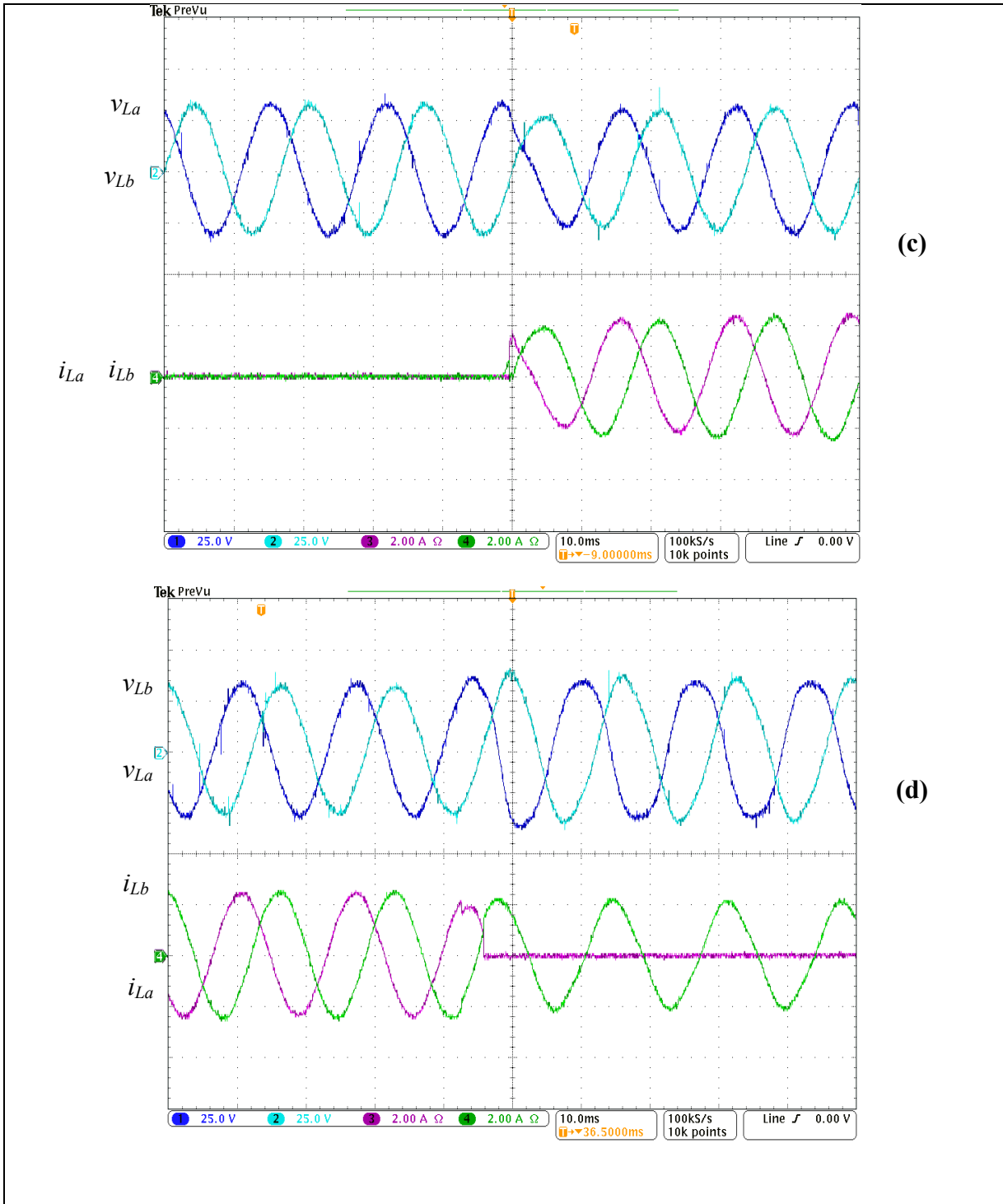


Figure 3.10 Dynamic performance of SPGS based on solar PV array under load variation

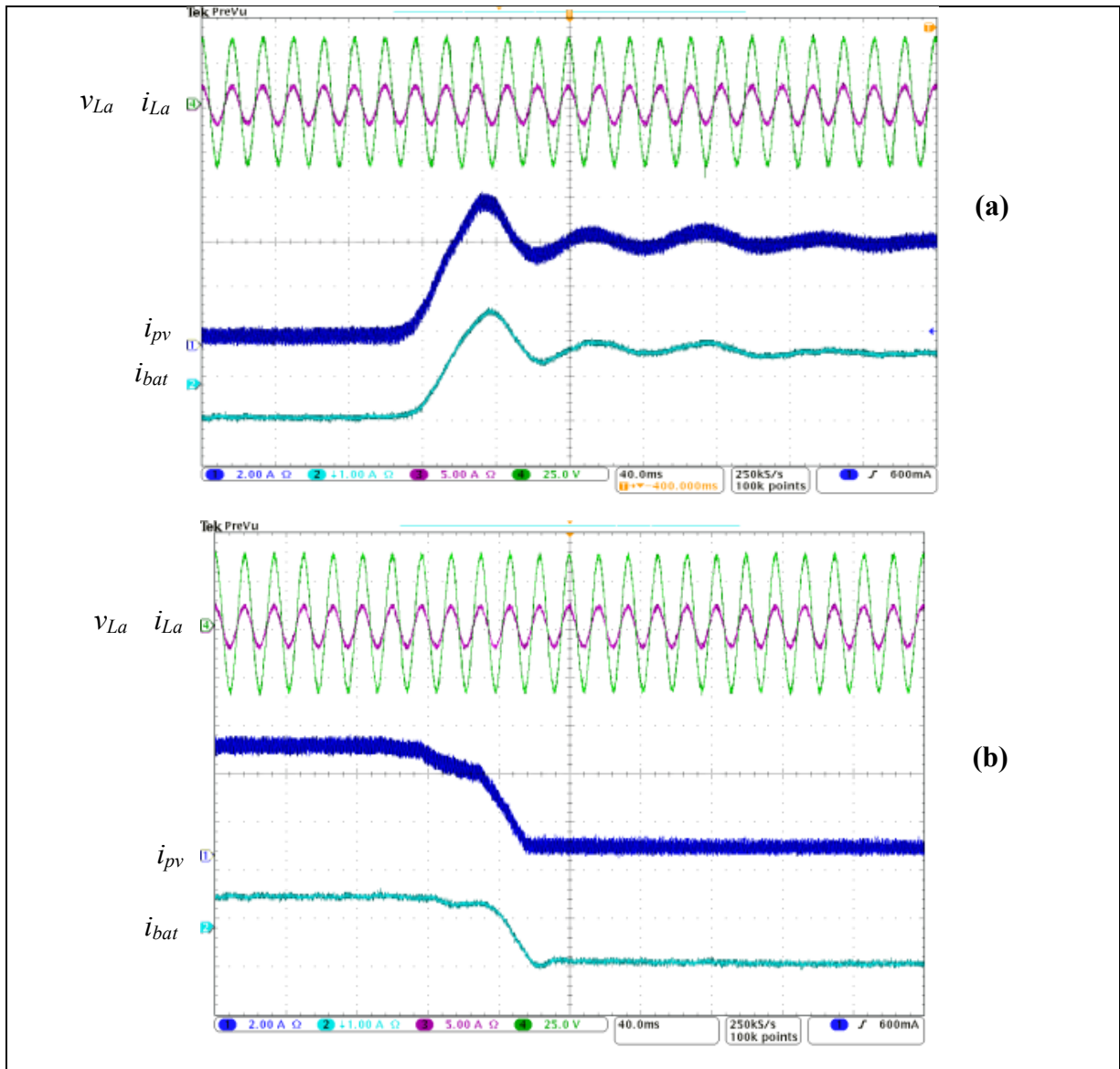


Figure 3.11 Dynamic performance of SPGS based on solar PV array under solar irradiation change

Fig. 3.11 shows the experimental results of the load voltages, load currents and PV and battery currents under varying insolation. It is observed in Fig.3.11 (a) that during the absence of the insolation the PV current is equal to zero and battery is providing power to the load. In the presence of the insolation the PV array is able to feed the load and charge the battery. Fig.3.11 (b) shows the reverse case. At the beginning, PV is providing power to the

load and to the battery. When the insolation varied one sees that battery supports the load demand. It is observed in the both cases that the voltage is kept constant and the load was fed continuously which confirms the effectiveness of the proposed control algorithm.

### **3.6 Conclusion**

This chapter was focused on the implementation of solar photovoltaic (PV) array feeding autonomous load. It uses SMC for controlling the DC-DC boost converter and the CC-VSC, respectively, to get maximum power from solar PV array and to maintain constant voltage and the frequency at the PCC. The system operates without dump load and offers protection of the BESS from overcharging. The proposed new current feedback control forces the solar PV array to deliver exactly the required load power demand, which makes the system more effective and less expensive. With the use of SMC control, linear PI controllers have been avoided for both proposed control algorithms. Furthermore, the modeling approach based on the second derivative allows minimising the number of sensors. The obtained simulation and experimental results for different conditions have shown satisfactory performance without adjusting the parameters.

## CHAPITRE 4

### HYBRID STANDALONE POWER GENERATION SYSTEMS EMPLOYING SOLAR PV ARRAY AND DIESEL GENERATOR

#### 4.1 Introduction

In this chapter, HSPGS topologies based on solar PV array and DE driven fixed and variable speed generators such as, SG, SCIG, PMSG SyRG, PMBLDCG and DFIG as shown in Fig. 4.1 are discussed. For each technology, one topology is selected for study. For the topologies, which are based on solar PV array and DE driven fixed speed generator, SG is selected. To control the proposed PV-DG HSPGS, modified p-q instantaneous power theory control and P&O technique are used. For the topologies, which are based on solar PV array and DE driven variable speed generator, DFIG is selected, and for its control algorithms, indirect stator flux oriented control and P&O technique are used to control the rotor of the DFIG and to get MPPT for solar PV array, respectively. For the AC voltage and the system frequency regulation, as well as power quality improvement at the PCC, modified indirect control is proposed. Simulation is carried out using MATLAB/Simulink to test the effectiveness of the selected topologies and their control algorithms.

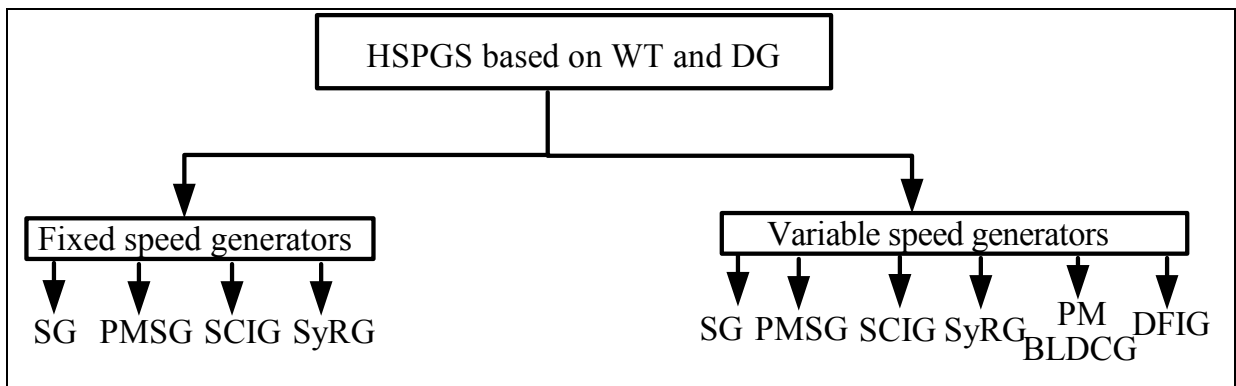


Figure 4.1 Classification of HSPGS based on PV array and DG driven fixed and variable speed generators

#### 4.2 Topology Designs for HSPGS based on Solar PV Array and DE Driven Fixed Speed Generators

Usually, HSPGS contains several elements such as, AC and DC ESs, storage elements, dump loads, as well as, power electronic converters. As for DC and AC ESs, DC/DC and DC/AC or AC/DC power converters are required to get MPPT from solar PV array, to regulate the system frequency and AC voltage and to improve the power quality at the PCC. The ESs which employs constant speed generators, power converters are not required; they provide energy directly to the local load. They are less efficient compared to the ESs with variable speed generators but are inexpensive. Mostly, SM is preferable as generator for DE (Mipoung, Lopes et Pillay, 2014) because it is equipped with an automatic voltage regulator (AVR), which is responsible for keeping the output voltage constant under normal operating conditions at various load levels (Hasan, Martis et Sadrul Ula, 1994). Recently, SyRG has been paid much attention because of simple construction, rugged rotor and low maintenance (Singh et al., 2014b). Furthermore, it provides constant frequency operation like SCIG (Rahim et Alyan, 1991) when is connected to grid. The main challenge of SyRG and SCIG is their voltage regulation and high excitation current. They are more sensitive to the supply voltage fluctuations, when the supply voltage is reduced, they draws more current. To solve this problem, additional equipment is required, such as STATCOM (Static Compensator) with a BESS connected on DC-link of VSC (Voltage Source Converter) (Singh et al., 2014b). According to (Bhende, Mishra et Malla, 2011; Orlando et al., 2013; Rahman et al., 1996; Singh, Niwas et Kumar Dube, 2014), PMSG can be a good alternative for DG sets in standalone system, if it is provided with voltage and frequency control. Therefore, design of HSPGS is highly dependent on the type of electrical generator and the number of the power electronic devices. Mostly, PV-DG HSPG (Hidayat, Kari et Mohd Arif, 2014; Kyoung-Jun et al., 2013) HSPGS, DG is kept connected to the grid at all time, which allows high fuel consumption, even at light load. Therefore, to reduce the fuel consumption and increase effectiveness of these types of HSPGS that uses fixed speed generators, the following combinations shown in Fig.4.2 are proposed.

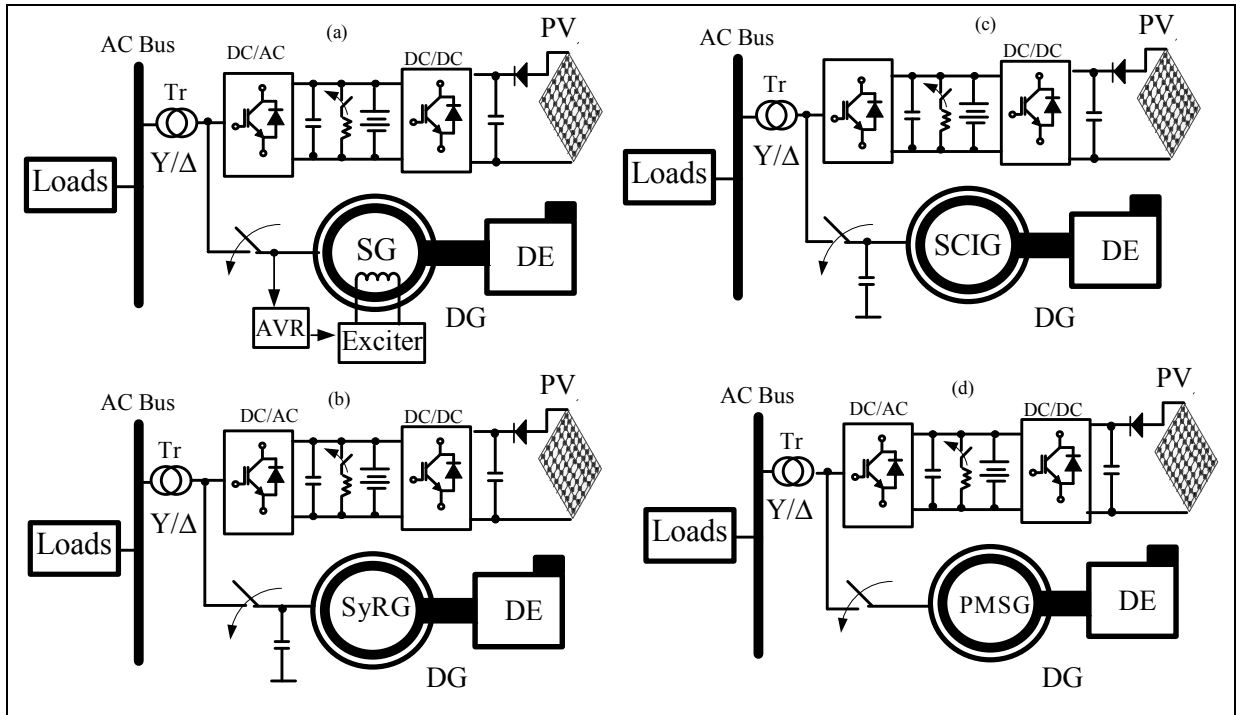


Figure 4.2 PV-DG HSPGS employing fixed speed generators

#### 4.2.1.1 System Description and Control

Fig.4.3 shows the selected DG-PV HSPGS for study. In this topology, DE driven fixed speed SG is equipped with automatic voltage regulation (AVR) and speed governor for SG terminal voltage and system frequency regulation at the PCC, and solar PV array is connected to the PCC through two-stage inverters, which are controlled to get MPPT from the solar PV array and regulate the AC voltage, system frequency, as well as improved power quality at the PCC. To get galvanic isolation between ESs and load, PV-DG HSPGS is reinforced by delta-star transformer. BESS is suggested for this topology in order to maintain power balance during variation of solar irradiation and during transition period of DG. Dump load is used to protect the BESS from overvoltage when it is fully charged by dumping the extra power. Moreover, RC output filter is connected in parallel at the output of the DC/AC inverter in order to compensate the voltage ripple created by high switching frequency.

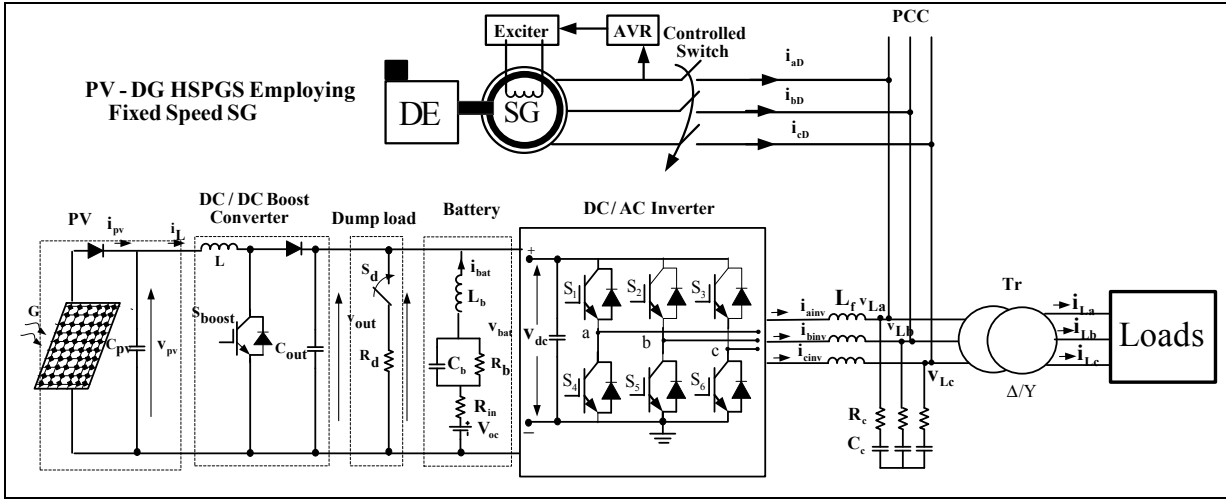


Figure 4.3 HSPGS based on solar PV array and DE driven fixed speed SG

### Control of the Solar PV Array

As shown in Fig.4.3, the solar PV array is connected to the DC bus via DC/DC boost converter to set-up the output DC voltage  $v_{out}$  and to get MPPT by controlling the output PV current  $i_{pv}$ . The control law of the DC/DC boost converter is obtained from the mathematical model already given in chapter two and expressed in (2.120). Based on this model, the dynamic of current, which passes through the inductance L is defined as:

$$L \frac{di_L}{dt} = v_{pv} - (1-d)v_{out} \quad (4.1)$$

And

$$u_i = v_{pv} - (1-d)v_{out} \quad (4.2)$$

From (4.2), one obtains the following expression:

$$d = 1 + \frac{u_i - v_{pv}}{v_{out}} \quad (4.3)$$

where  $d$  represents the control law.

$u_i$  represents the output PV current controller and is obtained as:

$$u_i = \left( k_p + \frac{k_i}{s} \right) (i_{mp} - i_{pv}) \quad (4.4)$$

where  $k_p$  and  $k_i$  denote proportional-integral gains, and  $i_{mp}$  represents the maximum current of PV, which is obtained using perturbation and observation (P&O) MPPT technique .

Fig.4.4 shows, the flowchart of the (P&O) MPPT technique (Chen et al., 2002).

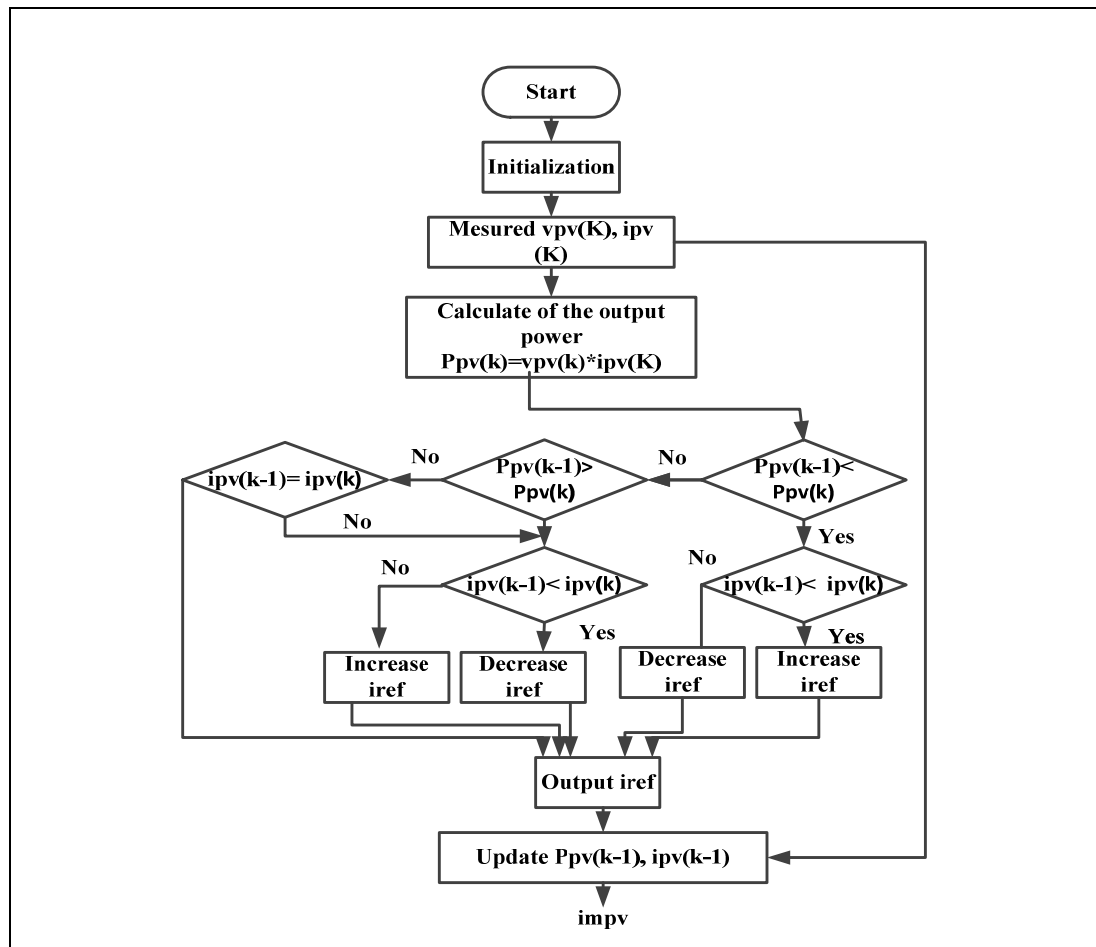


Figure 4.4 Flowchart of Perturbation and observation MPPT algorithm

In this technique, the output PV current is used as a control variable. Thus, the power of PV array ( $P_{pv}$ ) is calculated from the product of sensed PV current  $i_{pv}$  and voltage  $v_{out}$ . If  $P_{pv}$  increase with increasing  $i_{pv}$ , the reference current is increased by one perturbation step size; otherwise, the reference current is decreased by one perturbation step size, and if the  $P_{pv}$  decrease with increasing  $i_{pv}$ , the reference current is decreased by one perturbation step size; otherwise, the reference current is increased by one perturbation step size. Therefore, the peak power point ( $P_{pvmax}$ ) corresponds to the maximum current  $i_{mp}$ , which is used as reference current in (4.4).

### Control of the DG

As already indicate in the chapter two that the DG consists of two parts; mechanical part, which represents the DE and the electrical part that represents the electrical generator. As for DE, mostly in the literature authors use simplified model, which is already given in the chapter two. As for the electrical part, generally, SG is used as generator because it can regulate the SG terminal voltage and system frequency by itself as shown in Fig.4.5 (Darabi et Tindall, 2002).

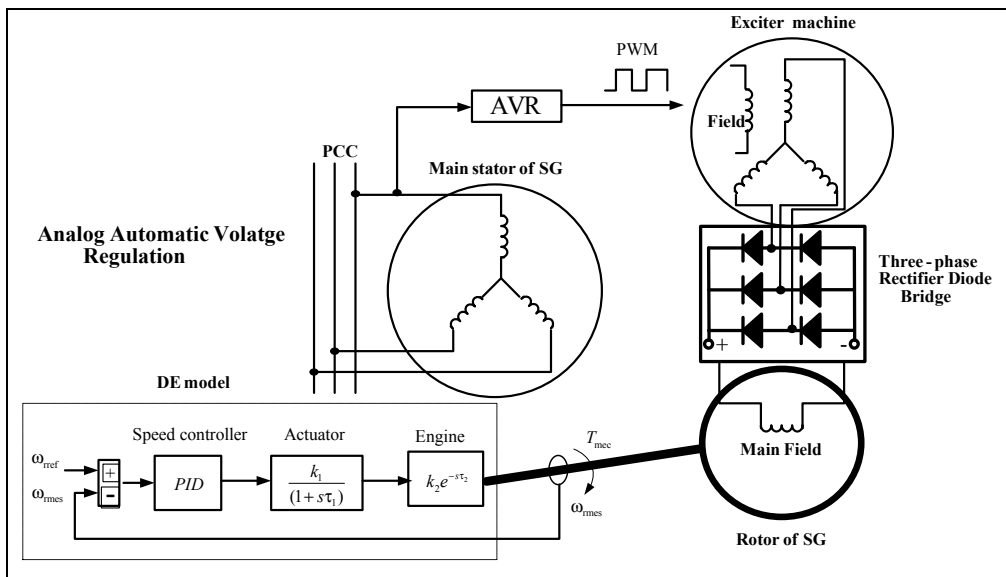


Figure 4.5 Block diagram for DG

Fig.4.5 shows a typical small DG, which consists of SG, an exciter machine, a three-phase rectifier diode bridge, and an analog automatic voltage regulation (AVR) (Darabi, Tindall et Ferguson, 2004). In this scheme, rotor of the SG is connected to the armature winding of the exciter machine through three-phase rectifier diode-bridge. The exciter field is fed by PWM signal from the AVR.

Usually, the AVR consists of sampling block, a PID controller, a power section and PWM output as shown in Fig.4.5. It adjusts the on-off ratio of the PWM output in response to change in phase voltage.

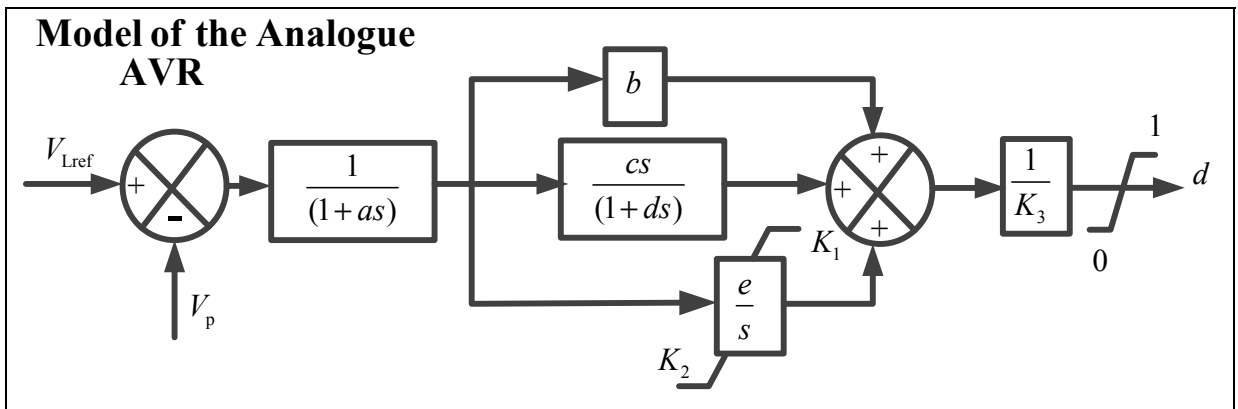


Figure 4.6 Model of the analogue AVR

The model of the analogue AVR, which is shown in Fig.4.6, uses the reference and the amplitude of the PCC voltage as input. In this study this reference voltage  $V_{Lref}$  is equal to 375V and its amplitude is calculated as follow:

$$V_p = \sqrt{\frac{2}{3}(v_{La}^2 + v_{Lb}^2 + v_{Lc}^2)} \tag{4.5}$$

where  $V_p$  denotes the amplitude of the measured AC voltage at the PCC.

Most of existing DGs installed in remote areas run at fixed speed. This operation mode shown in Fig.4.7 (Pena et al., 2008) is inefficient because of the high fuel consumption, especially when DG is operated at light load. However, variable speed operation works effectively.

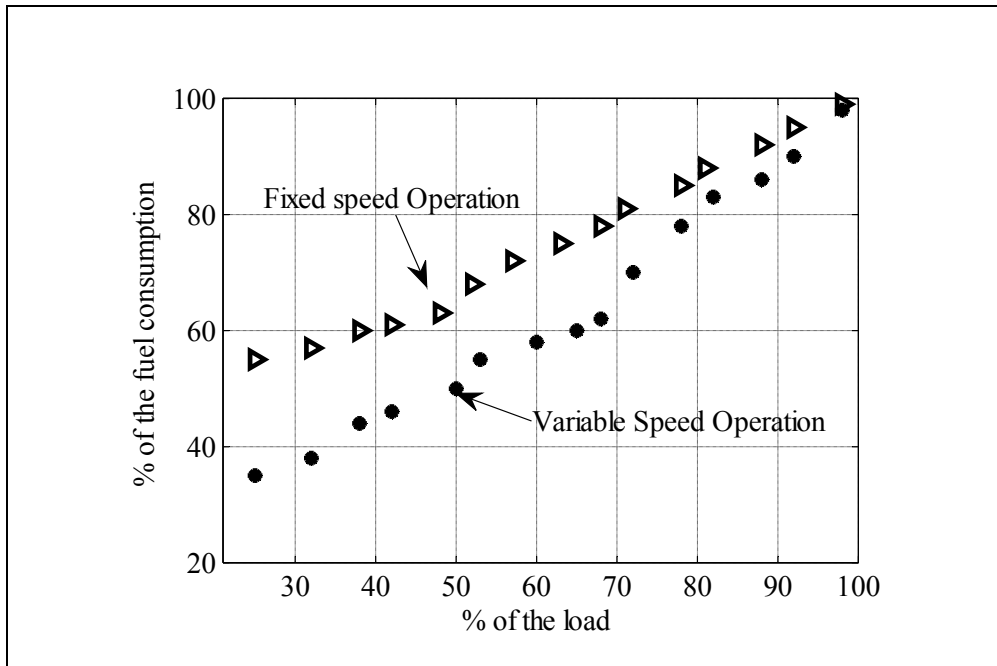


Figure 4.7 Fuel consumption for variable and fixed speed operation of DG  
(Pena et al., 2008)

In addition, during no-load, just a part of the fuel is burned by the engine and wetstacking is produced. Therefore, to improve the efficiency and avoid wetstacking, manufacturers suggest use a minimum load. This method is inefficient and costly. To remedy these drawbacks and increase the efficiency of DG, we propose the following solution;

DG should start-up only if the load power demand is greater than the generating power from PV and the SOC% of BESS is less than 50%. Therefore, DG must supply load and charge the battery simultaneously.

To connect DG to the PCC, the following synchronising conditions must be fulfilled:

1. Effective value and wave form of DG and AC voltage at the PCC must be equal,
2. Voltage phase of the DG and PCC must be equal,
3. Phase sequences of the DG and PCC must be equal.

Therefore, to connect or disconnect DG to the PCC, a controlled switch between PCC and DG is required.

Fig.4.8 shows the control algorithm developed to control the proposed switch. This control uses the sensed voltages ( $v_{Labc}$ ) at PCC and the terminal voltage of the DG ( $v_{DGabc}$ ) in order to calculate the peak voltages ( $V_P$ ) and ( $V_{PDG}$ ) using same equation given in (4.5). Based on the obtained peak voltages values, one calculates the phase's shift of DG and PCC voltages using in-phase and quadrature unites templates as:

$$u_{Lap} = \frac{v_{La}}{V_p} \quad (4.6)$$

And

$$u_{DGap} = \frac{v_{DGa}}{V_{pDG}} \quad (4.7)$$

The phase shift  $\theta_L$  of the AC voltage at the PCC and the phase shift  $\theta_{DG}$  of DG voltage are calculate as:

$$\theta_L = \arcsin(u_{Lap}) \quad (4.8)$$

And

$$\theta_{DG} = \arcsin(u_{DGap}) \quad (4.9)$$

Therefore, the switch will be closed only if the following conditions be satisfied:

$$\begin{cases} \Delta\theta = \theta_L - \theta_{DG} = 0 \\ P_L > P_{PV} \\ SOC\% \leq 50\% \end{cases} \quad (4.10)$$

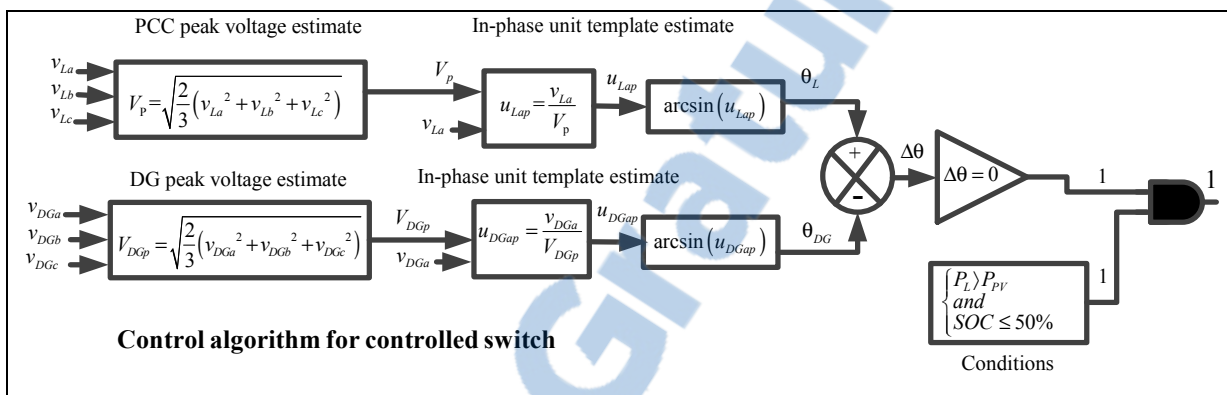


Figure 4.8 Proposed control algorithm for controlled switch

### Control of the dump loads

A dump load often called secondary load is mostly used in SPGS to dump excess of power generated from RESs in order to make equilibrium between RESs and load when BESS is fully charged. This element consists of an uncontrolled rectifier and chopper with series dump load (Singh, Murthy et Gupta, 2006).

Recently, (Chilipi, Singh et Murthy, 2014) has mentioned that electronic load controller (ELC) is not able to regulate the voltage and frequency if load is not purely resistive. Furthermore, it affects the power quality by injecting harmonics at the PCC. To avoid this problem, dump load and its controller in the proposed topologies shown in Fig.4.2 are tied to the DC side.

Fig.4.9 shows the block diagram of proposed control algorithm for a dump load. The reference battery voltage ( $V_{bat\_ref}$ ) is compared with measured battery voltage ( $V_{dc}=V_{bat}$ ) and the error is processed through a PI controller to generate switching signal for static switch ( $S_d$ ) of dump load controller.

A dump load resistance element rating is based on the rated active-power provided by the solar PV array. The value of dump load resistance is calculated as:

$$R_d = \frac{V_{dc}^2}{P_{PV}} \quad (4.11)$$

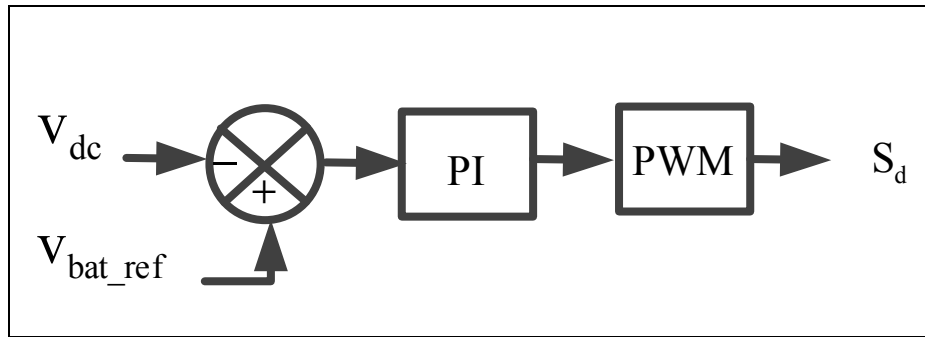


Figure 4.9 Dump load control algorithm

### Selecting the rating of BESS

The Thevenin-based equivalent battery model is used for modeling battery in this study. This model consists of capacitance  $C_b$ , which is calculated as:

$$C_b = \frac{kWh \times 3600 \times 10^3}{0.5(V_{oc\max}^2 - V_{oc\min}^2)} \quad (4.12)$$

where  $V_{ocmax}$ ,  $V_{ocmin}$ , kWh denote the maximum and minimum open circuit voltage of BESS under fully charged and discharged conditions and energy of the battery, respectively.

This model contains also  $R_{in}$ , which represents the equivalent resistance of parallel/series combinations of the battery, its value is smaller. Contrary, the value of  $R_b$  is higher because it represents the self-discharge resistance of battery.

The nominal DC link voltage  $V_{dc}$  is calculated using the following equation:

$$V_{dc} > \left( \frac{2\sqrt{2}}{\sqrt{3} m_a} \right) V_{LL} \quad (4.13)$$

where  $m_a$  and  $V_{LL}$  represents the index of modulation which is taken as 1, and  $V_{LL}$  is the AC line-line voltage. For  $V_{LL} = 460V$ ,  $V_{dc}$  should be greater than 752V, and is selected 1000V. Considering the ability of the proposed system to supply electricity to a load of 9 kW for 24h, the design storage capacity of the battery bank is taken 216kW.h. The commercially available battery bank consists of cells of 12 V. The nominal capacity of each cell is taken as 12Ah. To obtain 1000V through series connected cells of 12 V, the battery bank should have  $(1000/12) = 84$  number of cells in series. Since the storage capacity of this combination is 12 Ah. The total ampere hour required is  $(216kWh/1000V) = 216A.h$ , the number of such sets required to be connected in parallel would be  $(216Ah/12A h) = 18$ . The battery bank consists of 18parallel-connected sets of 84 series connected battery cells.

Taking the values of  $V_{ocmax} = 1088V$ ,  $V_{ocmin} = 980V$ , and the storage capacity of 216kW.h, the value of  $C_b$  is obtained using (4.12), and is equal to 6963F.

### **Modified instantaneous p-q theory control for DC/AC inverter**

Fig.4.10 shows the proposed control algorithm for the DC/AC inverter, which is based on instantaneous p-q theory. This theory, (Akagi, Kanazawa et Nabae, 1984) is based on instantaneous values in three-phase power system. It uses Clark transformation of the three-phase voltages and currents. This approach usually used for power quality improvement. To

achieve more tasks such as, AC voltage and the system frequency regulation, this control algorithm is modified by (Rezkallah et al., 2012), as shown in Fig.4.10.

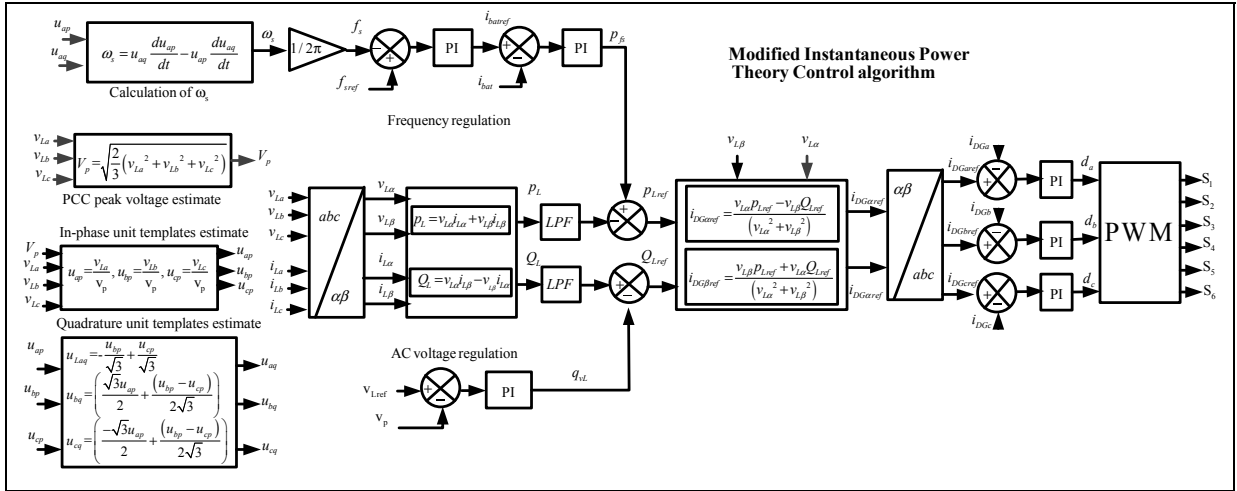


Figure 4.10 Modified instantaneous power theory control algorithm

The Clark transformations of the AC voltage and load currents are expressed as:

$$\begin{bmatrix} v_{L\alpha} \\ v_{L\beta} \end{bmatrix} = \sqrt{\frac{2}{3}} \begin{bmatrix} 1 & \frac{1}{2} & \frac{1}{2} \\ 0 & \frac{\sqrt{3}}{2} & \frac{\sqrt{3}}{2} \end{bmatrix} \begin{bmatrix} v_{La} \\ v_{Lb} \\ v_{Lc} \end{bmatrix} \quad (4.14)$$

$$\begin{bmatrix} i_{L\alpha} \\ i_{L\beta} \end{bmatrix} = \sqrt{\frac{2}{3}} \begin{bmatrix} 1 & \frac{1}{2} & \frac{1}{2} \\ 0 & \frac{\sqrt{3}}{2} & \frac{\sqrt{3}}{2} \end{bmatrix} \begin{bmatrix} i_{La} \\ i_{Lb} \\ i_{Lc} \end{bmatrix} \quad (4.15)$$

The instantaneous apparent complex power  $S$  is described as follow:

$$S_{ap} = (v_{L\alpha} + jv_{L\beta})(i_{L\alpha} - ji_{L\beta}) \quad (4.16)$$

Arrangement of (4.16) gives:

$$S_{ap} = \overbrace{(v_{L\alpha}i_{L\alpha} + v_{L\beta}i_{L\beta})}^{P_L} + j \overbrace{(v_{L\alpha}i_{L\beta} - v_{L\beta}i_{L\alpha})}^{Q_L} \quad (4.17)$$

where  $P_L$  and  $Q_L$  denote the real and imaginary alternating powers, which are composed of a continuous and alternating parts. The continuous part represents the fundamentals of current and voltage, and the alternating part represents the sum of harmonic components. Therefore, to separate the both parts, low-pass filters are used.

The active reference power ( $P_{Lref}$ ) is obtained by comparing the output of the low-pass filter to the output of the frequency PI battery current controller ( $p_{fs}$ ), and the reactive reference power ( $Q_{Lref}$ ) is obtained by compared the output of the low-pass filter to the output of the AC voltage PI controller ( $p_{vq}$ ). Based on the obtained references powers ( $P_{Lref}$  and  $Q_{Lref}$ ), the active and reactive source reference currents are calculated, which represent in this study the DG currents ( $i_{DG\alpha ref}$  and  $i_{DG\beta ref}$ ) as given in (4.18) and (4.19):

$$i_{DG\alpha ref} = \frac{v_{L\alpha}P_{Lref} - v_{L\beta}Q_{Lref}}{v_{L\alpha}^2 + v_{L\beta}^2} \quad (4.18)$$

And

$$i_{DG\beta ref} = \frac{v_{L\beta}P_{Lref} + v_{L\alpha}Q_{Lref}}{v_{L\alpha}^2 + v_{L\beta}^2} \quad (4.19)$$

To obtain the reference compensation currents in a-b-c coordinates, the inverse Clark transformation is used, which is expressed as follows:

$$\begin{bmatrix} i_{DGa_{ref}} \\ i_{DGb_{ref}} \\ i_{DGc_{ref}} \end{bmatrix} = \begin{bmatrix} 1 & 0 \\ \frac{1}{2} & \frac{\sqrt{3}}{2} \\ \frac{1}{2} & -\frac{\sqrt{3}}{2} \end{bmatrix} \begin{bmatrix} i_{DG\alpha_{ref}} \\ i_{DG\beta_{ref}} \end{bmatrix} \quad (4.20)$$

The reference source currents ( $i_{DGa_{ref}}$ ,  $i_{DGb_{ref}}$ ,  $i_{DGc_{ref}}$ ) are compared with the sensed source currents ( $i_{DGa}$ ,  $i_{DGb}$ ,  $i_{DGc}$ ) and the current errors are fed to PI current controllers. The output of PI controllers ( $d_a, d_b, d_c$ ) are compared with triangular carrier wave. The frequency of PWM control technique is set to 5 kHz and is used to generate switching signals to control the DC/AC inverter.

For the system frequency ( $f_s$ ) regulation, the estimated system frequency  $f_s$  is compared to its reference ( $f_{sref}$ ), which is equal to 60Hz, and the error is fed to PI frequency controller as follows:

$$i_{batref} = \left( k_{pfs} + \frac{k_{ifs}}{s} \right) (f_{sref} - f_s) \quad (4.21)$$

where  $k_{pfs}$ ,  $k_{ifs}$  denote proportional and integral gains, and  $f_s$  represent the system frequency, which is calculated as follows:

$$f_s = \frac{\omega_s}{2\pi} \quad (4.22)$$

where  $\omega_s$  denotes the angular frequency. It is expressed in rad/s, and is calculated as:

$$\omega_s = \cos(\theta_L) \frac{d}{dt}(\sin(\theta_L)) - \sin(\theta_L) \frac{d}{dt}(\cos(\theta_L)) \quad (4.23)$$

where  $\cos\theta_L$  and  $\sin\theta_L$  denote sin and cos of the phase shift of the PCC voltage, which is calculated using in-phase and quadrature unit templates as:

$$u_{ap} = \frac{v_{La}}{V_p}, u_{bp} = \frac{v_{Lb}}{V_p}, u_{cp} = \frac{v_{Lc}}{V_p} \quad (4.24)$$

And

$$\begin{aligned} u_{aq} &= \frac{1}{\sqrt{3}}(-u_{bp} + u_{Lcp}), u_{bq} = \left( \frac{\sqrt{3}}{2}u_{ap} + \frac{1}{2\sqrt{3}}(u_{bp} - u_{cp}) \right), \\ u_{cq} &= \left( -\frac{\sqrt{3}}{2}u_{ap} + \frac{1}{2\sqrt{3}}(u_{bp} - u_{cp}) \right) \end{aligned} \quad (4.25)$$

where  $u_{ap}$  and  $u_{aq}$  represent  $\sin\theta_L$  and  $\cos\theta_L$ , respectively and  $V_p$  represents the amplitude of the AC voltage already calculate using (4.5).

The obtained ( $i_{batref}$ ) is compared with the sensed battery current ( $i_{bat}$ ), and the output of the PI battery current controller is as follows:

$$p_{fs} = \left( k_{pbat} + \frac{k_{ibat}}{s} \right) (i_{batref} - i_{bat}) \quad (4.26)$$

where  $p_{fs}$ ,  $k_{pbat}$ ,  $k_{ibat}$  denote the estimated frequency active power component and the proportional and integral gains, respectively.

The output of the PI battery current controller ( $p_{fs}$ ) is compared with the output of low-pass filter; the obtained error represents the reference active power component ( $P_{Lref}$ ) of the source currents.

As for AC voltage regulation, the amplitude of the AC voltage ( $V_p$ ) which is expressed in (4.5) is compared with reference voltage ( $v_{Lref}$ ), and the error is fed to PI voltage controller as:

$$q_{vL} = \left( k_{pv} + \frac{k_{iv}}{s} \right) (v_{Lref} - v_{Li}) \quad (4.27)$$

where  $q_{vL}$ ,  $k_{pv}$ ,  $k_{iv}$  denote the estimated quadrature power component and the proportional and integral gains, respectively.

The output of the PI voltage controller ( $q_{vL}$ ) is compared with the output of low-pass filter; the obtained error represents the reference reactive power component ( $Q_{Lref}$ ) of the source currents.

#### 4.3 Topology Designs of Hybrid Standalone Power Generation System based on PV Array and DE Driven Variable Speed Generators

Fig.4.11 shows the proposed PV-DG HSPGS topologies which are based on two energy sources; 1) PV array connected to the DC bus through DC/DC boost converter, and 2) DE driven variable speed generators such as, SG, SyRG, PMBLDCG, SCIG, PMSG and DFIG.

The proposed topologies are designed in order to get high efficiency with reduced cost from the DG and the solar PV array. All are tied to the DC bus through only one AC/DC power converter instead of two power converters often used by (Joon-Hwan, Seung-Hwan et Seung-Ki, 2009; Leuchter et al., 2009), and they are controlled to get high efficiency from DGs.

Furthermore, dump load and BESS in the proposed PV-DG HSPGSs are tied to the DC bus instead of the AC bus as proposed by (Datta et al., 2011; Sekhar, Mishra et Sharma, 2015). Therefore, by tying dump loads to the DC side, one avoids risking power quality disturbance at the PCC. They are controlled to balance the power in the system by absorbing the extra power provided from the PV array in order to protect the BESS from the overvoltage.

Moreover, in the proposed PV-DG HSPGS only one interfacing DC/AC inverter is used instead of two DC/AC inverters used by (Whei-Min, Chih-Ming et Chiung-Hsing, 2011), and they are controlled to get high efficiency from DGs.

The solar PV arrays are connected to the DC bus through DC/DC boost converters, and to the PCC through common DC/AC interfacing inverters. DC/DC boost converters are controlled to get MPPT from solar PV array, to regulate the output PV voltage at the desired DC-bus voltage. DC/AC interfacing inverters are used to regulate the AC voltage and system frequency, as well as, improved the power quality at the PCC.

In the proposed PV-DG HSPGSs DEs are controlled in order to provide desired torque which corresponds to the exact load power demand.

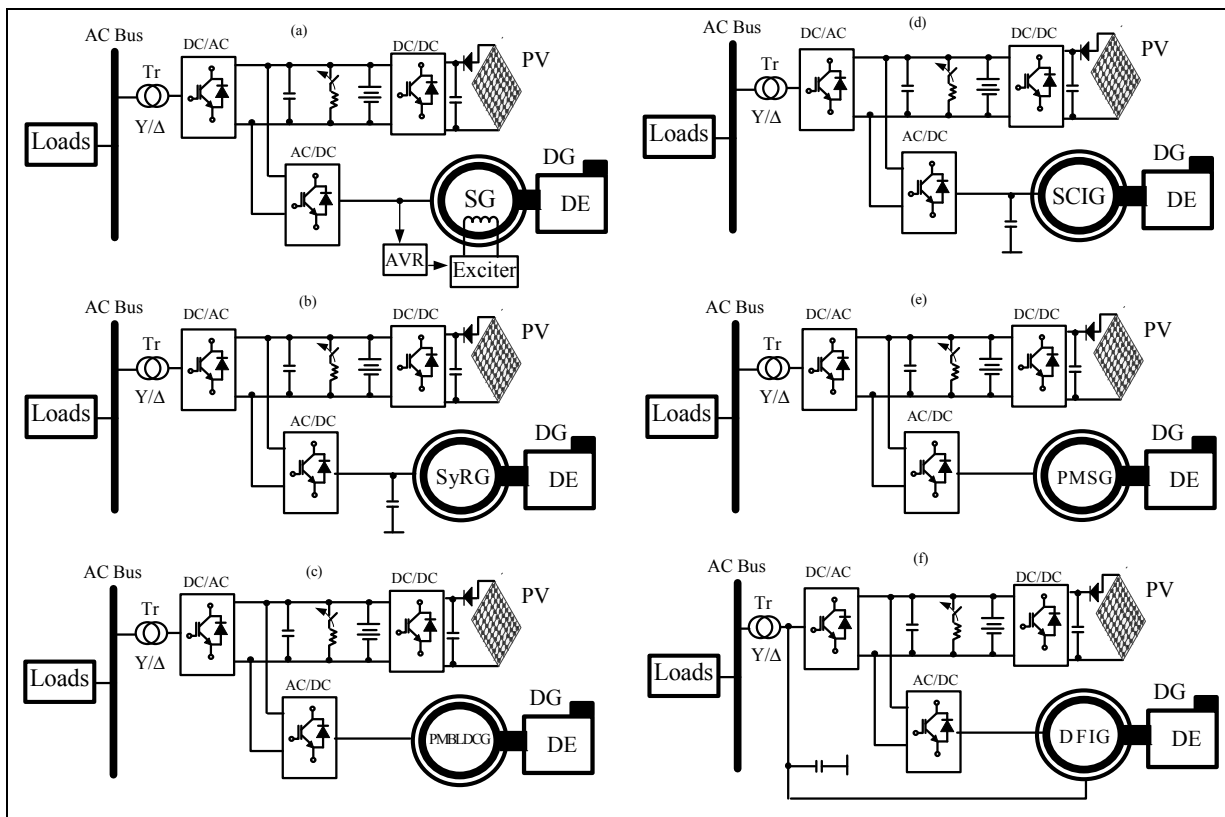


Figure 4.11 HSPGS based on solar PV array and DE driven variable speed generators

### 4.3.1 System Description and Control

Fig.4.12 shows the selected topology for study. It consists of DE as a prime mover coupled to a variable speed DFIG and a solar PV array. The stator of the DFIG is connected directly to the PCC and its rotor is tied to the common DC bus through a small size AC/DC converter. The solar PV array is connected to the PCC through two-stage inverters. The advantages of this proposed topology that only one DC/AC interfacing inverter is required to connect the rotor side of DFIG and the solar PV array to the PCC, and DE rotates variably according to the load power demand, which allows less fuel consumption especially at light loads.

As shown in Fig.4.12, capacitor bank is connected to the stator terminals in order to provide initial excitation current to the rotor of the DFIG. The proposed PV-DG HSPGS is reinforced by BESS connected at the DC bus in order to ensure system stability by compensating the fluctuations of the output solar PV power and loads, as well as to ensure a continuous power supply to the load during start-up of the DG.

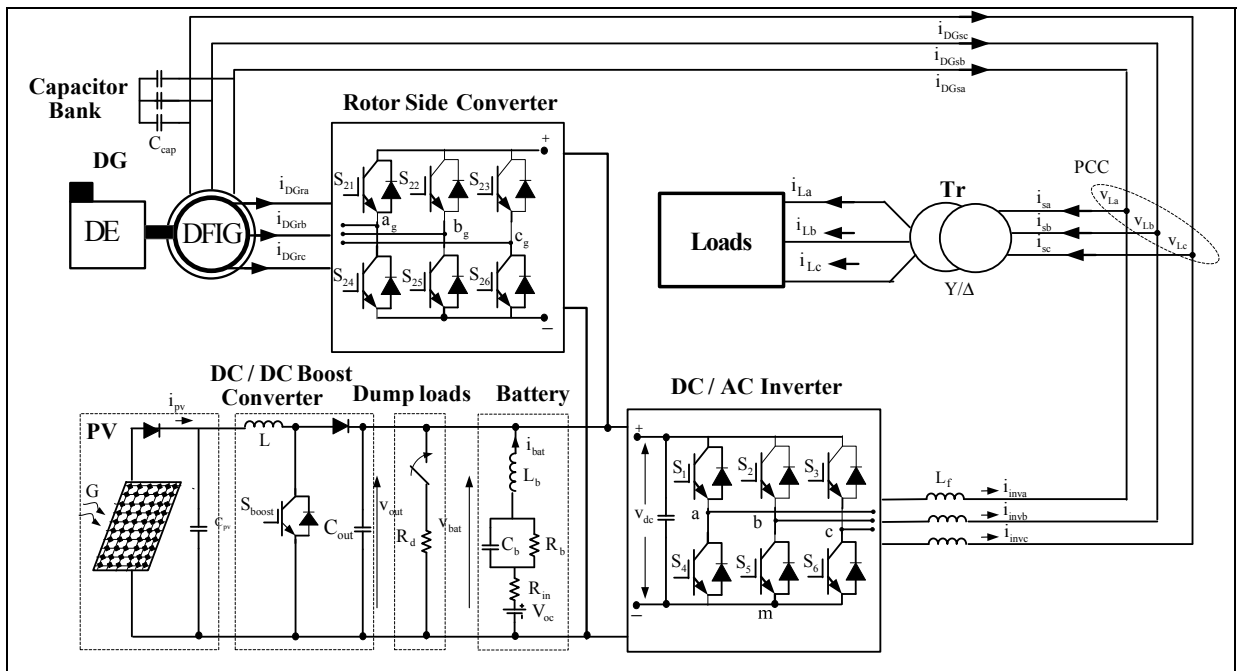


Figure 4.12 HSPGS based on solar PV array and DE driven variable speed DFIG

As shown in Fig.4.13, DFIG can deliver power to the connected loads through the stator and rotor. This is dependent upon the slip ( $S$ ), which is defined as follow:

$$S = \frac{\omega_r}{\omega_s} \quad (4.28)$$

where  $\omega_r$  and  $\omega_s$  denote the rotor and stator frequencies, respectively.

However, if  $S < 0$ , DFIG operates in super-synchronous mode as shown in Fig.4.13 (a). DFIG in this operation mode provides power to the loads through stator and rotor, and if  $S > 0$ , DFIG operates in sub-synchronous mode. In this case the produced power will be delivered to the loads through stator.

According to (Wang, Nayar et Wang, 2010), to maximize the fuel efficiency in SPGS that contains DG, DE speed should be determined by best speed torque relationship, which can be done with system performance curve.

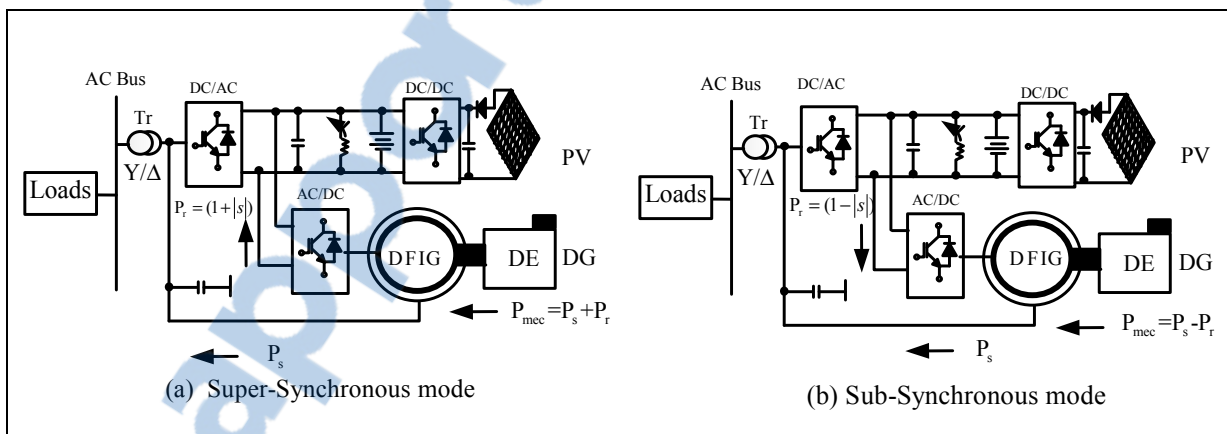


Figure 4.13 DFIG operation modes; a) super-synchronous mode and  
b) sub-synchronous mode

The solar PV array is connected to the DC bus via DC/DC boost converter as shown in Fig.4.13 in order to step up the output DC voltage ( $v_{out}$ ). Furthermore, to maximize the output PV power by controlling the output PV current ( $i_{pv}$ ) using the same MPPT-technique based on P&O already discussed is used. The control of the DC/DC boost is the same as given in detail before.

**4.3.1.1 Model of the variable speed DG**

The conventional approach used for sizing the DG is based on the peak load power demand. Unfortunately, this peak load power demand is occasional. Therefore, DG is oversized according to the prevalent load conditions. Nevertheless, to operate DG efficiently, its speed must be varied according to the load changes. That is to say the actuator will adjust the DE speed by adjusting the fuel flow, as shown in Fig.4.14.

The maximum fuel efficiency curve for 15 kW variable speed DG, which is used by (Waris et Nayar, 2008) and shown in Fig.4.14 is being used in this study.

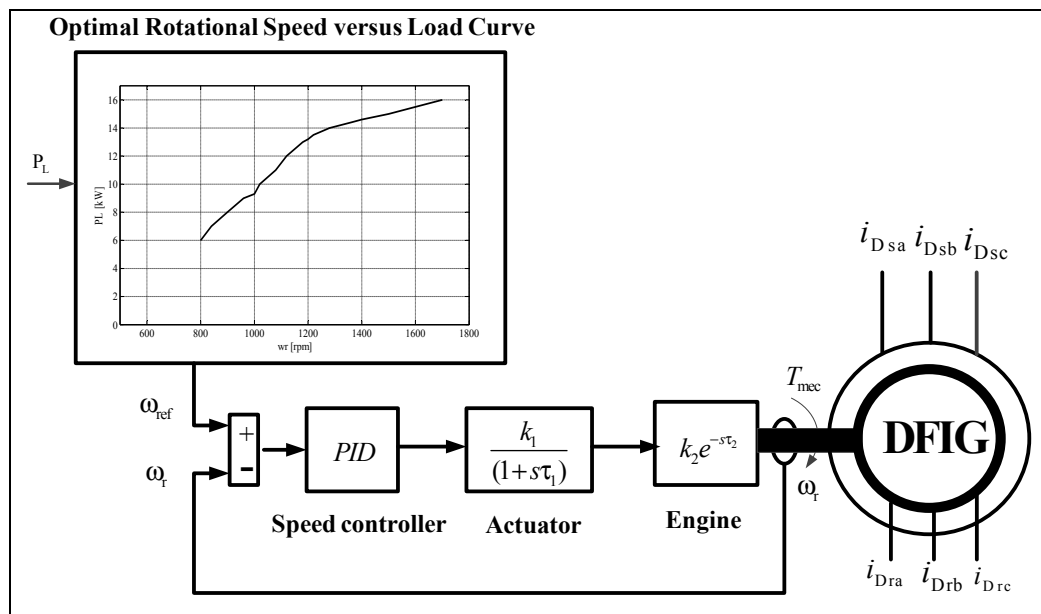


Figure 4.14 Model of the variable speed DE

#### 4.3.1.2 Control of the Rotor Side Converter

Seeing that the DE is running at a specific speed according to load changes, the developed mechanical torque ( $T_{mec}$ ) and DFIG rotor speed ( $\omega_r$ ) are altered accordingly. The proposed developed algorithm for the rotor side should ensure control of AC voltage at constant frequency. To achieve these tasks, indirect stator flux oriented control is used.

##### Indirect stator flux oriented control technique

Detailed diagram of the proposed control for RSC is shown in Fig.4.15. In this control algorithm, AC voltage is maintained at constant frequency and its magnitude is regulated through the stator flux. Usually, in grid-connected, the stator flux is determined by the grid voltage, but for SPGS is set by controlling the rotor excitation current (Pena, Clare et Asher, 1996). That is why the stator flux-oriented field control is used for decoupling the active and reactive current control loops. The d-axis is associated with the stator flux axis and the q-axis is associated with the stator voltage axis.

The q-axis current loop manages the torque of the DFIG by controlling the active power flow and the d-axis controls the machine flux by controlling its reactive power flow.

The detailed mathematical model of the DFIG given in chapter 2 is used to obtain the control laws for RSC.

$$\begin{cases} \lambda_{ds} = L_s i_{ds} + L_m i_{dr} \\ \lambda_{qs} = L_s i_{qs} + L_m i_{qr} \end{cases} \quad (4.29)$$

And

$$\begin{cases} v_{ds} = R_s i_{ds} + \frac{d\lambda_{ds}}{dt} - (\omega_s - \omega_r) \lambda_{qs} \\ v_{qs} = R_s i_{qs} + \frac{d\lambda_{qs}}{dt} + (\omega_s - \omega_r) \lambda_{ds} \end{cases} \quad (4.30)$$

Under steady-state conditions (i.e.,  $d\lambda_{ds}/dt = 0$ ,  $d\lambda_{qs}/dt = 0$ ) and in the stator-flux-oriented frame (i.e.,  $\lambda_{qs} = 0$ ), (4.29)–(4.30) are modified as:

$$\begin{cases} L_s i_{qs} + L_m i_{qr} = 0 \\ v_{ds} = R_s i_{ds} \\ v_{qs} = R_s i_{qs} + (\omega_s - \omega_r) \lambda_{ds} \end{cases} \quad (4.31)$$

From (4.31), one obtained  $i_{qr}$  as:

$$i_{qr} = -\frac{L_s}{L_m} i_{qs} \quad (4.32)$$

And the stator magnetising current ( $i_{ms}$ ) is calculated using the following equation:

$$\lambda_{ds} = L_s i_{ds} + L_m i_{dr} = L_m i_{ms} \quad (4.33)$$

Replacing the equivalent expression of  $i_{ds}$  expressed in (2.54), and eliminating  $i_{qs}$  using (4.29), with  $\lambda_{qs} = 0$ , one gets;

$$\tau_{ms} = \frac{d}{dt} i_{ms} + i_{ms} = i_{dr} + \frac{1 + \sigma_s}{R_s} v_{ds} \quad (4.34)$$

The electromagnetic torque, which is given in (2.57) in chapter 2, becomes as;

$$T_{eref} = -\left(\frac{3}{2}\right) \left(\frac{p}{2}\right) \frac{L_m^2}{L_s} i_{qr} i_{msref} \quad (4.35)$$

where  $\tau_{ms} = L_s/R_s$  and  $\sigma_s = 1 - (L_m^2/L_s L_r)$ , and  $i_{msref}$ ,  $T_{eref}$  denote the reference magnetising current and reference electromagnetic torque, respectively.

The reference magnetising current is obtained as:

$$i_{msref} = \frac{T_{eref}}{\left(\frac{3}{2}\right)\left(\frac{p}{2}\right)\frac{L_m^2}{L_s}i_{qr}} \quad (4.36)$$

The reference electromagnetic torque is calculated as;

$$T_{eref} = \left(k_{p\omega_r} + \frac{k_{i\omega_r}}{S}\right)(\omega_{rref} - \omega_r) \quad (4.37)$$

where  $k_{p\omega_r}$ ,  $k_{i\omega_r}$ ,  $\omega_r$  and  $\omega_{rref}$  denote proportional and integral gains, the rotor speed and its reference, which is obtained using the optimal rotational speed versus load characteristic, which is already shown in Fig.4.4 (Waris et Nayar, 2008).

The stator magnetising current is calculated using (4.33) as:

$$i_{ms} = \frac{\lambda_{ds}}{L_m} \quad (4.38)$$

where  $\lambda_{ds}$  represents the stator flux in d-axis and is calculated using the following expression:

$$\lambda_{ds} = \lambda_{\alpha s} \cos \theta_s + \lambda_{\beta s} \sin \theta_s \quad (4.39)$$

And

$$\lambda_{\alpha s} = \int (v_{\alpha s} - R_s i_{\alpha s}) dt \quad (4.40)$$

$$\lambda_{\beta s} = \int (v_{\beta s} - R_s i_{\beta s}) dt \quad (4.41)$$

The stator flux angle  $\theta_s$  is calculated as follow;

$$\theta_s = \arctan\left(\frac{v_{\beta s}}{v_{\alpha s}}\right) \quad (4.42)$$

where  $v_{\alpha s}$  and  $v_{\beta s}$  denote the transformed sensed stator voltages in Clarke's transformation.

The developed control algorithm for the RSC is obtained using the mathematical model of the DFIG already given in chapter 2 and expressed by equations (2.51) and (2.52).

Therefore, the control laws are obtained by substituting stator current expressions, which are derived from the stator flux relations into rotor flux and in rotor voltages as:

$$\begin{cases} v_{dr} = R_r i_{dr} + \sigma L_r \frac{di_{dr}}{dt} - \omega_{slip} \sigma L_r i_{qr} \\ v_{qr} = R_r i_{qr} + \sigma L_r \frac{di_{qr}}{dt} + \omega_{slip} \sigma L_r i_{dr} + \omega_{slip} \frac{L_m}{L_s} i_{ms} \end{cases} \quad (4.43)$$

where  $v_{dr}$ ,  $v_{qr}$ ,  $i_{dr}$ ,  $i_{qr}$ ,  $R_r$ ,  $L_r$ ,  $L_m$ ,  $L_s$  and  $\omega_{slip}$  denote rotor voltages and currents in d-q axis reference frame, rotor resistance and inductance, mutual inductance, stator inductance and slip angular frequency, respectively.

With help of inverse Park transformation expressed in (2.50), the d-q components of the rotor voltages ( $v_{drref}$  and  $v_{qrref}$ ) are transformed to three phase rotor voltages and compared with fixed-frequency (5 kHz) triangular carrier wave to generate gating signals for IGBTs of RSC.

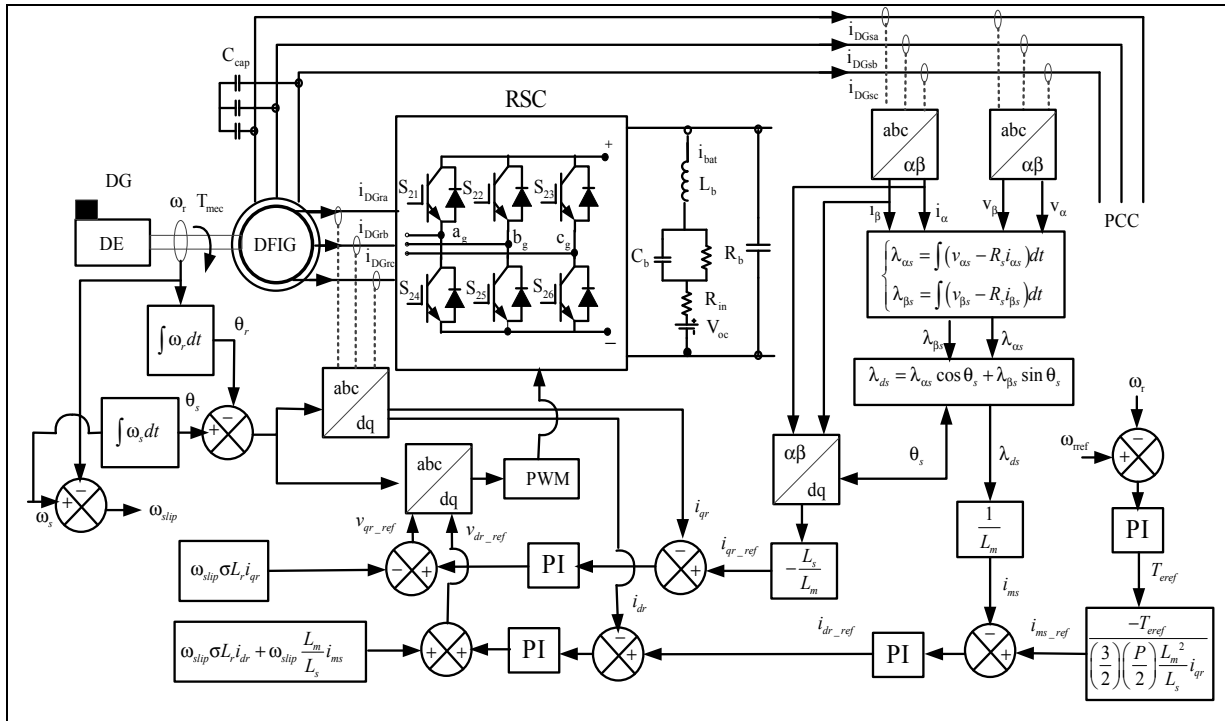


Figure 4.15 Control algorithm for rotor side converter

### 4.3.1.3 Control of the interfacing DC/AC inverter

As shown in Fig. 4.16, the functions of the DC/AC interfacing inverter are to regulate the system frequency and the AC voltage at the PCC at their rated value, as well as to compensate the harmonics and load balancing.

The system frequency is achieved by generating the stator flux angle  $\theta_s$  using the reference stator frequency as:

$$\theta_s = 2\pi f_s t \tag{4.44}$$

where  $t$  and  $f_s$  represent sampling time and the stator frequency, which is equal to 60Hz.

In the proposed control algorithm, the reference value of the d-component ( $I_{dsref}$ ) is obtained as:

$$I_{dsref} = \left( k_{pv} + \frac{k_{iv}}{S} \right) (V_{Lref} - V_p) \quad (4.45)$$

where  $K_{pv}$ ,  $K_{iv}$  denote proportional and integral gains of the AC voltage PI controller and  $V_{Lref}$  and  $V_p$  represents the reference amplitude voltage and its calculated value respectively.

$V_p$  is calculated using the following expression as;

$$V_p = \sqrt{\left( \frac{2}{3} \right) (v_{La}^2 + v_{Lb}^2 + v_{Lc}^2)} \quad (4.46)$$

where  $v_{Labc}$  denotes the instantaneous PCC voltages.

The reference value q-component  $I_{qsref}$  is obtained using the same equation (4.32) as:

$$I_{qsref} = -\frac{L_m}{L_s} i_{qr} \quad (4.47)$$

where  $i_{qr}$  represent the q-component of the rotor current.

The stator current errors are obtained from the difference of the sensed total currents at the PCC ( $i_{sabc}$ ) and their reference currents ( $i_{sabcref}$ ). The output signals from proportional-integral current controllers are compared with fixed-frequency triangular carrier wave to generate gating signals for IGBTs of DC/AC interfacing inverter as shown in Fig.4.16.



### Performance analysis under sudden variation of solar irradianations and with state of charge of battery is greater to 50% and under linear load

The waveforms of the AC voltages ( $v_{Labc}$ ), DG currents ( $i_{DGabc}$ ), load currents ( $i_{Labc}$ ), output inverter currents ( $i_{invabc}$ ), PV current and its reference ( $i_{pv}$  &  $i_{pvref}$ ), DC-link voltage ( $V_{dc}$ ), state of charge of battery (SOC%) and the system frequency ( $f_s$ ) when the SOC% is greater than 50% are shown in Fig.4.17. It is observed that the AC voltage and the system frequency at the PCC are kept constant in the presence of different conditions; 1) decreasing of the output PV current (Zoom1), and when 2) and 3) increasing and decreasing of the load currents (Zooms 2 and 3), as well as, decreasing the solar irradianations.

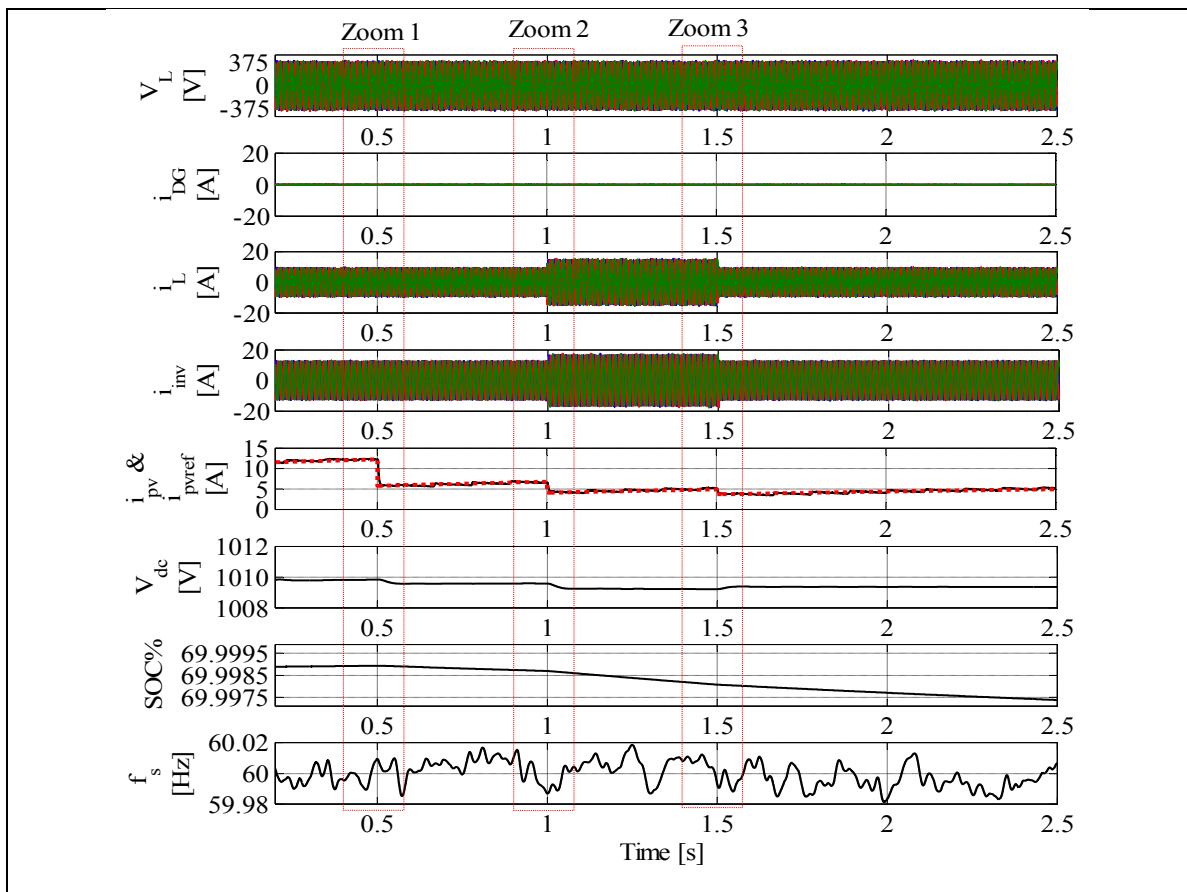


Figure 4.17 Dynamic response of PV-DG HSPGS based on fixed speed SG when the SOC% of BESS is greater to 50%

Fig.4.18 shows the zoom 1 of the simulation results shown in Fig.4.17 between  $t=0.4$  s and  $t=0.6$  s. It is observed that from  $t=0.4$  s to  $t=0.5$  s, the solar PV array is providing sufficient power that is why the battery is charging in this period of time. It is observed that the PV current follows its reference and the output DG current is kept equal to zero, because of the SOC% is greater than 50% and PV produces enough of power to the load. Furthermore, in this period of time, the AC voltage and the system frequency at the PCC are regulated at their rated values, confirming that the proposed approach for voltage and frequency regulation working well. It is observed that at  $t=0.5$  s, PV output current is decreased with its reference, verifying that P&O MPPT technique is able to track the maximum of output PV current. It is observed also that the DG output current is remaining equal to zero even though the load current is greater to the PV current, seeing that the second condition (SOC% < 50%) is not valid to run DG.

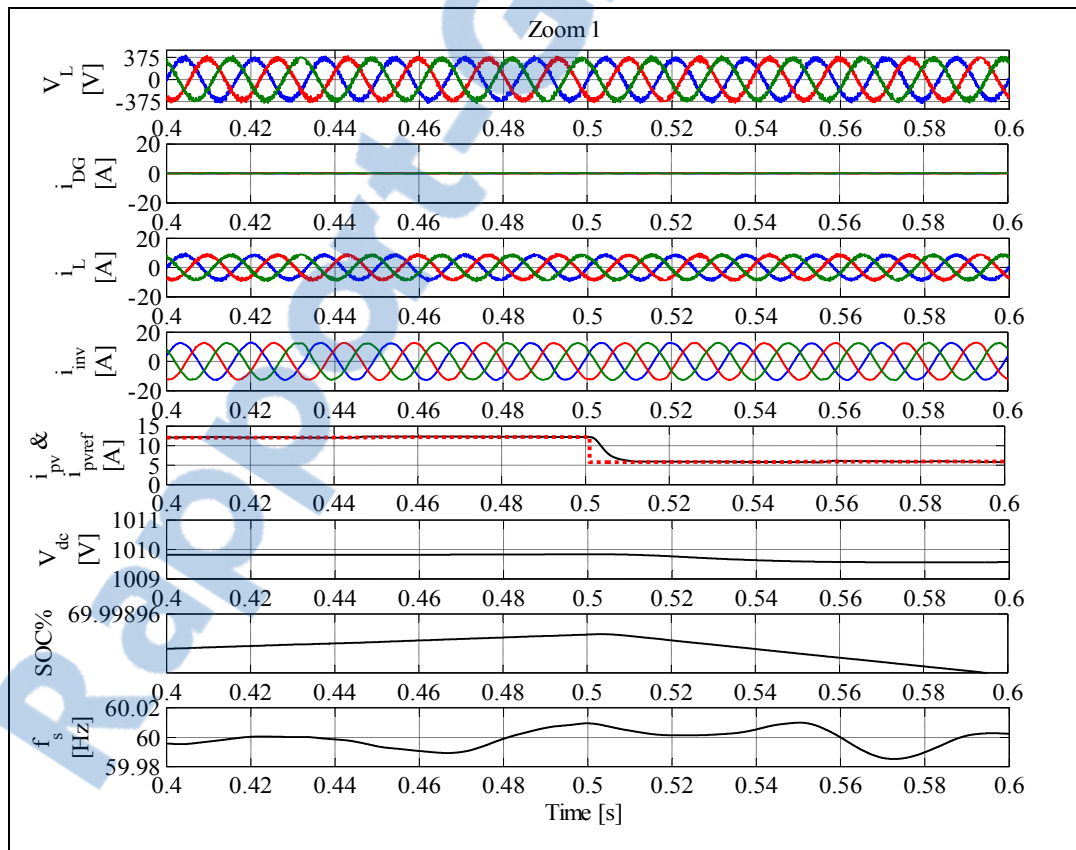


Figure 4.18 Zoom 1 of the results shown in Fig 4.17

Fig.4.19 shows the zoom 2 of the simulation results shown in Fig.4.17 between  $t=0.9$  s and  $t=1.1$  s. It is observed that from  $t=0.9$  s to  $t=1$  s, the output PV current is decreased and load current is increased but the SOC% is greater than 50%. Therefore, BESS should provide the deficit of power to the load. It is observed that  $v_{dc}$  and SOC% are decreased from  $t=1$  s. It is evident also in this period of time that the AC voltage and system frequency at the PCC are kept constant during the variation of solar irradiation and load, which confirms the robustness of the proposed control approach.

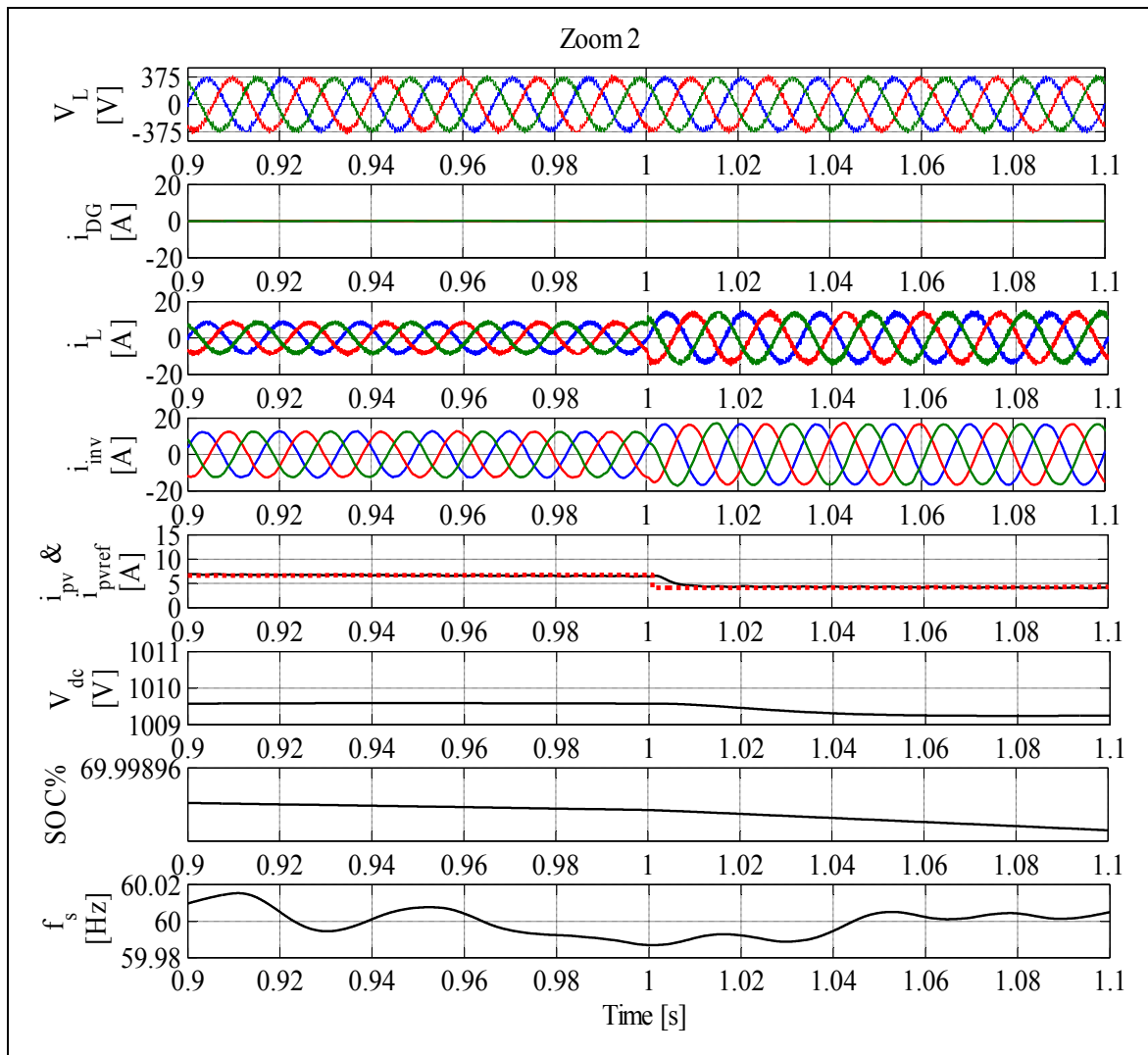


Figure 4.19 Zoom 2 of the results shown in Fig 4.17

Fig.4.20 shows the zoom 3 of the simulation results shown in Fig.4.17 between  $t=1.4$  s and  $t=1.6$  s. It is observed from  $t=1.5$  s, load current is decreased but the output PV current is still less to the load current and that is why BESS is discharging. DG in this period of time is turn off because the  $SOC\% > 50\%$ . The AC voltage and the system frequency at the PCC are regulated at their rated values and the output PV current follows its reference which leads that the proposed control algorithm for MPPT and voltage, as well as for frequency regulation are working well.

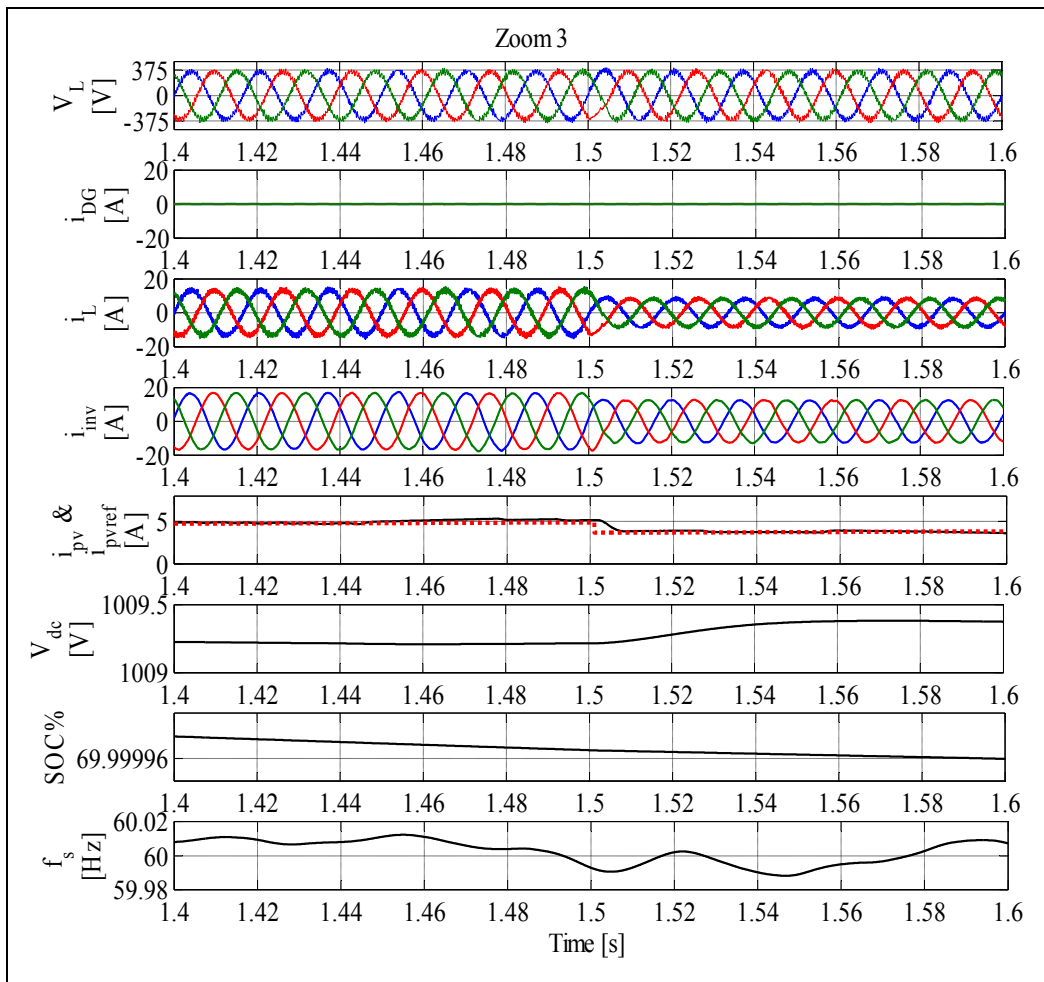


Figure 4.20 Zoom 3 of the results shown in Fig 4.17

**Performance analysis under sudden variation of solar irradiations and when the state of charge of battery is less to 50% under nonlinear load**

Fig.4.21 shows the waveforms of the AC voltage ( $v_L$ ), phase shift ( $\theta_L$ ) of the AC voltage, phase shift ( $\theta_{DG}$ ) of the DG terminal voltage, DG output current ( $i_{DG}$ ), load current ( $i_L$ ), PV output power ( $P_{pv}$ ), consumed load power ( $P_L$ ), DC-link voltage ( $V_{dc}$ ), state of charge of battery (SOC%) and the system frequency ( $f_s$ ). The objective of this test is to verify if the developed control algorithms for the proposed PV-DG HSPGS are able to regulate the AC voltage and the system frequency, as well as to improve the power quality at the PCC in the presence of nonlinear load and when the SOC% is less than 50%.

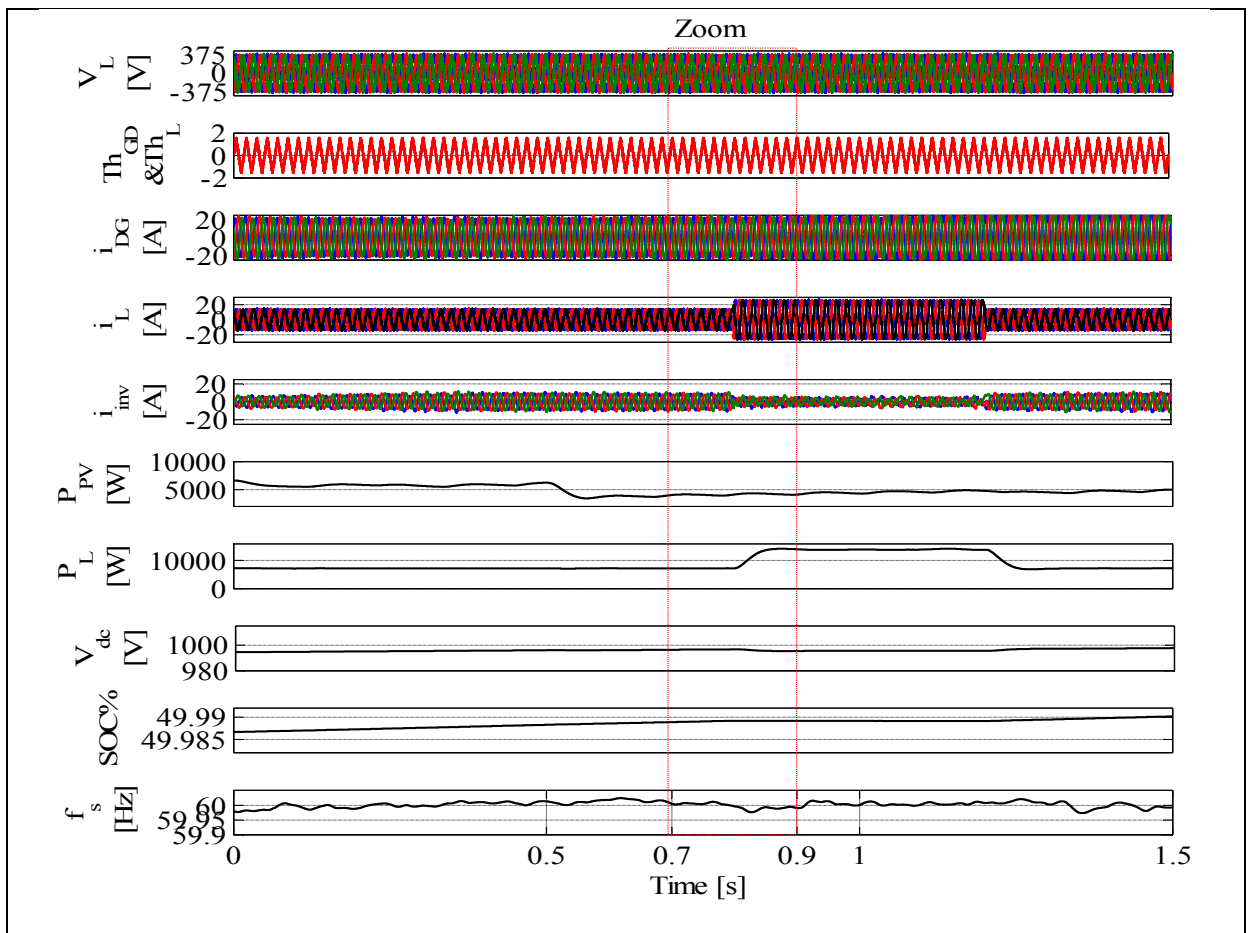


Figure 4.21 Dynamic response of PV-DG HSPGS based on fixed speed SG when the SOC% of BESS is less than 50%

It is observed that from  $t = 0$  s to 0.5 s, the output PV power is less than the consumed load power, the SOC% of BESS is less than 50% and  $\theta_L = \theta_{DG}$ . Therefore, conditions to turn on the DG are verified and that is why the DG currents are not equal to zero. As is already indicate that among our objectives are to improve the performance of the DG and that is why DG in this period of time provides power to the load and charges the BESS, simultaneously. In addition, the AC voltage and the system frequency are regulated at their rated values.

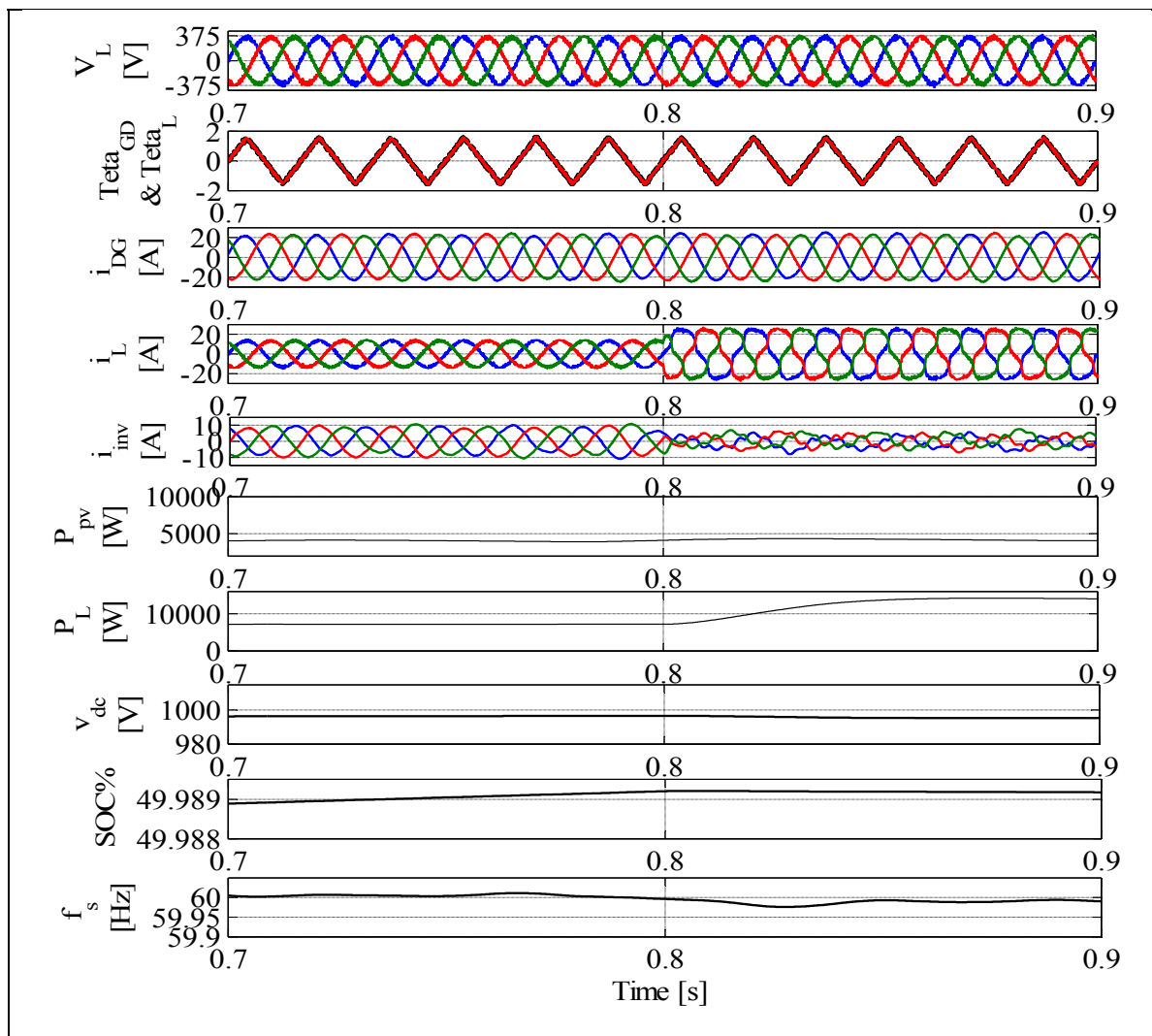


Figure 4.22 Zoom the results shown in Fig 4.21 between  $t=0.7$  s to  $t=0.9$  s.

Fig.4.22 shows the zoom of the simulation results shown in Fig.4.21 between  $t=0.7$  s and  $t=0.9$  s. It is observed that at  $t=0.8$  nonlinear load is connected and DC/AC inverter works as active filter, it compensates harmonics and balance the source currents. It is observed that after compensation DG currents ( $i_{DG}$ ) appear as pure sinusoidal balanced currents. It is observed at  $t=0.8$  s the study state error of the PCC voltage is equal to zero. In addition, the AC voltage and the system frequency are not affected during presence of nonlinear load, which confirms the robustness of the proposed control algorithm for AC voltage and system frequency regulation, as well as, for power quality improvement at the PCC.

#### **4.4.2 Performance of the HSPGS power generation using PV and DG driven variable speed DFIG**

Simulations are carried out using MATLAB/Simulink, to test the performance of the proposed PV-DG HSPGS shown in Fig.4.12 and the robustness of their proposed control algorithms, which are designed to achieve many tasks, such as, regulation of the AC voltage and system frequency at the PCC, harmonics compensation and load balancing, ensuring a continues power supply to the connected load, controlling the DE according to the load power demand, achieving MPPT from solar PV array and to protect the BESS from overvoltage. Design of the system parameters is given in Table A-3 in Appendix. Several scenarios such as, solar irradiations, load variations and when the SOC% of BESS is less or equal to 100% are also tested.

#### **Performance analysis under load and solar irradiations change when the SOC is less than 100% and greater than 50%**

The waveforms of the AC voltage ( $v_{sabc}$ ), stator current ( $i_{sabc}$ ), rotor current ( $i_{rabc}$ ), system frequency ( $f_s$ ), DFIG rotor speed ( $\omega_r$ ) and its reference speed which represents the DE speed, PV current and its reference ( $i_{pv}$  &  $i_{pvref}$ ), load currents ( $i_{Labc}$ ), inverter currents ( $i_{invabc}$ ), DC-link voltage ( $V_{dc}$ ), state of charge of battery (SOC%) when load and solar irradiations varies and when the SOC% is less than 100% and greater than 50%, are shown in Fig.4.23.

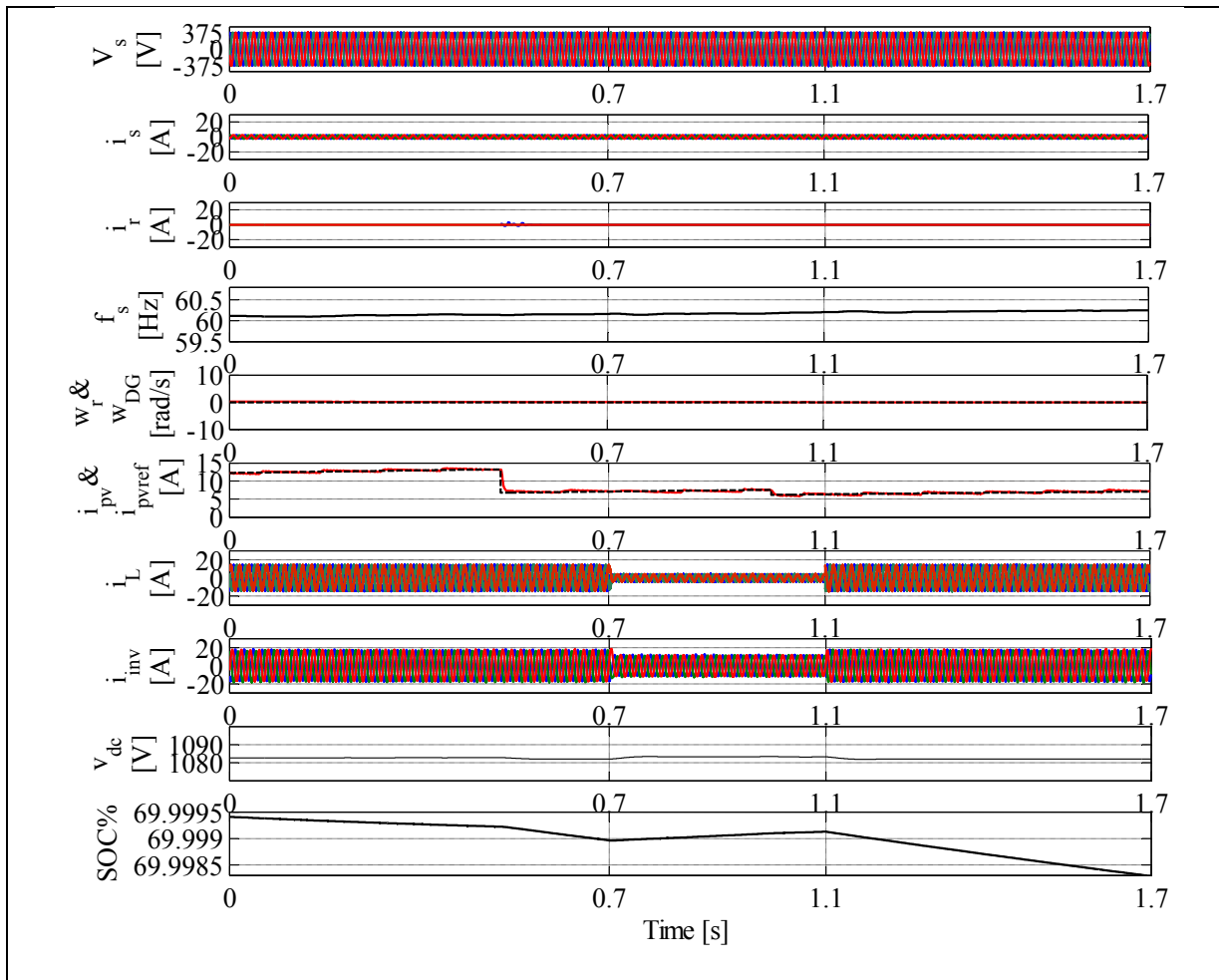


Figure 4.23 Dynamic response of the PV-DG HSPGS based on variable speed DFIG when the SOC% of BESS is less than 100% and greater than 50%

It is observed that the DFIG stator and rotor current, as well as, its rotor speed are equal to zero because of the SOC% is greater than 50%. In this operation mode, only solar PV array with help of BESS should ensure the load power demand. It is observed that the output PV current is decreased at  $t=0.5$  s and decreased more at  $t=1.1$ s. Therefore, to keep the system stable, BESS is discharging between  $t=0$  s to  $t=0.7$  s and between  $t=1.1$  s to  $t=1.7$  s. It is observed also that BESS is charging from  $t=0.7$  s to  $t=1.1$  s because of load is decreased in this period of time, AC load voltage and system frequency are regulated constant, and the output PV current follows its reference, which confirms the robustness of the proposed control approaches for controlling the DC/DC boost converter and DC/AC inverter.

Using only solar PV array and BESS, it makes possible to completely turn off the DG when SOC% is greater to 50%, which leads to maximum fuel savings and a 100% reliable energy system.

### Performance analysis under linear load change and fixed solar irradianations when the SOC% is less than 50%

The dynamic performance of the proposed PV-DG HSPG under variation of load and fixed solar irradiation when the SOC% is less than 50%, are presented in Fig.4.24

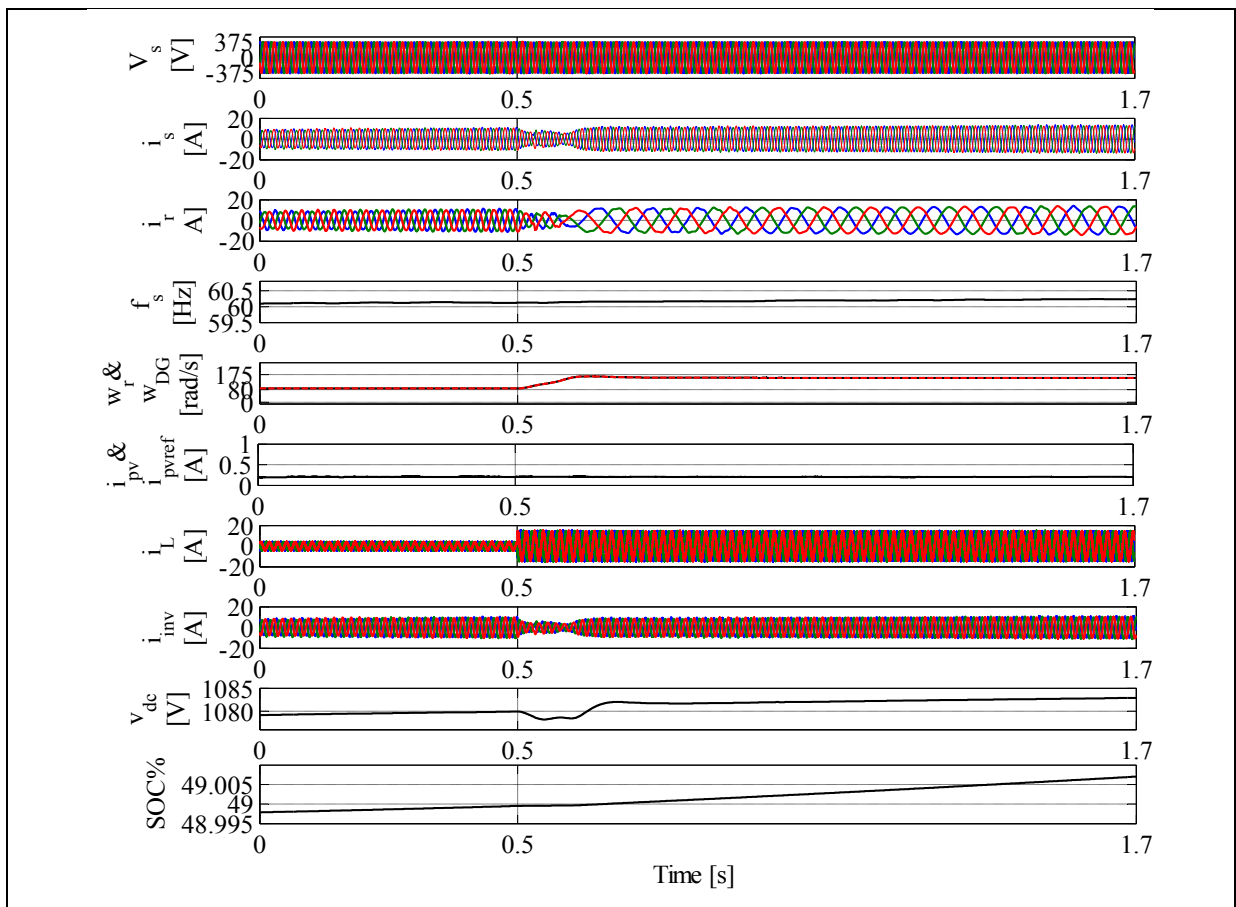


Figure 4.24 Dynamic performance of PV-DG HSPG based on variable speed DFIG under linear load change and fixed solar irradiation and when the state charge of battery is less than 50%

To maximize the efficiency of the DG especially at light load it should supply load and charge the BESS simultaneously. At  $t=0.5$  s, load is increased and BESS is less than 50%, therefore, DG speed is increased in order to satisfy the load power demand. In this operation mode DFIG operates at sub-synchronous mode Fig.4.13 (b), the rotor side converter works as inverter and DC/AC inverter as rectifier. It is observed that DFIG rotor speed and output PV current follow their references, which confirms the robustness of the proposed control approaches for controlling the AC/DC and DC/DC boost converters. Furthermore, the AC voltage and the system frequency are not affected in this operation mode and during transition, they are kept constant.

#### **Performance analysis under balanced and unbalanced nonlinear load and the SOC% is less than 50%**

Dynamic performance of the proposed PV-DG HSPGS, are shown in Fig.4.25. Simulations have been carried out considering that the SOC% is less than 50% and solar PV array is unable to provide require load power demand. Balanced and unbalanced nonlinear load is considered in this test. It is observed that system is subjected to sudden load variation between  $t=0.5$  s and  $t=1$  s. To satisfy the load power demand, DFIG rotor speed is increased and reaches 230rad/s. This speed is greater than the synchronous speed. As results that DFIG operates in super-synchronous mode. In this case, rotor side converter acts as rectifier and load side converter, as inverter. It is observed that the rotor speed of DFIG follows its reference, which represents the speed of DE. Despite this transition from sub-synchronous to super-synchronous mode, load is continually supplied and the AC voltage and the system frequency are kept constant, which confirms the robustness of the proposed control algorithms for the DC/AC inverter and the AC/DC converter.

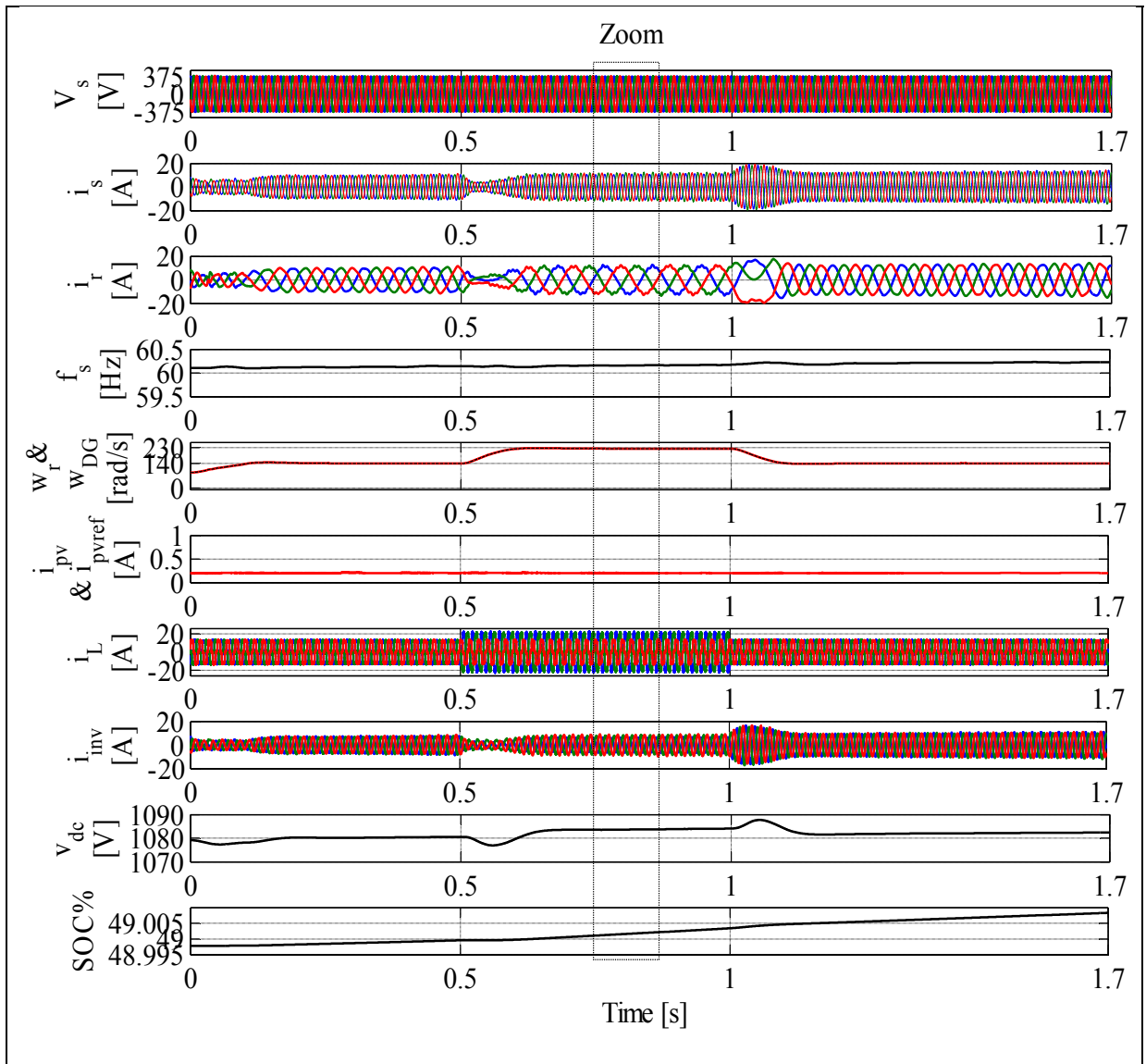


Figure 4.25 Dynamic performance of PV-DG HSPG under balanced and unbalanced nonlinear load and fixed solar irradiation and when the state charge of battery is less than 50%

Fig.4.27 shows the zoomed waveforms of the simulation results shown in Fig.4.23. It is observed that from  $t=0.7\text{s}$  to  $0.9\text{s}$  unbalanced nonlinear load is connected to the system but the stator current is perfectly balanced and sinusoidal confirming the active filter operation of the interfacing inverter.

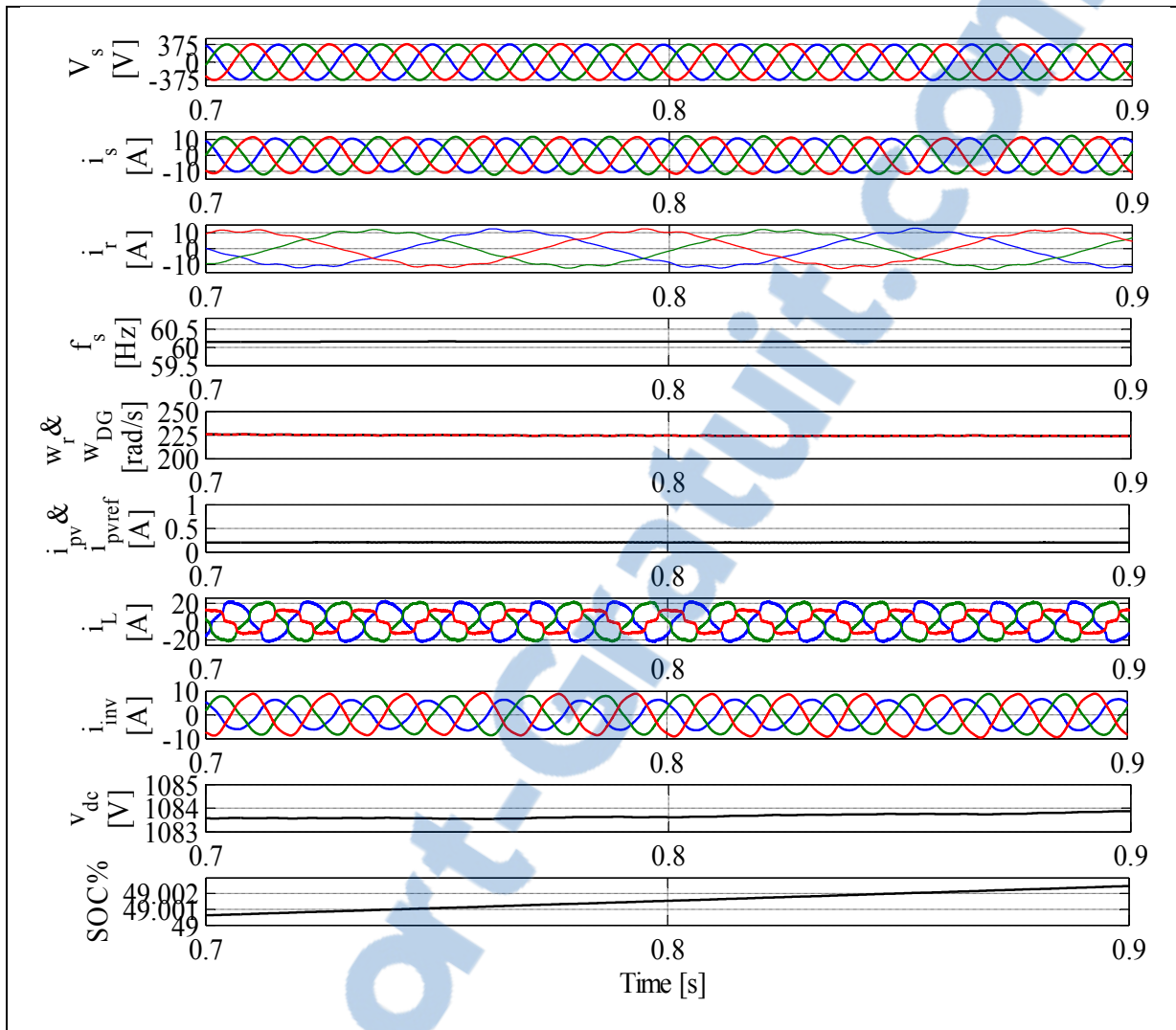


Figure 4.26 Zoom of the results shown in Fig.4.25 between  $t= 0.7$  s and  $t= 0.9$ s

### Performance analysis when the SOC% of BESS is equal to 100%

Fig.4.27 shows the simulation results of the AC voltage, system frequency, and state of charge of BESS, PV power, DG power, inverter power, BESS power, dump load power and load power. In this test SOC% is considered equal to 100% and only solar PV array is used to provide power to the load and charge the BESS. DG in this test is turn off. It is observed that from  $t= 0$  s to  $t=0.28$  s SOC% is still less than 100%, and that is why dump load is turn off and BESS is charging. At  $t= 0.28$  s SOC% becomes equal to 100%, so to protect BESS from

overcharging, dump load is turned on. It is observed that from  $t=0.28\text{ s}$  to  $t=0.8\text{ s}$  BESS current is equal to zero and the extra power is dissipated in dump load. From  $t=0.8\text{ s}$  to  $1.4\text{ s}$  load is increased more. Therefore, dump load is turned off and BESS is discharging in order to balance the power between solar PV array and load. It is observed that the AC voltage and the system frequency are kept constant, which confirms that the system perform well when BESS becomes fully charged.

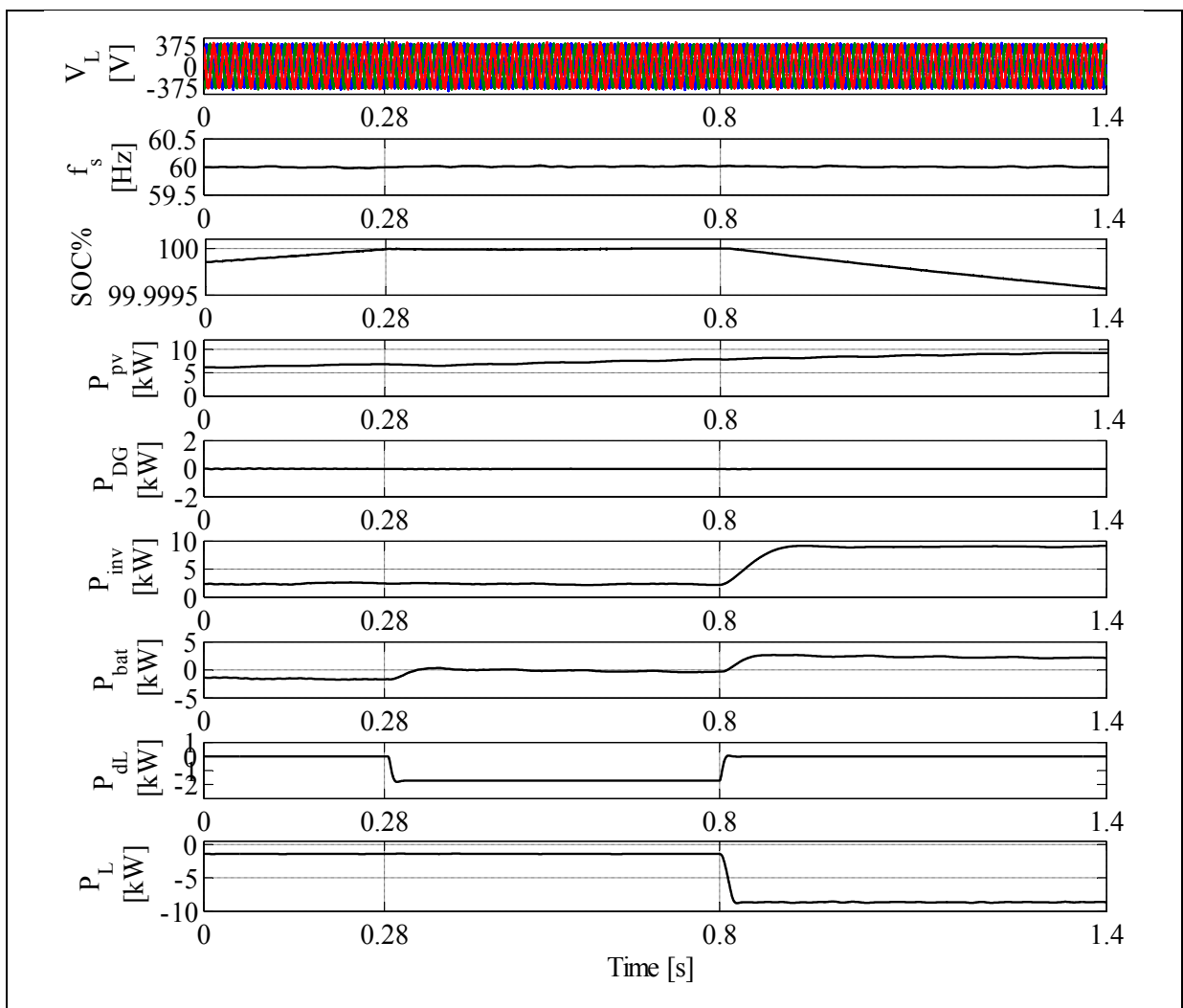


Figure 4.27 Dynamic performance PV-DG HSPGS based on DFIG when SOC % of BESS is equal to 100%

#### 4.5 Conclusion

Several HSPGS topologies based on solar PV array and DG driven fixed and variable speed generators are discussed. Two different topologies are selected and studied in detail. In the first architecture, solar PV array is tied to the PCC through two-stage inverters and DG driven fixed speed SG is connected directly to the PCC. P&O technique is used to achieve MPPT from solar PV array. System frequency and the AC voltage regulation and the power quality improvement at the PCC are achieved using the modified p-q instantaneous power theory control. The obtained results during load and solar irradiation change and when the BESS becomes fully charged show satisfactory performance. Furthermore, it is shown that DG becomes as backup ES instead of principal ES. It is turned on only if the provided power from solar PV array is less than the load power demand and when the SOC% is less than 50%, which leads to saving fuel and increasing DE span life. The proposed topologies based on fixed speed generators that use SG as generator shows a good performance compared to that using SCIG, SyRG or PMSG view point output frequency and terminal AC voltage regulation when DG is operating as emergency ES. It is because of the AVR and speed governor of the SG and DE. For the second topology PV-DG HSPGS based on DE driven variable speed DFIG, the rotor side converter is controlled using indirect stator flux oriented control technique to ensure control of the AC voltage at constant frequency, and the DC/AC inverter is controlled using indirect current control technique in order to regulate the AC load voltage and the system frequency constant, as well as to compensate load current harmonic and to balance the stator current. For the solar PV array, DC/DC boost converter is controlled to achieve MPT. It has been observed that the PV-DG HSPGS demonstrates satisfactory performance under different dynamic conditions while maintaining constant voltage and frequency, harmonic elimination, and load balancing at the PCC. Moreover, it has shown capability of MPT from solar PV array. Furthermore, DG efficiency is improved, its life span is extended and the cost of kWh is reduced by saving the Fuel. DFIG compared to five electrical machines proposed for variable speed DG is more efficient because of only 25% of the provided power is fed to the PCC through the rotor side converter and the rest of the provide power, which represents 75% is injected directly through the stator to the PCC.

## CHAPITRE 5

### HYBRID STANDALONE POWER GENERATION SYSTEM EMPLOYING SOLAR PV ARRAY AND MHP

#### 5.1 Introduction

HSPGS topologies employing solar PV array and MHP driven fixed speed generators are discussed in this chapter. These topologies are designed in order to achieve high efficiency from solar PV array, ensures stability and continuous power supply to the load with high power quality with reduced cost in the presence of several conditions, such as variation of solar irradiations and loads, as well as when the water level varies because of drought or when it is frozen. Two different topologies are selected and studied in detail. In the first topology, two-stage converters are used to tie the solar PV array to the PCC, and MHP which is driving fixed speed SyRG is connected directly to the PCC. To get MPPT from solar PV array, P&O technique is used for controlling the DC/DC boost converter. The system frequency and the AC voltage regulation, as well as, the power quality improvement at the PCC are achieved by controlling the DC/AC interfacing inverter using modified instantaneous p-q power theory control algorithm. In the second selected topology, MHP which is driving fixed speed SCIG is connected directly to the PCC and the solar PV array is tied to the PCC through single-stage inverter. To achieve MPPT from solar PV array, regulate the AC voltage, as well as, improving the power quality at the PCC, DC/AC interfacing inverter is controlled using P&O technique and modified Anti-Hebbian control algorithm. The system frequency regulation in this PV-MHP HSPGS is obtained by controlling the DC/DC buck-boost converter using in phase and quadrature unit templates to estimate the system frequency at the PCC. Simulation is carried out using MATLAB/Simulink to test the effectiveness of the selected topologies and their control algorithms.

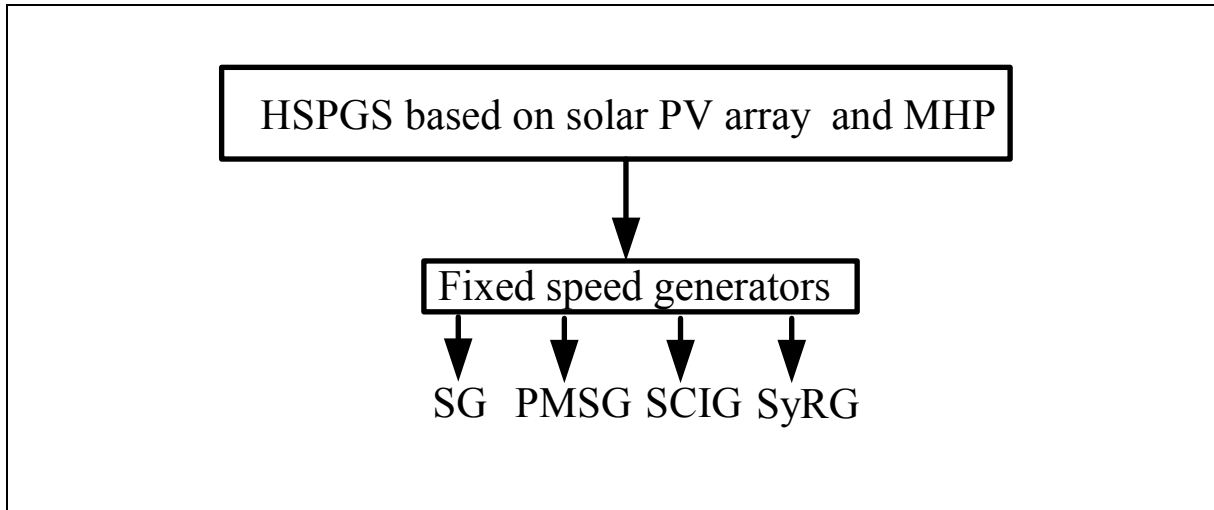


Figure 5.1 Classification of HSPGS power generation based on PV array and MHP driven fixed speed generators

## 5.2 Topology designs of hybrid standalone power generation system based on PV array and MHP driven fixed speed generators

Fig.5.2 shows the proposed new topologies, which are based on solar PV array and fixed speed MHP. Usually, MHP is advocated to ensure continuous power supply for remote areas beside rivers because it can offer clean energy with reduced cost compared to the conventional DG. Unfortunately, it cannot satisfy the load power demand, especially in dry season and when river becomes frozen in winter. Therefore, additional ES such as, solar PV array with BESS have been suggested to complement the power deficiency in this period of time (Ekanayake, 2002). Mostly, MHP drives fixed speed SCIG (Chauhan, Jain et Singh, 2010; Li et al., 2013), as shown in Fig.5.2 (c). Usually, for this PV-MHP HSPGS, speed governor is used to regulate the system and the AC voltage at the PCC is regulated through reactive power control using DC/AC inverter(Scherer et de Camargo, 2011). According to (Magureanu et al., 2008), the overall efficiency of MHP driven SCIG is lower compared to MHP that uses SG as generator, because the SCIG gets its excitation from the same AC supply grid. To overcome this drawback, in the proposed architecture shown in Fig.5.2 (c), the initial excitation of the SCIG is provided from capacitor bank and the rest of required reactive power is provided by BESS by controlling the DC/AC inverter. From the viewpoint

efficiency SyRG, which is shown in Fig.5.2 (b), it is more effective compared to the SCIG. The MHP driven PMSG, which is shown in Fig.5.2 (d), is more effective but costly compared to SCIG, SG and SyRG.

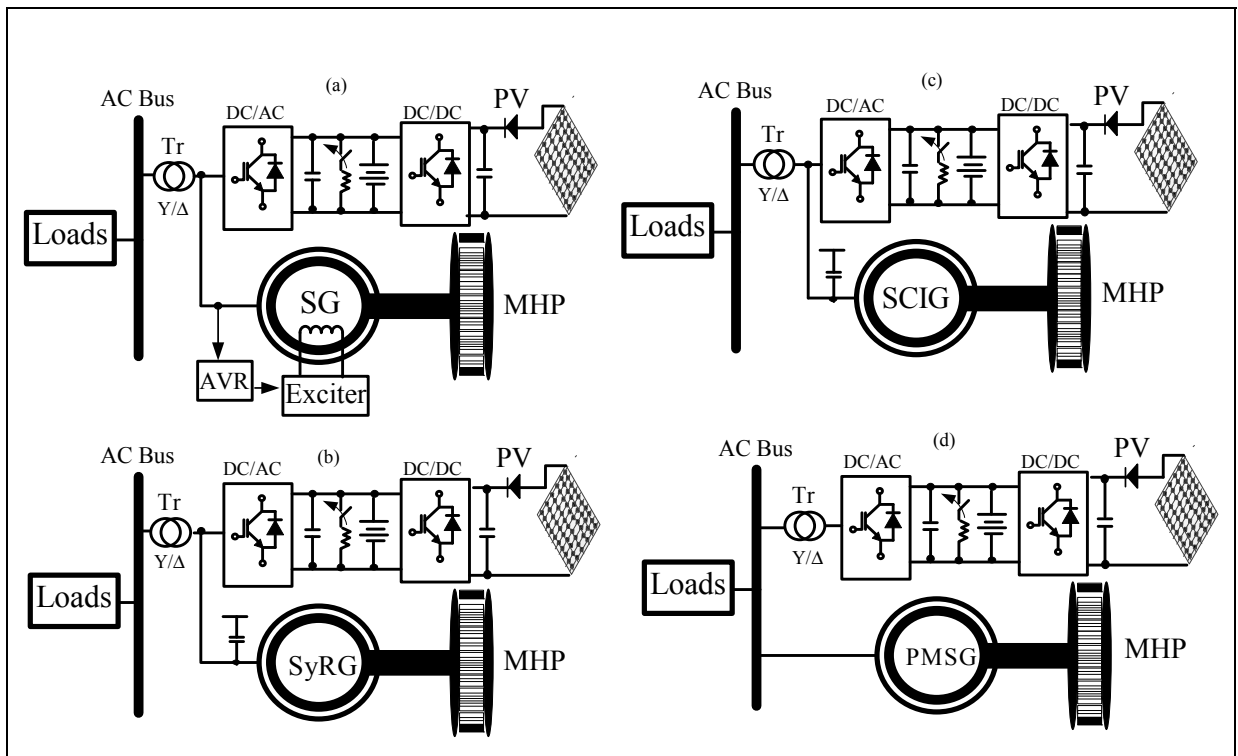


Figure 5.2 HSPGS based on solar PV array and MHP driven fixed speed generators

### 5.2.1.1 Description and control of hybrid standalone power generation system based on PV and MHP driven fixed speed SyRG

Among the topologies shown in Fig.5.2, scheme which is based on SyRG is discussed. As shown in Fig. 5.3, the proposed MHP-PV HSPGS consists of two RES; 1) solar PV array, which is connected to the PCC through two-stage converter, and 2) MHP driven SyRG, which is tied directly to the PCC. For the proposed topologies, BESS and dump load are tied to the DC bus. Furthermore, a (star-delta) transformer is placed between the loads and ESs in order to create galvanic isolation between loads and ESs.

The AC voltage ( $v_L$ ) and the system frequency ( $f_s$ ), as well as the power quality improvement at the PCC are achieved by controlling the DC/AC inverter using the same control approach used already in chapter 4, which is based on instantaneous p-q theory. In addition, same control approaches used for controlling different elements of the previous PV-DG HSPGS, such as DC/DC boost converter and dump load are used to control same elements of the proposed PV-MHP HSPGS shown in Fig. 5.3.

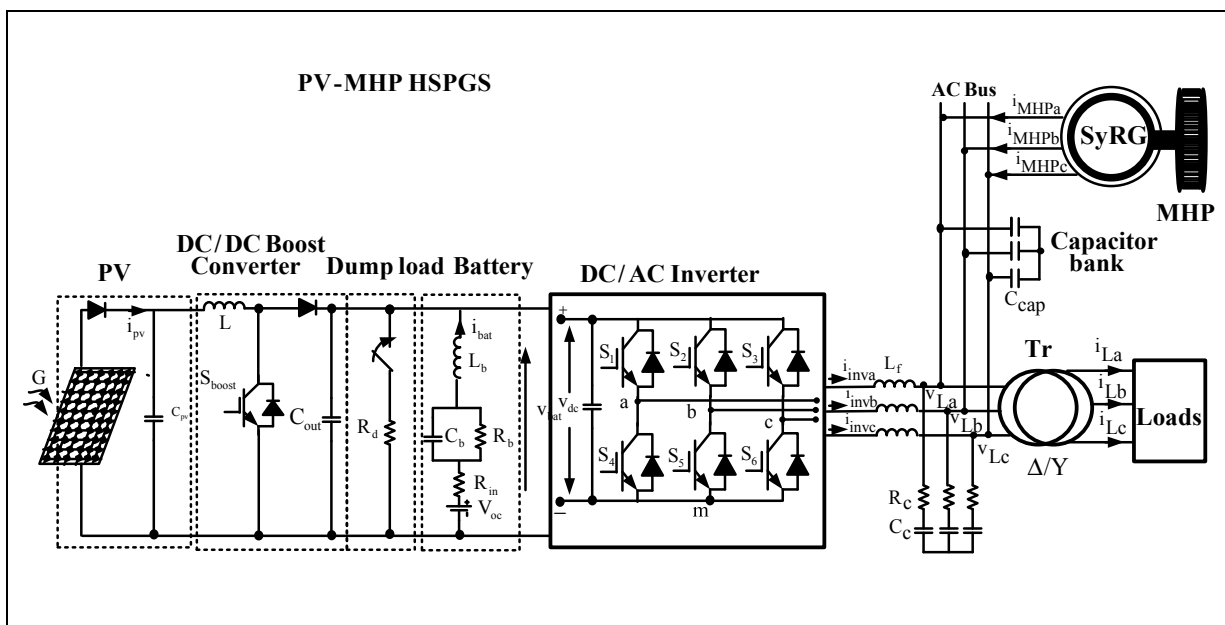


Figure 5.3 HSPGS based on solar PV array and MHP driven fixed speed SyRG

### Model of the MHP System

Usually, in small-scale hydro-power generation, the run-of-the river builds constant pressure head at the gate of the turbine. Therefore, with help of adjustable gate valve, the water discharge rate stays constant. Consequently, the input power of the turbine remains constant, implying the torque-speed characteristic of the hydro-turbine is linear function (Gulliver et Arndt, 1991), which is given as follows:

$$T_m = T_0 - m\Omega \tag{5.1}$$

where  $T_m, T_0, \Omega$ , and  $m$  denote the shaft torque of Micro Hydro-turbine (MHT), torque at zero speed rotational speed of MHT, and the slop of the linear torque-speed characteristics, which is shown in the Fig.5.4 and calculated as follows:

$$P_{m\_max} = \frac{T_0^2}{4m} \quad (5.2)$$

where  $P_{m\_max}$  is the maximum MHT output power.

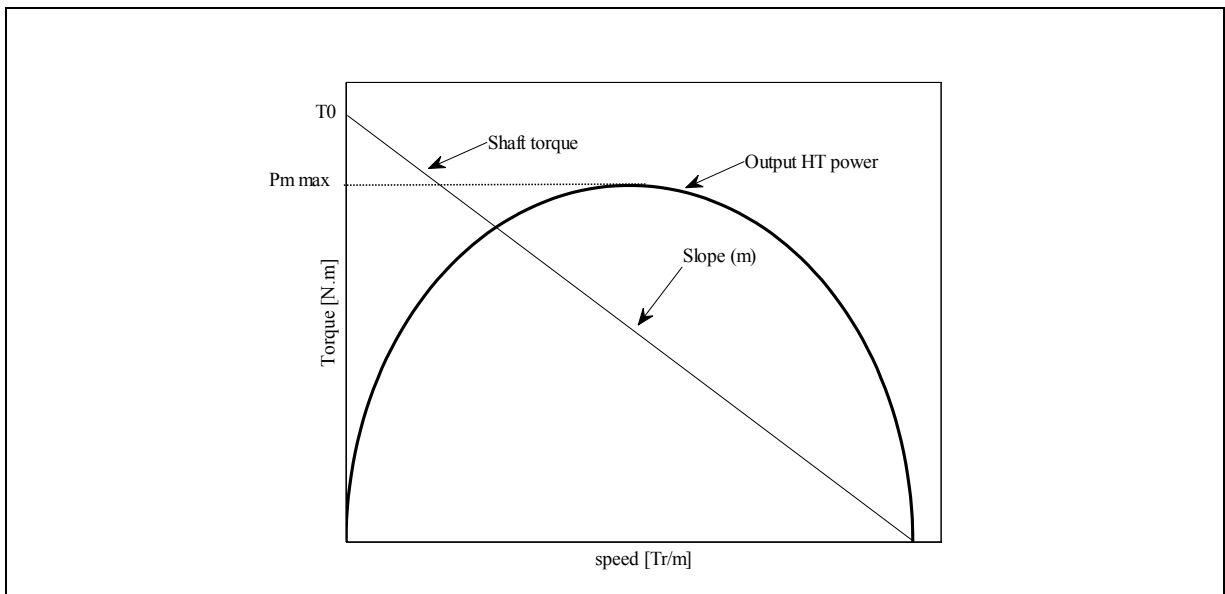


Figure 5.4 Characteristics torque-speed of MHT

Using (5.1), (5.2) and parameters of the SyRG, which are summarized in Appendix Table A-4, one can define the characteristic torque-speed of the MHP as follow:

$$T_m = 19.89 - 0.1069 \Omega \quad (5.3)$$

where 19.89 and 0.1039 represent the torque at zero speed and the slop of the linear torque-speed characteristics.

**5.2.1.2 Description and control of hybrid standalone power generation system based on PV and MHP driven fixed speed SCIG**

Fig.5.5 shows proposed PV-MHP HSPGS employing fixed speed SCIG which is connected directly to AC local grid. A three-leg VSC, a solar PV connected at common DC bus of a three-leg VSC, a BESS connected to the common DC bus through a DC-DC buck-boost converter, and a dump load connected at DC bus through a pulse-width modulated (PWM) controlled static switch. In the proposed PV-MHP HSPGS, VSC is controlled to regulate the AC terminal voltage, to control common DC bus voltage for achieving MPPT for PV system under change in solar irradiation and to compensate load currents harmonics. The AC local grid frequency is controlled by employing control of DC-DC buck-boost converter. The proposed system is mostly suitable to serve the power needs of any small size residential green building situated near a small river or canal.

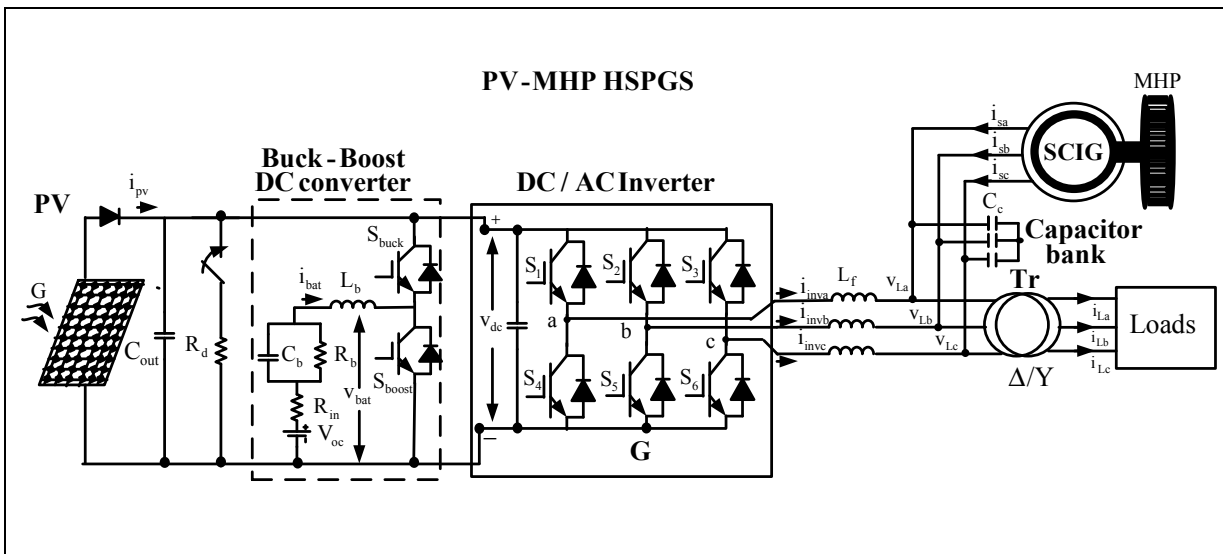


Figure 5.5 Proposed HSPGS based on solar PV array and MHP driven fixed speed SCIG

## Maximum Power Point Tracking

For controlling the solar PV array, perturbation and observation (P&O) is used. Measured PV voltage in this study represents DC link voltage ( $v_{dc}$ ) and the output PV current ( $i_{pv}$ ) as shown in the flow chart in Fig.5.6. The DC voltage reference ( $V_{dcref}$ ) in this case represents the voltage for maximum power ( $V_{dcref} = v_{mp}$ ). The output PV voltage ( $v_{pv}$ ) and current ( $i_{pv}$ ) are sensed.

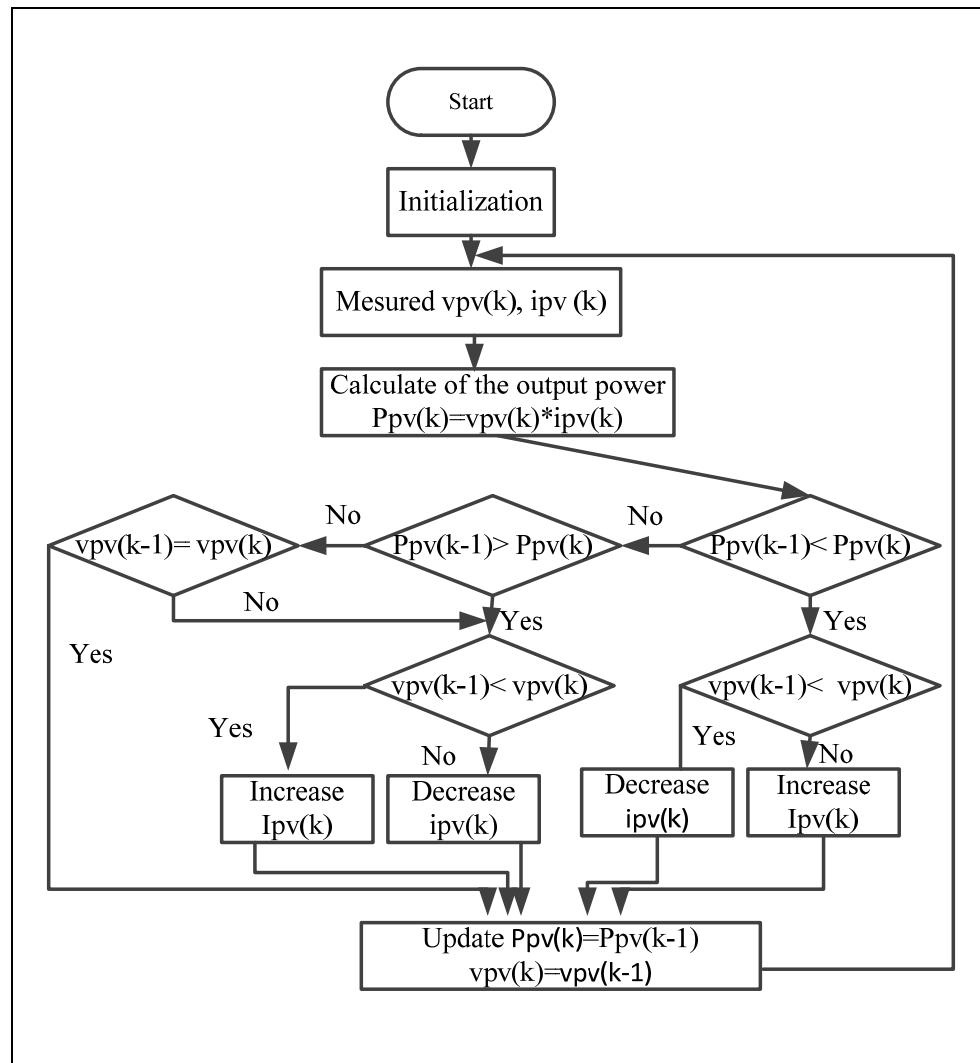


Figure 5.6 Perturbation and Observation MPPT Method

As shown in Fig.5.7 that for specific solar irradiation, there is one operating point where the solar PV array can generate its maximum output. It is observed that there are two possible operating regions A and B for a given output PV power except the maximum power point can be defined. Therefore, the current operating point location can be determined by a perturbation of the PV power ( $P_{pv}$ ) as:

$$\begin{cases} P_{pv}(k-1) = P_{pv2} \langle P_{pv}(k) = P_{pv1} \\ v_{pv}(k-1) = v_{pv2} \rangle v_{pv}(k) = v_{pv1} \end{cases}$$

where the parameters  $(k-1)$  and  $(k)$  present the measured quantities before and after perturbation, respectively.

It is observed in Fig.5.7 that the correct operating point is located in region B. Therefore, to track the maximum power point for the solar PV array, the next changing direction is to increase  $i_{pv}$ , which leads to a reduction of  $v_{pv}$ . From where the operating point is moving from  $B_2$  to  $B_1$ . However, if the operating point of the solar PV array is located in region A, the next changing direction is decreased  $i_{pv}$

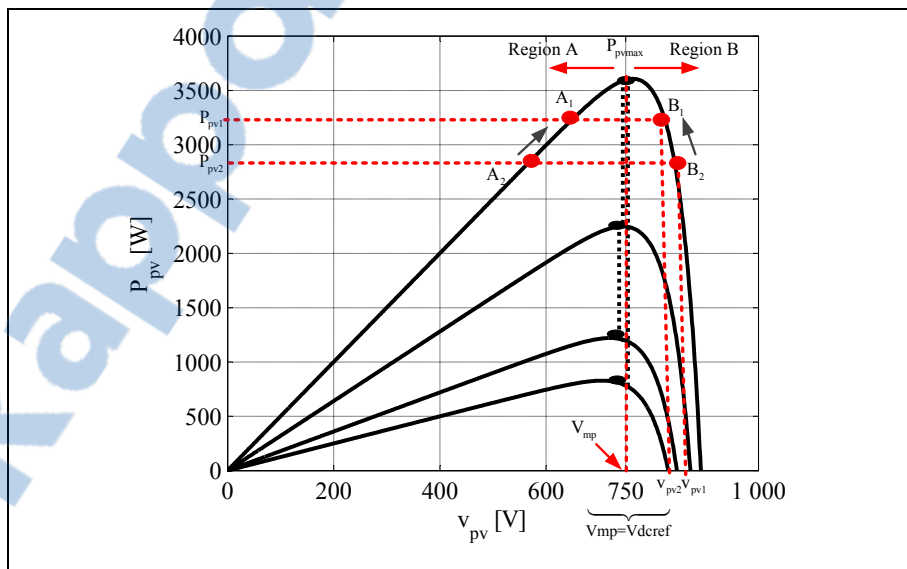


Figure 5.7 Ppv-Vpv Characteristic of the proposed solar PV array

### Control of dump loads

Fig. 5.8 shows the block diagram of proposed control algorithm for a dump load, which is controlled in order to dissipate the excess of power provided by primary energy sources MHP and solar PV array. The reference battery voltage ( $v_{batref}$ ) is compared with measured battery voltage ( $v_{bat}$ ). The error is processed through a PI controller to generate switching signal for static switch of dump load controller.

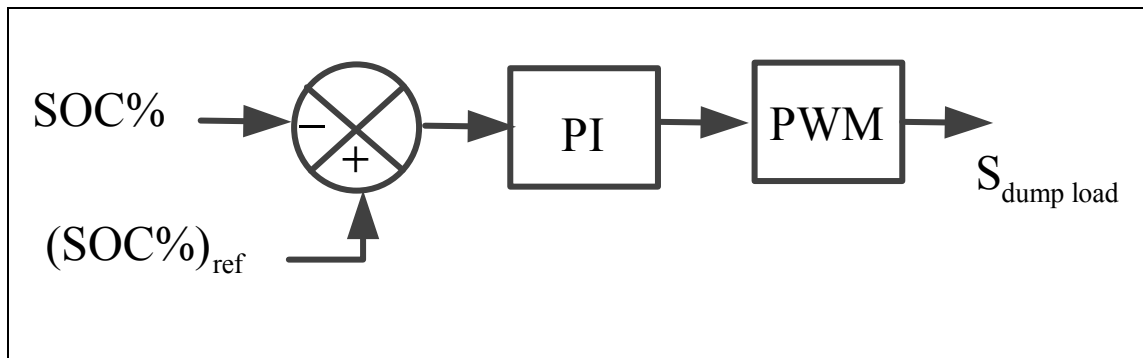


Figure 5.8 Dump load control algorithm

### Selecting of dump load resistance rating

A dump load resistance element rating is based on the rated active-powers provided by the PV and the MHP. Therefore, the value of the resistance is calculated as follows:

$$R_{dumpload} = \frac{V_{dc}^2}{P_{MHP} + P_{pV}} \quad (5.4)$$

### System frequency control

Fig. 5.9 shows the control algorithm used for the control of DC-DC buck-boost converter. The system frequency at the PCC is estimated using in-phase and quadrature unit templates as:

$$V_p = \sqrt{\frac{2}{3}(v_{La}^2 + v_{Lb}^2 + v_{Lc}^2)} \quad (5.5)$$

where  $V_p$  denotes the amplitude of the AC voltage, which is equal to PCC voltage and  $v_{La}$ ,  $v_{Lb}$  and  $v_{Lc}$  are the instantaneous AC voltages for a, b and c phases, respectively.

The in-phase unit templates are calculated as:

$$u_{ap} = \frac{v_{La}}{V_p}, u_{bp} = \frac{v_{Lb}}{V_p}, u_{cp} = \frac{v_{Lc}}{V_p} \quad (5.6)$$

The quadrature unit templates are obtained as,

$$u_{aq} = \frac{1}{\sqrt{3}}(-u_{bp} + u_{cp}), u_{bq} = \left( \frac{\sqrt{3}}{2}u_{ap} + \frac{1}{2\sqrt{3}}(u_{bp} - u_{cp}) \right), u_{cq} = \left( -\frac{\sqrt{3}}{2}u_{ap} + \frac{1}{2\sqrt{3}}(u_{bp} - u_{cp}) \right) \quad (5.7)$$

Using the estimated in-phase unit and quadrature templates, the frequency is estimated as:

$$\omega_s = \cos \theta \frac{d}{dt}(\sin \theta) - \sin \theta \frac{d}{dt}(\cos \theta) \quad (5.8)$$

where  $\omega_s$  represents the angular frequency in rad/s and  $\cos \theta = u_{aq}$ ,  $\sin \theta = u_{ad}$ , respectively.

The system frequency  $f_s$  is estimated using (5.8) as,

$$f_s = \frac{\omega_s}{2\pi} \quad (5.9)$$

The error between reference and estimated frequency is calculated as:

$$\Delta f_s = f_s - f_{sref} \quad (5.10)$$

The obtained error is fed to PI frequency controller and the output represents the reference battery current,

$$i_{batref} = (f_{sref} - f_s) \left( K_p + \frac{K_i}{s} \right) \quad (5.11)$$

where  $i_{batref}$ ,  $K_p$ ,  $K_i$  denote reference battery current, proportional and integral gains, respectively.

The obtained reference battery current is compared with the sensed battery current ( $i_{bat}$ ), and the error is processed using a PI current controller. The output of the PI controller represents the modulation index  $d$ , which is compared with the saw-tooth carrier waveform to generate switching signals for buck and boost switches ( $S_{boost}$  and  $S_{buck}$ ), as shown in Fig.5.9.

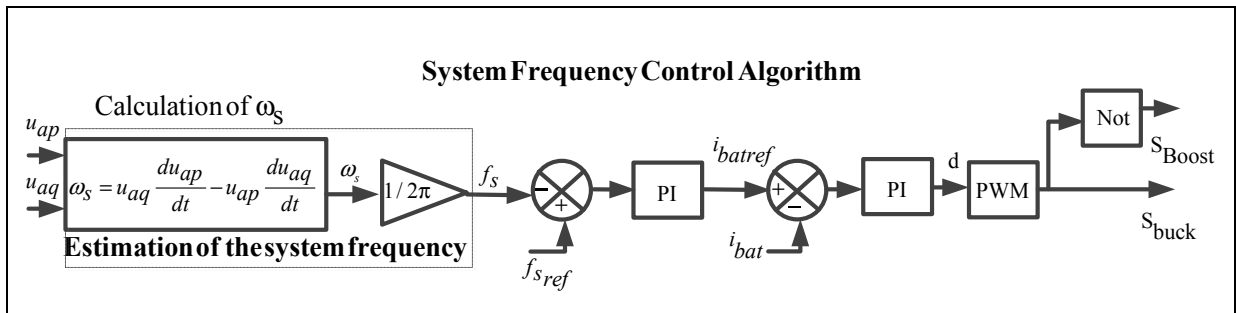


Figure 5.9 System Frequency Control Algorithm

### Selection of BESS Rating

The Thevenin-based equivalent battery model is used for modeling battery in this study as shown in Fig.5.5. This model consists of capacitance  $C_b$ , which is calculated as,

$$C_b = \frac{kWh * 3600 * 10^3}{0.5(V_{ocmax}^2 - V_{ocmin}^2)} \quad (5.12)$$

where  $V_{ocmax}$ ,  $V_{ocmin}$  and  $kWh$  denote the maximum and minimum open circuit voltage of BESS under fully charged and discharged conditions and energy of the battery, respectively.

This model contains also  $R_{in}$ , which represents the equivalent resistance of parallel/series combinations of the batteries. Its value is smaller. Contrarian,  $R_b$  has high value because it represents the self-discharge resistance of battery.

The nominal DC link voltage  $V_{dc}$  is calculated using the following equation;

$$V_{dc} > \left( \frac{2\sqrt{2}}{\sqrt{3}m_a} \right) V_L \quad (5.13)$$

where  $m_a$  and  $V_L$  represents the index of modulation and root mean square of the line voltage respectively. Using (5.13), one calculates  $V_{dc}$ , which should be equal or greater than to 750V.

The minimum battery rack voltage is selected as 350V. The rack of battery should be able to satisfy the load power demand for 24 hours. Therefore, the storage capacity of the battery bank is selected as 12 kWh. For  $V_{ocmax}$  equals to 450 V and  $V_{ocmin}$  equals to 350V, the value of  $C_b$  is equal to 1080 F.

### Control algorithm for Voltage Source Converter

The proposed control algorithm for VSC is shown in Fig. 5.10(Rezkallah et al., 2015b). This control is developed in order to regulate the AC voltage at PCC, to maintain the DC voltage at its reference value, as well as, to improve AC source currents quality by compensating harmonics. For these tasks, load voltages ( $v_{Lab}$ ,  $v_{Lbc}$ ), source currents ( $i_{sab}$ ,  $i_{sbc}$ ), load currents ( $i_{La}$ ,  $i_{Lb}$ ), PV voltage, current ( $v_{pv}$ ,  $i_{pv}$ ) and the DC voltage ( $v_{dc}$ ) are sensed. As for estimating the reference active and reactive power components of source currents; Anti-Hebbian learning control algorithm (Arya et al., 2012; 2014) is used to extract weights of the fundamental active and reactive power components of the load currents. The active power components of load currents are extracted using the following expressions:

$$\begin{cases} W_{pa}(n) = \eta \sum \left[ \left\{ \hat{i}_{La}(n) - u_{pa}(n) W_{pa}(n-1) \right\} \left\{ u_{pa}(n) + K \hat{i}_{La}(n) W_{pa}(n-1) \right\} \right] \\ W_{pb}(n) = \eta \sum \left[ \left\{ \hat{i}_{Lb}(n) - u_{pb}(n) W_{pb}(n-1) \right\} \left\{ u_{pb}(n) + K \hat{i}_{Lb}(n) W_{pb}(n-1) \right\} \right] \\ W_{pc}(n) = \eta \sum \left[ \left\{ \hat{i}_{Lc}(n) - u_{pc}(n) W_{pc}(n-1) \right\} \left\{ u_{pc}(n) + K \hat{i}_{Lc}(n) W_{pc}(n-1) \right\} \right] \end{cases} \quad (5.14)$$

And for extracting of the reactive power component of the load currents, following equations are used:

$$\begin{cases} W_{qa}(n) = \eta \sum \left[ \left\{ \hat{i}_{La}(n) - u_{qa}(n) W_{qa}(n-1) \right\} \left\{ u_{qa}(n) + K \hat{i}_{La}(n) W_{qa}(n-1) \right\} \right] \\ W_{qb}(n) = \eta \sum \left[ \left\{ \hat{i}_{Lb}(n) - u_{qb}(n) W_{qb}(n-1) \right\} \left\{ u_{qb}(n) + K \hat{i}_{Lb}(n) W_{qb}(n-1) \right\} \right] \\ W_{qc}(n) = \eta \sum \left[ \left\{ \hat{i}_{Lc}(n) - u_{qc}(n) W_{qc}(n-1) \right\} \left\{ u_{qc}(n) + K \hat{i}_{Lc}(n) W_{qc}(n-1) \right\} \right] \end{cases} \quad (5.15)$$

where the subscript «p» and «q» represent the active and reactive power components, respectively, and  $x_{abc pq}$ ,  $\eta$ , denote in phase and quadrature-unit templates, the iterative factor, which varies between 0.001 and 1.

where  $K$  is constant and is equal to 1, and  $W_{abc pq}$  are the weights of active and reactive power components of the load currents.

The average weight of the fundamental active and reactive power components of the load currents is expressed as,

$$\begin{cases} W_{pA} = \frac{W_{pa} + W_{pb} + W_{pc}}{3} \\ W_{qA} = \frac{W_{qa} + W_{qb} + W_{qc}}{3} \end{cases} \quad (5.16)$$

Including DC bus losses component ( $W_{cp}$ ) and the reactive power required for AC voltage regulation ( $W_{cq}$ ), the total weight of the fundamental active and reactive components of source currents are expressed as:

$$\begin{cases} W_p = W_{pA} + W_{pc} \\ W_q = W_{qA} - W_{qc} \end{cases} \quad (5.17)$$

Now, one calculates the three-phase fundamental active and reactive power components of load currents as:

$$\begin{cases} i_{sap}^* = W_p u_{ap}, i_{sbp}^* = W_p u_{bp}, i_{scp}^* = W_p u_{cp} \\ i_{saq}^* = W_q u_{aq}, i_{sbaq}^* = W_q u_{bq}, i_{scaq}^* = W_q u_{cq} \end{cases} \quad (5.18)$$

The DC losses component is obtained by subtraction of the output of PI DC voltage controller ( $i_{dcp}$ ) and the instantaneous compensation term for PV ( $i_{pvp}$ ), which is calculated as (Rezkallah et al., 2015b)

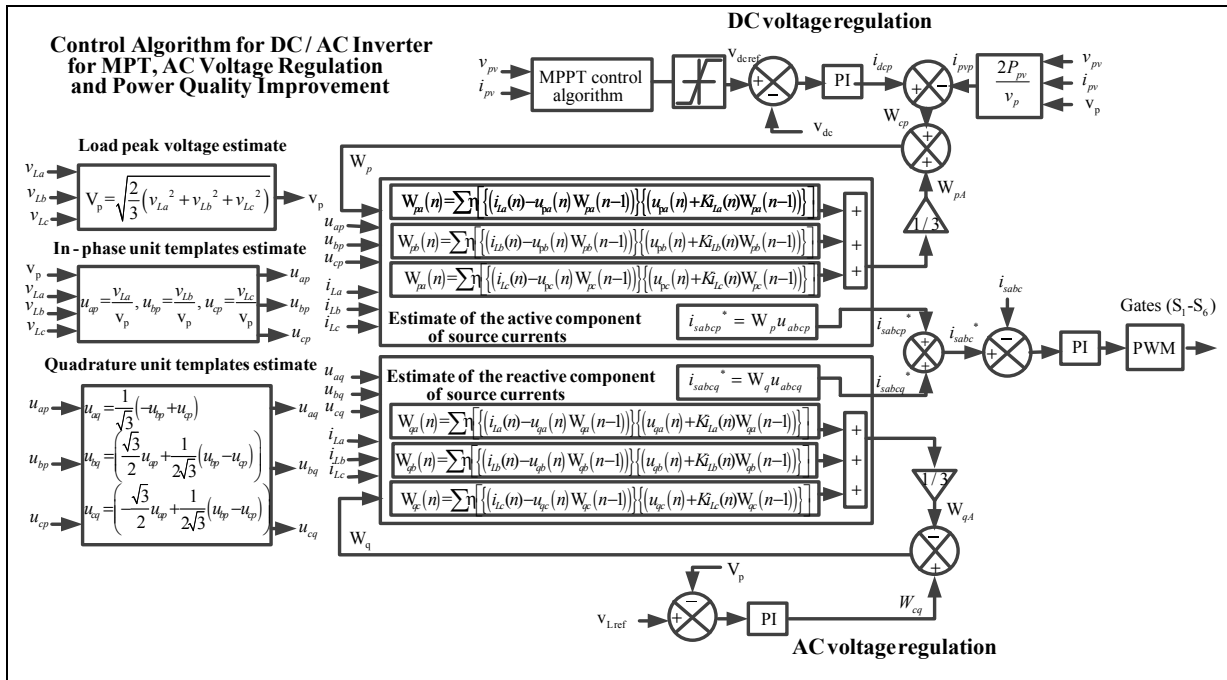


Figure 5.10 Proposed control algorithm for the DC/AC interfacing inverter

$$i_{pvp} = \frac{2P_{pv}}{V_p} \quad (5.19)$$

Finally, the estimated source currents are given as:

$$\begin{cases} i_{sa}^* = i_{sap}^* + i_{saq}^* \\ i_{sb}^* = i_{sbp}^* + i_{sbq}^* \\ i_{sc}^* = i_{scp}^* + i_{scq}^* \end{cases} \quad (5.20)$$

These reference source currents are compared with sensed source currents ( $i_{sabc}$ ) for each phase in the current controller for generating gating signals.

### 5.3 Simulation results and discussion

#### 5.3.1 Performance of the hybrid standalone power generation system based on solar PV and MHP driven fixed speed SyRG

An extensive simulation study is carried out using MATLAB/Simulink to test the performance of the selected PV-MHP HSPGS, which is shown in Fig.5.3 and its proposed controls approach during: 1) sudden increase and decrease of linear load, 2) balanced and unbalanced nonlinear load, and 3) when the BESS becomes fully charged (SOC%=100%). The system parameters are summarized in Appendix Table A-5.

##### 5.3.1.1 Performance analysis under load and solar irradiation change

Fig. 5.11 shows the waveforms of the AC voltage ( $v_L$ ), MHP current from SyRG ( $i_{MHP}$ ), load current ( $i_L$ ), output of the DC/AC inverter current ( $i_{inv}$ ), output solar PV array current and its reference ( $i_{pv}$  &  $i_{pvref}$ ), mechanical torque ( $T_m$ ), DC voltage ( $V_{dc}$ ), state of charge of BESS (SOC%), and the system frequency ( $f_s$ ). It is observed that the mechanical torque ( $T_m$ ) is remaining constant throughout the simulation period and that is why the MHP current is kept constant. For the solar PV array, its output current varies with variation of the solar irradiations, it decreases at  $t = 0.75s$ . It is observed that the output PV current follow its reference, which leads to say that the proposed P&O MPPT-technique is able to track

maximum power point. It is observed that from  $t=0$  s to  $t=0.75$  s, the sum of currents ( $i_{MHP+} + i_{pv}$ ) is greater than load current ( $i_L$ ) and that is why BESS in this period of time is charging. At  $t=0.75$  s, the proposed PV-MHP HSPGS system is subjected to sudden increasing of linear load. The load current is greater to the output RESs currents ( $(i_{MHP+} + i_{pv}) < i_L$ ), therefore, BESS is discharging. Between  $t=0.75$ s and  $t=2.25$ s, inverter current ( $i_{inv}$ ) is increased and the DC voltage ( $V_{dc}$ ), as well as, SOC% are decreasing. From  $t=3$  s to  $t=4$  s, ( $(i_{MHP+} + i_{pv}) > i_L$ ), that why,  $V_{dc}$  and SOC% are increasing. Despite load and weather conditions change, AC voltage ( $v_L$ ) and the system frequency ( $f_s$ ) are kept constant.

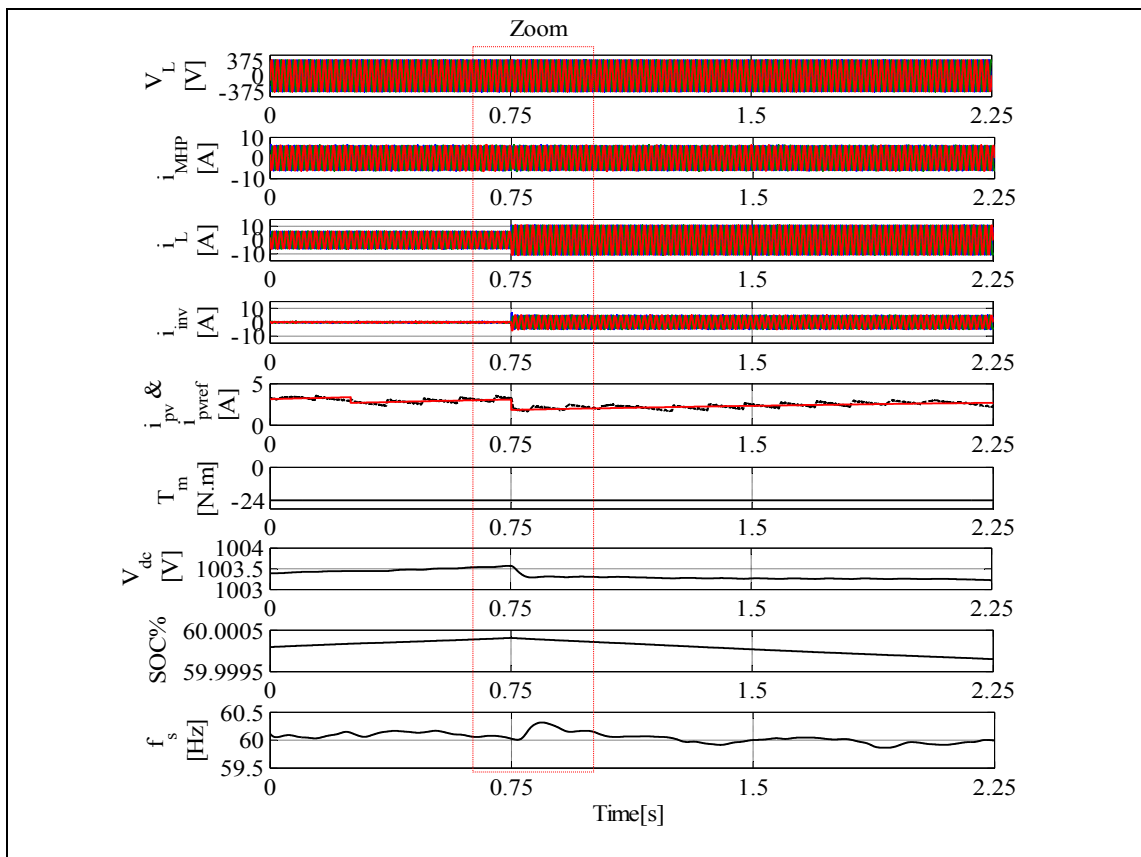


Figure 5.11 Dynamic performance of PV-MHP HSPGS based on fixed speed SyRG during load and solar irradiation change

Fig.5.12 shows the zoomed waveforms of the results shown in Fig.5.11 between  $t=1.98$  s and  $t=2.05$  s. It is observed that at  $t=0.75$  s the load current ( $i_L$ ) is suddenly increased. Seeing that  $i_L$  is greater than the sum of currents provided by RESs ( $i_{MHP+} + i_{pv}$ ), inverter

current ( $i_{inv}$ ) is increased and the DC voltage starts decreasing, which confirm that BESS is discharging in order to balance the power in PV-MHP HSPGS. It is observed that the steady state error of the AC voltage is equal to zero and the system frequency is not affected by this variation, which confirms the robustness of the proposed control approach.

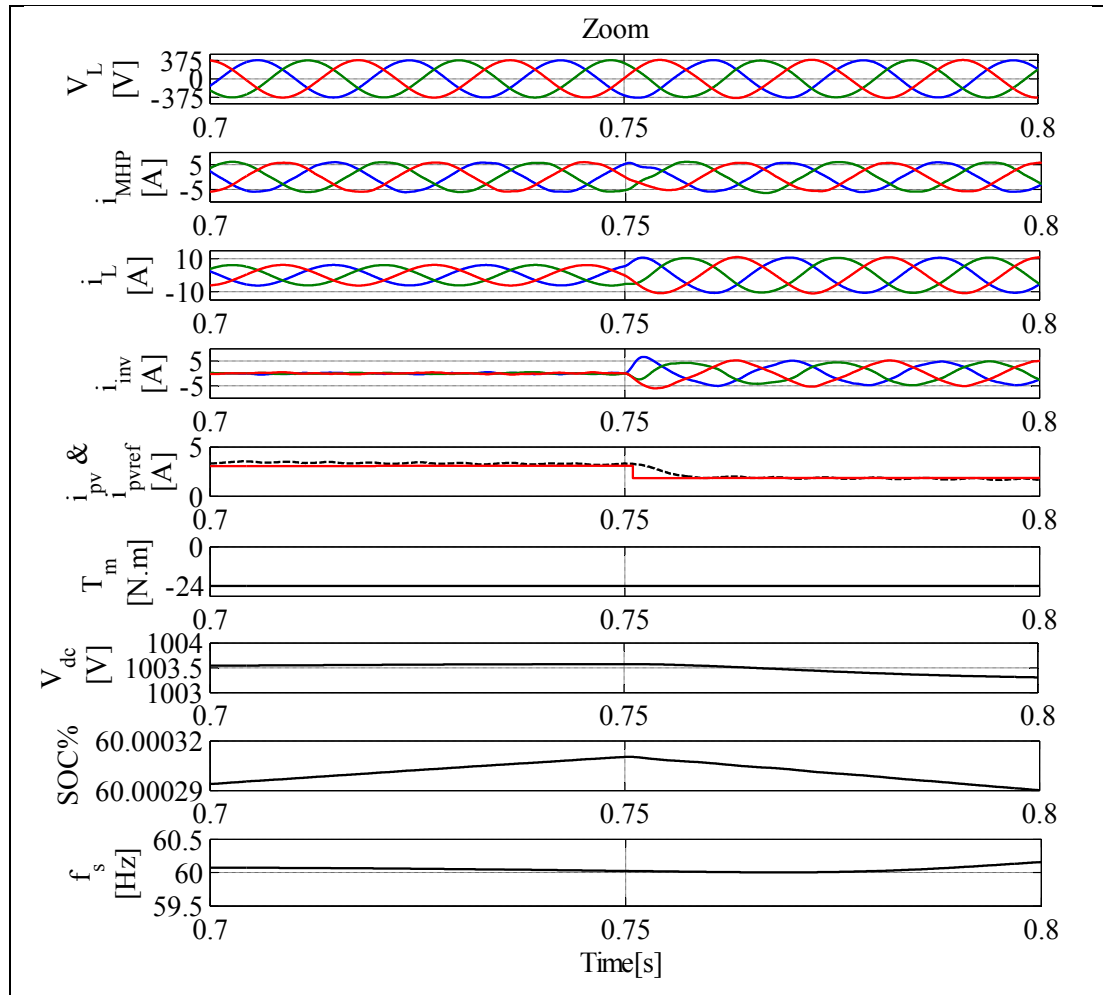


Figure 5.12 Zoom of the results shown in Fig 5-11

### 5.3.1.2 Performance analysis under balanced and unbalanced nonlinear loads

Fig. 5.13 shows the waveforms of the AC voltage ( $v_L$ ), MHP current ( $i_{MHP}$ ), total load current ( $i_L+i_{NL}$ ), nonlinear load current ( $i_{NL}$ ), output of the DC/AC inverter current ( $i_{inv}$ ), output PV

array current and its reference ( $i_{pv}$  &  $i_{pvref}$ ), mechanical torque ( $T_m$ ), DC-Link voltage ( $V_{dc}$ ), state of charge battery (SOC%), and the system frequency ( $f_s$ ). In this test, balanced nonlinear load is connected to the system from  $t = 0.75$  s to  $t = 0.8$  s. Moreover, the proposed PV-MHP HSPGS is subjected to variation of the solar irradiation at  $t = 0.75$ . As for water flow, which represents the input variable for MHP, is kept constant. The SOC% in this test is kept equal to 60%.

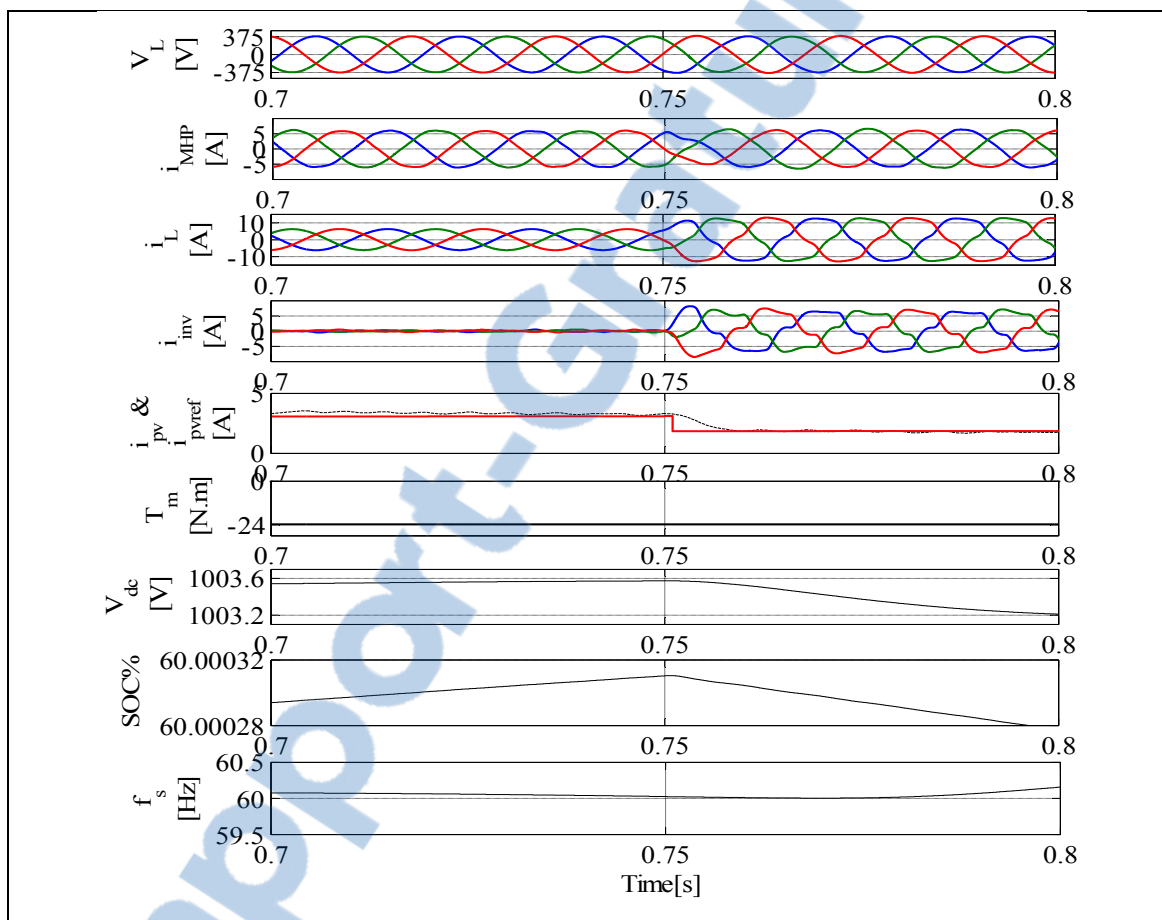


Figure 5.13 Dynamic performance of PV-MHP HSPGS based on fixed speed SyRG under balanced nonlinear load

It is observed that from  $t = 0.75$  s, a three-phase non-linear load is applied and that is why inverter current is increased. It is observed that the AC voltage and the source current, which represents in this study the MHP current, are completely balanced and its waveforms are sinusoidal. In addition, the presence of nonlinear load is not affected the system frequency,

which confirm the robustness of the proposed approach to estimate the frequency, which is based on the in-phase and quadrature units templates., and that for power quality improvement at the PCC.

Fig.5.14 shows the zoomed waveforms of the simulation during presence of unbalanced nonlinear load and fixed solar irradiation. It is observed from  $t=1.1$  s to  $t=1.3$  s unbalanced nonlinear load is applied, and  $v_L$  and  $i_{MHP}$  waveforms are not affected by the load current harmonics. Furthermore,  $i_{MHP}$  are balanced and sinusoidal waves with nearly unity power factor.

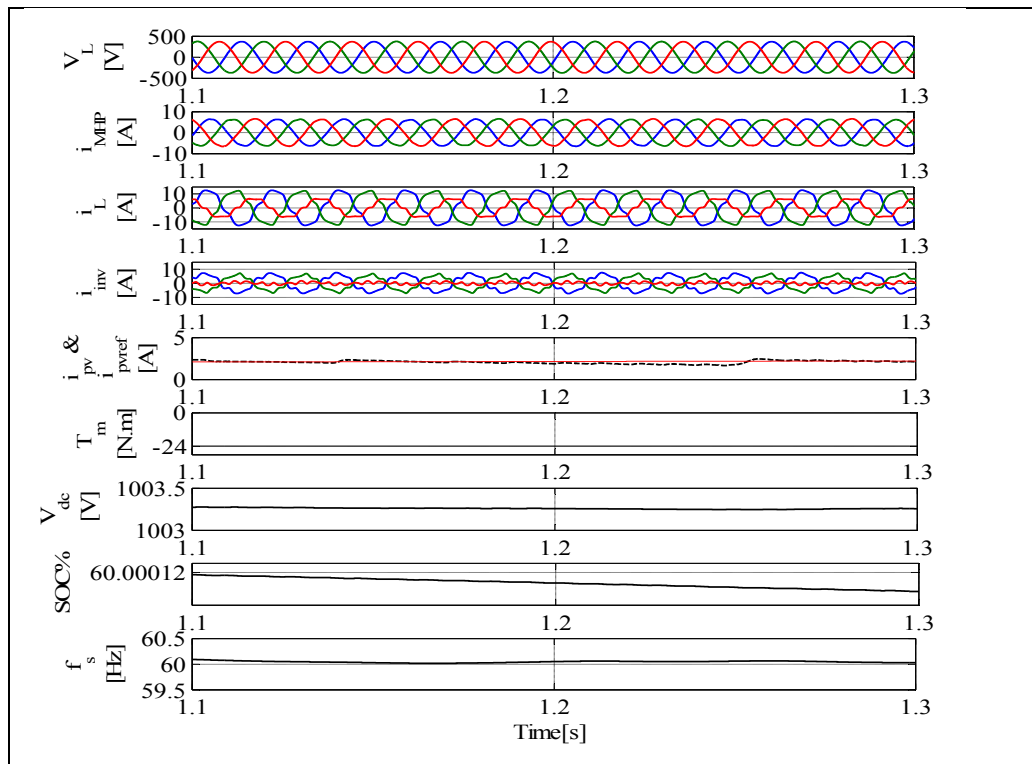


Figure 5.14 Dynamic performance of PV-MHP HSPGS based on fixed speed SyRG under unbalanced nonlinear load

These satisfactory results demonstrate the capability of the proposed control approach, which is based on instantaneous p-q theory to improve the power quality, to regulate the AC voltage and the system frequency at the PCC. In addition, BESS as storage element has shown its

capability to improve the performance of the proposed HSPGS by compensating the of the PV and load power fluctuation.

### 5.3.1.3 Performance analysis when the BESS becomes fully charged (SOC%=100%)

Fig. 5.17 shows the waveforms of the AC voltage ( $v_L$ ), system frequency ( $f_s$ ), DC-bus voltage ( $V_{dc}$ ), state of charge battery (SOC%), output MHP power ( $P_{MHP}$ ), output PV power ( $P_{pv}$ ), load power ( $P_L$ ) and that dissipated in dump loads ( $P_d$ ) when the BESS becomes fully charged.

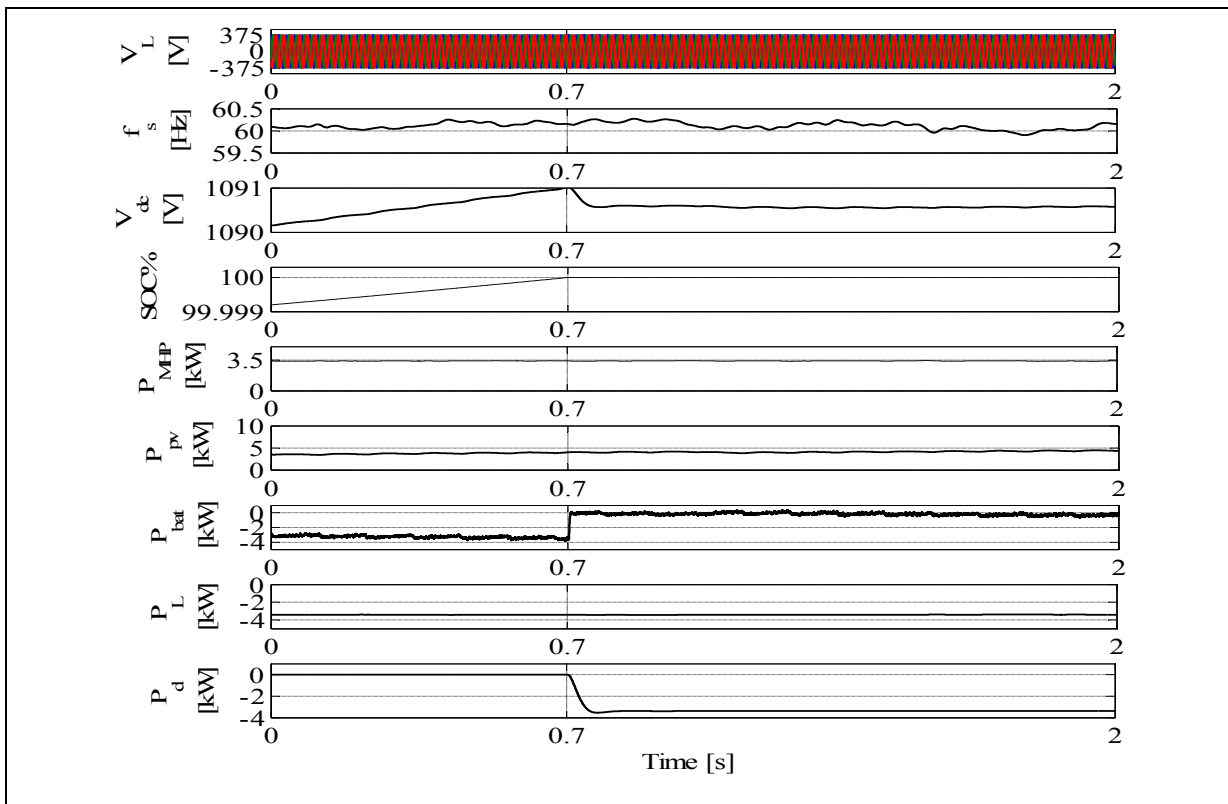


Figure 5.15 Dynamic performance of the PV-MHP HSPGS based on fixed speed SyRG when the SOC% of BESS is equal to 100%

It is observed that from  $t = 0$  s to  $t = 0.7$  s, the sum of power provided by RESs ( $P_{pv} + P_{MHP}$ ) is greater than load power ( $P_L$ ) and that is why dump load is turn off ( $P_d=0$ ). From  $t=0.7$  s to

$t = 2$  s, SOC% of BESS becomes equal to 100%. Moreover, the DC-link voltage is equal to 1091 V, which represents the maximum BESS voltage  $V_{ocmax}$ . In addition,  $(P_{pv} + P_{MHP}) > P_L$ , therefore, condition to put on dump load is fulfilling. It is observed that the difference of power ( $P_d = (P_L - (P_{pv} + P_{MHP}))$ ) is dissipated in dump load, DC link voltage is kept constant BESS power is equal to zero ( $P_{bat} = 0$ ), and the system frequency, as well as, the AC voltage are kept constant, which confirms the robustness of the proposed control approaches to ensure optimal operation of the proposed PV-MHP HSPGS and high protection of BESS against overcharging.

### **5.3.2 Performance of the hybrid standalone power generation system based on solar PV and MHP driven fixed speed SCIG**

An extensive simulation study is carried out using MATLAB/Simulink to test the performance of the proposed system. Many scenarios are tested such as, 1) sudden increasing and decreasing of linear load as well as the solar irradiation, 2) balanced and unbalanced nonlinear load, and 3) when the BESS becomes fully charged (SOC%=100%). In this study the water flow used to operate MHP is considered constant. The system parameters are given in Appendix Table A-5.

#### **5.3.2.1 Performance analysis under load and solar irradiation change**

To test the performance of the proposed control algorithms for hybrid standalone system based on MHP driven SCIG and PV, which uses single stage inverter, simulations are carried out using MATLAB/Simulink. Fig. 5.16 shows simulation results of the terminal load voltage, source current, mechanical torque developed by MHP, DC voltage and its reference output PV voltage, output PV current, total load current, nonlinear load current, output inverter current, battery current and its reference current, and the system frequency. It is observed that the waveforms of the source current, which represents in this case the output MHP and that of the AC voltage, are sinusoidal despite presence of balanced and unbalanced linear and nonlinear loads. In addition the DC voltage and the battery current follow their references. It is observed that the DC/AC interfacing inverter acts as bidirectional power

converter in order to allow power flow in either direction (from AC to the DC side and from DC to AC side). Moreover, to improve the power quality it is used as an active filter. It is also used to extract the maximum of power from PV array by regulating the DC bus voltage at its desired value, which represents the output maximum PV voltage. For the system frequency which is regulated by controlling the Buck-boost DC converter, it is observed that the battery current follows its reference and the system frequency is kept constant.

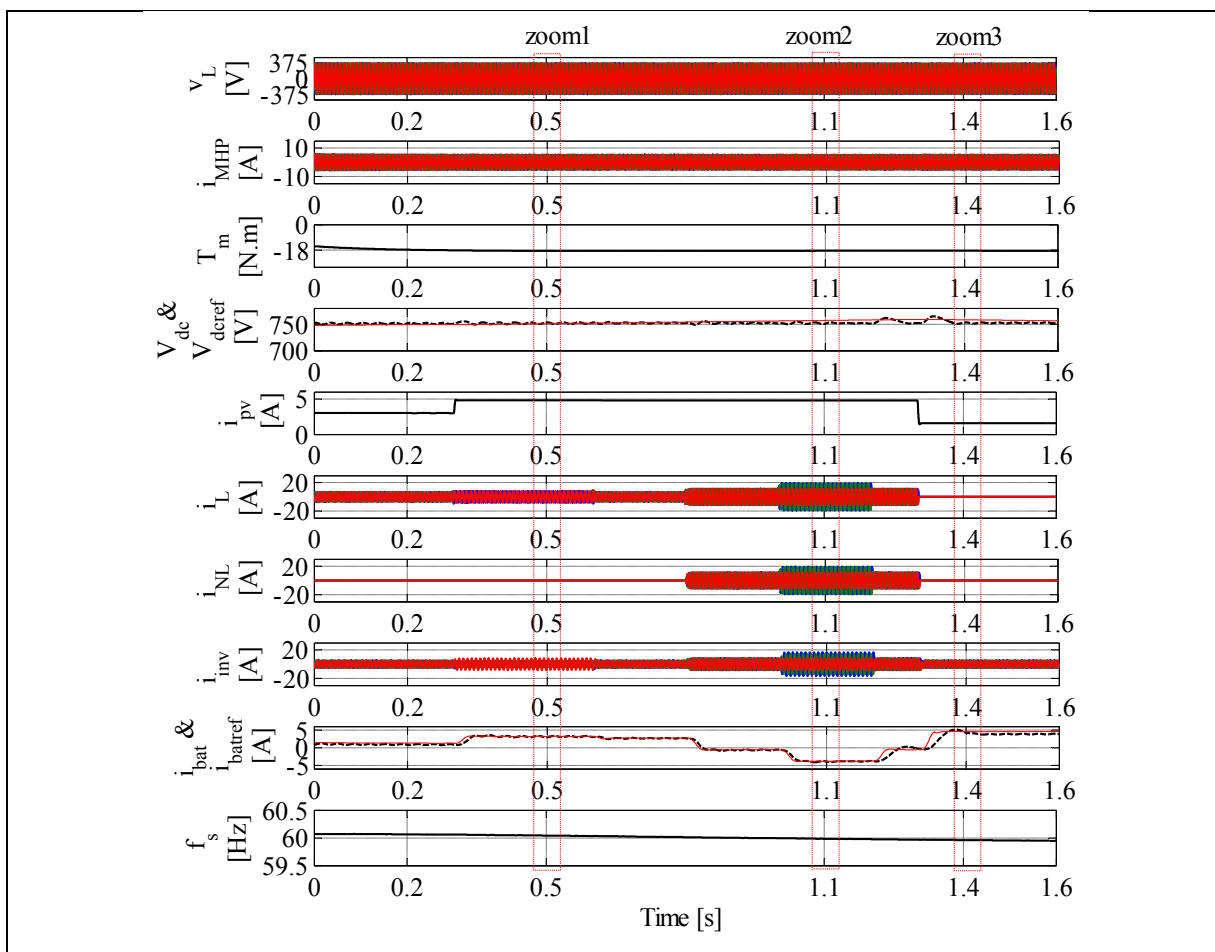


Figure 5.16 Dynamic performance under solar and load irradiation change

### 5.3.2.2 Performance analysis under unbalanced linear load

Figure.5.17 shows the zoomed waveforms of the simulation results shown in Fig.5.16 between  $t= 0.45$  s and  $t= 0.55$  s. It is observed that in this period of time unbalance linear load is connected to the PV-MHP HSPGS. Despite presence of this sever condition, the AC voltage and system frequency, are not affected. The waveforms of the AC voltage and source current are perfectly balanced, and the DC link voltage follows its reference. One conclude that the proposed control technique, which is based Anti-Hebbian learning technique for power quality improvement at the PCC and P&O technique for MPT from the solar PV array perform well the desired tasks.

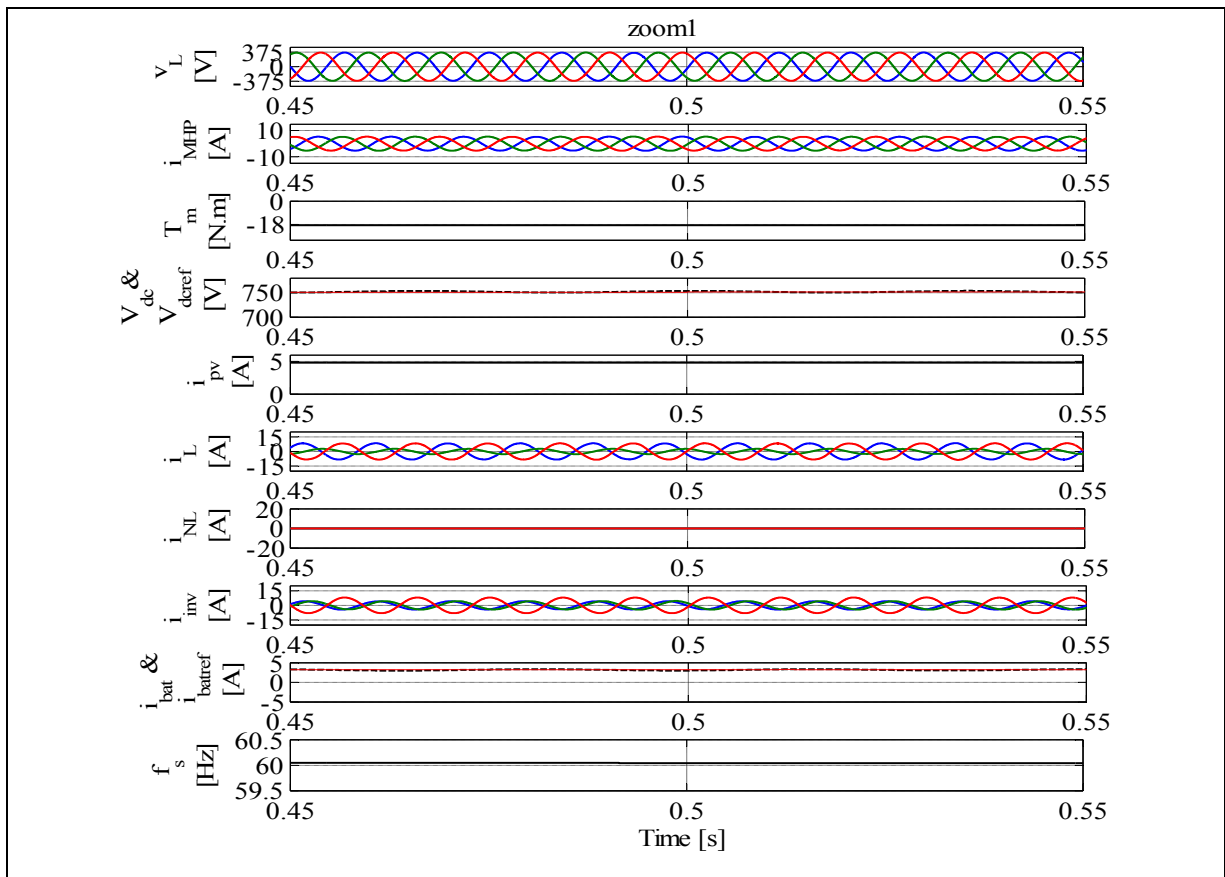


Figure 5.17 Zoom1 of the results shown in Fig.5.16 between  $t=0.45$ s and  $t= 0.55$  s

It is observed that the system frequency is regulated at its rated value and the battery current follows its reference, which confirms the robustness of the proposed approach control for the Buck-Boost DC converter.

### 5.3.2.3 Performance analysis under unbalanced nonlinear load

In Fig.5.18 the zoomed waveforms of the simulation results shown in Fig.5.16 between  $t=1.05$  s and  $t=1.15$ s are presented.

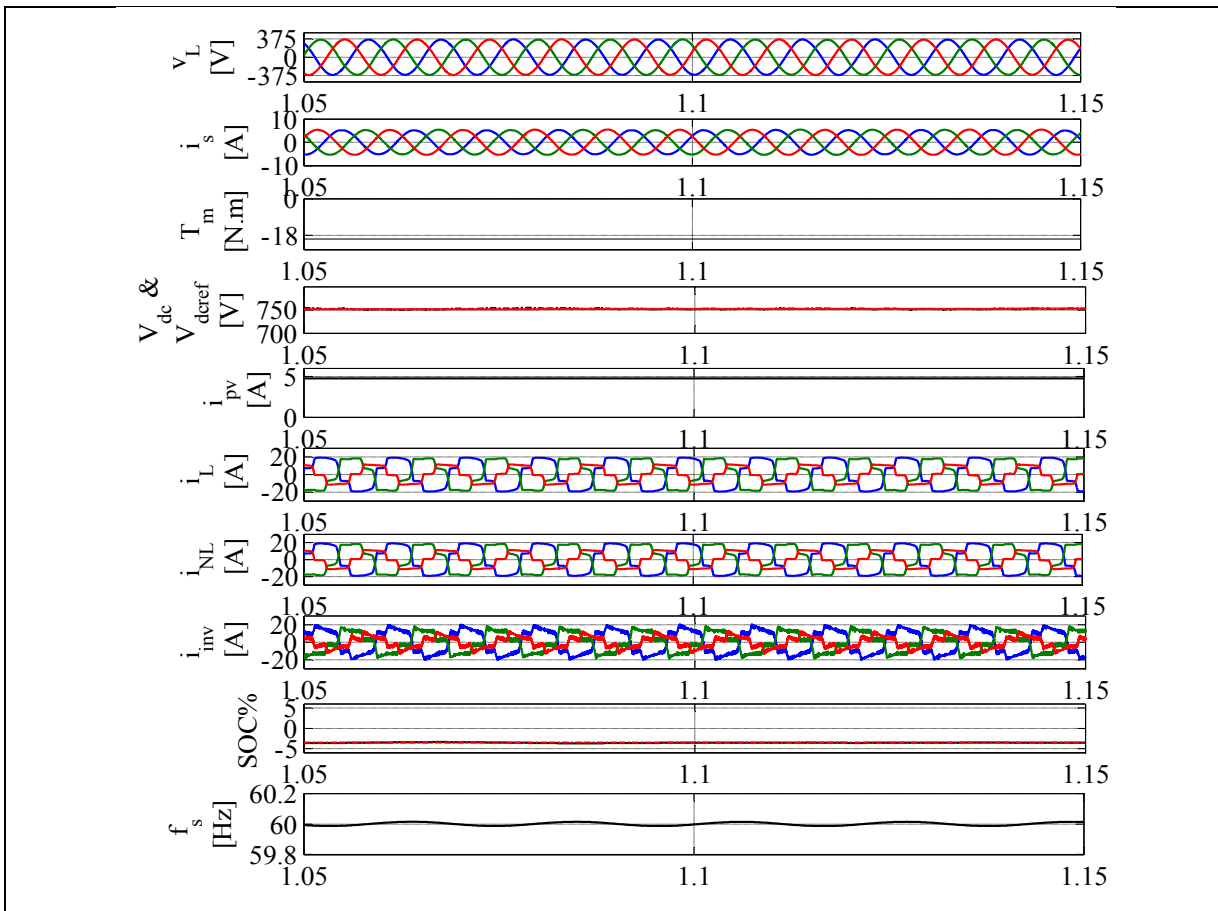


Figure 5.18 Zoom2 of the results shown in Fig.5.16 between  $t=1.05$  s and  $t= 1.15$  s

It is observed that unbalanced nonlinear load is connected to the system, but the AC voltage and the source current are perfectly balanced and sinusoidal. Seeing that the load current is

greater than source current, BESS is discharging (negative sign of current). It is observed that DC/AC interfacing inverter acts as active filter; it compensates harmonics and balance source current. BESS current follows its reference and the system frequency is maintaining constant.

**5.3.2.4 Performance analysis under completely removed load**

Figure 5.19 shows the zoomed waveforms of the simulation results shown in Fig.5.16 between t=1.35s to t=1.45 s.

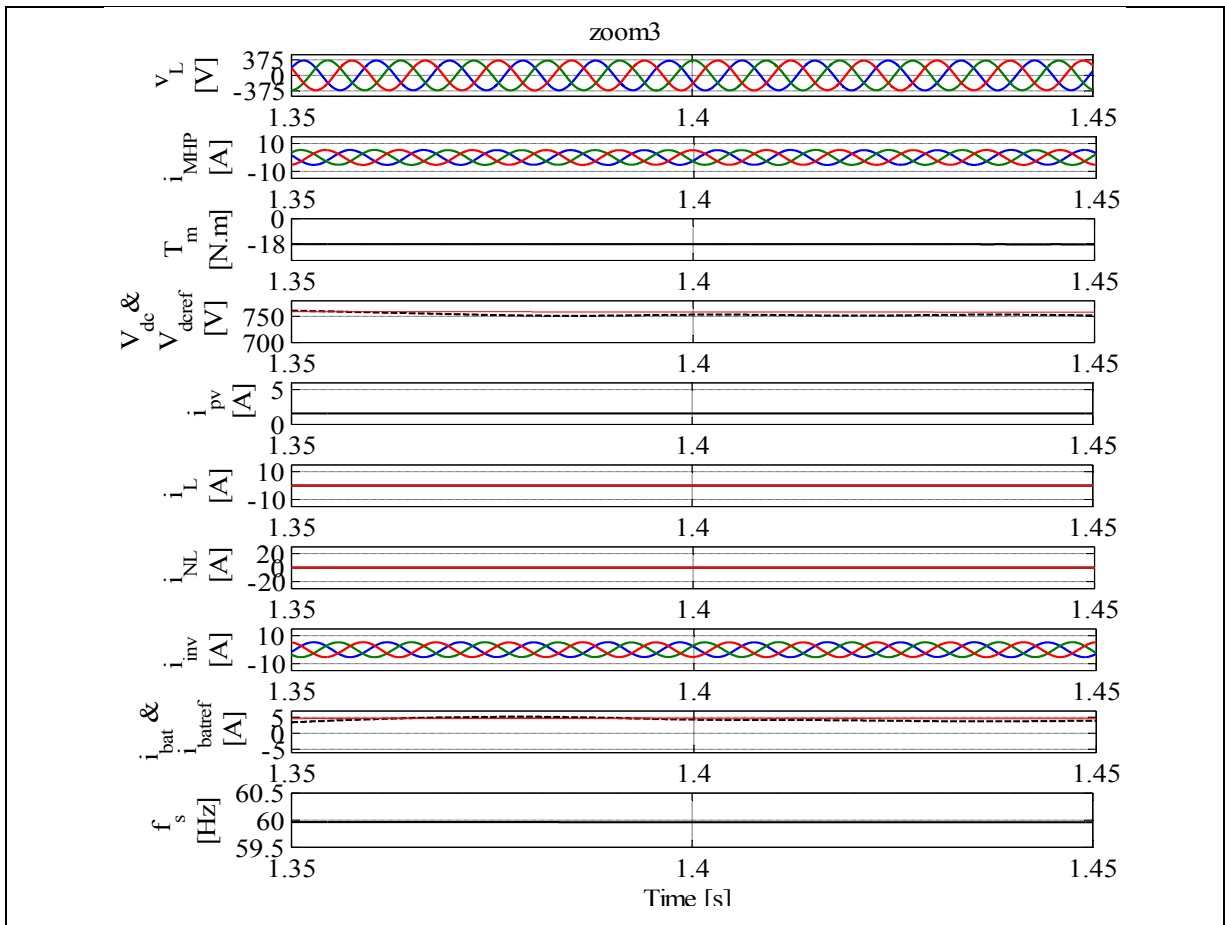


Figure 5.19 Zoom3 of the results shown in Fig.5.16 between t=1.35 s and t= 1.45 s

It is observed that no load is connected to the PV-MHP HSPGS and the output PV current in this period of time is decreased. Despite these variations, AC voltage and source current are

perfectly balanced and sinusoidal. Furthermore, the system frequency is kept constant. One sees clearly that the generated powers from solar PV array and MHP are injected in BESS and that is why its current becomes positive. It is found that DC bus voltage follows its reference, which is corresponding to the maximum PV power tracking and is obtained using P&O method, implying the smooth operation of the proposed control algorithms for MPT, AC voltage and frequency regulation.

#### **5.4 Conclusion**

Several topologies which are based on PV array and MHP driven fixed speed generators such as, SG, SCIG, PMSG and SyRG are presented. Performances of two different topologies are tested during variation of the solar irradiations and presence of different kind of loads, as well as when the BESS becomes fully charged using Matlab/Simulink. The obtained results for the both topologies show satisfactory. The AC voltage and system frequency are regulated at their rated values. Furthermore, the waveforms of the MHP output currents for the both configurations are kept sinusoidal during presence of balanced and unbalanced nonlinear loads. SyRG and SCIG are the ideal choice as, electrical generators for MHP due to its structures which are robust and simple. In addition, they don't require sliding contacts or a dedicated exciter. Furthermore, the AC voltage and the system frequency regulation can perform by controlling the DC/AC inverter, as is presented in the first topology or using additional Buck-Boost DC converter, as is presented in the second topology. The second topology compared the first topology possesses more advantages because of less BESS voltage due to the use of the Buck-Boost DC converter. Modified Anti-Hebbian and modified instantaneous p-q theory control have proved its capability to achieve the desired tasks, the only difference between is that the modified Anti-Hebbian requires more sampling time.

## CHAPITRE 6

### HYBRID STANDALONE POWER GENERATION SYSTEM EMPLOYING SOLAR PV ARRAY AND WT

#### 6.1 Introduction

In this chapter, several topologies, which are based on solar PV array and WT driven fixed and variable speed generators such as, SCIG, SG, PMSG, SyRG, PMBLDCG and DFIG as shown in Fig.6.1 are discussed. The proposed topologies are designed in order to achieve several tasks, such as maximization of energy provided by WT and of solar PV array, ensure stability and continuously supplying load with high power quality with reduced cost. In this chapter, a detailed study of three selected topologies is offered. The performances of selected topologies are tested using MATLAB/Simulink during loads and weather conditions changes. In this chapter, implementation in real time of new scheme and new nonlinear control algorithms for maximum power point tracking, AC voltage and system frequency regulation for PV-WT HSPGS employing variable speed PMBLDCG, are also discussed.

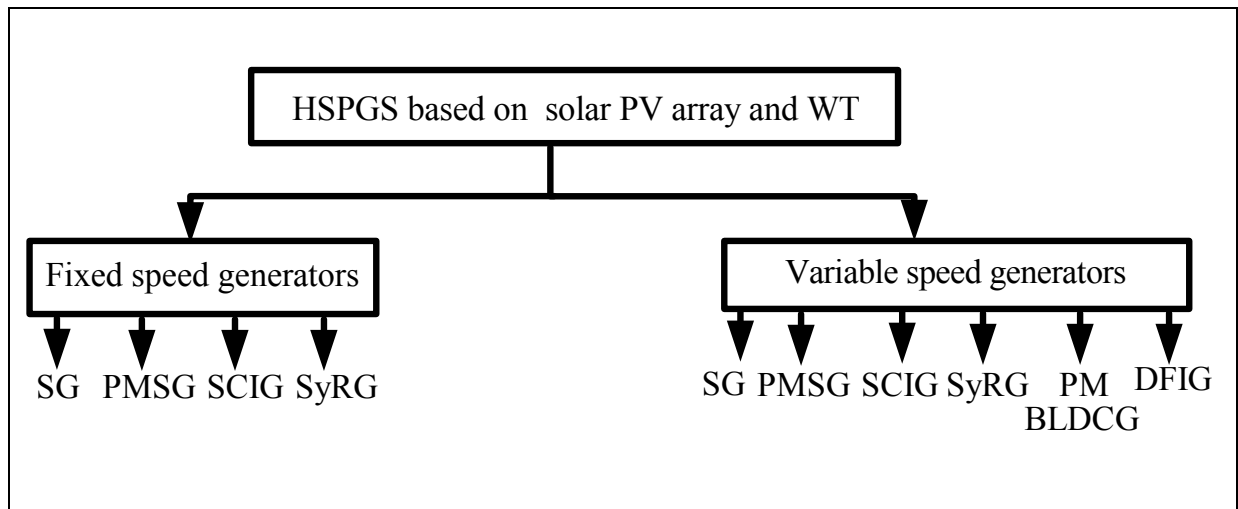


Figure 6.1 Classification of HSPGS based on PV array and WT driven fixed and variable speed generators

## 6.2 Topology designs of hybrid standalone power generation system based on PV array and WT driven fixed speed generators

Fig.6.2 shows the proposed topologies for PV-WT HSPGS employing fixed speed generators such as, SG, SyRG, SCIG, and PMSG. WTs in these topologies are tied directly to PCC without using power converters. This technology is simple and inexpensive, but according to (Papathanassiou et Papadopoulos, 2001), it causes important mechanical stress because all fluctuations in wind speed are transmitted into mechanical torque and further, as electrical fluctuations, into the PCC. These fluctuations introduce a change in the voltage drop and system frequency deviation.

Many solutions have been proposed in the literature to solve the problem caused by WT fluctuations. In (El Moursi et al., 2014) static series compensators (SSC) is proposed, and in (Leon et al., 2011) dynamic voltage restorers (DVR) are suggested. In terms of voltage support, these devices are costly, and require complicated protection system (Xia et al., 2015). Usually, for solar PV array, single-stage PV inverter or two-stage inverters are required to connect it to the PCC (Yang et al., 2015). A comparative study realized by (Zhu, Yao et Wu, 2011) indicated that single-stage inverter is more effective than two-stage inverter, but from point view of DC and AC voltage stability and power quality improvement at PCC, two-stage inverters are preferred. Furthermore, in HSPGS that uses PV and WT and reliable energy source, such as, BESS is suggested to fill the shortfall intermittency (Bo et al., 2013). This element requires protection from the overvoltage and additional elements in order to extend its life span. To protect BESS from overvoltage and ensure power balance by dissipating the excess of generating power when BESS is fully charged, dump load is advised by (Hirose et Matsuo, 2012).

Thereby, for effective integration of solar PV array and WT in HSPGS, the topologies shown in Fig.6.2 are proposed. WT is connected directly to the PCC and solar PV array uses two-stage inverters. To protect BESS from overvoltage, dump load is used and is placed in parallel with BESS at the DC bus. Delta-star transformer is used in order to get galvanic isolation between RESs and loads.

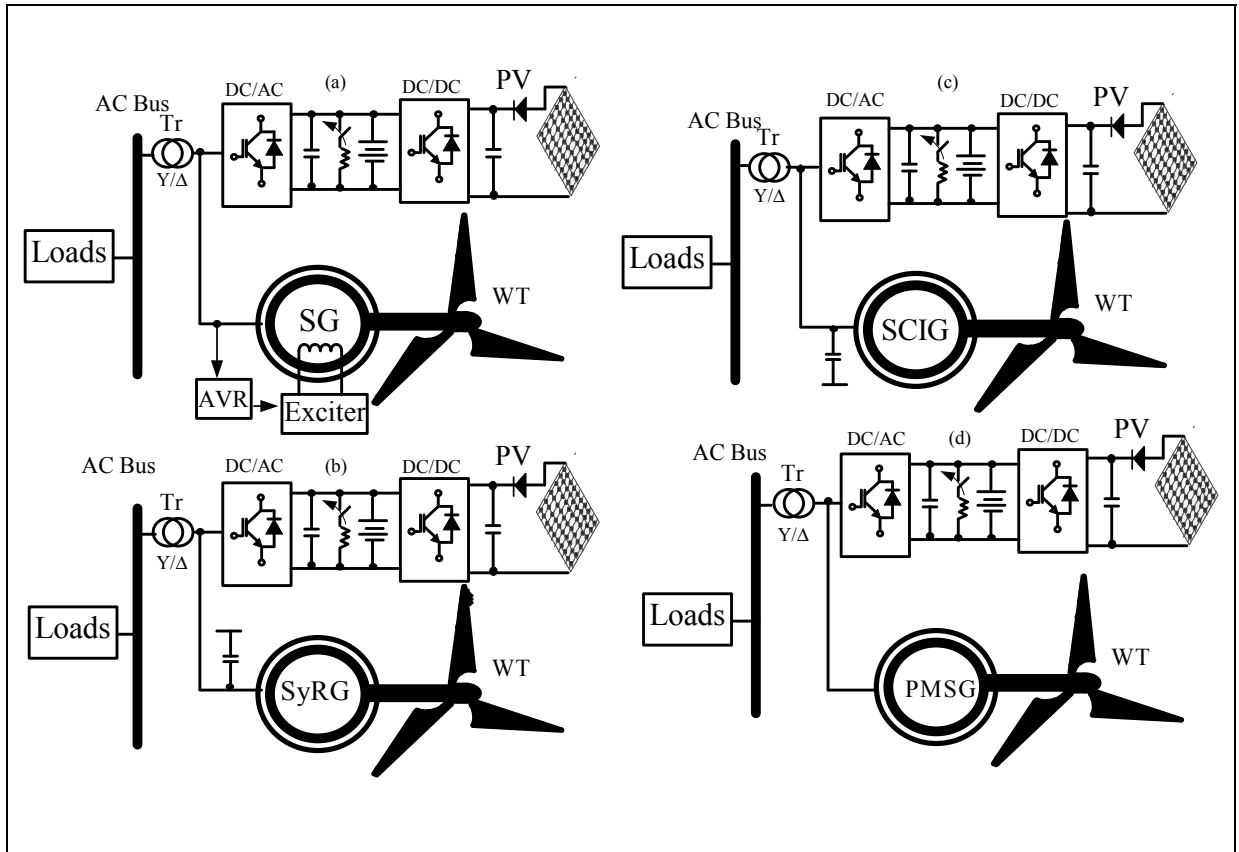


Figure 6.2 HSPGS based on solar PV array and WT driven fixed speed generators

#### 6.2.1.1 Description and control of hybrid standalone power generation system based on solar PV array and WT driven fixed speed SCIG

As shown in Fig.6.3, terminals of the fixed speed SCIG are connected directly to the PCC. A capacitor bank is used to provide excitation current to this generator in order to built-up its voltage. The second RES in this proposed HSPGS is the solar PV array, which is tied to the PCC through two-stage inverter. To get galvanic isolation between RESs and loads this PV-WT HSPGS is coupled by Delta -start transformer. Additional elements, such as, BESS and dump load are used in order to maintain the power balance during variation of solar irradiation, wind speed, as well as, loads.

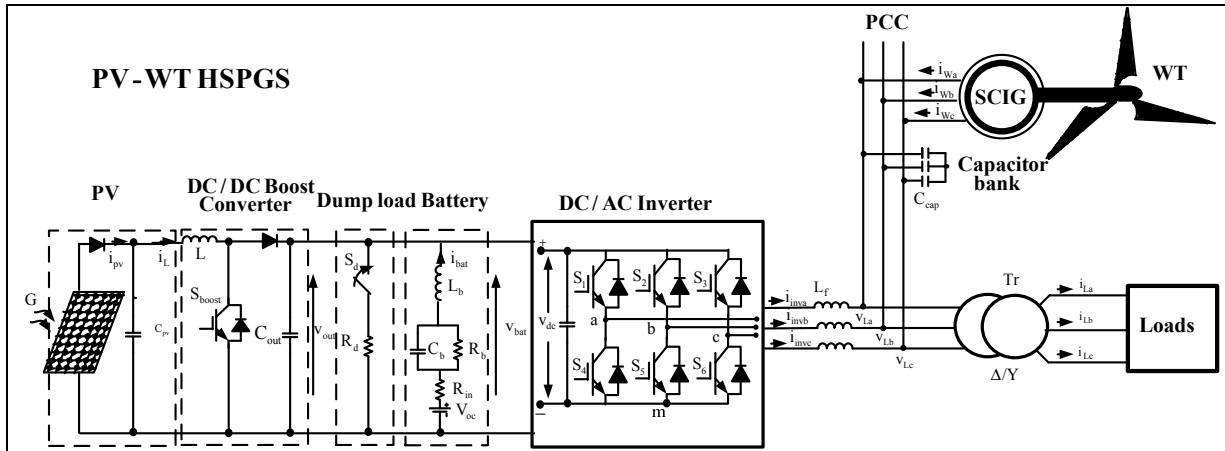


Figure 6.3 HSPGS based on PV array and WT driven fixed speed SCIG

### Model of the constant-speed WT system

Fig.6.4 shows the turbine power-speed characteristics obtained by using the model of the WT already given in chapter 2 and shown in Fig.2.5. For this model, therefore is no control over tip speed ratio  $\lambda$ , and the pitch angle  $\beta$  is kept equal to 0. Therefore, there is no optimum turbine power over a wide range of  $V_{wind}$ .

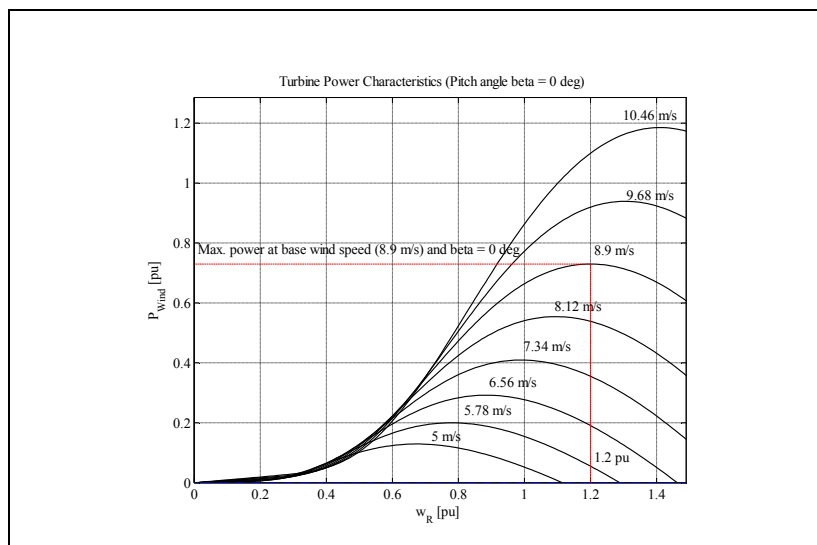


Figure 6.4 Turbine power-speed characteristics for  $\beta = 0^\circ$

The power captured from the wind is described as:

$$P_{wind} = \frac{1}{2} \rho R^2 V_{wind}^3 C_p(\lambda) \tag{6.1}$$

where  $\rho$ ,  $R$ ,  $V_{wind}$ ,  $C_p$  are the air density, radius of the wind turbine blades, wind speed and the power coefficient respectively.

### 6.2.1.2 Control algorithms for solar PV array and WT driven fixed speed SCIG

The proposed control algorithm for DC/AC inverter is developed to achieve regulation of the AC voltage, system frequency and improve the power quality improvement at the PCC as shown in Fig.6.5 (Rezkallah et Chandra, 2009). The MPPT control algorithm for solar PV array and dump load, is the same as already proposed and discussed in detail in chapter 4 for PV-DG HSPGS.

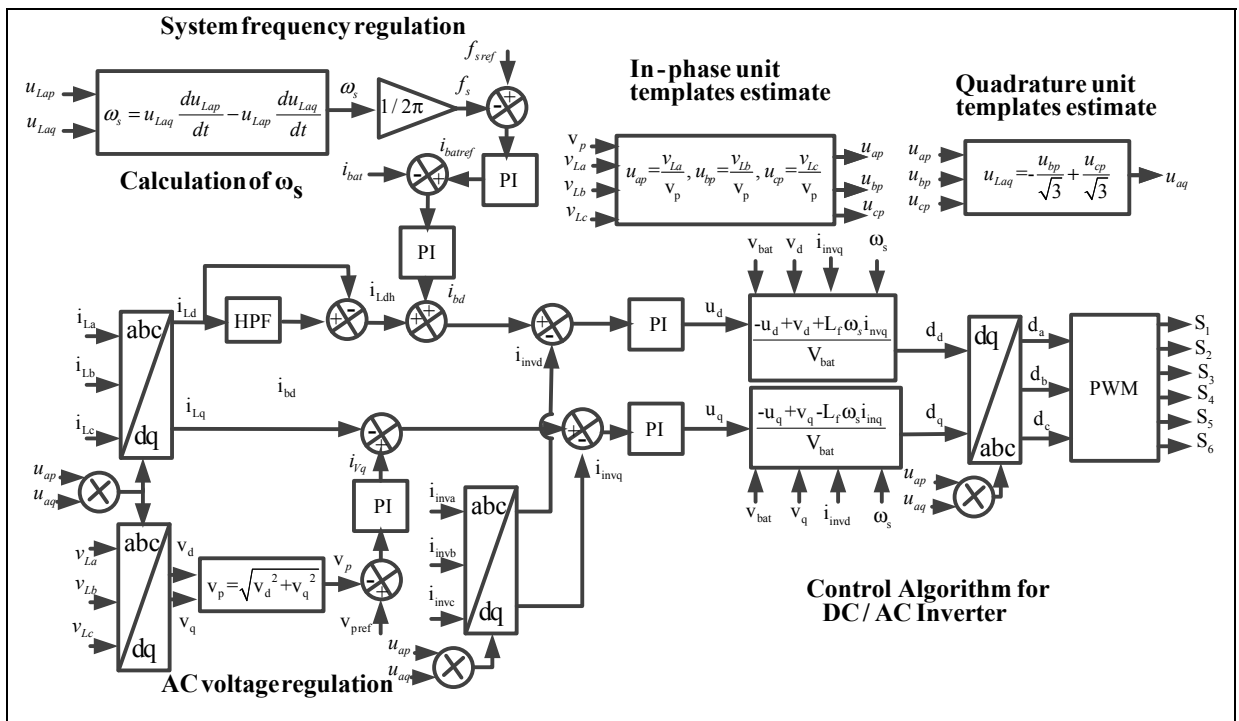


Figure 6.5 d-q control algorithm for DC/AC inverter

In this technique, the currents injected by the DC/AC inverter are controlled in the synchronous d-q reference frame using a decoupled nonlinear control approach. The output of the frequency control loop ( $i_{bd}$ ) is added to harmonics load current ( $i_{dLh}$ ), which is obtained using high pass filter and the output of the AC voltage loop ( $i_{vq}$ ) is subtracted from q-load current ( $i_{Lq}$ ).

The total d-q axis inverter currents are subtracted from the total d-q axis load currents and the errors are fed to the PI current controllers in order to obtain the control laws  $d_d$  and  $d_q$  using the mathematical model of the inverter in d-q synchronous reference frame expressed by equation (2.117) given in chapter two as:

$$\begin{cases} \overbrace{L_f \frac{di_{dinv}}{dt}}^{u_d} = L_f \omega_s i_{qinv} - d_d v_{bat} + v_{Ld} = u_d \\ \overbrace{L_f \frac{di_{qinv}}{dt}}^{u_q} = -L_f \omega_s i_{dinv} - d_q v_{bat} + v_{Lq} = u_q \end{cases} \quad (6.2)$$

where  $u_d$  and  $u_q$  represents the output of the PI current controllers.

And the control laws are obtained using (6.2) as:

$$\begin{cases} d_d = \frac{-u_d + v_{Ld} + L_f \omega_s i_{qinv}}{v_{bat}} \\ d_q = \frac{-u_q + v_{Lq} - L_f \omega_s i_{dinv}}{v_{bat}} \end{cases} \quad (6.3)$$

The d-q axis control laws are transformed to abc stationary frame ( $d_a$ ,  $d_b$  and  $d_c$ ) using inverse Park transformation and fed PWM controller to generate the switching signal for the switches of the DC/AC inverter.

### 6.3 Topology designs of hybrid standalone power generation system based on solar PV array and WT driven variable speed generators

Fig.6.6 shows the proposed PV-WT HSPGS topologies. The solar PV arrays and WTs in PV-WT HSPGSs are tied to the DC bus through controlled DC/DC boost converters and AC/DC converters and to the PCC through DC /AC interfacing inverters. Many electrical generators as shown in Fig.6.6 (a-e) are used. They are controlled to get high efficiency from the WTs

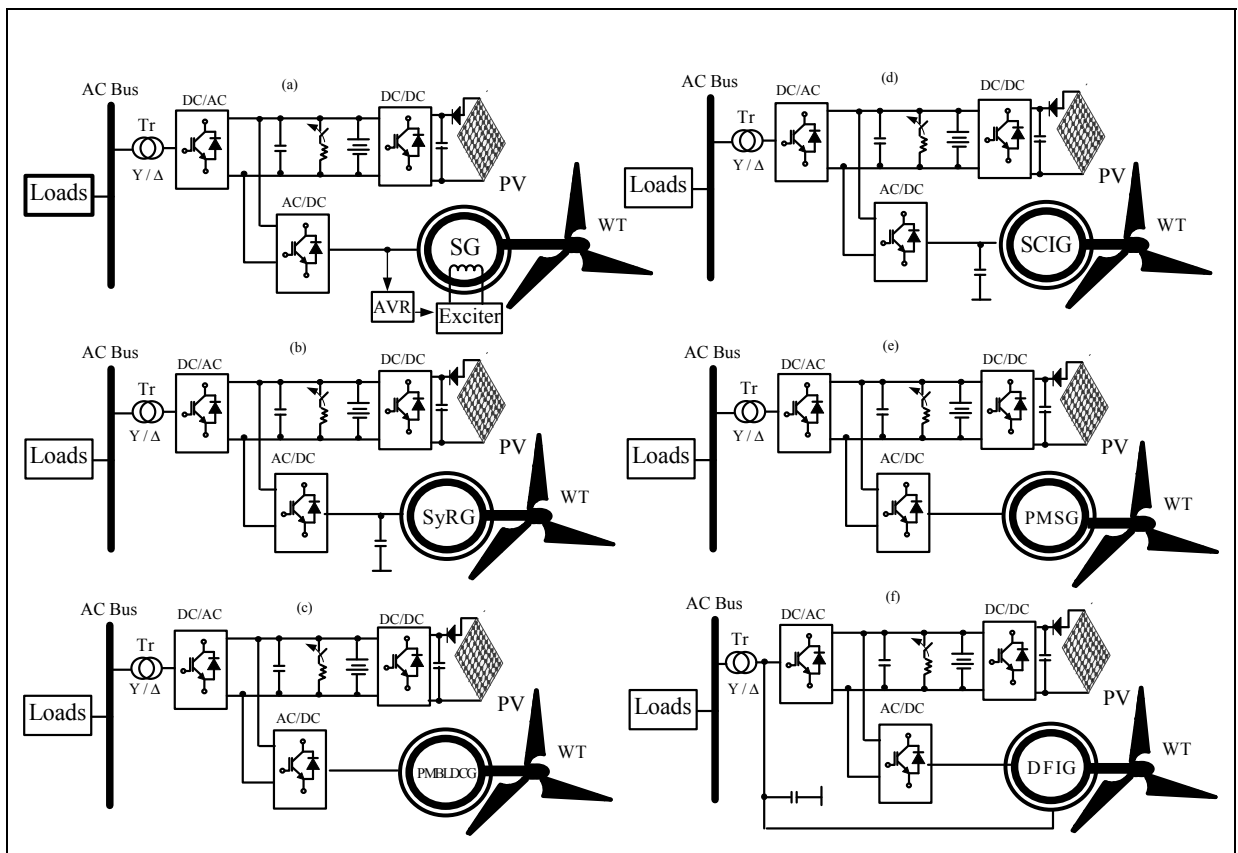


Figure 6.6 HSPGS based on solar PV array and WT driven variable speed generators

Usually for this type of application, two power converters are required as, has been proposed by (Caisheng et Nehrir, 2008; Dong-Jing et Li, 2008) (Whei-Min, Chih-Ming et Chiung-Hsing, 2011), to tie WT and solar PV array to the PCC. But in the proposed PV-WT HSPGSs, only one DC/AC interfacing inverter is used, which makes the proposed PV-WT

HSPGS efficient, inexpensive and less complicate from point of view the control. To ensure, interruptible power to the connected loads at all times, BESS is used and to protect it against overvoltage dump load is employed. Dump load in all proposed PV-WT HSPGSs is connected in the DC side, instead of the AC side, which allows minimizing the risk of power quality deterioration at the PCC. These topologies are cost-effective due to the use of the technology of the variable speed generators and using less number of power converters. As shown in Fig.6.6, solar PV array is connected to the DC/DC boost converter, which is controlled in order to achieve MPPT and to regulate the output PV voltage at the desired DC-link voltage. Regarding, the AC voltage and system frequency regulation, as well as, power quality improvement at the PCC, a DC/AC interfacing inverter is controlled. The proposed electrical generators, which are driven by WTs, are controlled using the AC/DC converter in order to achieve high efficiency from WTs.

### **6.3.1.1 Control algorithms for solar PV array and WT driven variable speed SyRG**

Fig.6.6 shows the selected PV-WT HSPGS which is based on variable speed SyRG for study. Solar PV array and WT are tied to the DC bus through DC/DC boost converter and controlled three-phase AC/DC converter and to the PCC through controlled three-phase DC/AC interfacing inverter. The proposed variable speed SyRG starts as squirrel induction generator and synchronizes ones with a supply near synchronous speed. Therefore, its terminal voltage is built-up by connecting sufficient capacitance across its terminal. In addition, this generator requires more reactive power when its rotor speed increases. This reactive power can be provided by the main grid if it is interfaced with connected grid and from BESS in HSPGS. According to (Guha et Kar, 2005), the frequency of generated voltage of this generator depends only upon the mechanical speed of rotation, which makes it easier to control.

In this proposed PV-WT HSPGS the AC/DC converter and the DC/DC boost converter are controlled to achieve MPPT from WT and solar PV array using rotor oriented control and P&O method.

The control of the AC voltage, system frequency, as well as the power quality improvement at the PCC are ensured by controlling the DC/AC interfacing inverter using modified indirect control, and dump load is controlled using same control approach as used in chapter 4.

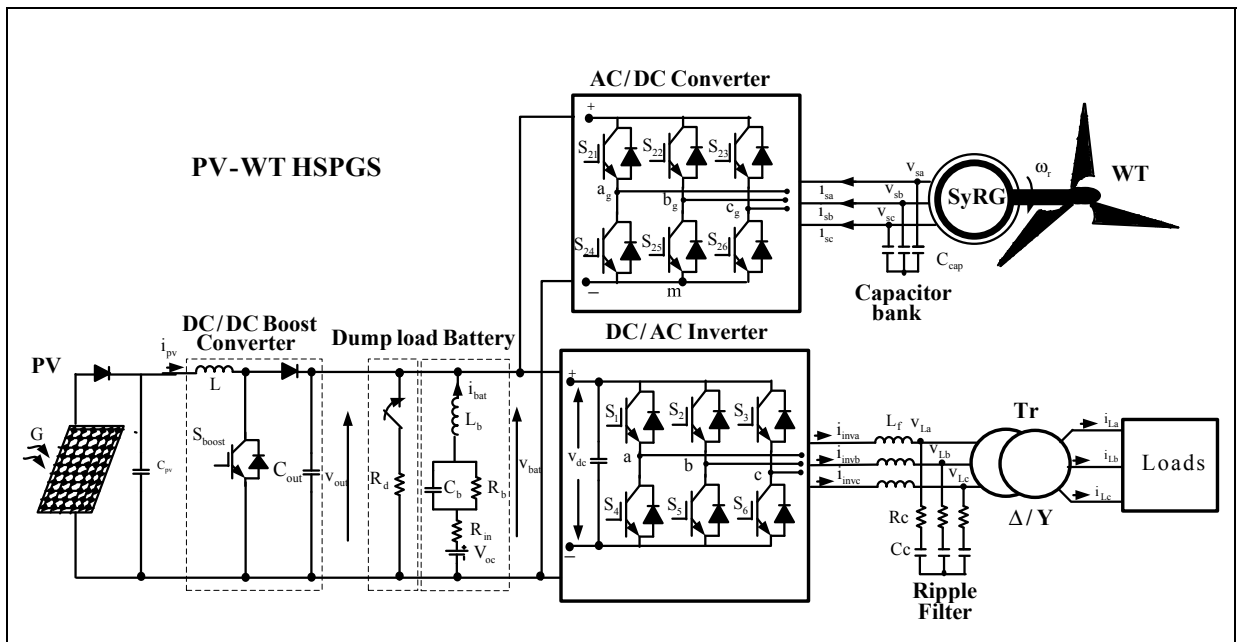


Figure 6.7 HSPGS based on solar PV array and WT driven variable speed SyRG

### Control of the AC/DC Converter for WT side

As shown in Fig. 6.7, WT driven variable speed SyRG and is connected to the DC-bus through three-phase AC/DC converter, which is controlled in order to get MPPT from WT by controlling its rotor speed ( $\omega_r$ ). Mostly, SyRM is used as motor drive (Capecchi et al., 2001; Vagati et al., 1999), but as generator it is relatively unexplored through having robust structure (Tokunaga et Kesamaru, 2011). Furthermore, it can be used in high speed and high temperature environments (Wen-Bin, Huann-Keng et Chen-Hsiang, 2013). As is already shown in Fig.2.18, the flux linkage of SyRG is directly proportional to the stator currents. Therefore, the torque of this generator can be controlled by adjusting the stator currents. Many control approaches are proposed in the literature to achieve this task, such as, direct

control (DTC), field oriented control (FOC) and direct power control (DPC) (Tremblay, Atayde et Chandra, 2011). It is reported in (Busca et al., 2010) that the FOC possess more advantages compared to DTC and DPC, from the point view of torque response and accurate speed control. Furthermore, using this control approach is possible to obtain full torque at zero speed. In this study, rotor oriented control (ROC) is selected, as shown in Fig.6.9.

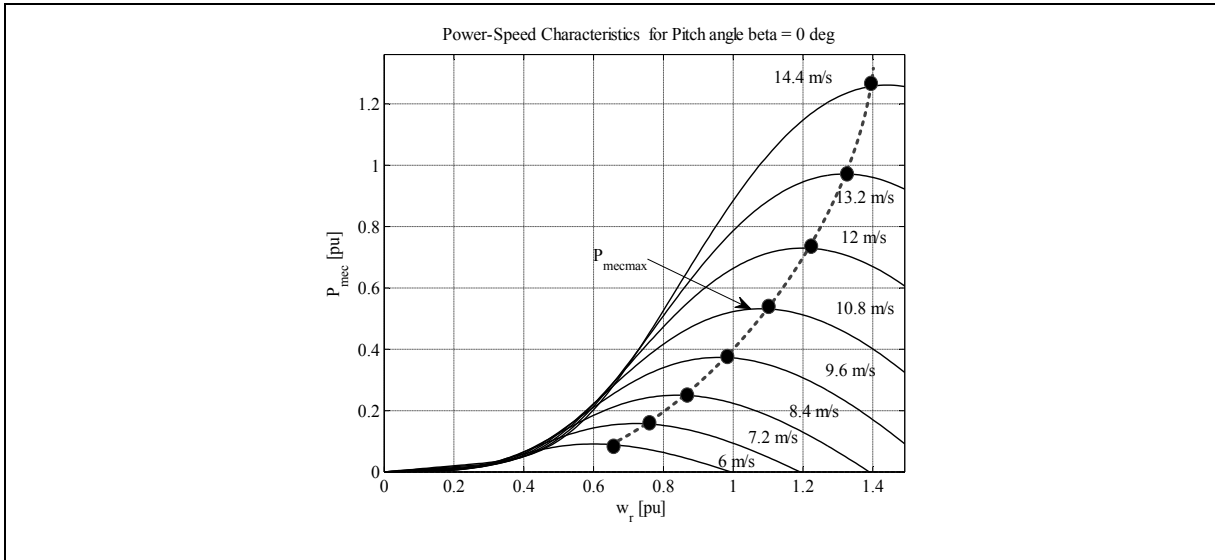


Figure 6.8 Power-speed characteristics

The q-reference stator current ( $i_{qs}$ ) is obtained from speed control loop and the d-reference stator current ( $i_{ds}$ ) is obtained using flux control loop. The sensed rotor speed ( $\omega_r$ ) is compared to its reference speed ( $\omega_{ref}$ ), which is obtained using the mechanical power-speed characteristics shown in Fig.6.8.

The obtained rotor speed error is fed to PI speed controller, and its output represents the reference electromagnetic torque ( $T_{eref}$ ) as:

$$T_{eref} = (\omega_{ref} - \omega_r) \left( k_{por} + \frac{k_{ior}}{s} \right) \quad (6.4)$$

where  $k_{por}$  and  $k_{ior}$  denotes proportional and integral gains.

In this control algorithm, the q-reference stator current is obtained using equations (2.108, 2.109 and 2.110) of the flux linkages and electromagnetic torque, which are given in chapter 2. Replacing (2.108, 2.109 and 2.110) gives the following expression:

$$i_{qsref} = \frac{1}{\lambda_{ds}} \left( \frac{2}{3P} T_{eref} + \lambda_{qs} i_{ds} \right) \quad (6.5)$$

where  $P$ ,  $\lambda_{ds}$ ,  $\lambda_{qs}$  represent number of poles and stator d-q axis flux linkages, which are calculated as:

$$\begin{cases} \lambda_{ds} = \lambda_{\alpha s} \cos \theta_s + \lambda_{\beta s} \sin \theta_s \\ \lambda_{qs} = \lambda_{\beta s} \cos \theta_s - \lambda_{\alpha s} \sin \theta_s \end{cases} \quad (6.6)$$

And

$$\theta_s = \arcsin \left( \frac{v_{\beta s}}{v_{\alpha s}} \right) \quad (6.7)$$

where  $\theta_s$ ,  $\lambda_{\alpha s}$ ,  $\lambda_{\beta s}$  represents shift stator angle and stator  $\alpha$ - $\beta$  axis flux linkages, which are obtained as:

$$\begin{cases} \lambda_{\alpha s} = \int (v_{\alpha s} - r i_{\alpha s}) dt \\ \lambda_{\beta s} = \int (v_{\beta s} - r i_{\beta s}) dt \end{cases} \quad (6.8)$$

where  $v_{\alpha s}$ ,  $v_{\beta s}$ ,  $i_{\alpha s}$ ,  $i_{\beta s}$  represents the estimated stator voltages and currents in  $\alpha$ - $\beta$  axis.

The estimated stator current ( $i_{qs}$ ) is compared to its reference ( $i_{qsref}$ ) and the error is fed to PI current controller. The output of the PI current controller is added to the term  $(\omega_r \lambda_{ds})$  in order to obtain d- reference stator voltage ( $v_{dsref}$ ).

The estimated stator current ( $i_{ds}$ ) is compared to  $i_{dsref}$ , which is obtained using d-axis magnetic characteristic ( $\lambda_{dsref} = f(\omega_r)$ ), and the error is fed to PI current controller. The output of the PI current controller is added to the term  $(-\omega_r \lambda_{qs})$ .

The obtained result represents the q- reference stator voltage ( $v_{qsref}$ ).

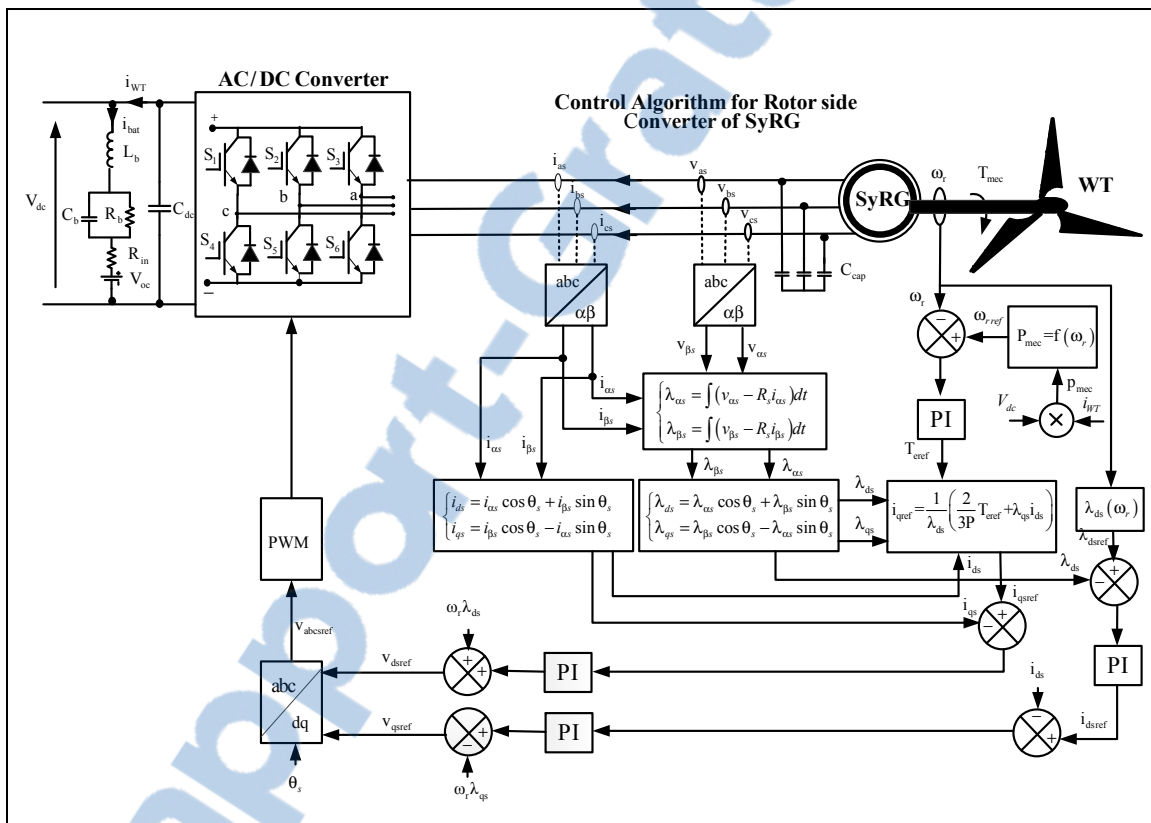


Figure 6.9 Rotor oriented control (ROC) for SyRG

Using the inverse Park transformation given in (2.50), the d-q reference stator voltages are transformed to reference stationary frame and compared after with fixed-frequency triangular carrier wave to generate gating signals for IGBTs of AC/DC converter.

### Control of the DC/AC interfacing inverter

Fig.6.10 shows the proposed control algorithm for controlling the DC/AC inverter in order to regulate the AC voltage and the system frequency for the load.

For AC voltage regulation, the sensed load voltages ( $v_{La}$ ,  $v_{Lb}$ ,  $v_{Lc}$ ) are compared with reference load voltages ( $v_{Laref}$ ,  $v_{Lbref}$ ,  $v_{Lcref}$ ) as:

$$\begin{cases} v_{Laerr}(t) = v_{Laref}(t) - v_{La}(t) \\ v_{Lberr}(t) = v_{Lbref}(t) - v_{Lb}(t) \\ v_{Lcerr}(t) = v_{Lcref}(t) - v_{Lc}(t) \end{cases} \quad (6.9)$$

where  $v_{L(abc)err}(t)$ ,  $v_{L(abc)}(t)$  and  $v_{L(abc)ref}(t)$  denote the load voltages errors, sensed load voltages and its references, which are expressed as:

$$\begin{cases} v_{Laref}(t) = V_{Lpref} \sin(\omega t) \\ v_{Lbref}(t) = V_{Lpref} \sin\left(\omega t - \frac{2\pi}{3}\right) \\ v_{Lcref}(t) = V_{Lpref} \sin\left(\omega t - \frac{4\pi}{3}\right) \end{cases} \quad (6.10)$$

where  $V_{Lpref}$  and  $\omega$  and denotes the reference peak value of the load voltage and the angular frequency, respectively.

The obtained  $v_{L(abc)err}(t)$  are fed to PI voltage controller, and the outputs represents the references inverter currents as:

$$\begin{cases} i_{invaref}(t) = (v_{Laref}(t) - v_{La}(t)) \left( k_{pv} + \frac{k_{iv}}{s} \right) \\ i_{invbref}(t) = (v_{Lbref}(t) - v_{Lb}(t)) \left( k_{pv} + \frac{k_{iv}}{s} \right) \\ i_{invcref}(t) = (v_{Lcref}(t) - v_{Lc}(t)) \left( k_{pv} + \frac{k_{iv}}{s} \right) \end{cases} \quad (6.11)$$

where  $k_{pv}$ ,  $k_{iv}$  and  $i_{inv(abc)ref}$  denote the proportional-integral gains and the references inverter currents, respectively, which are then compared with the sensed inverter currents ( $i_{inv(abc)}$ ). The obtained current errors are fed to PI current controllers and the output of the PI controllers are fed to PWM controller with fixed frequency triangular carrier wave of unit amplitude to generate the switching signals for DC/AC inverter.

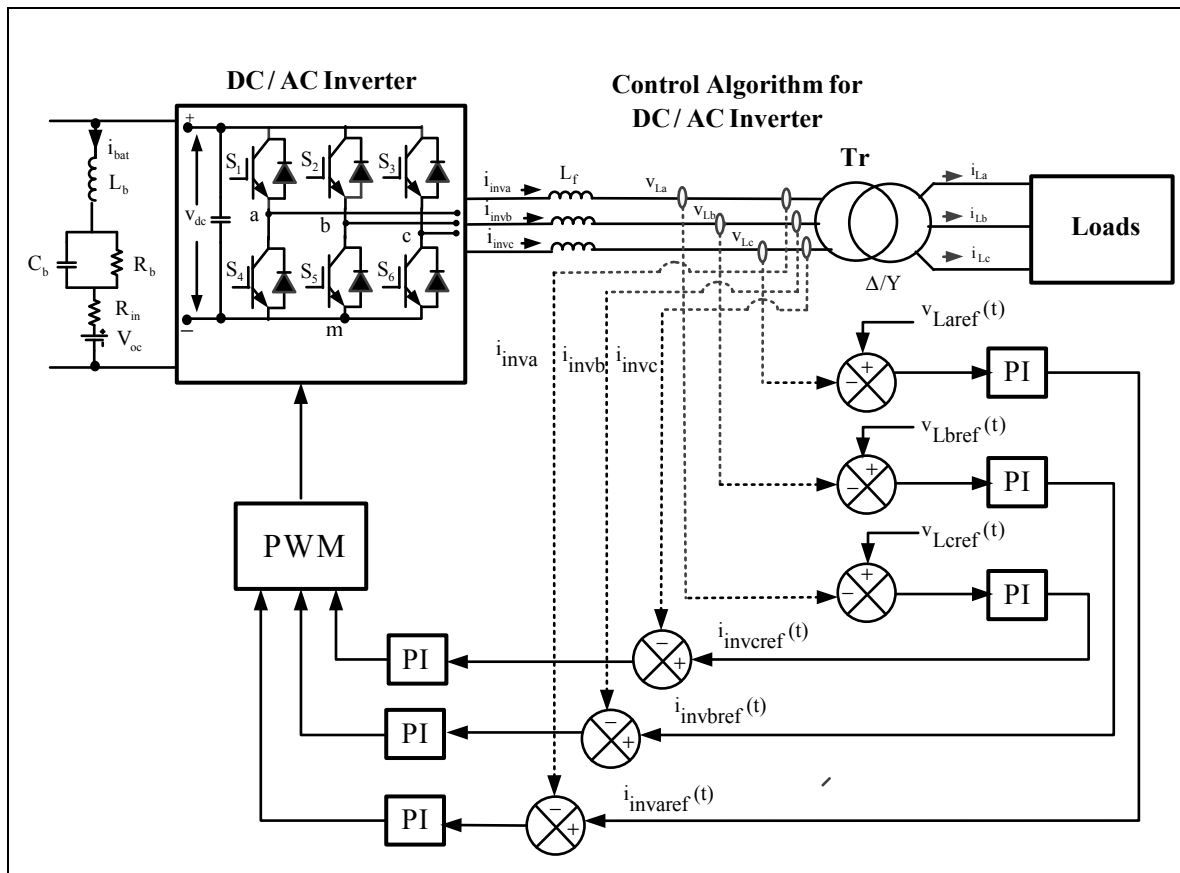


Figure 6.10 Control of the DC/AC interfacing inverter

### 6.3.1.2 Description and control of hybrid standalone power generation system based on solar PV array and WT driven variable speed PMBLDCG

Fig.6.11 shows the proposed small scale PV-WT HSPGS employing variable speed PMBLDCG containing BESS, two DC-DC boost converters, three-phase diode-bridge, current control voltage source converter (CC-VSC), LC low-pass filter and loads.

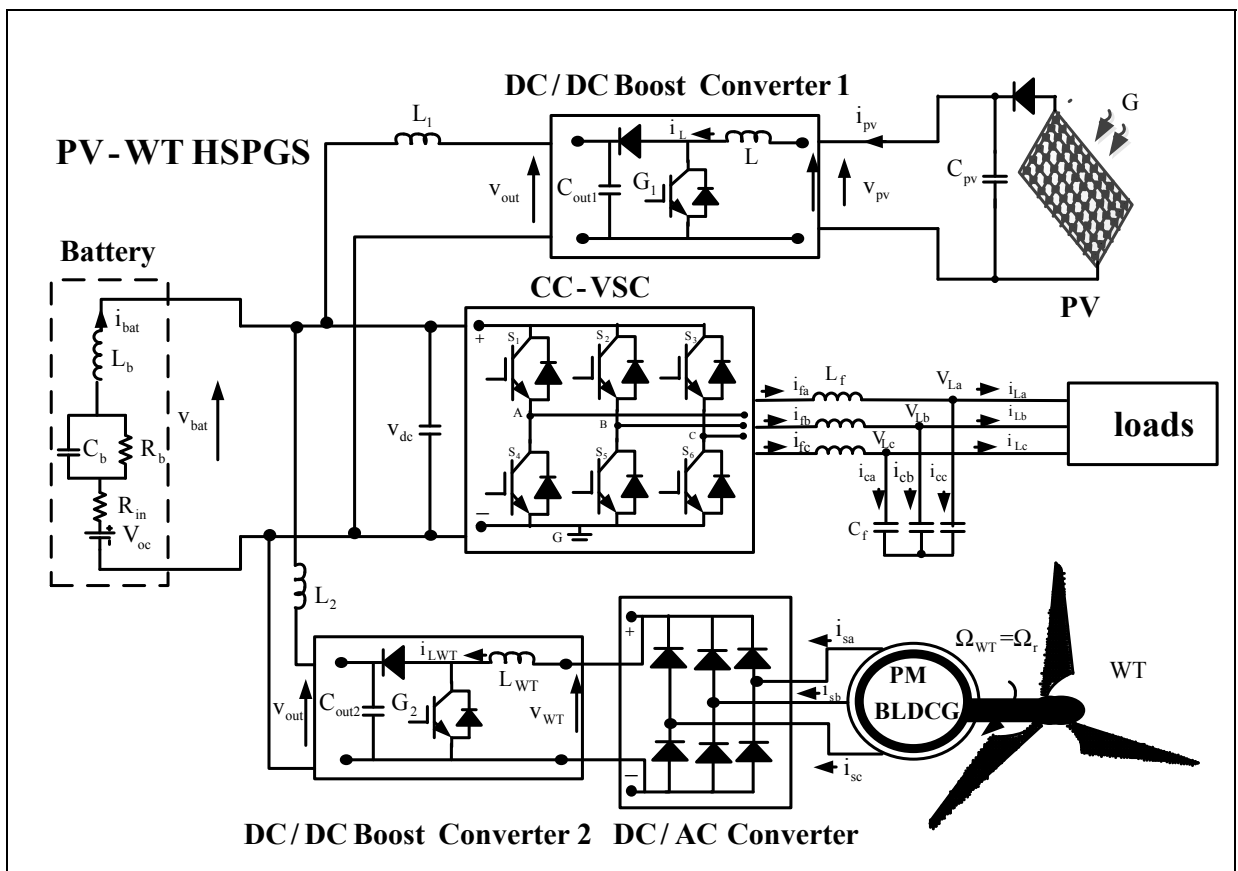


Figure 6.11 HSPGS based on solar PV array and WT driven variable speed PMBLDCG

A sliding mode approach control is proposed to obtain MPPT from the solar PVs and WT. A new feedback-current control is proposed to protect the BESS from the overcharging without resort to dump load and ensure uninterruptable power supply to the connected local loads by providing the required load power demand. A simple and robust nonlinear control using (Quasilinear controller) QLC is proposed for a fast dynamic tracking response of the voltage

and frequency regulation. Modeling and stability analysis are well detailed in this study. The robustness of the proposed scheme and its control algorithms are validated through simulation and experiments.

### 6.3.2 Control design of the DC/DC Boost Converter for PV side

The mathematical model of the DC/DC boost converter, as shown in Fig.2.19 (d), is obtained using the Kirchoff's voltage and current laws. Based on the switching position function ( $G_1=1$  or  $G_1=0$ ), the dynamics of the DC-DC boost converter is described by the following set of equations.

When the switch position function is set to  $G_1=1$ , following equations are obtained:

$$L \left( \frac{di_L}{dt} \right) = v_{pv} \quad (6.12)$$

And

$$C_{out1} \left( \frac{dv_{out}}{dt} \right) = -\frac{v_{out}}{R} \quad (6.13)$$

When the switch position function is set to  $G_1=0$ , following equations are obtained:

$$L \left( \frac{di_L}{dt} \right) = v_{pv} - v_{out} \quad (6.14)$$

$$C_{out1} \left( \frac{dv_{out}}{dt} \right) = i_L - \frac{v_{out}}{R} \quad (6.15)$$

where  $L$ ,  $C_{out1}$ ,  $R$  denote inductance of the input circuit, capacitance of the output filter and the output load resistance, respectively.

Based on (6.14) to (6.16), the following equation for DC-DC boost converter 1 are obtained,

$$\left(\frac{di_L}{dt}\right) = \left(\frac{v_{pv}}{L}\right) - (1-d)\left(\frac{v_{out}}{L}\right) \tag{6.16}$$

$$\left(\frac{dv_{out}}{dt}\right) = \left(\frac{1}{C_{out1}}\right)\left[\left(i_L(1-d)\right) - \left(\frac{v_{out}}{R}\right)\right] \tag{6.17}$$

where  $d$  is the duty cycle.

### 6.3.2.1 MPPT Algorithm Based on Sliding Mode Approach for solar PV array

The proposed control algorithm for MPPT based on SMC is shown in Fig.6.12. Its design is based on the following steps.

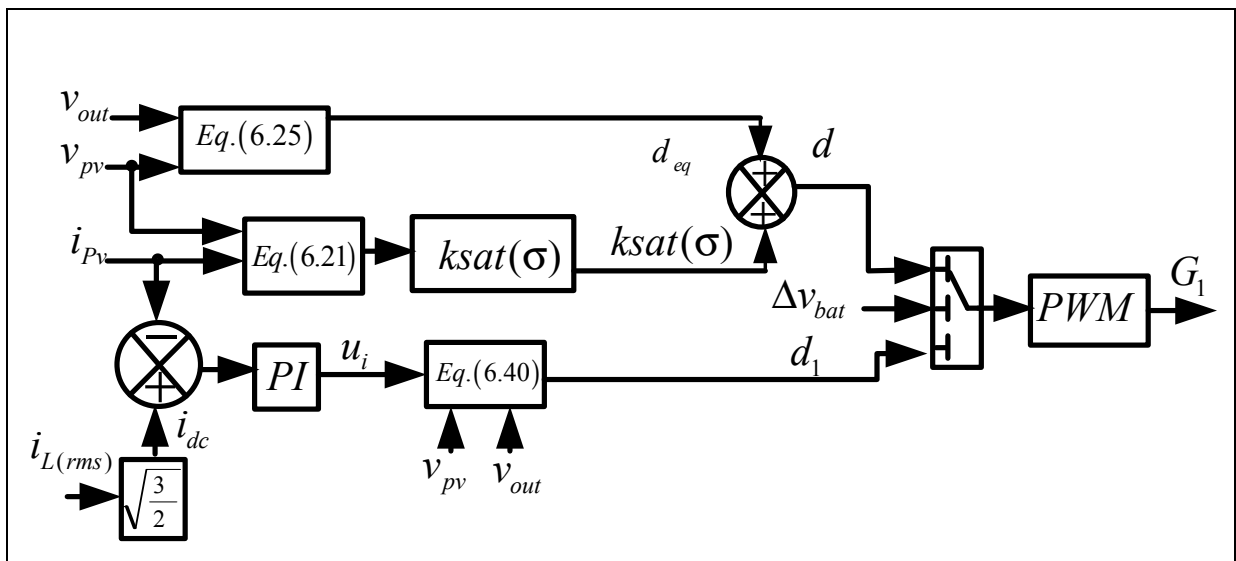


Figure 6.12 Proposed SMC based control algorithm for the DC-DC boost converter 1 for solar PV array side

### Choice of Sliding Surface

In this study, the sliding surface  $\sigma$  is selected as given in (6.18), to ensure reaching the surface and extracting the maximum power from the solar PV array,

$$\sigma = \left( \frac{\partial P_{pv}}{\partial i_{pv}} \right) = 0 \quad (6.18)$$

where  $P_{pv}$  is the PV output power, which is defined as,

$$P_{pv} = v_{pv} i_{pv} \quad (6.19)$$

Replacing (6.19) in (6.20), the following expression is achieved,

$$\sigma = \left( \frac{\partial P_{pv}}{\partial i_{pv}} \right) = \frac{\partial (v_{pv} i_{pv})}{\partial i_{pv}} \quad (6.20)$$

Rearranging (6.21), the sliding surface is defined as,

$$\sigma = v_{pv} + i_{pv} \left( \frac{\partial v_{pv}}{\partial i_{pv}} \right) \quad (6.21)$$

### Determination of the equivalent control

The equivalent control is obtained by setting the derivative of (6.23) to 0. So, the structure of the desired control is defined as,

$$d = deq + k \operatorname{sgn}(\sigma) \quad (6.22)$$

where  $k$  is a positive gain and  $d_{eq}$  is the equivalent control, which is obtained as,

$$\left(\frac{\partial \sigma}{\partial t}\right) = \left(\frac{\partial \sigma}{\partial i_L}\right) \left(\frac{\partial i_L}{\partial t}\right) = \left(\frac{\partial \sigma}{\partial i_L}\right) \left[ \left(\frac{v_{pv}}{L}\right) - (1-d) \left(\frac{v_{out}}{L}\right) \right] \quad (6.23)$$

The non-trivial solution of (6.24) is given as,

$$v_{pv} - (1-d)v_{out} = 0 \quad (6.24)$$

From (6.26), the following equivalent control is obtained,

$$d_{eq} = 1 - \left(\frac{v_{pv}}{v_{out}}\right) \quad (6.25)$$

The duty cycle  $d$  is limited between (0 1). Therefore, the structure of SMC is defined as:

$$d = \begin{cases} 1 & \text{if } d_{eq} + k \operatorname{sgn}(\sigma) \geq 0 \\ 0 & \text{if } d_{eq} + k \operatorname{sgn}(\sigma) \leq 0 \end{cases} \quad (6.26)$$

### System stability analysis

The objective of SMC is to guarantee the convergence of the operation points to predetermine the sliding boundary. Therefore, to verify the stability of the system, Lyapunov function candidate is used:

$$V = (1/2)\sigma^2 \quad (6.27)$$

The system is globally stable if the derivative of (6.21) is negative.

$$\left(\frac{\partial V}{\partial t}\right) = \sigma \left(\frac{\partial \sigma}{\partial t}\right) \langle 0 \quad (6.28)$$

Replacing (6.17) and (6.22) in (6.29), the following relationship, which is composed of three terms, is obtained:

$$\overbrace{\left(v_{pv} + i_L \left(\frac{\partial v_{pv}}{\partial i_L}\right)\right)}^{Term1} \overbrace{\left(2 \left(\frac{\partial v_{pv}}{\partial i_L}\right) + i_L \left(\frac{\partial^2 v_{pv}}{\partial^2 i_L}\right)\right)}^{Term2} \overbrace{\left(\left(\frac{v_{pv}}{L}\right) - (1-d) \left(\frac{v_{out}}{L}\right)\right)}^{Term3} \langle 0 \quad (6.29)$$

where,  $v_{pv}$  is the PV output voltage, and is defined as:

$$v_{pv} = \left(\frac{k_b T A}{q}\right) \ln \left(\frac{(i_{ph} + i_D - i_L)}{i_D}\right) \quad (6.30)$$

where,  $k_b$ ,  $T$ ,  $A$ ,  $q$ ,  $i_{ph}$ ,  $i_D$ ,  $i_L$ , denote Boltzmann's constant, cell temperature, ideality factor, charge of an electron, light-generated current, saturation and the PV currents, respectively. The terms in (6.31) contain the derivative and the second derivative of (6.33), which are given as,

$$\left(\frac{\partial v_{pv}}{\partial i_L}\right) = - \overbrace{\left(\frac{k_b T A}{q}\right)}^{Term1} \overbrace{\left(\frac{i_D}{(i_{ph} + i_D - i_L)}\right)}^{Term2} \quad (6.31)$$

And

$$\left(\frac{\partial^2 v_{pv}}{\partial^2 i_L}\right) = - \overbrace{\left(\frac{k_b T A}{q}\right)}^{Term1} \overbrace{\left(\frac{i_D}{(i_{ph} + i_D - i_L)^2}\right)}^{Term2} \quad (6.32)$$

To verify the condition of stability given in (6.28), the sign of each term in (6.29) is checked independently. Therefore, based on the first and second derivative of the output PV voltage given in (6.31) and (6.32), the signs of the first and the second term in (6.29) are deduced. It is clear that the current  $i_{ph}$  is greater than  $i_D$  and  $i_L$ , which implies that the second term in (6.31) is less than the first one. Based on the parameters given in Table A-8 in the Appendix, the value of the first term in (6.31) is calculated, which is equal to  $(k_bTA/q=0.0026)$ . From this result, it is concluded that the whole term in (6.31) is negative and smaller. Therefore, the first term in (6.29) is always positive. The sign of the second term in (6.29) is negative because of the negative signs of (6.31) and (6.32). As a result, the sign of the third term in (6.29) should be positive to verify the condition given in (6.28). Replacing  $d$  in the third term using (6.22), (2.24) and (6.25), the following expression, which is composed of two terms, is obtained,

$$\left( \overbrace{\left( \frac{v_{out}}{L} \right)}^{Term1} \overbrace{k \operatorname{sgn}(\sigma)}^{Term2} \right) > 0 \quad (6.33)$$

The first term is always positive. Therefore, to satisfy the condition given in (6.28), the second term in (6.33) should be positive, which is obtained by applying the following conditions,

$$\begin{cases} \text{if } \operatorname{sgn}(\sigma) < 0, & k < -1 \\ \text{if } \operatorname{sgn}(\sigma) > 0, & k > 1 \end{cases} \quad (6.34)$$

Based on the above discussion, it is verified that proposed control approach is stable for DC-DC boost converter.

The chattering phenomenon caused by the continuous jumping of the system trajectory when is operating near sliding surface ( $\sigma=0$ ), is the major drawbacks of the proposed SMC

approach given in (6.26). Therefore, to eliminate this undesired chattering phenomenon, sliding layer concept is used as shown in Fig.2 and described below:

$$sat(\sigma, \Phi) = \begin{cases} 1 & \sigma > \Phi \\ \frac{\sigma}{\Phi} & |\sigma| \leq \Phi \\ -1 & \sigma < -\Phi \end{cases} \quad (6.35)$$

Or

$$sat(\sigma, \Phi) = \begin{cases} sign(\sigma) & |\sigma| > \Phi \\ \frac{\sigma}{\Phi} & |\sigma| \leq \Phi \end{cases} \quad (6.36)$$

where  $\Phi$  represents the sliding layer and is located between -0.5 and +0.5.

### Controller gain design

To ensure that the proposed SMC perform better, the control gain ( $k$ ) should be selected to drive the trajectory to the slide surface in infinite time. The dynamic response of the inductor current, which represent the output PV current for different values of ( $k$ ) is shown in Fig.13. It is observed that for high values of  $k$ , the dynamic response of the inductor current is faster. Therefore, for fast dynamic response value control gain is selected equal to ( $k=50$ ).

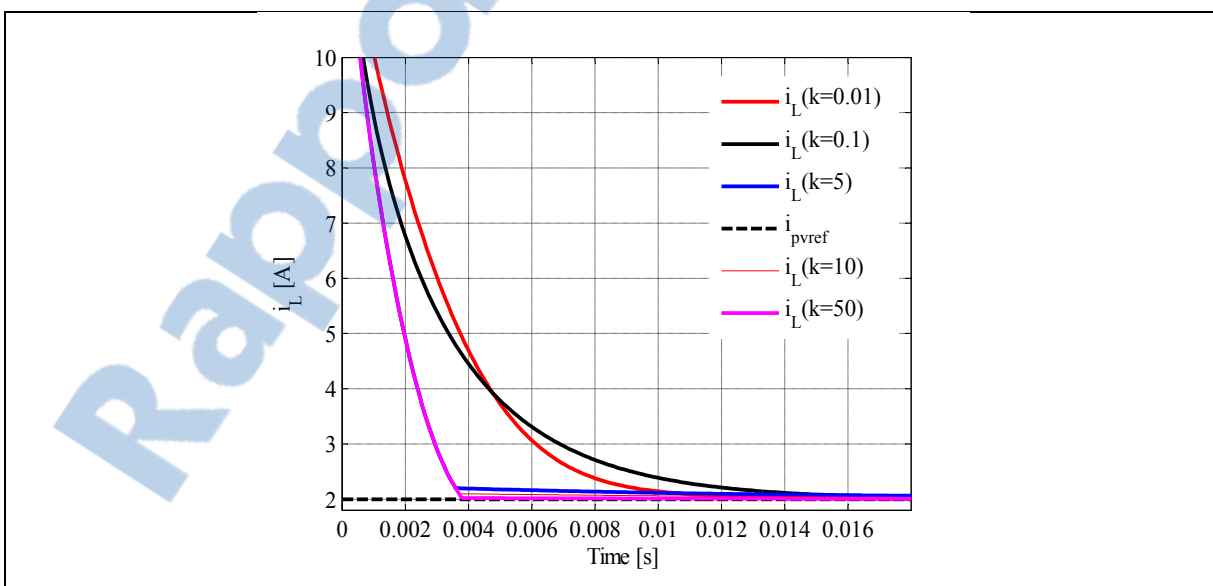


Figure 6.13 Dynamic response of the inductor current for different gain control values

### PV current Control Feedback

The power balance in PV-WT HSPGS is achieved by dissipating the excess power generated using dump loads whenever the BESS is fully charged. Since, the dump loads is not used in this application; a new current control feedback is added to the developed control algorithm for MPPT, in order to protect the BESS from the overvoltage. This is achieved by selecting automatically  $d_i$ , as explained below, while controlling solar PV array, supplying the actual load demand by selecting the points P<sub>1</sub>, P<sub>2</sub> or P<sub>3</sub> on the power-voltage characteristic shown in Fig.6.14, depending on the load requirement.

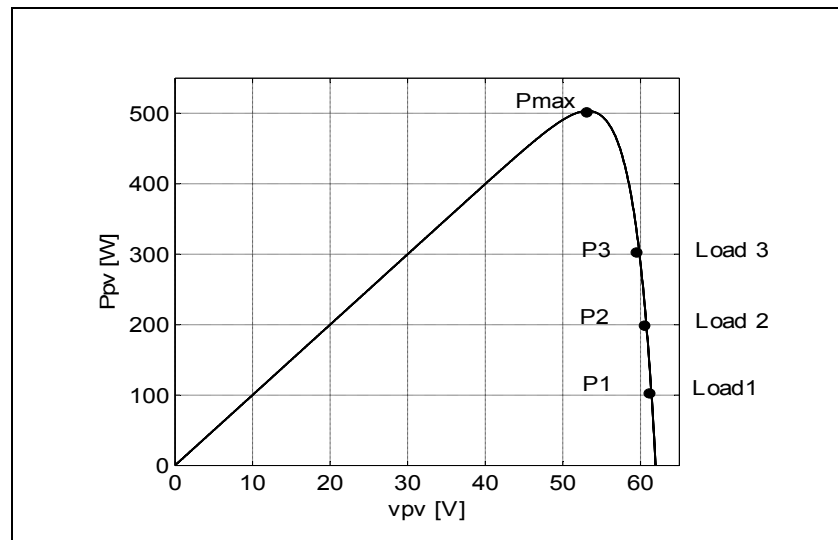


Figure 6.14 Power-voltage characteristic of the solar PV array

Therefore, the conditions to select the desired control are as follows,

$$\begin{cases} \text{if } \Delta v_{bat} > 0, d \text{ selected} \\ \text{if } \Delta v_{bat} < 0, d_1 \text{ selected} \end{cases} \quad (6.37)$$

And

$$\Delta v_{bat} = v_{bat\max} - v_{bat}(n) \quad (6.38)$$

where  $v_{batmax}$ ,  $v_{bat}(n)$  and  $d_1$  are the maximum battery voltage rated by manufacturer, the sensed battery voltage and the control of the additional current control feedback, which is defined as:

$$u_i = L \left( \frac{di_L}{dt} \right) = v_{pv} - (1 - d_1)v_{out} \tag{6.39}$$

And

$$d_1 = 1 + \left( \frac{(u_i - v_{pv})}{v_{out}} \right) \tag{6.40}$$

where,  $u_i$  is the output of the PI current controller.

### 6.3.3 Control Design for DC-DC Boost Converter for WT side

Fig.6.15 shows the proposed control algorithm for the DC-DC boost converter 2 for WT side.

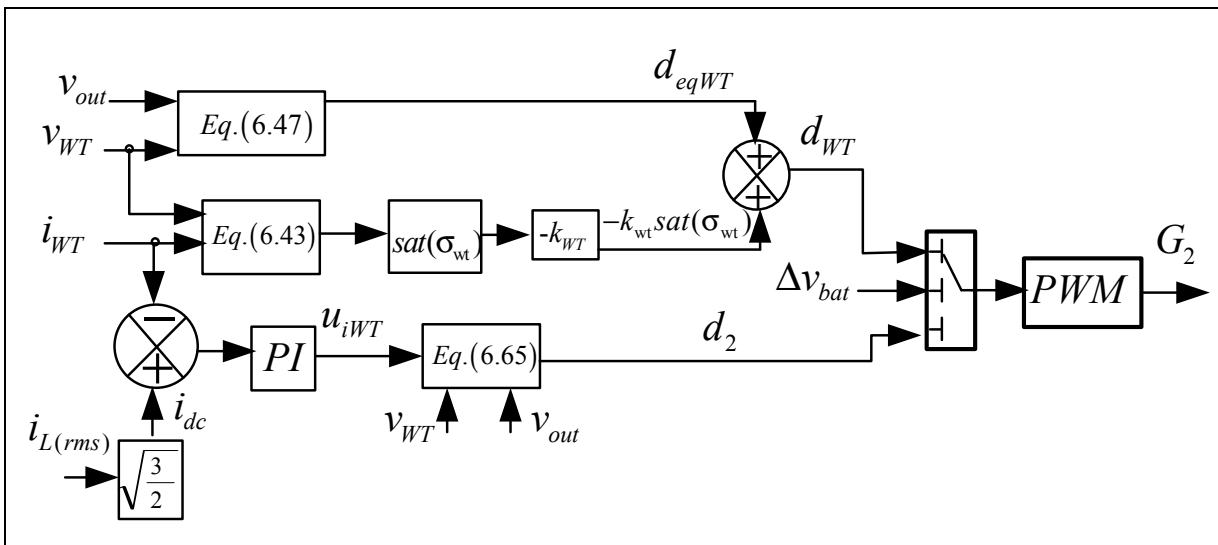


Figure 6.15 Proposed feedback control algorithm for the DC-DC boost converter WT side

As explained earlier, the DC voltage ( $v_{wt}$ ) stays constant and the DC current ( $i_{wt}$ ) varies with the variation of the rotor speed. Therefore, the PMBLDCG possesses the same characteristics as the PV array, allowing thereby the use of the same approach and same steps as those used to design the PV control algorithm.

### 6.3.3.1 Maximum Power Tracking Based on Sliding Mode Approach for WT

#### Choice of sliding surface

The sliding surface  $\sigma_{WT}$  is chosen using (6.41), which represents the necessary condition to obtain the maximum available power from the WT. Therefore, the condition is defined as follows:

$$\sigma_{WT} = \left( \frac{\partial P_{dcWT}}{\partial i_{WT}} \right) = 0 \quad (6.41)$$

where  $i_{WT}$ ,  $P_{dcWT}$  are the DC current and the power provided by the WT, which is defined as:

$$P_{dcWT} = v_{WT} i_{WT} \quad (6.42)$$

where  $v_{WT}$  is the output DC voltage.

Therefore, to reach the surface and extract the maximum of power from the WT, the sliding surface  $\sigma_{WT}$  given in (6.43) is used. Therefore, replacing (6.42) in (6.41), the following equation is obtained,

$$\sigma_{WT} = v_{WT} + i_{WT} \left( \frac{\partial v_{WT}}{\partial i_{WT}} \right) \quad (6.43)$$

### Determination of the equivalent control

The structure of the desired control is defined as,

$$d_{WT} = deq_{WT} + k_{WT} \operatorname{sgn}(\sigma_{WT}) \quad (6.44)$$

where  $k_{WT}$  is the control gain and  $deq_{WT}$  is the equivalent control, which is obtained by setting the derivative of (6.43) equal to 0 as:

$$\left( \frac{\partial \sigma_{WT}}{\partial t} \right) = \left( \frac{\partial \sigma_{WT}}{\partial i_{WT}} \right) \left( \frac{\partial i_{WT}}{\partial t} \right) = \left( \frac{\partial \sigma_{WT}}{\partial i_{WT}} \right) \left[ \left( \frac{v_{WT}}{L_{WT}} \right) - (1 - d_{WT}) \left( \frac{v_{out}}{L_{WT}} \right) \right] = 0 \quad (6.45)$$

The non-trivial solution of (6.45) is given as,

$$(v_{WT} - (1 - d_{WT})v_{out}) = 0 \quad (6.46)$$

Finally,  $deq_{WT}$  is expressed as follow,

$$deq_{WT} = 1 - \left( \frac{v_{WT}}{v_{out}} \right) \quad (6.47)$$

As mentioned earlier, the duty cycle  $d_{eqWT}$  varies between [0 1]. Therefore, the structure of SMC is defined as,

$$d_{WT} = \begin{cases} 1 & \text{if } deq_{WT} + k_{WT} \operatorname{sgn}(\sigma_{WT}) \geq 0 \\ 0 & \text{if } deq_{WT} + k_{WT} \operatorname{sgn}(\sigma_{WT}) \leq 0 \end{cases} \quad (6.48)$$

### System stability analysis

To verify if the system converges to the sliding surface, Lyapunov function candidate is used, which is defined as follow,

$$V = \left(\frac{1}{2}\right) \sigma_{WT}^2 \quad (6.49)$$

Therefore, the system is said globally stable if the derivative of (6.49) is negative.

$$\left(\frac{\partial V}{\partial t}\right) = \sigma_{WT} \left(\frac{\partial \sigma_{WT}}{\partial t}\right) < 0 \quad (6.50)$$

Replacing (6.43) and its derivative in (6.50), one obtained:

$$\left(\frac{\partial V}{\partial t}\right) = \overbrace{\left(v_{WT} + i_{WT} \left(\frac{\partial v_{WT}}{\partial i_{WT}}\right)\right)}^{Term1} \overbrace{\left(2 \left(\frac{\partial v_{WT}}{\partial i_{WT}}\right) + i_{WT} \left(\frac{\partial^2 v_{WT}}{\partial^2 i_{WT}}\right)\right)}^{Term2} \overbrace{\left(\left(\frac{v_{WT}}{L_{WT}}\right) - (1 - d_{WT}) \left(\frac{v_{out}}{L_{WT}}\right)\right)}^{Term3} < 0 \quad (6.51)$$

It is observed that the three terms in (6.51) are depending on the DC voltage  $v_{WT}$ , which is defined (neglecting the semiconductor voltage drops and commutation overlaps) as follows (Boldea, 2006; Krause, Wasynczuk et Sudhoff, 2002a),

$$v_{WT} = 2k_m \omega_r \quad (6.52)$$

where  $k_m$  is motor back EMF, which is proportionality constant, and  $\omega_r$  is the rotor mechanical speed, which is obtained from the experimental characteristic of PMBLDCG, presented in Table 6-1 and depicted in Fig.6.16. The relationship that expresses the mechanical rotor speed of the PMBLDCG versus the output DC current  $i_{WT}$  is as follows:

$$\omega_r = 3.1i_{WT} + 46 \tag{6.53}$$

Table 6.1 Characteristic of the PMBLDCG

$i_{WT}$ [A]	0.290	1.9	3.7	5.3
$\omega_r$ [RPM]	451	501	551	601

The relationship of  $v_{wt}$  versus the  $i_{wt}$  of the WT side is obtained by replacing (6.53) in (6.52) and is expressed as:

$$v_{WT} = k_m (6.2i_{WT} + 92) \tag{6.54}$$

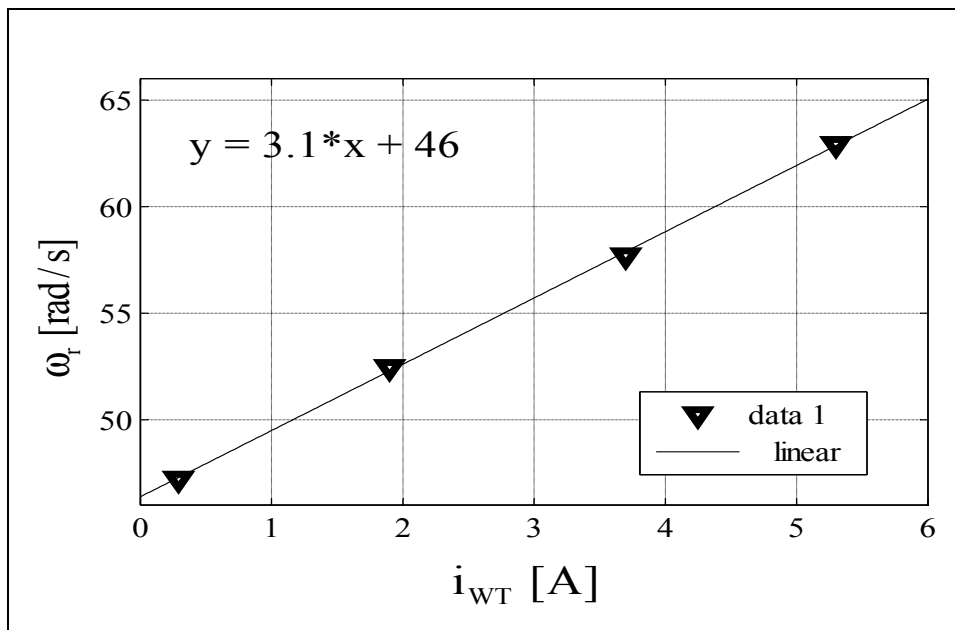


Figure 6.16 Experimental characteristic of  $\omega_r=f(i_{WT})$

Therefore, to satisfy the stability condition given in (6.50), the sign of each term in (6.51) is checked independently. As previously mentioned, the terms depend on the first and second derivatives of (6.54), which are given by:

$$\frac{k_m \partial (6.2i_{WT} + 92)}{\partial i_{WT}} = 6.2k_m > 0 \quad (6.55)$$

And

$$\frac{k_m \partial^2 (6.2i_{WT} + 92)}{\partial^2 i_{WT}} = 0 \quad (6.56)$$

Replacing (6.55) and (6.56) in the first and the second terms of (6.51), we obtain:

$$k_m (6.2i_{WT} + 92) + 6.2k_m i_{WT} > 0 \quad (6.57)$$

And

$$12.4k_m > 0 \quad (6.58)$$

Replacing (6.57) and (6.58) in the first and the second term of (6.51), one get a positive signs. Therefore, the sign of the third term should be negative in order to satisfy the stability condition given in (6.50). Replacing  $d_{wt}$  of the third term in (6.51) by (6.46) and (6.47) gives (6.59), which is composed of two terms. The sign of the first term in (6.59) is always positive; implying that the sign of the second term in (6.59) should be negative to satisfy the stability condition given in (6.50).

$$\left( \overbrace{\left( \frac{v_{out}}{L_{WT}} \right)}^{Term1} \overbrace{k_{WT} \operatorname{sgn}(\sigma_{WT})}^{Term2} \right) < 0 \quad (6.59)$$

where

$$\text{sgn}(\sigma_{WT}) \begin{cases} 1 & \text{if } \sigma_{WT} > 0 \\ 0 & \text{if } \sigma_{WT} = 0 \\ -1 & \text{if } \sigma_{WT} < 0 \end{cases} \quad (6.60)$$

Therefore, to ensure stability condition, the control gain  $k_{WT}$  must be negative.

The chattering phenomenon caused by the continuous jumping of the system trajectory when is operating near sliding surface ( $\sigma_{wt}=0$ ), is the major drawbacks of the proposed SMC approach given in (6.48). Therefore, to eliminate this undesired chattering phenomenon, sliding layer concept is used as shown in Fig.6.15 and described below:

$$\text{sat}(\sigma_{wt}, \Phi) \begin{cases} 1 & \sigma_{wt} > \Phi \\ \frac{\sigma_{wt}}{\Phi} & |\sigma_{wt}| \leq \Phi \\ -1 & \sigma_{wt} < -\Phi \end{cases} \quad (6.61)$$

Or

$$\text{sat}(\sigma_{wt}, \Phi) = \begin{cases} \text{sign}(\sigma_{wt}) & |\sigma_{wt}| > \Phi \\ \frac{\sigma_{wt}}{\Phi} & |\sigma_{wt}| \leq \Phi \end{cases} \quad (6.62)$$

where  $\Phi$  represents the sliding layer, which is located between -0.5 and +0.5.

### WT current feedback

A new current control feedback, explained below, is added to the developed control algorithm for the WT side, which is used also to protect the BESS from the overvoltage by selecting automatically  $d_2$ . Based on this new current control feedback,  $\omega_r$  is increased or decreased depending on the required load demand. Therefore, the desired control is selected as follows:

$$\begin{cases} \text{if } \Delta v_{bat} > 0, d_{WT} \text{ is selected} \\ \text{if } \Delta v_{bat} < 0, d_2 \text{ is selected} \end{cases} \quad (6.63)$$

where  $d_2$  is the control law of the feedback current control, which is obtained using the following equation:

$$u_i = L \left( \frac{di_{WT}}{dt} \right) = v_{WT} - (1 - d_2)v_{out} \quad (6.64)$$

And

$$d_2 = 1 + \left( \frac{(u_{iWT} - v_{WT})}{v_{out}} \right) \quad (6.65)$$

where  $u_{iWT}$  is the output of the PI current controller.

#### 6.3.4 Control of CC-VSC

The block diagram of the proposed nonlinear control algorithm for load voltage and frequency regulation based on QLC controller is shown in Fig.6.17. The sensed load voltages and currents are transferred to the d-q rotating reference frame. The d-axis component of the load voltage is compared with its reference, and the q-axis reference is set equal to zero. The voltage errors are the inputs of the QLC controllers and the equivalent inputs are used to determine the control laws, which are obtained using the following equations.

$$\begin{cases} \left( \frac{di_{fa}}{dt} \right) = \left( \frac{1}{L_f} \right) (d_1 v_{dc} - v_{La}) \\ \left( \frac{di_{fb}}{dt} \right) = \left( \frac{1}{L_f} \right) (d_2 v_{dc} - v_{Lb}) \\ \left( \frac{di_{fc}}{dt} \right) = \left( \frac{1}{L_f} \right) (d_3 v_{dc} - v_{Lc}) \end{cases} \quad (6.66)$$

And

$$\begin{cases} \left(\frac{dv_{La}}{dt}\right) = \left(\frac{1}{C_f}\right)(i_{fa} - i_{La}) \\ \left(\frac{dv_{Lb}}{dt}\right) = \left(\frac{1}{C_f}\right)(i_{fb} - i_{Lb}) \\ \left(\frac{dv_{Lc}}{dt}\right) = \left(\frac{1}{C_f}\right)(i_{fc} - i_{Lc}) \end{cases} \quad (6.67)$$

where  $d_{123}$ ,  $v_{Labc}$ ,  $i_{fabc}$ ,  $C_f$ ,  $L_f$  denote the control laws, load voltages, inverter currents, the capacitance and the inductance of the output filter, respectively.

Replacing (6.66) in the derivative of (6.67), the following expressions are obtained:

$$\begin{cases} C_f \left(\frac{d^2v_{La}}{dt^2}\right) + \left(\frac{v_{La}}{L_f}\right) = \left(\left(\frac{d_1}{L_f}\right) - \left(\frac{di_{La}}{dt}\right)\right) \\ C_f \left(\frac{d^2v_{Lb}}{dt^2}\right) + \left(\frac{v_{Lb}}{L_f}\right) = \left(\left(\frac{d_2}{L_f}\right) - \left(\frac{di_{Lb}}{dt}\right)\right) \\ C_f \left(\frac{d^2v_{Lc}}{dt^2}\right) + \left(\frac{v_{Lc}}{L_f}\right) = \left(\left(\frac{d_3}{L_f}\right) - \left(\frac{di_{Lc}}{dt}\right)\right) \end{cases} \quad (6.68)$$

Applying Park's transformation given in (2.48) to (6.68), the following equation is obtained,

$$\begin{cases} u_d = \left(\frac{v_{dc}}{C_f L_f}\right) d_d + \left(\frac{1}{C_f}\right) \left(\frac{di_{Ld}}{dt}\right) - \left(\frac{\omega}{C_f}\right) i_{Ld} + 2\omega \left(\frac{dv_{Lq}}{dt}\right) \\ u_q = \left(\frac{v_{dc}}{C_f L_f}\right) d_q + \left(\frac{1}{C_f}\right) \left(\frac{di_{Lq}}{dt}\right) + \left(\frac{\omega}{C_f}\right) i_{Lq} - 2\omega \left(\frac{dv_{Ld}}{dt}\right) \end{cases} \quad (6.69)$$

And

$$\begin{cases} u_d = \left( \frac{d^2 v_{Ld}}{dt^2} \right) + \left( \left( \frac{1}{C_f L_f} \right) - \omega^2 \right) v_{Ld} \\ u_q = \left( \frac{d^2 v_{Lq}}{dt^2} \right) + \left( \left( \frac{1}{C_f L_f} \right) - \omega^2 \right) v_{Lq} \end{cases}$$

where  $u_d$  and  $u_q$  are the new equivalent inputs. Based on (6.69), the control laws are obtained as follows,

$$\begin{cases} d_d = \left( \frac{L_f}{v_{dc}} \right) \left[ \left( \frac{u_d}{C_f} \right) - \left( \frac{di_{Ld}}{dt} \right) + (\omega i_{Ld}) - \frac{2\omega}{C_f} \left( \frac{dv_{Lq}}{dt} \right) \right] \\ d_q = \left( \frac{L_f}{v_{dc}} \right) \left[ \left( \frac{u_q}{C_f} \right) - \left( \frac{di_{Lq}}{dt} \right) - (\omega i_{Lq}) + \frac{2\omega}{C_f} \left( \frac{dv_{Ld}}{dt} \right) \right] \end{cases} \quad (6.70)$$

where  $d_{dq}$  are the control laws in d-q frame.

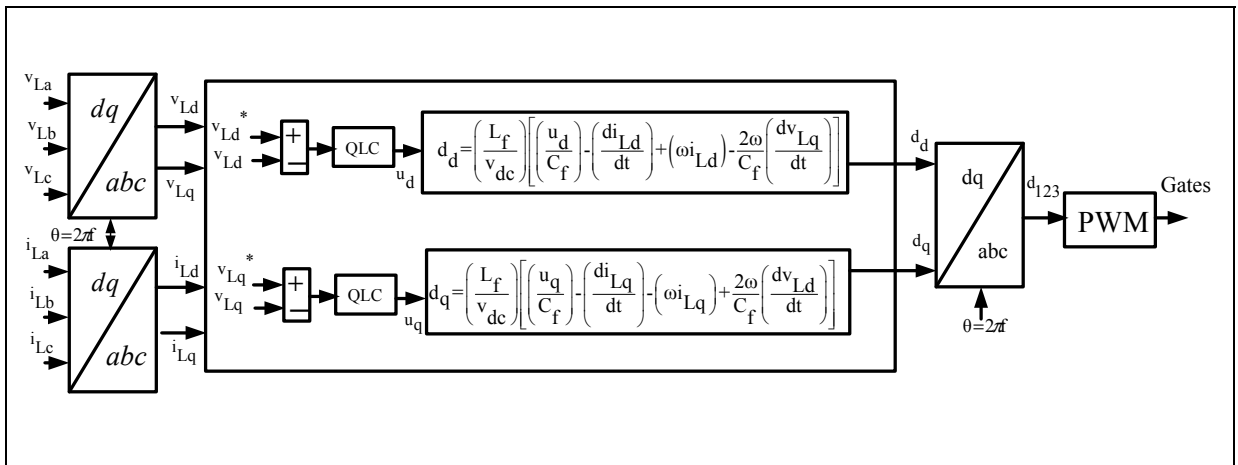


Figure 6.17 QLC based proposed control algorithm of CC-VSC

The transfer functions in open loop  $G_{dq}(s)$  of the equivalent inputs  $u_{dq}$  are as follow,

$$\begin{cases} G_d = \left( \frac{v_{Ld}(s)}{u_d(s)} \right) = \frac{1}{(s^2 + 1.998 \cdot 10^7)} \\ G_q = \left( \frac{v_{Lq}(s)}{u_q(s)} \right) = \frac{1}{(s^2 + 1.998 \cdot 10^7)} \end{cases} \quad (6.71)$$

QLC is defined by its general form given in (6.72) to obtain a fast dynamic response (Kelemen et Bensoussan, 2004)

$$G(s) = K \left( \frac{\prod_{i=1}^{d-1} (s + z_i)}{\prod_{i=1}^{d-1} (s + a_i k^f)} \right) \quad (6.72)$$

where,  $K$  is positive gain and is as large as possible to ensure the stability of the system in closed loop.  $a_i$  and  $z_i$  are lead/lag elements and they are small real positive, and  $f$  is an exponent. Therefore, the transfer functions in closed loop  $T_{dq}(s)$  are expressed as follows,

$$\begin{cases} T_d(s) = \frac{G_o(s)}{1 + G_o(s)} = \frac{K(s + z)}{s^3 + aK^f s^2 + s(K + 1.998 \cdot 10^7) + Kz + 1.998 \cdot 10^7 aK^f} \\ T_q(s) = \frac{G_o(s)}{1 + G_o(s)} = \frac{K(s + z)}{s^3 + aK^f s^2 + s(K + 1.998 \cdot 10^7) + Kz + 1.998 \cdot 10^7 aK^f} \end{cases} \quad (6.73)$$

The QLC parameters have been chosen according to the guideline given in (Kelemen et Bensoussan, 2004). Therefore, the exponent ( $f$ ), the parameters ( $k$ ) and ( $a$ ) are chosen for optimal dynamic response.

## 6.4 Simulation results and discussion

### 6.4.1 Performance of HSPGS based on solar PV array and WT driven fixed speed SCIG

#### Performance analysis under sudden variation of the wind velocity and solar irradianations when SOC% of BESS is less than 100%

Simulation is carried out using MATLAB/Simulink in order to test the performance of the proposed PV-WT HSPGS shown in Fig.6.3 during fluctuation of wind/solar/load. The system parameters are summarized in Appendix Table A-6.

The waveforms of the AC voltage ( $v_L$ ), WT current ( $i_{WT}$ ), load current ( $i_L$ ), output DC-AC inverter current ( $i_{inv}$ ), PV current and its reference ( $i_{pv}$  &  $i_{pvref}$ ), mechanical torque developed by the WT, DC-link voltage ( $V_{dc}$ ), state of charge of battery (SOC%) and system frequency ( $f_s$ ) when the SOC% is greater than 50% are shown in Fig.6.18. It is observed that the AC voltage and the system frequency are kept constant during: 1) decreasing of the output PV current, and 2) decreasing of the WT current. It is observed that between  $t=0$  s and  $t=0.8$  s, the sum of currents provided by PV and WT ( $i_{WT}+i_{pv}$ ) is greater than the load current and that is why BESS is charging. It is observed that the PV current follows its reference when the solar irradianations vary, which confirms the robustness of the proposed MPPT method. At  $t=0.8$  s the wind speed is decreased to 9.5 m/s, and that is why the mechanical torque is decreased to (-50) N.m. From  $t=0.8$  s the sum of currents ( $i_{WT}+i_{pv}$ ) becomes less than load current ( $i_L$ ), the difference of current in this case is provided by the BESS. It is observed that PV-WT HSPGS stays stable during the transition period and load is supplied without disruption. This confirms the accuracy of the proposed control approaches and the robustness of the PV-WT HSPGS against severe conditions.

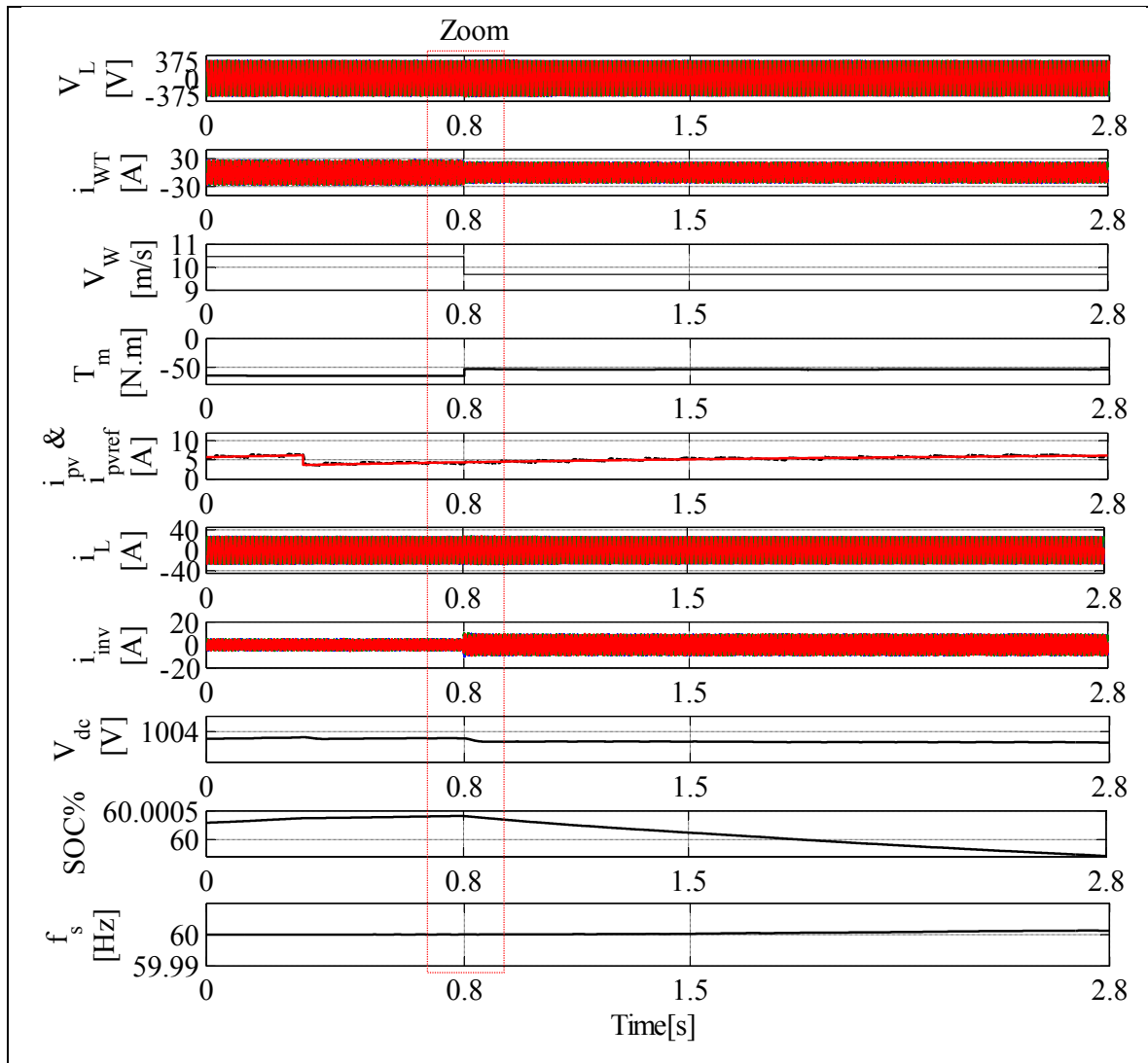


Figure 6.18 Dynamic performance of the PV-WT HSPGS based on fixed speed SCIG under weather conditions change

Fig. 6-19 shows the zoom of the waveforms shown in Fig.6-18 between  $t=0.75$  s and  $0.85$  s. The system frequency and the AC voltage at the PCC are regulated at their rated values. The proposed control for the interfacing inverter has responded instantaneously when the wind velocity is decreased at  $t=0.8$  s. It is observed that the steady state error of AC voltage at  $t=0.8$  s is equal to zero and the load current is not affected, which confirms the smooth functioning of our proposed PV-WT HSPGS, as well as the proposed control algorithms.

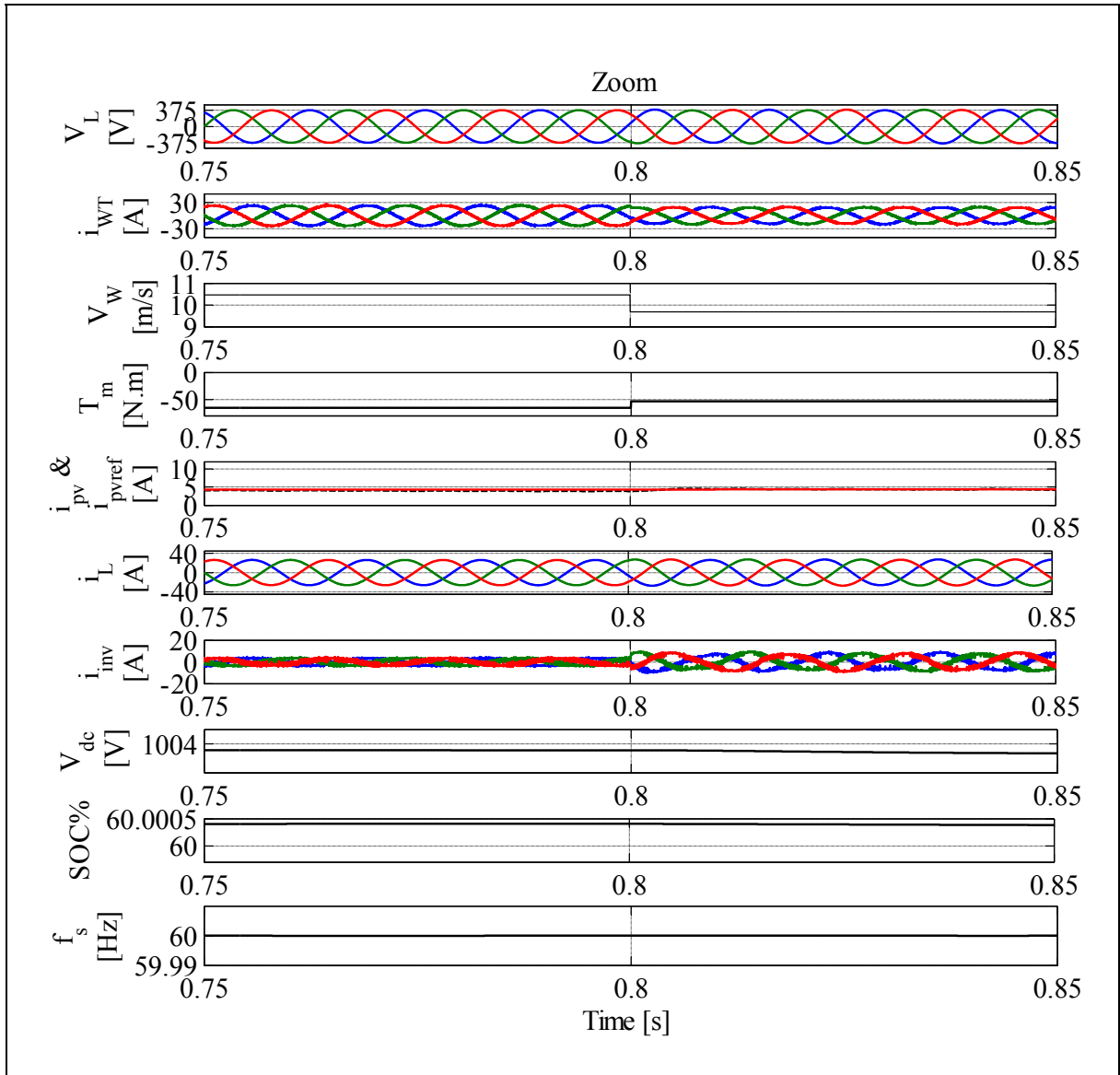


Figure 6.19 Zoom of the results shown in Fig 6.18 between t=0.75 s and t=0.85s

**Performance analysis under balanced and unbalanced nonlinear load when the SOC% of BESS is less than 100%**

Fig.6.20 show the simulation results of the AC voltage ( $v_L$ ), WT current ( $i_{WT}$ ), load current ( $i_L$ ), inverter current ( $i_{inv}$ ), PV current and its reference ( $i_{pv}$  &  $i_{pvref}$ ), mechanical torque developed by the WT ( $T_m$ ), DC-link voltage ( $V_{dc}$ ), state of charge of battery (SOC%) and

system frequency ( $f_s$ ) when the SOC% is less than 100% and during fixed wind speed and fixed solar irradianations.

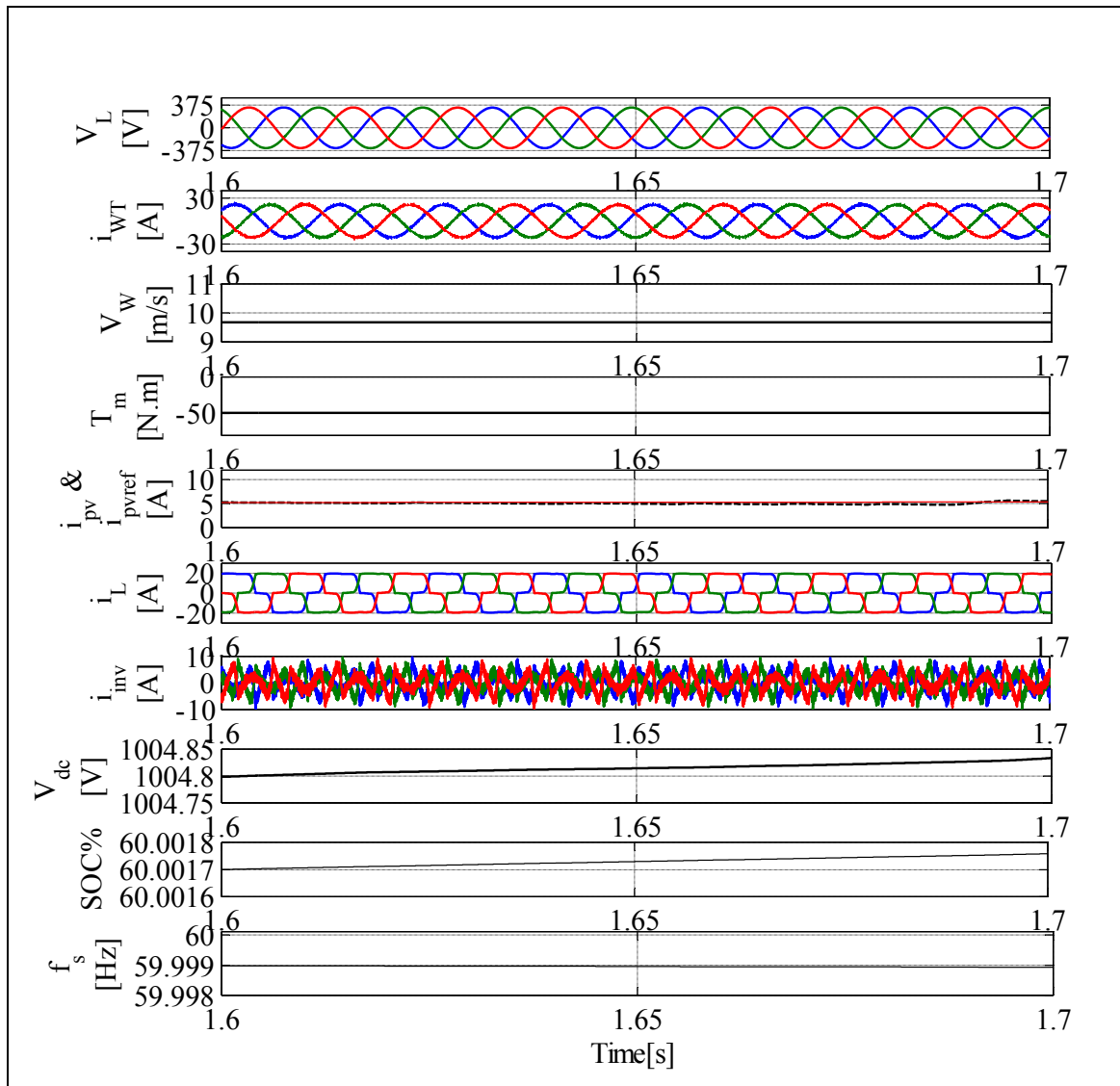


Figure 6.20 Steady state performance of PV-WT HSPGS employing fixed speed SCIG under balanced nonlinear load

It is observed in Figs. 21 and 22 that the AC voltage and the system frequency at the PCC are kept constant during presence of balanced and unbalanced nonlinear load. Furthermore,  $i_{WT}$  and  $v_L$  are balanced and their waveforms are purely sinusoidal. It is observed that the DC/AC

inverter is able to simultaneously compensate current harmonics and balance the wind turbine current.

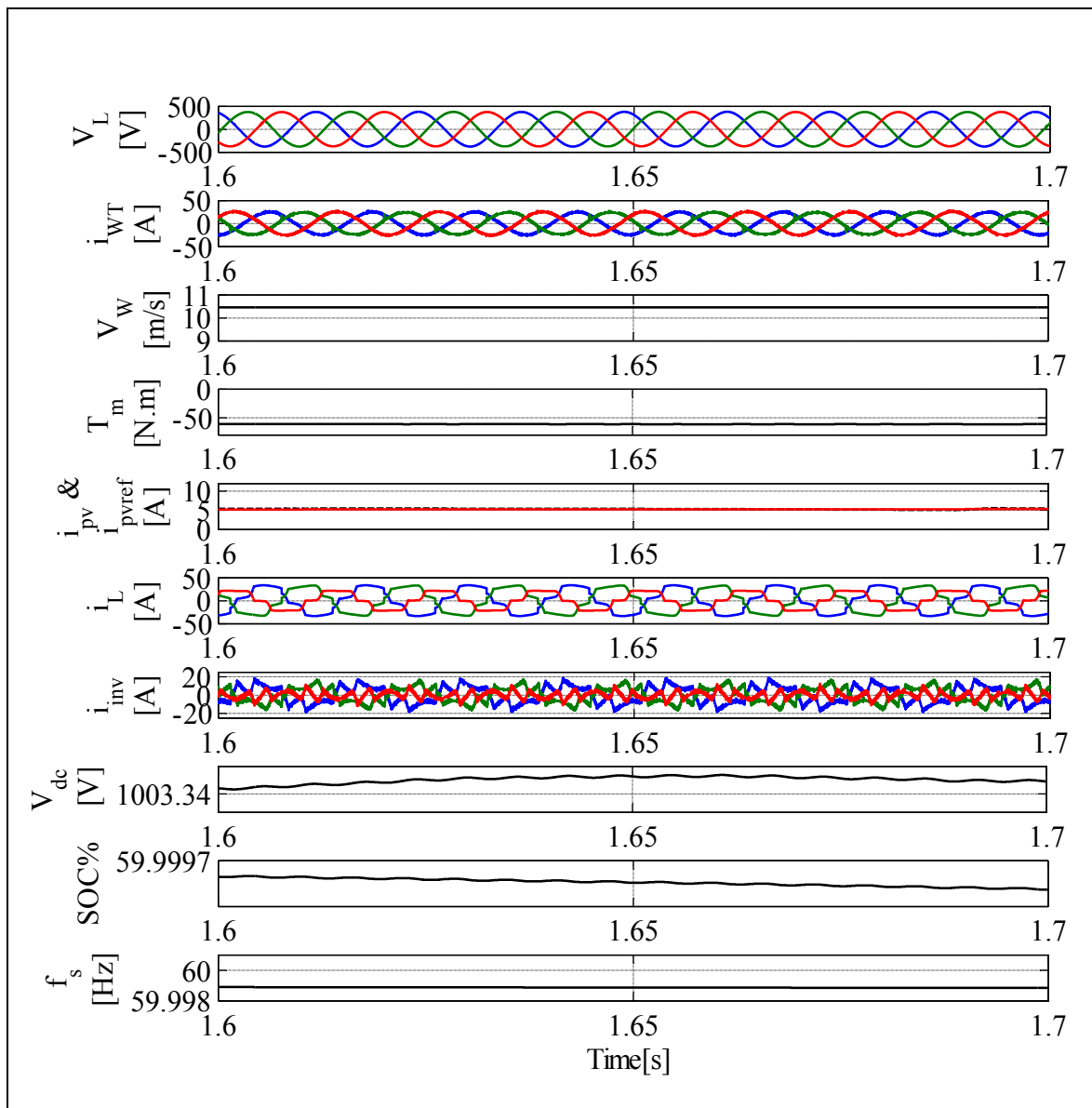


Figure 6.21 Steady state performance of PV-WT HSPGS employing fixed speed SCIG under unbalanced nonlinear load

**Performance analysis when the SOC% of BESS is equal to 100%**

Fig. 6.22 shows the waveforms of AC voltage ( $v_L$ ), system frequency ( $f_s$ ), DC voltage ( $V_{dc}$ ), state of charge battery (SOC%), power provided by WT ( $P_{WT}$ ), power provided by solar PV array ( $P_{pv}$ ), consumed power by load ( $P_L$ ), BESS power, and that dissipated in dump loads ( $P_d$ ) when the BESS becomes fully charged.

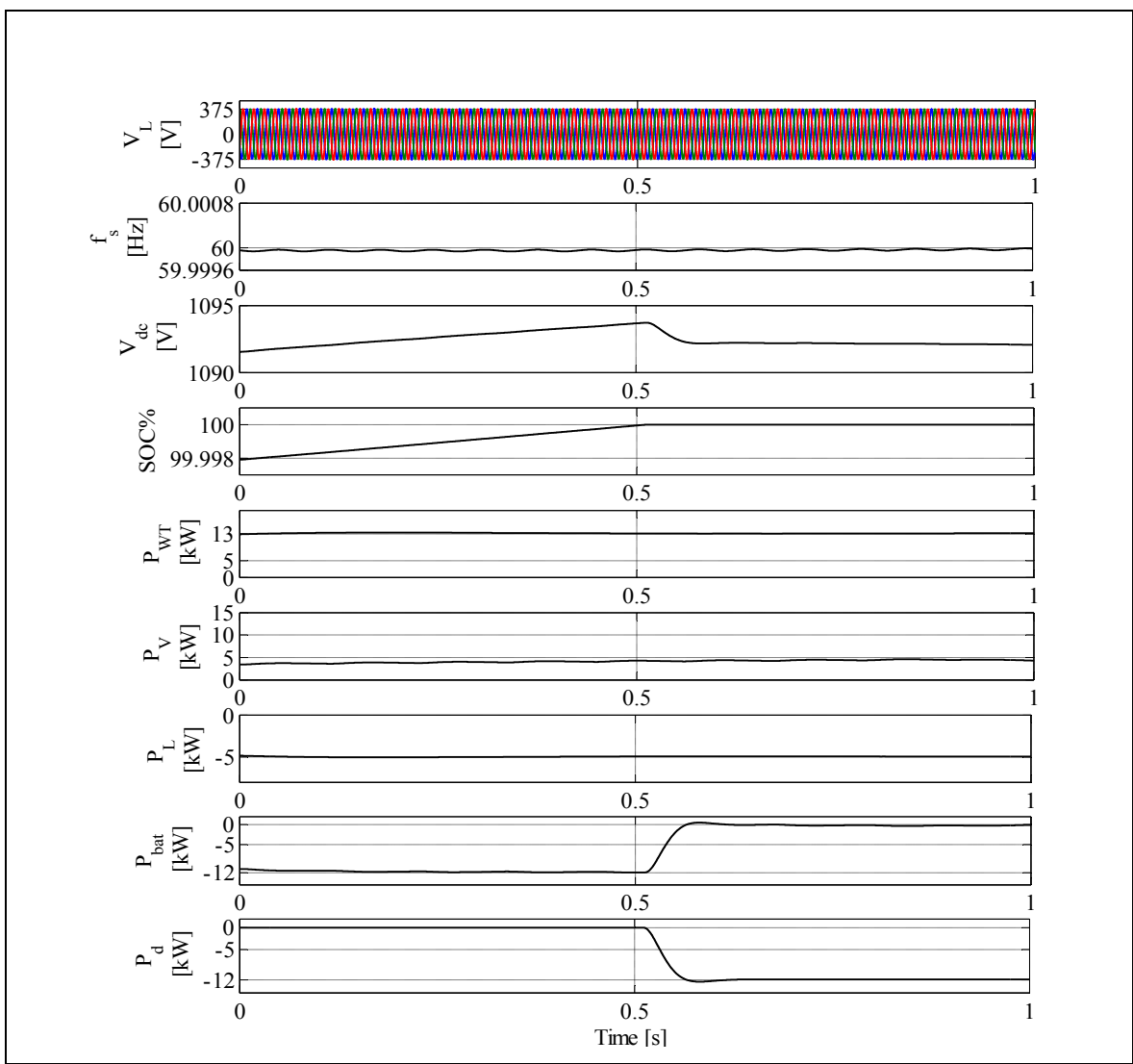


Figure 6.22 Dynamic performance of the PV-WT HSPGS employing fixed speed SCIG when SOC% is equal to 100%

It is observed that from  $t = 0$  s to  $t = 0.5$  s, the sum of power provided by RES ( $P_{pv} + P_{WT}$ ) is greater than consumed power load ( $P_L$ ). The extra power is used to charge the battery and that is why dump load is not operating ( $P_d=0$ ). From  $t=0.5$  s to  $t = 1$  s the SOC% of BESS becomes equal to 100%, and the DC voltage reach its maximum, which is equal to 1091. Therefore, conditions to put on dump load are fulfilling. To protect the BESS from overcharging, the extra power is dissipated in dump load. The DC link, which is equal to battery voltage ( $v_{bat}$ ), is kept constant and the AC voltage and the system frequency are regulated at their rated values. This confirms that BESS is protected against overcharging.

#### **6.4.2 Performance of HSPGS system based on solar PV array and WT driven variable speed SyRG**

Simulations are carried out using MATLAB/Simulink in order to test the performance of the proposed PV-WT HSPGS employing variable speed SyRG as shown in Fig.6.7, as well as their proposed control algorithms. The system parameters values are given in Table A-7 in Appendix. Several scenarios such a, sudden change of the solar irradiations, wind speed, as well as, variation of loads are tested. In addition, these tests are realized when the SOC% of BESS is equal or less than 100%.

#### **Performance analysis under fixed linear load and weather conditions change when the SOC% of BESS is less than 100%**

Fig. 6.23 shows the simulation results of the AC voltage ( $v_L$ ), load current ( $i_L$ ), system frequency ( $f_s$ ), wind speed ( $V_{wind}$ ), mechanical torque developed by the WT ( $T_{mec}$ ), SyRG rotor speed and its reference ( $\omega_r$  and  $\omega_{ref}$ ), output WT current ( $i_{WT}$ ), output PV current and its reference ( $i_{pv}$  and  $i_{pvref}$ ), DC-bus voltage ( $v_{dc}$ ) and the state of charge of battery (SOC%). It is observed that the output PV current is increased at  $t=0.4$  s and is increased more at  $t=0.9$  s. However, the stator current of the SyRG varies with the variation of the wind speed is decreased at  $t=0.4$  s and decreased more at  $t=0.9$  s. It is observed that  $i_{pv}$  follows  $i_{pvref}$  and  $\omega_r$  follows  $\omega_{ref}$  during change of solar irradiations and wind speed. This confirmed that the developed control algorithms for the DC/DC boost converter and the AC/DC converter,

which are based on P&O technique and optimal WT power characteristic, provide better MPPT performance.

Furthermore, The AC voltage and the system frequency at the PCC are regulated at their rated values, which involve the smooth functioning of the proposed indirect control algorithm. Seeing that  $(i_{WT} + i_{pv}) > (i_L)$ , the extra power is used to charge the BESS. For this reason the SOC% is increased.

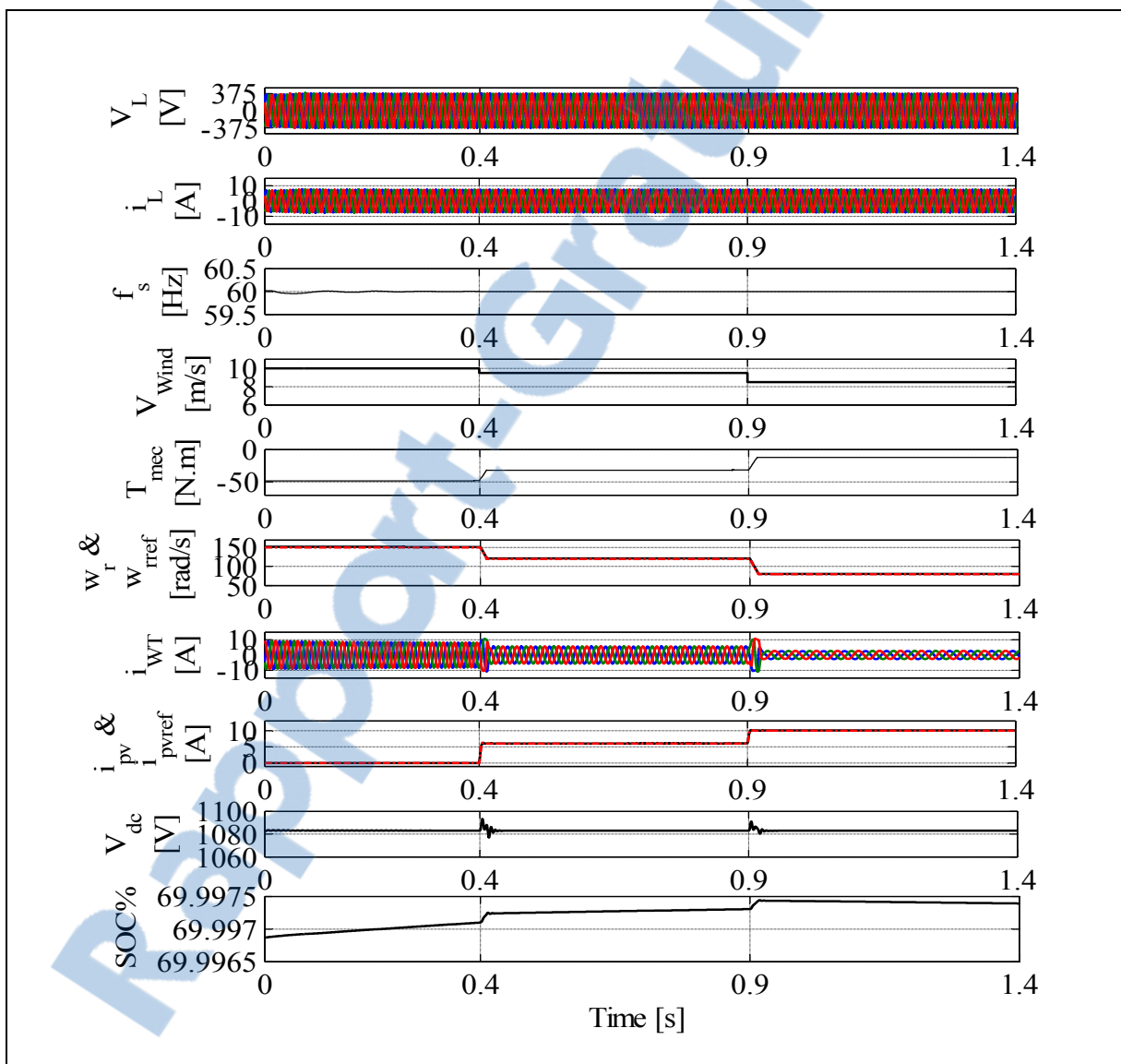


Figure 6.23 Dynamic performance of PV-WT HSPGS employing variable speed SyRG under weather conditions change

**Performance analysis under fixed weather conditions and load change when the SOC% of BESS is less than 100%**

Waveforms in Fig.6.24 show the AC voltage ( $v_L$ ), load current ( $i_L$ ), system frequency ( $f_s$ ), SyRG output current ( $i_{WT}$ ), output PV current and its reference ( $i_{pv}$  &  $i_{pvref}$ ), and the state of charge of BESS (SOC%). It is observed that from  $t=0$  s to  $t=0.15$  s and from  $t=0.65$  s to  $t=0.85$  s, load is completely removed but  $v_L$  and  $f_s$  are maintained at their reference value of 375V and 60Hz, respectively. Linear load is connected to the system at  $t=0.15$  s and disconnected at  $t=0.45$  s, and an unbalancing in loads is created when phase «a» of dynamic load is switched off from  $t=0.35$  s to 0.45 s. It is observed that even during unbalanced load condition,  $v_L$  is balanced and sinusoidal with zero steady-state error.

**Performance analysis under fixed weather conditions and nonlinear load change when the SOC% of BESS is less than 100%**

Fig.6.25 depicts the dynamic performance of the DC/AC interfacing inverter under balanced and unbalanced nonlinear load. It is observed that from  $t=0$  s to  $t=0.15$  s and from  $t=0.65$  s to  $t=0.85$  s, load is completely removed but the AC voltage and the system frequency are maintained at their reference value of 375V and 60Hz, respectively. Nonlinear load is connected to the system at  $t=0.15$  s and disconnected at  $t=0.45$  s, and an unbalancing in loads is created when phase «a» of dynamic load is switched off from  $t=0.35$  s to 0.45 s. It is observed that during unbalanced load condition, AC voltage is balanced and sinusoidal with zero steady-state error.

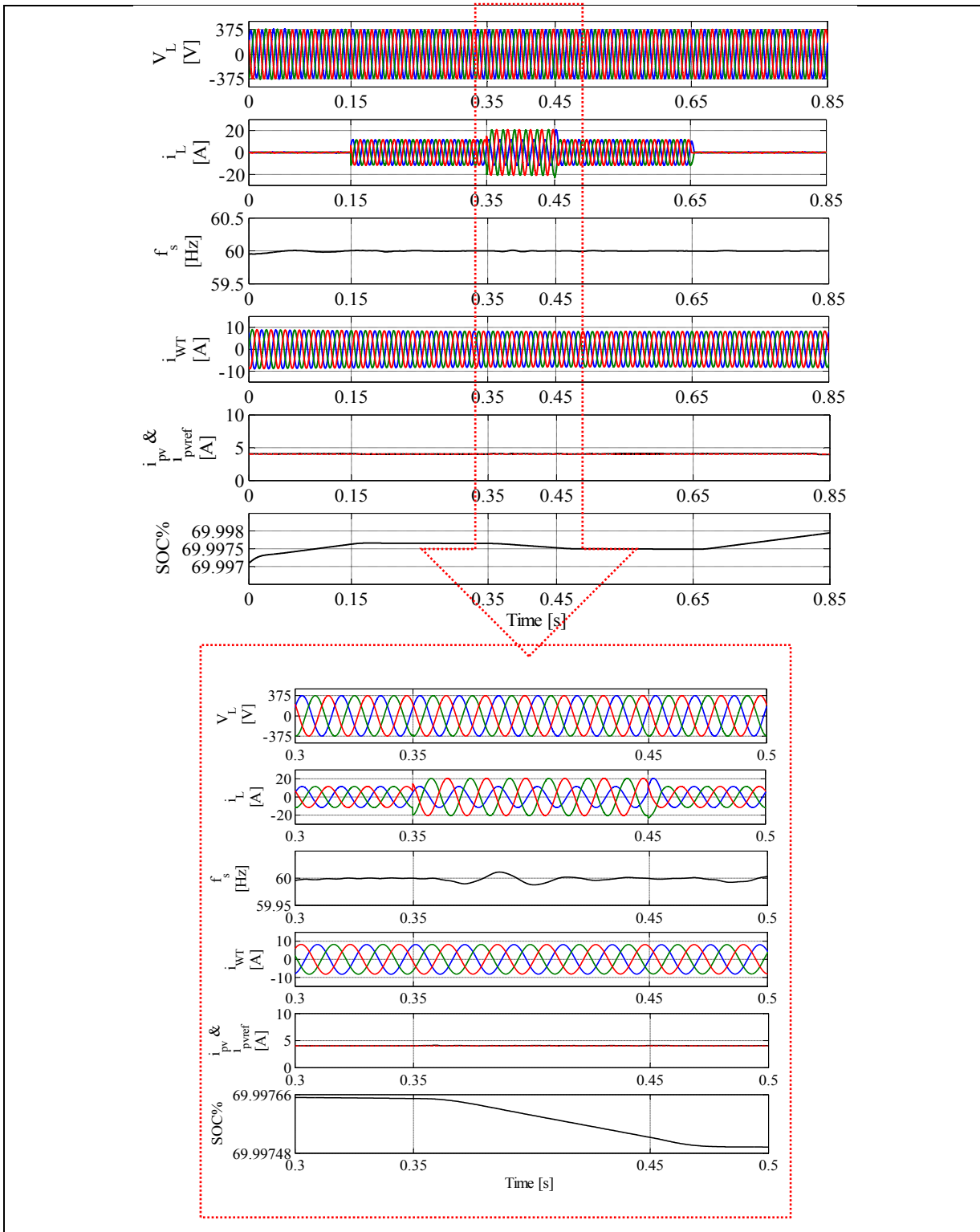


Figure 6.24 Dynamic performance of PV-WT HSPGS employing variable speed SyRG under balanced and unbalanced linear load

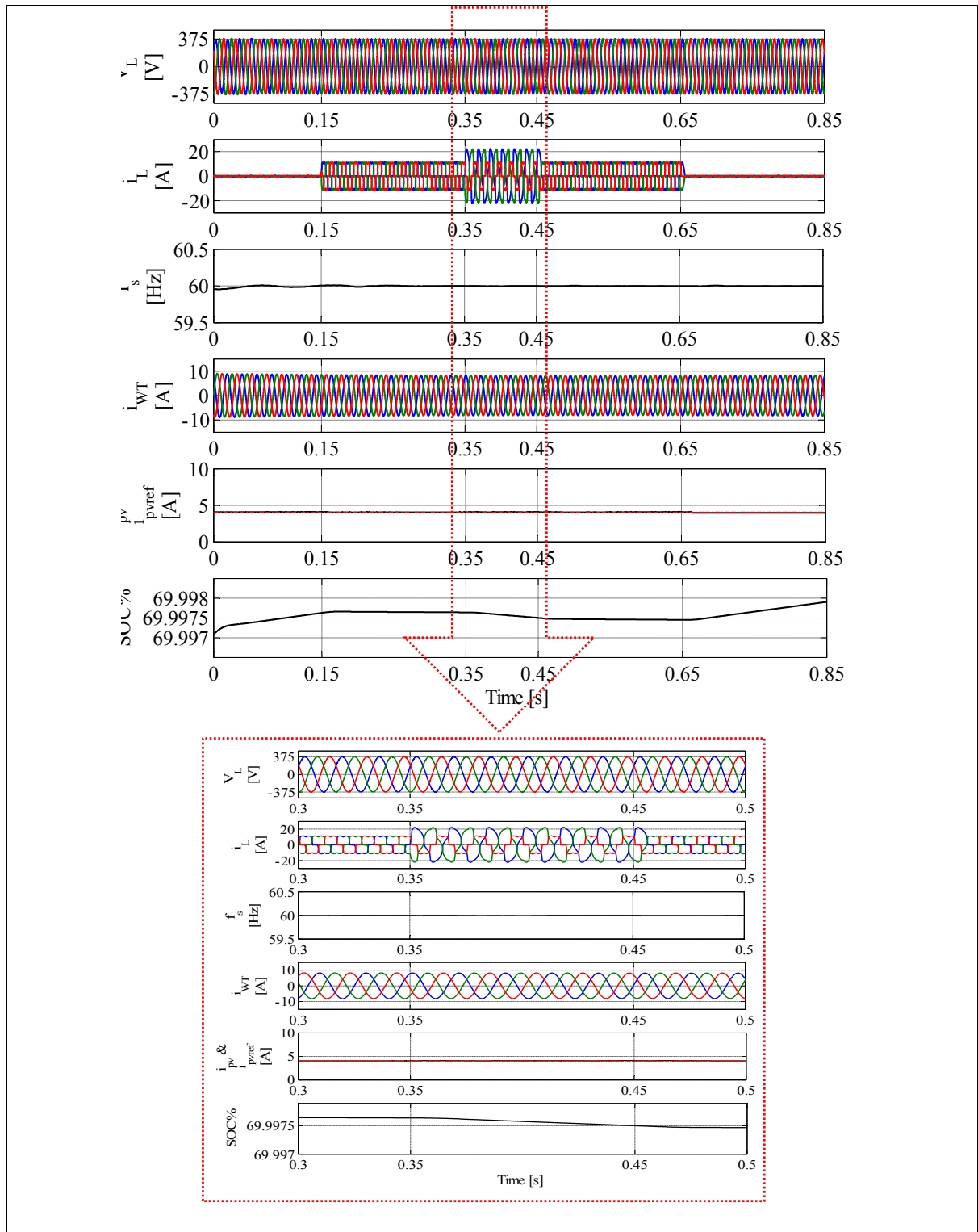


Figure 6.25 Dynamic performance of PV-WT HSPGS employing variable speed SyRG under balanced and unbalanced nonlinear load

**Performance analysis under load and weather conditions change when the SOC% is equal to 100%**

Fig.6.26 shows the waveforms of the AC voltage, system frequency, and state of charge of battery, WT power, PV power, battery power, dump load power and load demand power. It is observed that at  $t=25$  s, BESS becomes fully charged and the total power provided by the WT and PV array is greater than the load demand power and that is why from  $t=0.25$ s dump-load is turned on immediately. It is observed that from  $t=0.25$ , DC link voltage ( $v_{dc}$ ), which represents the BESS voltage, is kept constant, BESS power is equal to zero ( $P_{bat}$ ) and dump load power ( $P_d=P_{pv}+P_{WT}$ ), which confirms the robustness of the proposed approach to protect BESS from overcharging.

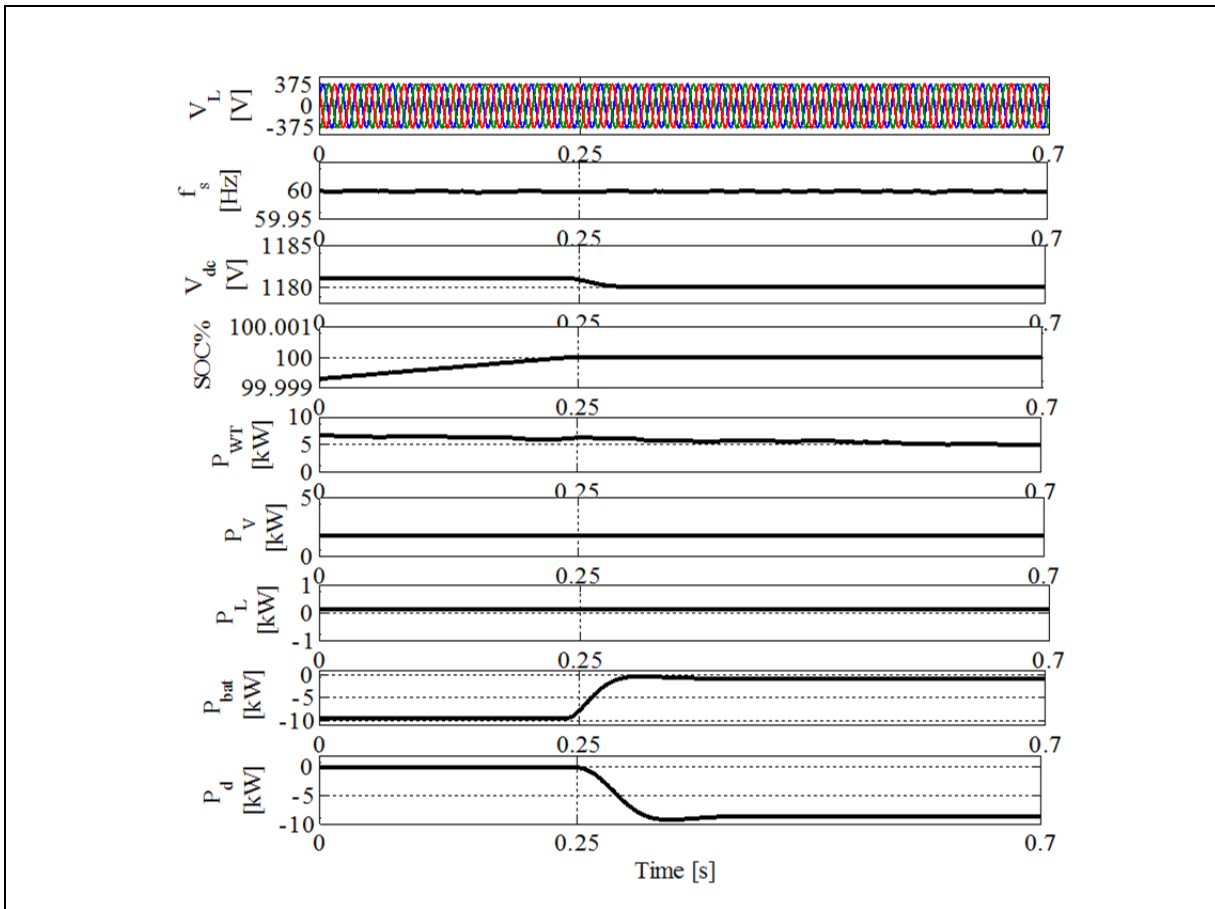


Figure 6.26 Dynamic performance of PV-WT HSPGS employing variable speed SyRG when SOC% of BESS becomes equal to 100%

### 6.4.3 Performance of HSPGS based on solar PV array and WT driven variable speed PMLDCG

#### 6.4.3.1 Simulation results

To test the performance of the proposed control algorithms for the PV-WT HSPGS as shown in Fig.6.11, simulations are carried out using Matlab/Simulink. Figs.6.27 shows the overall simulation of the terminal load voltage and current and their zooms in the presence of several scenarios: a) and b) sudden linear load variation, c) disconnecting of one phase of the linear load, d) unbalanced nonlinear load, e) nonlinear load, f) removed loads. It is observed that the linear load is increased and decreased by 50% at  $t=0.15$ s and  $t=0.4$  s, respectively. At  $t=0.6$ s one phase is removed and between 0.8s to 1.2s unbalanced and balanced nonlinear loads are connected and after 1.2 s all loads are removed. It is observed that for all the tests, the proposed nonlinear control algorithm using QLC controller confirms the fast dynamic response and zero steady state error in the load voltage in the presence of all conditions.

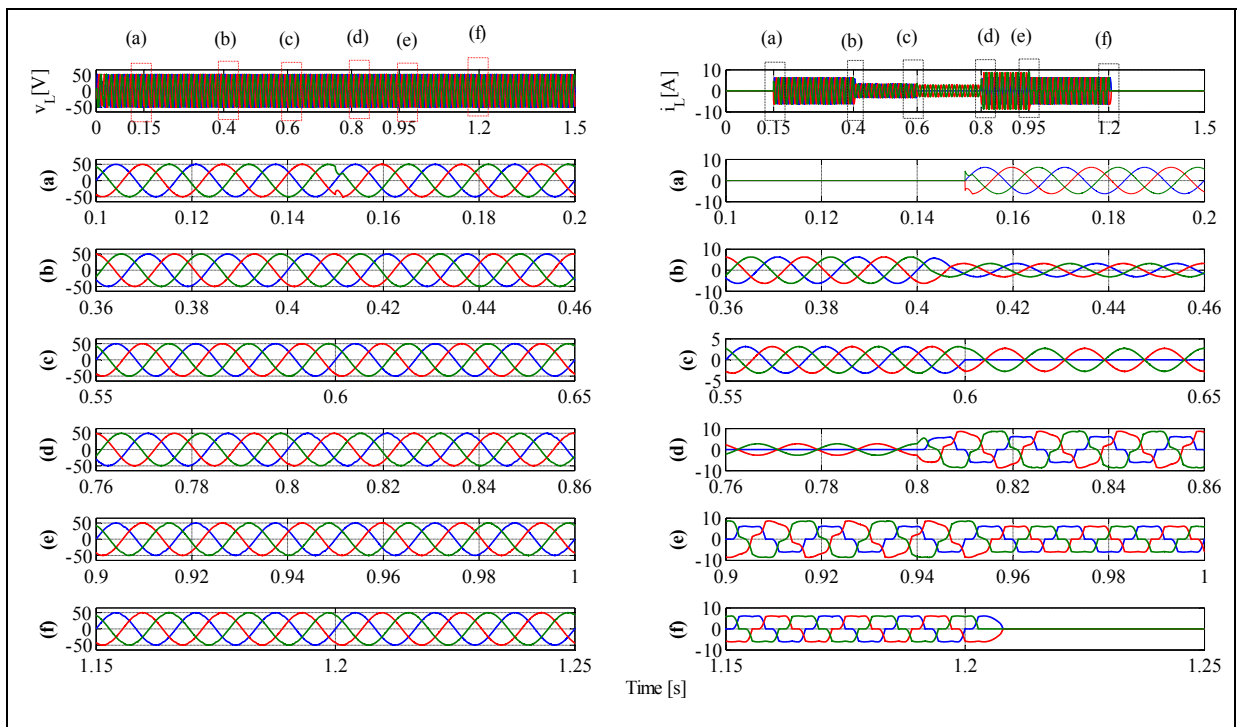


Figure 6.27 Dynamic performance of PV-WT HSPGS under load variation

Figs.6.28 (a) and (b) show the simulation results of the WT, solar PV array and BESS. It is observed in Fig .6.28 (a) that the stator currents of the PMPBLDCG vary with variation of the rotor speed. The dc voltage stays constant during the variation of the rotor speed but the dc current varies. Regarding the results given in Fig.6.32 (b), it is observed that the output PV current varies with variation of insolation, the dc voltage is almost staying constant and the sign of the BES current (discharge and charge) is related to the power provided by the WT and the PV array and that consumed by the loads.

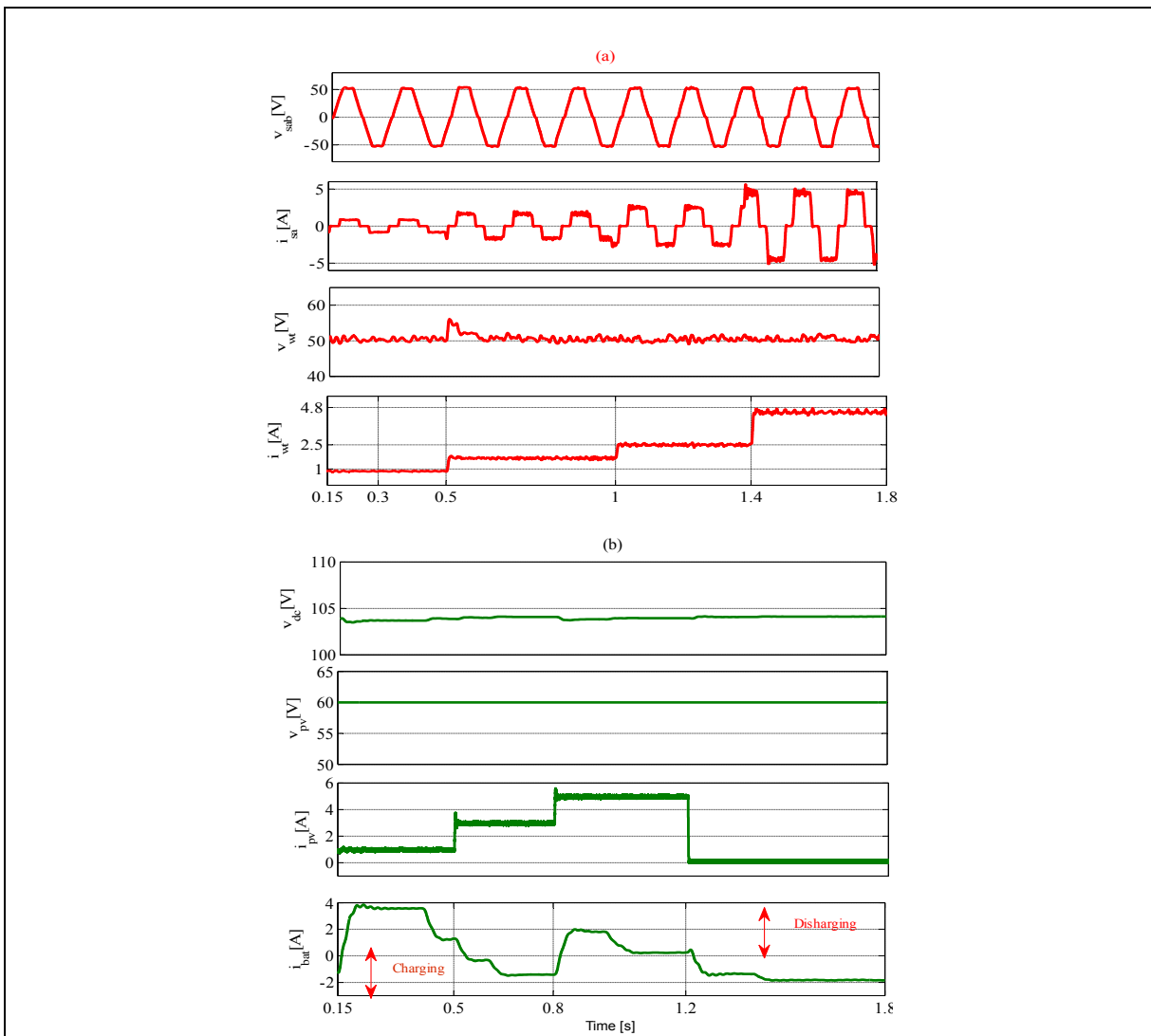
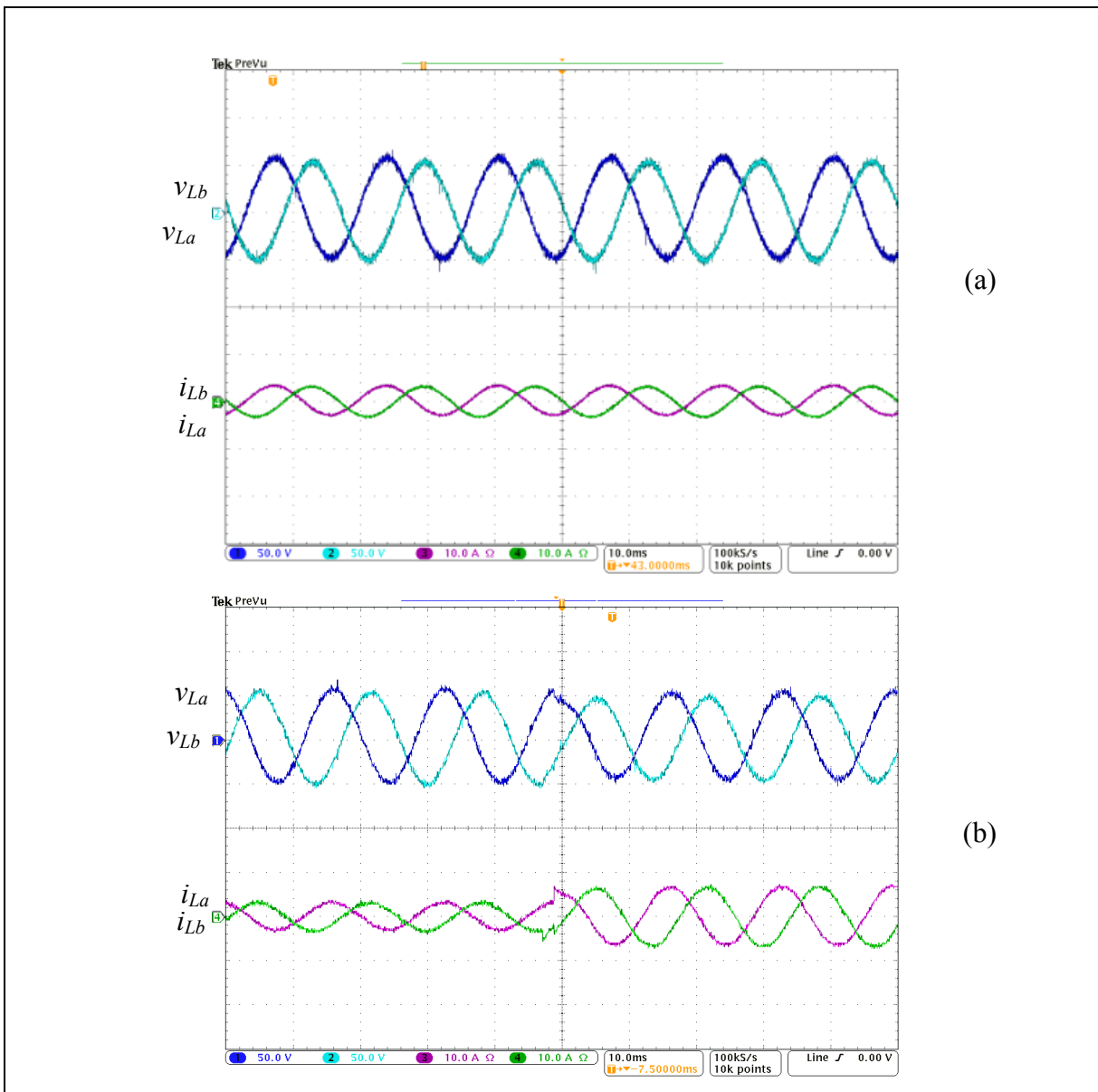


Figure 6.28 Dynamic performance of: a) PMPBLDCG under wind speed variation  
 b) solar PV array and solar irradianations change



Figs.6.30 shows the experimental results of the load voltages and currents under presence of different kinds of loads; a) linear load, b) sudden linear load variation, c) removal of one phase of linear load, d) complete removal of linear load and nonlinear load. It is observed that the voltages are maintained constant during all tests and reach their desired value within less than two cycles. The obtained simulation results were validated experimentally, which confirms the effectiveness of the proposed control algorithm for voltage and frequency regulation.



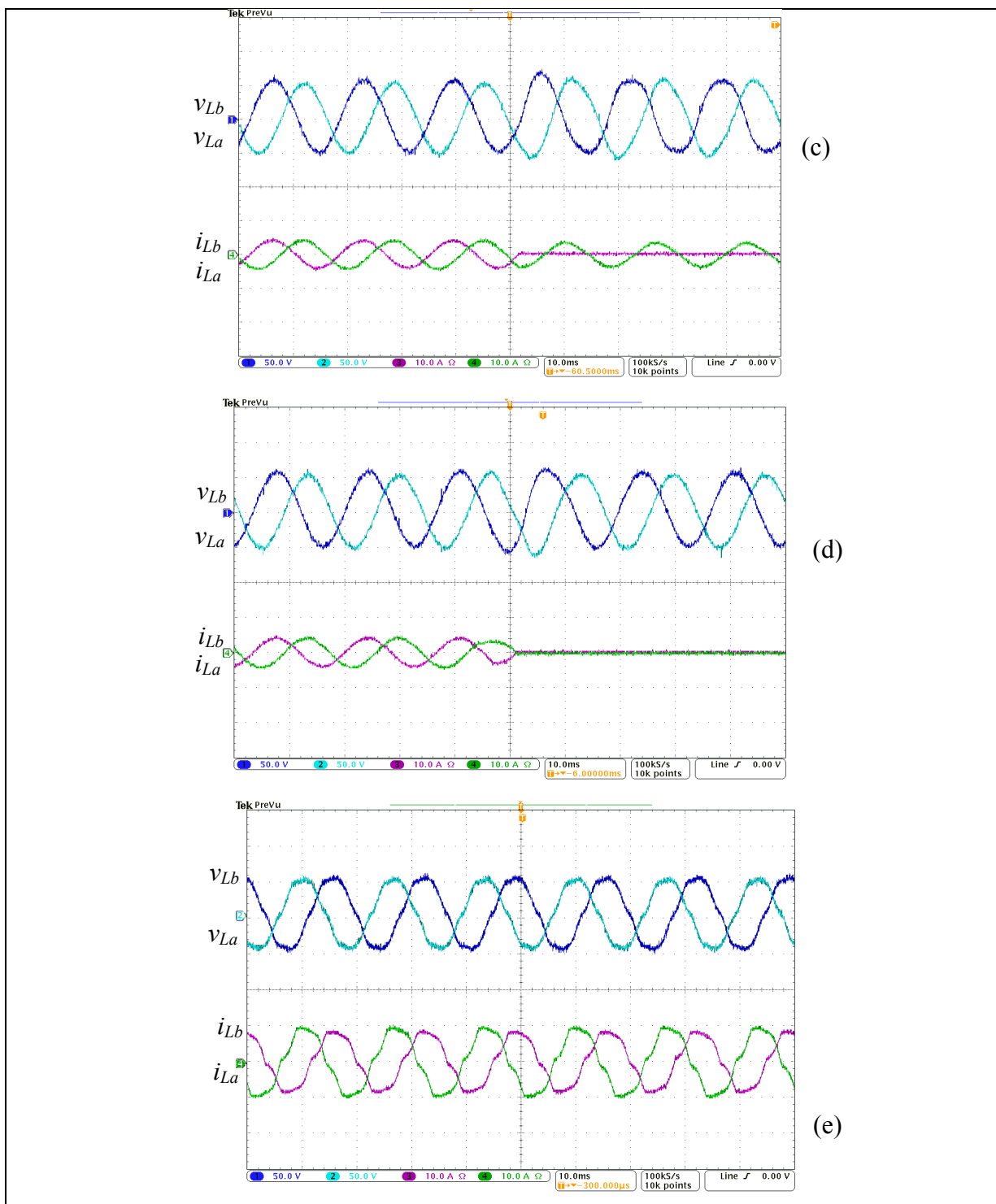


Figure 6.30 Dynamic performance of the proposed PV-WT HSPGS employing variable speed PMBLDCG under load change

Figs.6.31 shows the experimental results of: a) voltage and current in ac and dc sides of the WT and their zoom in b). It is observed that the dc voltage  $v_{WT}$  stays constant, the stator currents  $i_s$  and dc current  $i_{WT}$  varies with the variation of the rotor speed. We observe that the obtained experimental results are similar to the simulation results shown in Fig.6.32 (a).

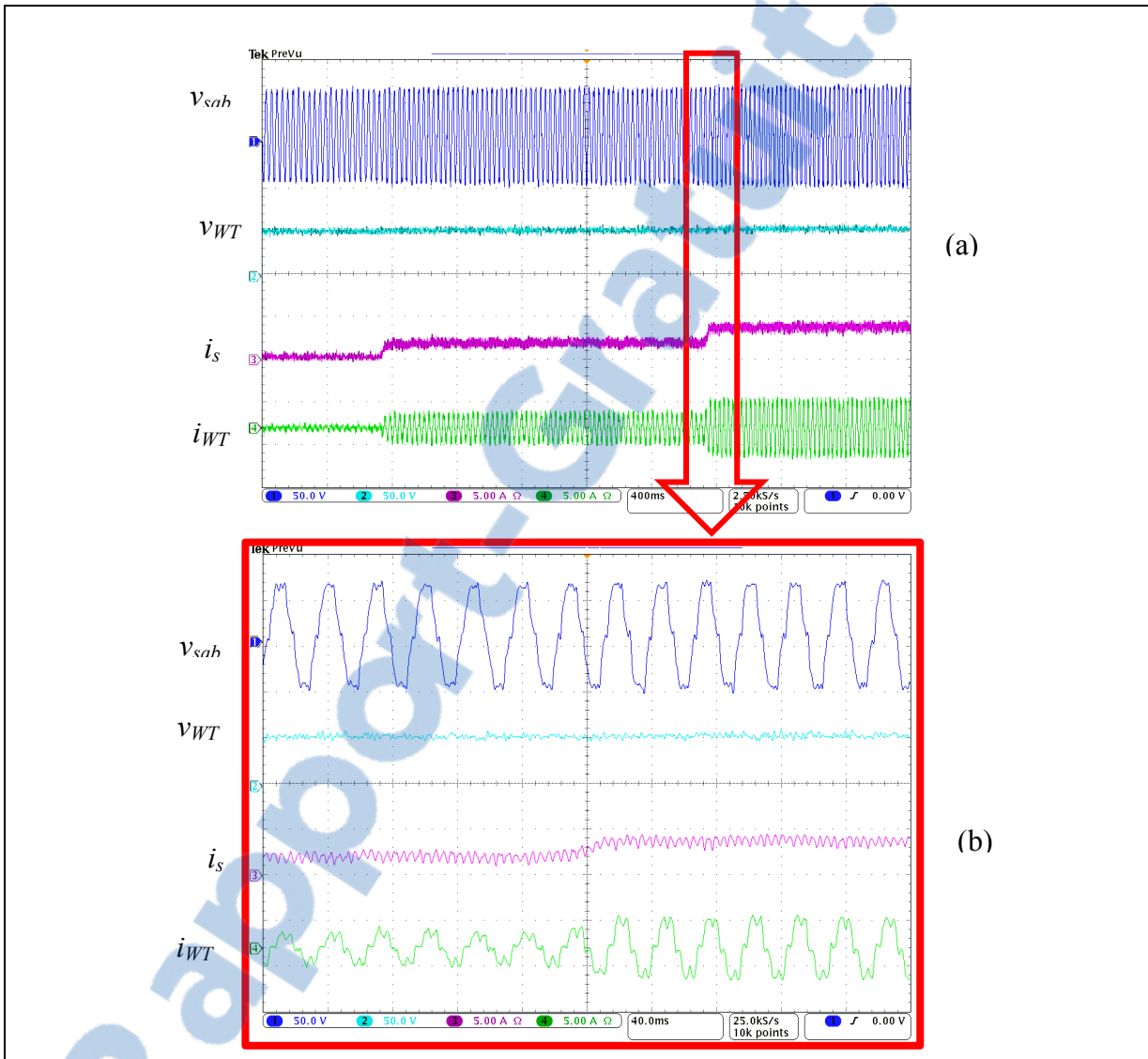
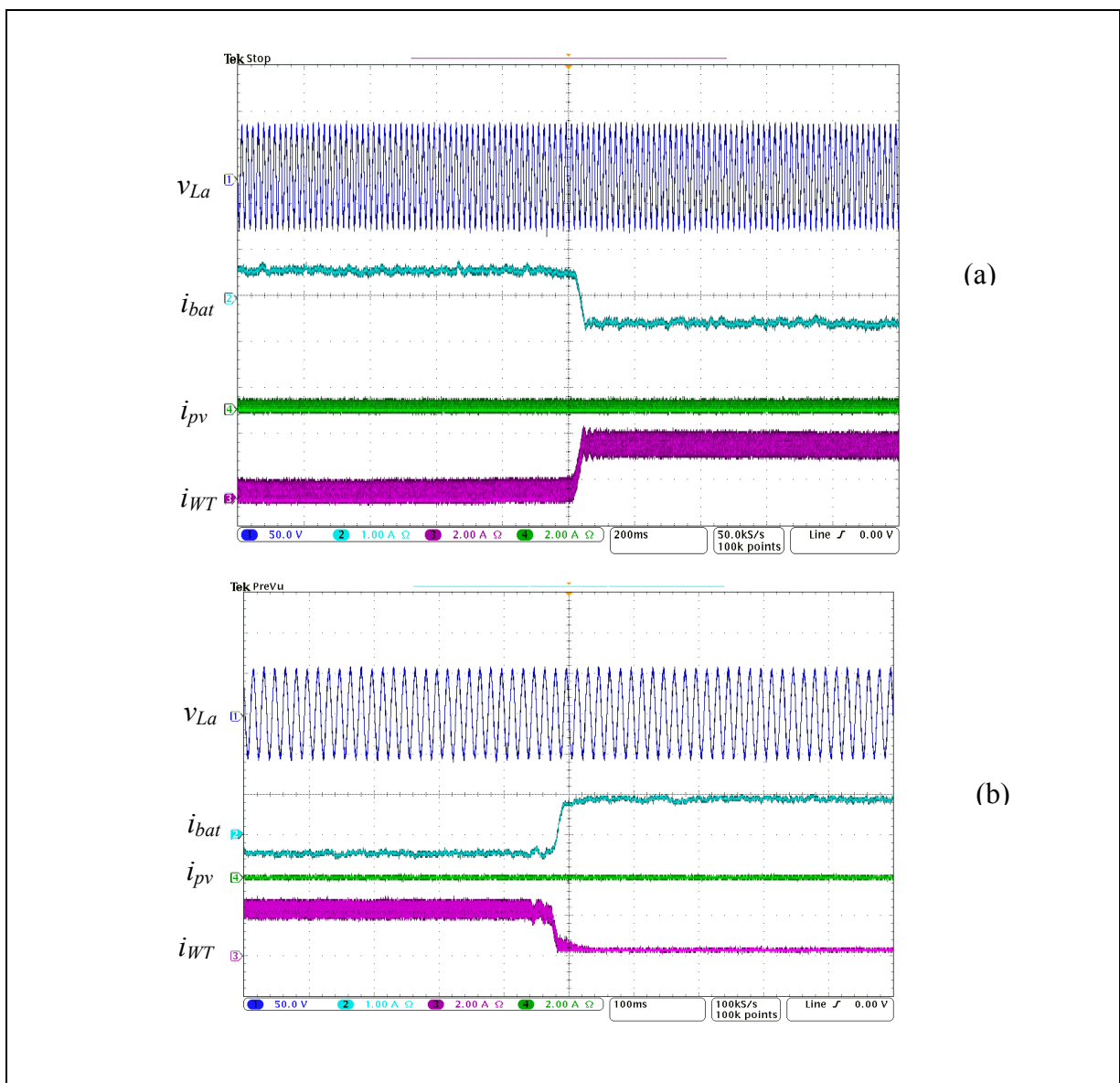


Figure 6.31 Dynamic performance of the PMBLDCG under wind speed variation

Figs.6.32. shows the load voltage, battery current, dc output current of the solar PV and the WT. To confirm the robustness of the proposed control algorithms for the solar PV and the

WT, several scenarios have been tested: a) absence of the solar insolation and wind speed in the beginning and sudden increase of wind speed, b) absence of the solar insolation and sudden decreasing of the wind speed, c) absence of the wind speed and sudden decrease of the insolation, d) presence of the wind speed and insolation at the beginning and sudden decreasing of insolation. It is observed in all the operating conditions, load voltage stays sinusoidal and its magnitude is kept constant, the charge and discharge of BESS depends on the load power demanded and the generated power. The transient and steady-state performances are good with fast transient responses and zero steady-state errors.



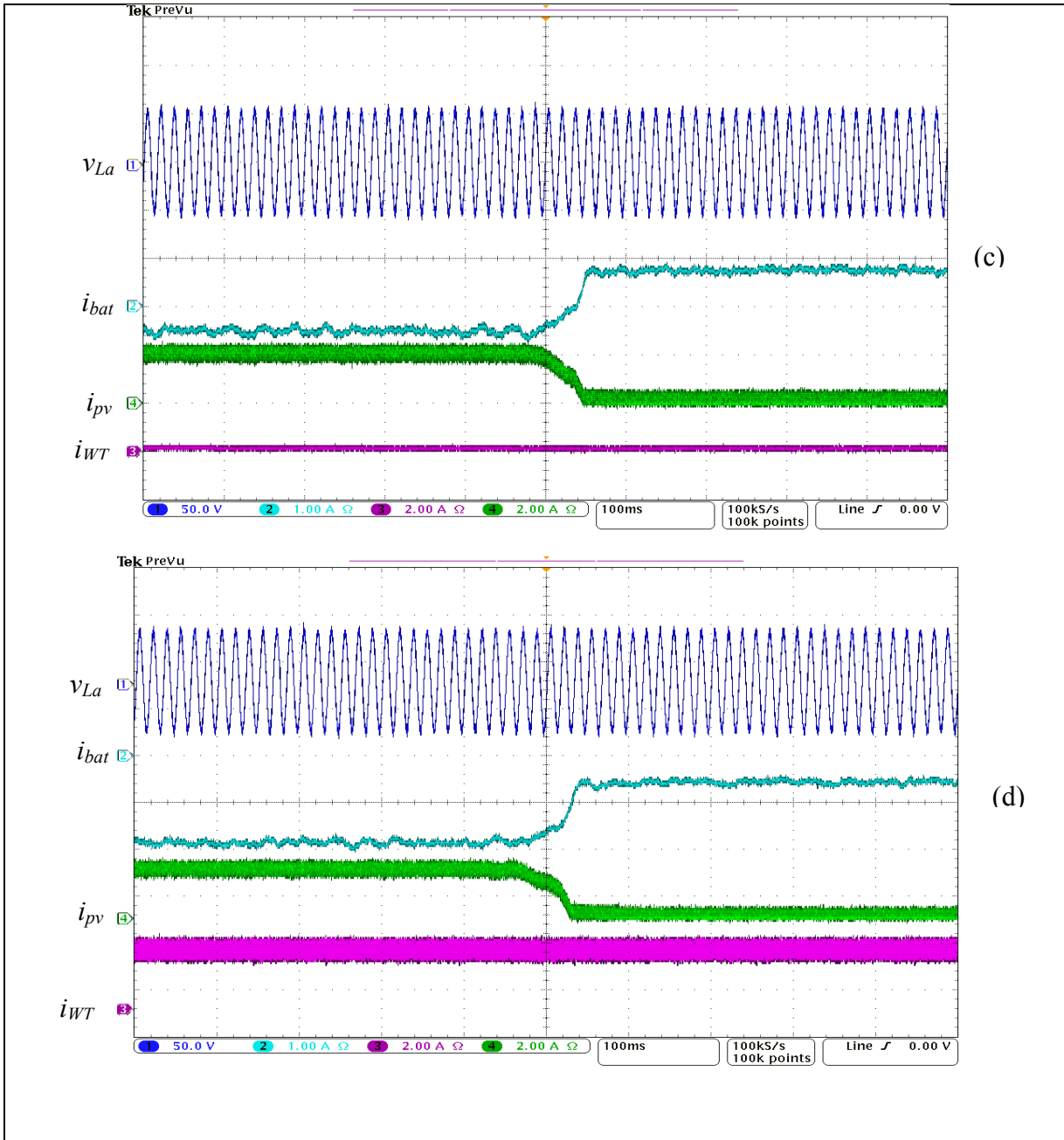


Figure 6.32 Dynamic performance of PV-WT HSPGS under solar insolation and wind speed change

## 6.5 Conclusion

Several PV-WT HSPGS topologies employing fixed and variable speed generators are discussed in this chapter, and three different topologies are selected for studying in detail. Based on these new designs it becomes possible to supply isolated load continuously without using DG. In the first topology, WT is driven fixed speed SCIG and is connected directly to the PCC, and PV solar through two-stage inverters. The obtained results using P&O technique and instantaneous p-q theory show satisfactory performance. In the second PV-WT HSPGS employing variable speed SyRG, two-stage inverters and AC/DC converter are used to connect the both RESs to the PCC. To achieve MPPT from the solar PV array and WT, as well as to regulate the AC frequency, the system frequency and improving the power quality power quality at the PCC, P&O, rotor oriented control and indirect control are used. The obtained results during presence of different conditions such as, wind speed and solar irradianations change, as well as, during load variation and when BESS becomes fully charged show satisfactory. In the third proposed PV-WT HSPGS employing variable speed PMBLDCG, detailed modeling and stability analysis have been developed, and to achieve a MPPT from PV array and WT driven PMBLDCG, a sliding mode control approach was proposed which avoids the use of linear PI controller, and related problems. A new feedback current control technique was integrated in the both developed control algorithms for MPPT in order to protect the battery from overvoltage and to maintain the energy sources supplying the actual load demand without resort to a dump load. The performance of the proposed HSPGS was successfully tested under various conditions, such as climate changes and different kind of loads, by simulation as well as by experimentation with satisfactory results without any adjustment to parameters, with current harmonics elimination and frequency and voltage regulation at the PCC.



## CHAPITRE 7

### HYBRID STANDALONE POWER GENERATION SYSTEM EMPLOYING WT AND DG

#### 7.1 Introduction

This chapter is dedicated to the control of WT-DG HSPGS employing fixed and variable speed generators such as, SCIG, SG, PMSG, SyRG, PMBLDCG and DFIG as shown in Fig.7.1 are discussed. These proposed topologies are designed in order to achieve high efficiency from WT and DG and ensuring stability and uninterruptible power supply to the load with high power quality, as well as, with reduced cost. To regulate AC voltage, frequency, to improve the power quality, as well as, to achieve MPPT from WT and maximize the efficiency of DG, several control approaches such as, modified SRF control and new approach which is based on decomposition of symmetrical components, as well as P&O technique control are used. The effectiveness and the robustness of proposed controllers are validated by simulation using MATLAB/Simulink during loads and weather conditions changes, as well as, when BESS becomes fully charged.

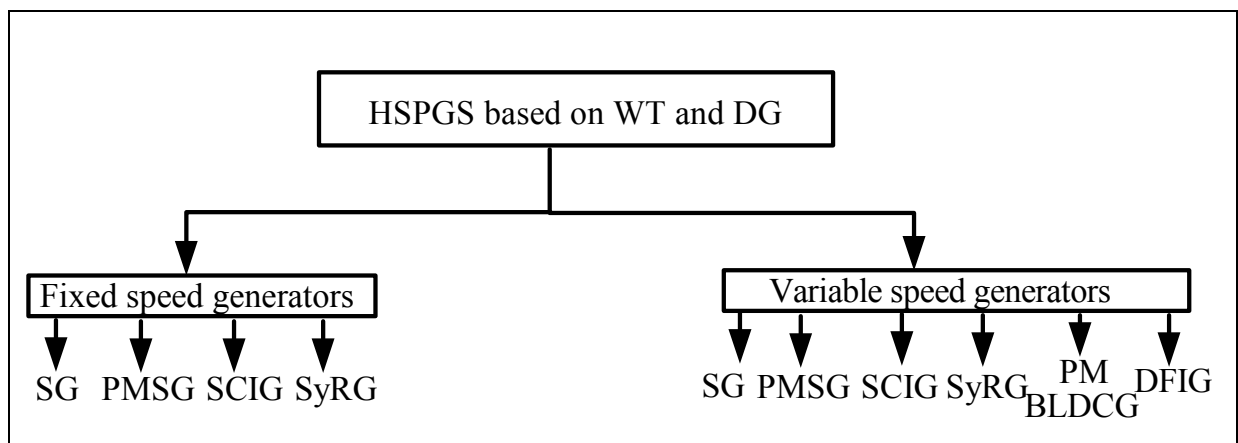


Figure 7.1 Classification of HSPGS based on PV array and WT driven fixed and variable speed generators

## 7.2 Topology designs of HSPGS based on DG and WT driven fixed speed generators

Fig.7.2 shows the proposed WT-DG HSPGS topologies employing fixed speed generators such as, SG, SyRG, SCIG and PMSG. Usually, this type of HSPGS is less effective and costly because of the DG remains operational at all times, which allows high fuel consumption, especially at light load. In addition, at high wind penetration and less load power demand, extra power is dissipated in dump load in order to keep the system frequency constant. Moreover, the fluctuations in the wind speed are directly transferred to the PCC, which allows deviation in system frequency (Carrillo et al., 2004; Jin et al., 2013). In kind of HSPGS, the power quality is a big issue due to the frequency switching of the dump load control.

To remedy these drawbacks and make WT-DG HSPGS employing fixed speed generators more effective, it is suggested to add new elements, such as, three-phase inverter, BESS and controlled breaker between DG and the PCC. In addition, dump load should be tied to the DC side. Based on these new proposed WT-DG HSPGS, DG is used in emergency, and the extra wind power mostly dumped in dump loads is stored in BESS. Therefore, by adding those new elements to the classical hybrid WT-DG SPGS, the efficiency of the fixed speed DG will be improved by operating it at optimum load. It is expected to be operational only when:

- State of charge of BESS is less than 50%,
- Power produced by the WT is less than load power demand.

Therefore, in this case DG provides maximum of power with a minimum of fuel consumption. Moreover, the proposed new topologies, dump load is tied to the DC link, instead to AC side, which allows minimization of the risk of power quality disturbances. Furthermore, BESS can ensure power supply during transition period of DG and smoothing output power oscillation caused by intermittent nature of WT energy.

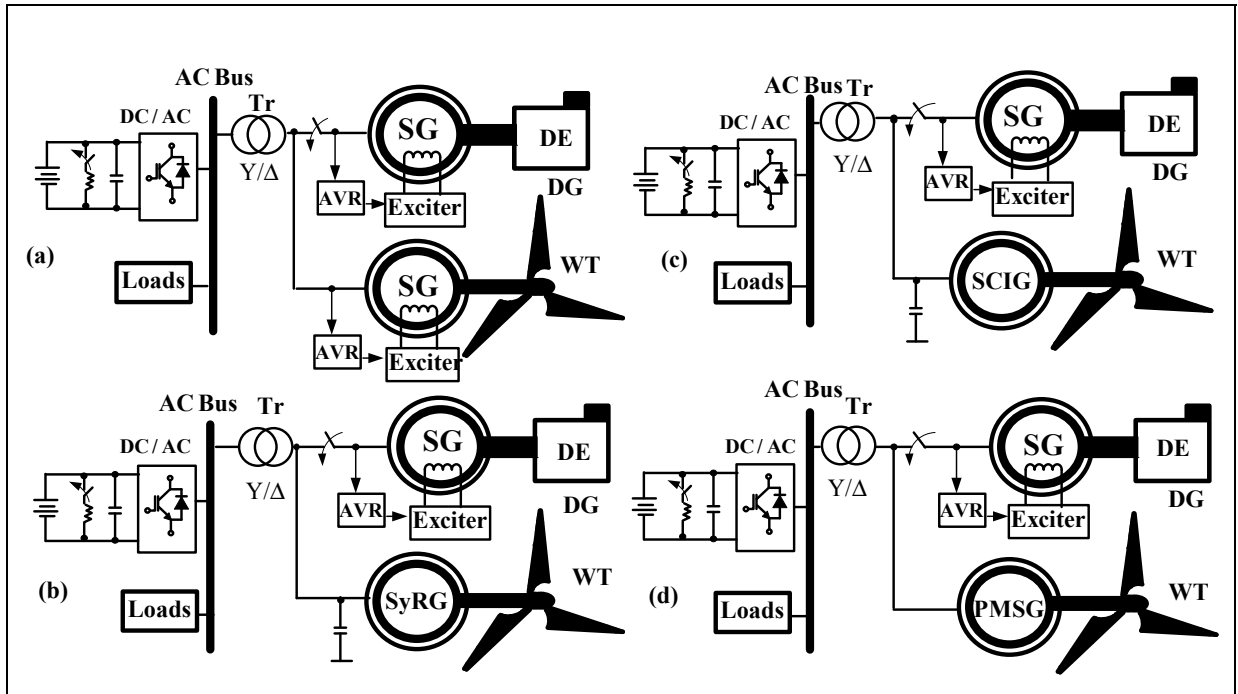


Figure 7.2 HSPGS based on WT and DG driven fixed speed generators

### 7.2.1.1 Description and control of hybrid standalone power generation system based on WT and DG driven fixed speed SG and PMSG

Fig.7.3 shows a detailed selected WT-DG HSPGS employing fixed speed SG and PMSG. DE is coupled to SG and connected to the PCC through controlled switch, and WT is driving PMSG. BESS and dump loads are tied to the PCC through DC/AC inverter which is controlled to charge and discharge BESS and to improve the power quality at the PCC. To improve the efficiency and to increase the lifespan of DG it should turn on only when the following conditions, are fulfilling:

- $SOC\% < 50\%$ ,
- $P_L > P_{WT}$ .

Therefore, if these two conditions are verified, DG is turn on; it should provide power to the connected load and charge the BESS, simultaneously.

To achieve this connection of DG to the PCC, the same control algorithm developed before for PV-DG HSPGS in chapter 4 and shown in Fig.4-8 is used. As for WT, the same power-speed characteristics as shown in Fig. 6-4, is used. To achieve regulation of the AC voltage and the system frequency regulation, as well as, the power quality improvement at the PCC, modified synchronous reference frame control (SRF) is used. For dump load the same control algorithm already given in chapter 4 and shown in Fig.4-9 is used.

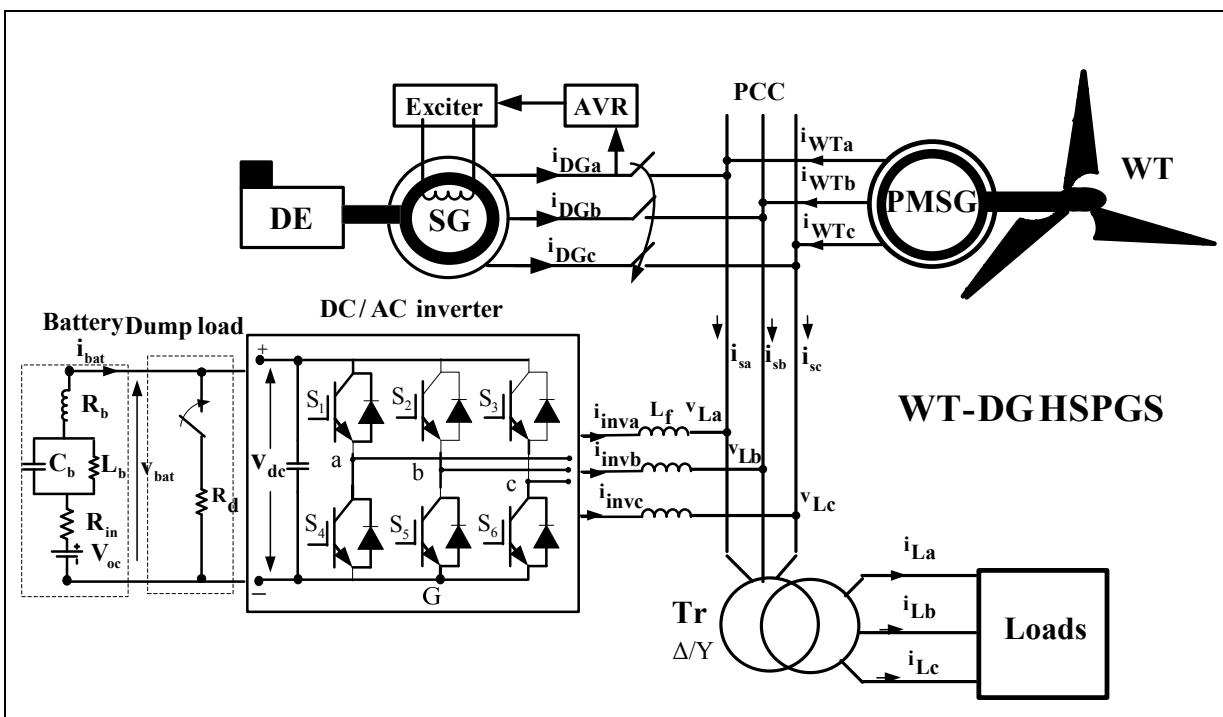


Figure 7.3 HSPGS based on WT and DG driven fixed speed PMSG and SG

**Modified SRF control for DC/AC inverter**

Fig.7.4. shows the block diagram of the proposed control algorithm for the DC/AC inverter. This control algorithm is developed in order to regulate the AC voltage and the system frequency ( $f_s$ ), as well as, improving the AC source currents quality by eliminating harmonics at PCC. For these tasks, load voltages ( $v_{Lab}, v_{Lbc}$ ), source currents ( $i_{sa}, i_{sb}, i_{sc}$ ), which represents the sum of the output DG currents ( $i_{Da}, i_{Db}$ ) and output WT currents ( $i_{WTa}, i_{WTb}$ ), load currents

( $i_{La}$ ,  $i_{Lb}$ ), and BESS current ( $i_{bat}$ ) are sensed.

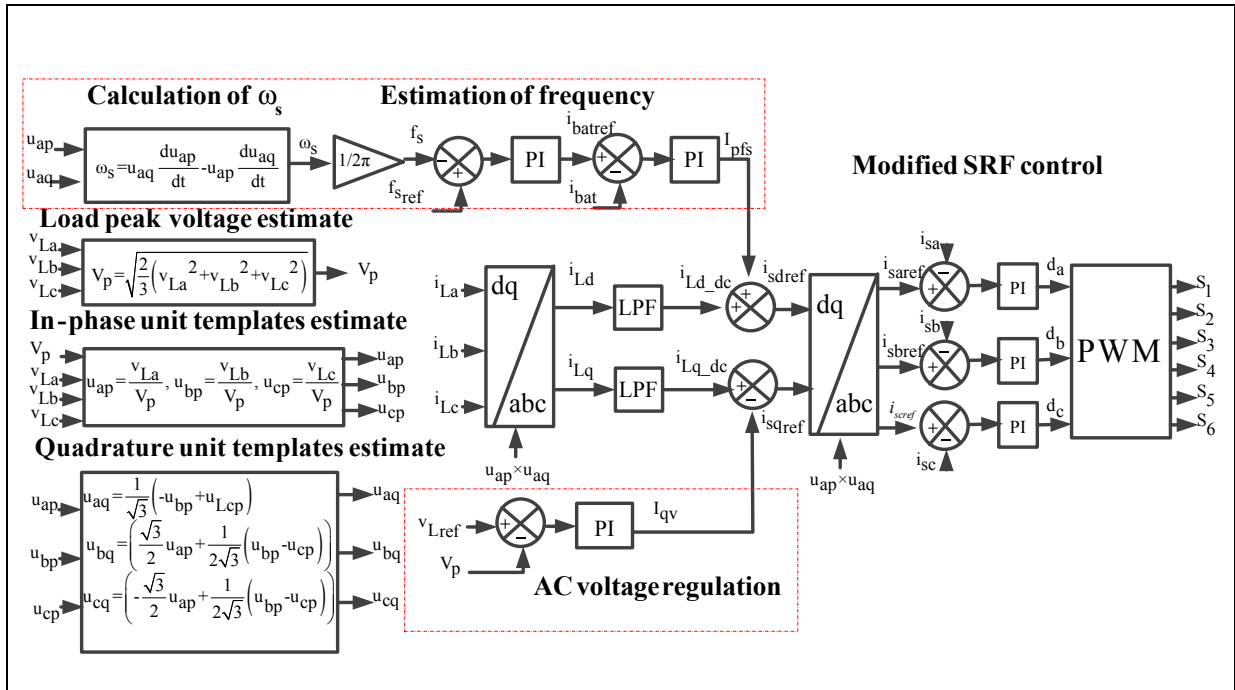


Figure 7.4 Modified SRF control algorithm

### System Frequency Regulation

As shown in Fig.7.4, the system frequency ( $f_s$ ) at the PCC is estimated using in-phase and quadrature unit templates as:

$$V_p = \sqrt{\frac{2}{3}(v_{La}^2 + v_{Lb}^2 + v_{Lc}^2)} \tag{7.1}$$

where  $V_p$  and  $v_{Labc}$  denote the amplitude and the instantaneous PCC voltages, respectively.

The in-phase unit templates are calculated as:

$$u_{ap} = \frac{v_{La}}{V_p}, u_{bp} = \frac{v_{Lb}}{V_p}, u_{cp} = \frac{v_{Lc}}{V_p} \quad (7.2)$$

The quadrature unit templates are obtained as:

$$\begin{aligned} u_{aq} &= \frac{1}{\sqrt{3}}(-u_{bp} + u_{cp}), u_{bq} = \left( \frac{\sqrt{3}}{2}u_{ap} + \frac{1}{2\sqrt{3}}(u_{bp} - u_{cp}) \right) \\ u_{cq} &= \left( -\frac{\sqrt{3}}{2}u_{ap} + \frac{1}{2\sqrt{3}}(u_{bp} - u_{cp}) \right) \end{aligned} \quad (7.3)$$

Using the estimated in-phase unit and quadrature templates, the frequency is estimated as:

$$\omega_s = \cos \theta_L \frac{d}{dt}(\sin \theta_L) - \sin \theta_L \frac{d}{dt}(\cos \theta_L) \quad (7.4)$$

where  $\omega_s$  represents the angular frequency in rad/s and  $\cos \theta_L = u_{aq}$ ,  $\sin \theta_L = u_{ap}$ .

The system frequency  $f_s$  is estimated using (7.5) as:

$$f_s = \frac{\omega_s}{2\pi} \quad (7.5)$$

The error between reference and estimated frequency is as,

$$\Delta f_s = f_{sref} - f_s \quad (7.6)$$

The output of frequency PI controller represents the battery current reference ( $i_{batref}$ ), which is obtained as:

$$i_{batref} = \left( k_{pfs} + \frac{k_{if_s}}{s} \right) (f_{sref} - f_s) \quad (7.7)$$

where  $K_{pfs}$  and  $K_{if_s}$  denote proportional and integral gains of the frequency PI controller, respectively.

The sensed battery current ( $i_{bat}$ ) is compared with the output of the frequency PI controller and the obtained active component ( $I_{pfs}$ ) is as follow:

$$I_{pfs} = \left( k_{pbat} + \frac{k_{ibat}}{s} \right) (i_{batref} - i_{bat}) \quad (7.8)$$

where  $K_{pbat}$ ,  $K_{ibat}$  denotes proportional and integral gains of the battery PI controller, respectively.

$I_{pfs}$  is added to the estimate active load component and the sum represents the reference active components of the source current as in (7.11).

### AC Voltage Regulation

As shown in Fig.7.4, to regulate the AC voltage at the PCC, we need to estimate first the PCC peak voltage ( $V_p$ ) as in (7.1). This estimated value is compared with PCC peak voltage reference ( $V_{Lref}$ ). The output of the PCC voltage PI controller represents the reactive component ( $I_{qv}$ ) as follow:

$$I_{qv} = \left( k_{pv} + \frac{k_{iv}}{s} \right) (V_{Lref} - V_p) \quad (7.9)$$

where  $K_{pv}$ ,  $K_{iv}$  denotes proportional and integral gains of the AC line voltage PI controller respectively.

$I_{qv}$  is added after with the estimate reactive load component in order to obtain the reference component of the reactive sources currents as in (7.12).

### Estimation of Active and Reactive Power Components of Load currents

To extract the active and reactive components of the load currents from its original currents, the following procedure which is based on synchronous reference frame (SRF) given in (Rezkallah et al., 2014) .

The load currents  $i_{Labc}$  and the voltage at the PCC  $v_{Labc}$  are sensed and transformed to d-q frame using Park's transformation already expressed in (2.49) as,

$$\begin{bmatrix} i_{Ld} \\ i_{Lq} \end{bmatrix} = \sqrt{\frac{2}{3}} \begin{bmatrix} \cos \theta_L & \cos\left(\theta_L - \frac{2\pi}{3}\right) & \cos\left(\theta_L + \frac{2\pi}{3}\right) \\ \sin \theta_L & \sin\left(\theta_L - \frac{2\pi}{3}\right) & \sin\left(\theta_L + \frac{2\pi}{3}\right) \end{bmatrix} \begin{bmatrix} i_{La} \\ i_{Lb} \\ i_{Lc} \end{bmatrix} \quad (7.10)$$

where  $\theta_L$  represents the phase shift of the PCC voltage, and is calculated using (7.2). With the help of low-pass filters (LPFs), the (d-q) dc-components  $i_{Ld\_dc}$  and  $i_{Lq\_dc}$  from the obtained d-q load currents ( $i_{Ld}$  and  $i_{Lq}$ ) are extracted.

The d-q estimate source currents are calculated by adding the errors getting from the frequency and AC voltage regulation loops as;

$$i_{sdref} = i_{Ld\_dc} + I_{pfs} \quad (7.11)$$

And

$$i_{sqref} = i_{Lq\_dc} - I_{qv} \quad (7.12)$$

Using inverse Park transformation given in (2.50), the references source currents ( $i_{saref}$ ,  $i_{sbref}$ ,  $i_{scref}$ ) are obtained as:

$$\begin{bmatrix} i_{saref} \\ i_{sbref} \\ i_{scref} \end{bmatrix} = \begin{bmatrix} \cos \theta_L & -\sin \theta_L \\ \cos \left( \theta_L - \frac{2\pi}{3} \right) & -\sin \left( \theta_L - \frac{2\pi}{3} \right) \\ \cos \left( \theta_L + \frac{2\pi}{3} \right) & -\sin \left( \theta_L + \frac{2\pi}{3} \right) \end{bmatrix} \begin{bmatrix} i_{sdref} \\ i_{sqref} \end{bmatrix} \quad (7.13)$$

The sensed source currents ( $i_{sa}$ ,  $i_{sb}$ ,  $i_{sc}$ ) are compared with reference source currents ( $i_{saref}$ ,  $i_{sbref}$ ,  $i_{scref}$ ), the obtained error is processed through a PI controller and its outputs are used as inputs for pulse width modulation controller (PWM) to generate signals for controlling the DC/AC inverter switches ( $S_1$  to  $S_6$ ).

### Model of the diesel generator and their control algorithms

For the proposed WT-DG HSPGS shown in Fig.7.3, DE driven fixed speed SG and is connected to the PCC through controlled switch. The same model of AVR and control algorithm for controlled switch studied in detail in chapter 4 and shown in Figs.4.6 and 4.8, respectively are used for this study.

### 7.3 Topology designs of hybrid standalone power generation system employing DG and WT driven variable speed generators

Fig.7.5 shows the proposed WT-DG HSPGS topologies employing variable speed generators such as, SG, SyRG, PMBLDCG, SCIG, PMSG and DFIG.

For the proposed schemes, the stator of the both electrical generators, which are driven by WT and DG are connected to the common DC bus through AC/DC converter except the topology which is employing DFIG, the stator is tied directly to PCC. These proposed WT-DG HSPGS are more effective because they use a variable speed generator technology instead of fixed speed technology. In addition, they are inexpensive due to the reduced

number of power converters used compared to the existing WT-DG HSPGS topologies proposed by (Cardenas et al., 2006; Li et al., 2014).

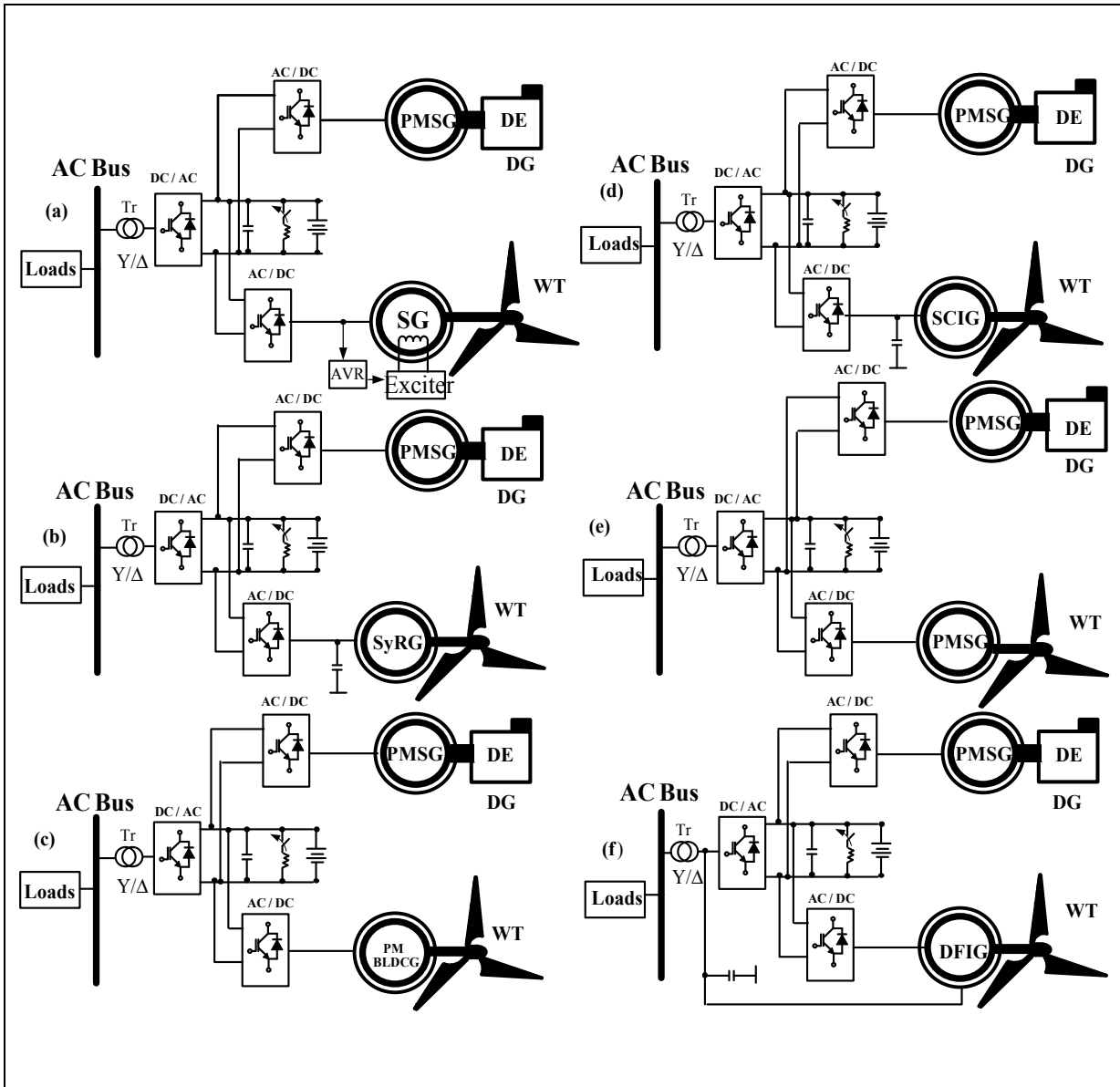


Figure 7.5 HSPGS based on WT and DG driven variable speed generators

**7.3.1 Description and control of HSPGS employing WT and DG driven variable speed PMBLDCG and PMSG**

Fig 7.6 shows the selected WT-DG HSPGS employing DE driven variable speed PMSG and WT driven variable speed PMBLDCG. The both ESs are connected to common DC-bus through three-phase diode bridges and DC/DC boost converters, and to the PCC through DC/AC inverter. BESS and dump load are tied to the common DC-bus. As shown in Fig.7.6, WT-DG HSPGS is reinforced by RC ripple filter connected at the output of the DC/AC interfacing inverter in order to compensate the voltage ripple created by high a frequency switching. In the proposed topology, neutral point is tied to the midpoint of the two capacitors in the DC bus.

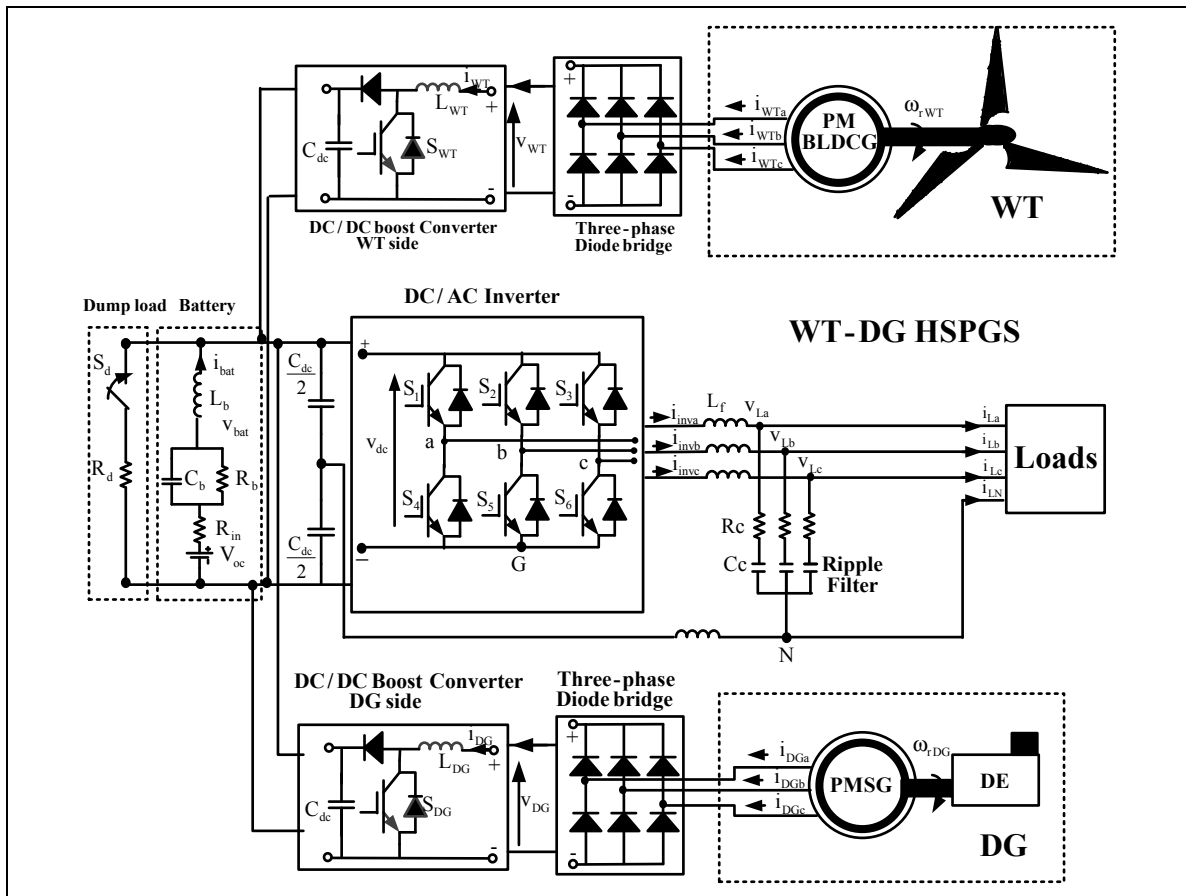


Figure 7.6 HSPGS based on WT and DG driven variable speed PMBLDCG and PMSG

**Control of the DC/DC Boost converter for DG side**

Fig 7.7 shows the proposed control algorithm for the DG side DC/DC boost converter. In this proposed control algorithm, the output DG power is calculated by multiplying the sensed output voltage ( $v_{DG}$ ) and current ( $i_{DG}$ ) of the DG as:

$$P_{DG} = v_{DG} i_{DG} \tag{7.14}$$

The obtained  $P_{DG}$  is used to determine the reference rotor speed of the PMSG ( $\omega_{r\_ref}$ ) using the optimal rotational speed vs load curve characteristic given by (Waris et Nayar, 2008). The obtained  $\omega_{r\_ref}$  is used next to determine the reference electromagnetic torque ( $T_{e\_ref}$ ) as:

$$T_{e\_ref} = (\omega_{r\_ref} - \omega_r) \left( k_{por} + \frac{k_{ior}}{s} \right) \tag{7.15}$$

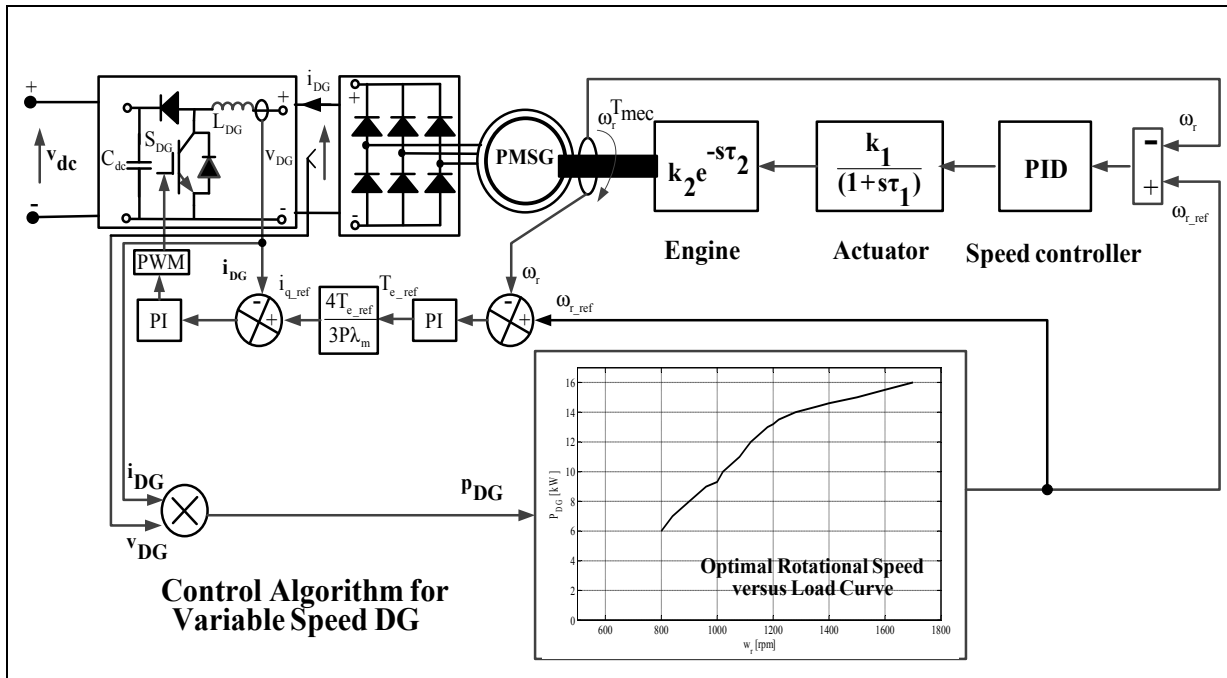


Figure 7.7 Control of the DG side DC-DC boost converter

where  $\omega_r$ ,  $k_{por}$  and  $k_{ior}$  denotes the sensed rotor speed of the PMSG and the proportional and integral gains.

The obtained reference electromagnetic torque ( $T_{e\_ref}$ ) is used to calculate the q-axis reference current component using equation (2.99) given in chapter 2 as:

$$T_e = \frac{3}{2} \left( \frac{P}{2} \right) (\lambda_m i_q - (L_q - L_d) i_q i_d)$$

In case of cylindrical rotor,  $L_d \approx L_q$ . Therefore, the expression becomes as follow:

$$i_{q\_ref} = \left( \frac{4}{3P} \right) \left( \frac{T_{e\_ref}}{\lambda_m} \right) \quad (7.16)$$

The obtained q-axis reference current ( $i_{q\_ref}$ ) is compared to sensed  $i_{DG}$  current and the error is fed to PI current controller, and its output is fed to PWM controller to generate the switching signal for the switch of the DC-DC boost converter ( $S_{DG}$ ).

### Control of the WT side DC-DC Boost converter

Fig. 7.8 shows the proposed control algorithm to extract the maximum power from WT. The proposed MPPT technique is based on a comparison of perturbation voltage and change in provided power using P&O technique.

$v_{WT(n)}$  is multiplied by the sensed output current ( $i_{WT(n)}$ ), and then  $p_{WT(n)}$  and previous instantaneous power  $p_{WT(n-1)}$  are compared, as well as,  $v_{WT(n)}$  and previous output voltage ( $v_{WT(n-1)}$ ) are compared.

Therefore, if the product ( $\Delta p_{WT(n)} \Delta v_{WT(n)} > 0$ ),  $k$  is equal to -1, and if the product ( $\Delta p_{WT(n)} \Delta v_{WT(n)} < 0$ ),  $k$  is equal to 1.

Therefore, to calculate the instantaneous generated power ( $p_{WT(n)}$ ), the sensed output voltage (

The obtained  $k$  is multiplied by duty cycle variation amplitude ( $\Delta d$ ), which varies between 0.1% to 2.7% as given in (Dolara, Faranda et Leva, 2009).

Term ( $\Delta d k$ ) is added to the duty cycle ( $d_{(n)}$ ), which is stored at pervious sampling time. The obtained duty cycle  $d_{(n+1)}$  is used for controlling the DC/DC boost converter of the WT side as shown in Fig.7-8.

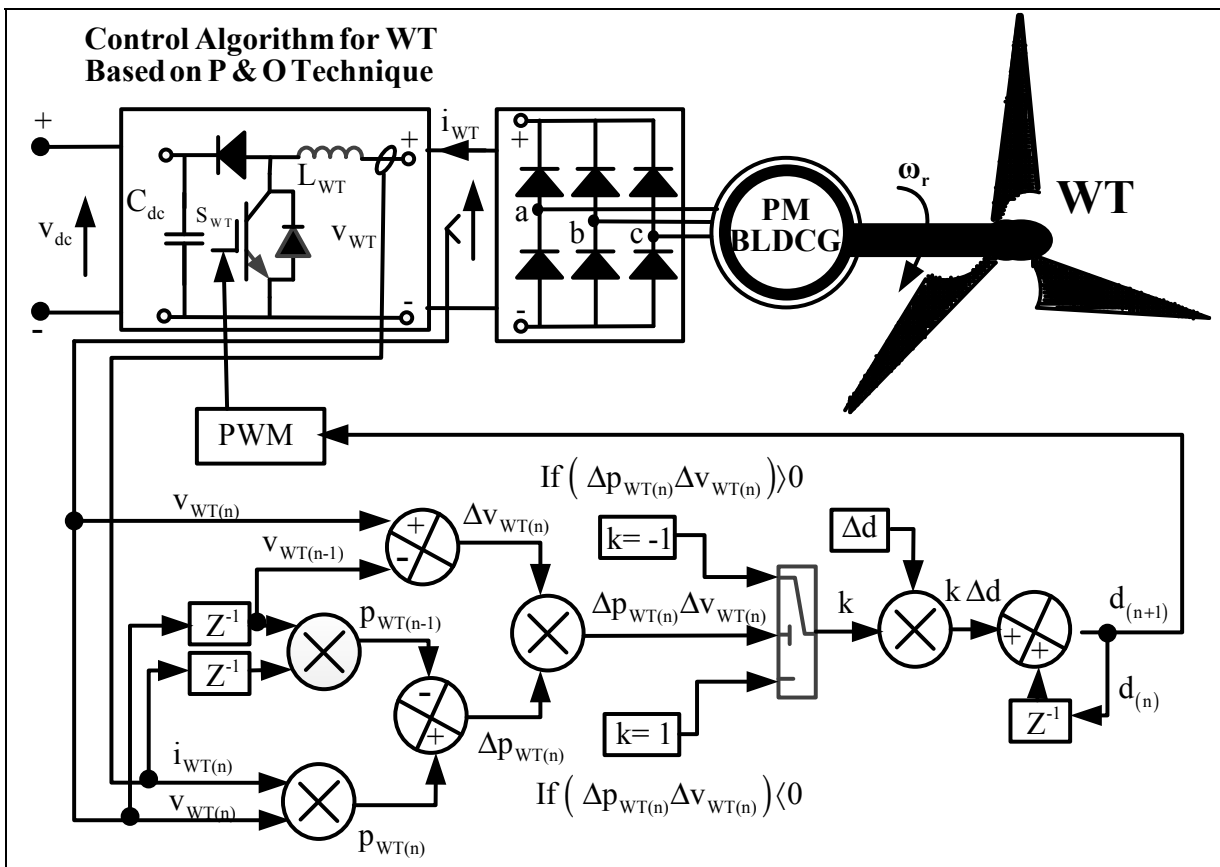


Figure 7.8 Control of the DC-DC WT side boost converter

**Control of the DC/AC inverter**

Fig.7.10 shows the control algorithm of the DC/AC inverter, which is designed to supply power permanently to the load with fixed voltage and frequency and to keep the waveforms

of the AC voltage purely sinusoidal (Rezkallah, Chandra et Singh, 2013) . The proposed control algorithm uses the decomposition into symmetrical sequences of the sensed AC voltage ( $v_{Labc}$ ) and load current ( $i_{Labc}$ ) as;

$$\begin{bmatrix} v_{LO} \\ v_{LN} \\ v_{LP} \end{bmatrix} = \frac{1}{3} \begin{bmatrix} 1 & 1 & 1 \\ 1 & a^2 & a \\ 1 & a & a^2 \end{bmatrix} \begin{bmatrix} v_{La} \\ v_{Lb} \\ v_{Lc} \end{bmatrix} \tag{7.17}$$

And

$$\begin{bmatrix} i_{LO} \\ i_{LN} \\ i_{LP} \end{bmatrix} = \frac{1}{3} \begin{bmatrix} 1 & 1 & 1 \\ 1 & a^2 & a \\ 1 & a & a^2 \end{bmatrix} \begin{bmatrix} i_{La} \\ i_{Lb} \\ i_{Lc} \end{bmatrix} \tag{7.18}$$

where indices  $P, N, O$  represent the positive, negative and zero sequences and «a», is the  $120^\circ$  rotation operator as shown in Fig.7.9.

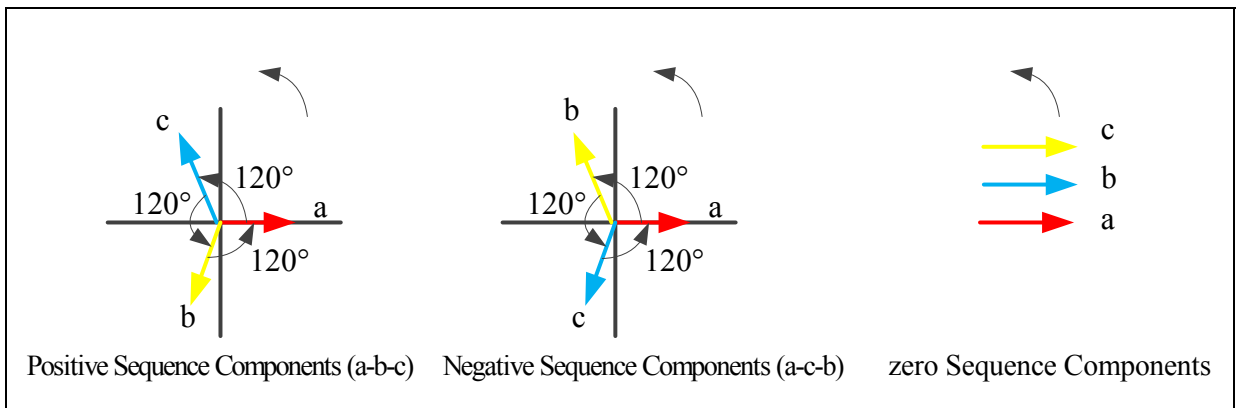


Figure 7.9 Positive, Negative and Zero sequence components

The symmetrical components of  $v_{Labc}$  and  $i_{Labc}$  are projected into rotating reference frame using Park’s transformation already expressed by (2.49) in chapter 2, and regulated after in inner current and outer voltage loops.

In inner current loop, the positive currents ( $i_{LPdp}$  and  $i_{LPdq}$ ) are regulated using proportional integral controller in positive rotating reference frame as:

$$U_{pd} = (i_{LPdq}^* - i_{LPdq}) \left( k_{pi} + \frac{k_{ii}}{s} \right) \quad (7.19)$$

The negative currents ( $i_{LNp}$  and  $i_{LNq}$ ) are regulated using proportional integral controller in negative rotating reference frame as:

$$U_{Ndq} = (i_{LNdq}^* - i_{LNdq}) \left( k_{pi} + \frac{k_{ii}}{s} \right) \quad (7.20)$$

The zero currents ( $i_{LOp}$  and  $i_{LOq}$ ) are regulated using proportional integral controller in negative zero reference frame as:

$$U_{odq} = (i_{LOpq}^* - i_{LOpq}) \left( k_{pi} + \frac{k_{ii}}{s} \right) \quad (7.21)$$

where,  $U_{Pdq}$ ,  $U_{Ndq}$ ,  $U_{Odq}$ ,  $i_{LPpq}^*$ ,  $i_{LNpq}^*$  and  $i_{LOpq}^*$  represent the output of the PI current controllers of the inner loops and estimated load currents, respectively.

The d-q estimated positive load current is obtained from the outer loop positive voltage sequence as:

$$i_{LPdq}^* = (v_{LPdq\_ref} - v_{LPdq}) \left( k_{pv} + \frac{k_{iv}}{s} \right) \quad (7.22)$$

The d-q estimated positive load current is obtained from the outer loop negative voltage sequence as:

$$i_{LNdq}^* = (v_{LNdq\_ref} - v_{LNdq}) \left( k_{pv} + \frac{k_{iv}}{s} \right) \quad (7.23)$$

The d-q estimated Zero load current is obtained from the outer loop Zero voltage sequence as:

$$i_{LOdq}^* = (v_{LOdq\_ref} - v_{LOdq}) \left( k_{pv} + \frac{k_{iv}}{s} \right) \quad (7.24)$$

where  $k_{pv}$ ,  $k_{iv}$ ,  $k_{pi}$  and  $k_{ii}$  denote proportional and integral gains for inner and outer loops, respectively.

To regulate the AC voltage at its rated value, d-axis positive sequence AC voltage ( $v_{LPdref}$ ) is compared with the desired AC voltage, which is equal to 375V. Regarding,  $v_{LNdref}$  and  $v_{LOdref}$  are kept equal to zero.

As shown in Fig. 7.10, terms  $(-\omega_s L_f i_{LPd}, \omega_s L_f i_{LPq})$  and  $(\omega_s L_f i_{LNd}, -\omega_s L_f i_{LNq})$  are used to decouple d-q axis dynamics in positive and negative sequence, respectively.

where  $\omega_s$  denotes the fundamental frequency and is equal 377 rad/s.

The estimated AC voltage ( $v_{Labc}^*$ ) are obtained by the addition of the positive, negative and zero sequence AC voltage as:

$$v_{Labc}^* = v_{LPabc}^* + v_{LNabc}^* + v_{LOabc}^* \quad (7.25)$$

where  $v_{LPabc}^*$ ,  $v_{LNabc}^*$  and  $v_{LOabc}^*$  represent the positive, negative and zero sequence load voltages into (a-b-c) frame.

The reference AC voltage ( $v_{Labc}^*$ ) are compared with fixed-frequency triangular carrier wave to generate gating signals for IGBTs of DC/AC inverter.

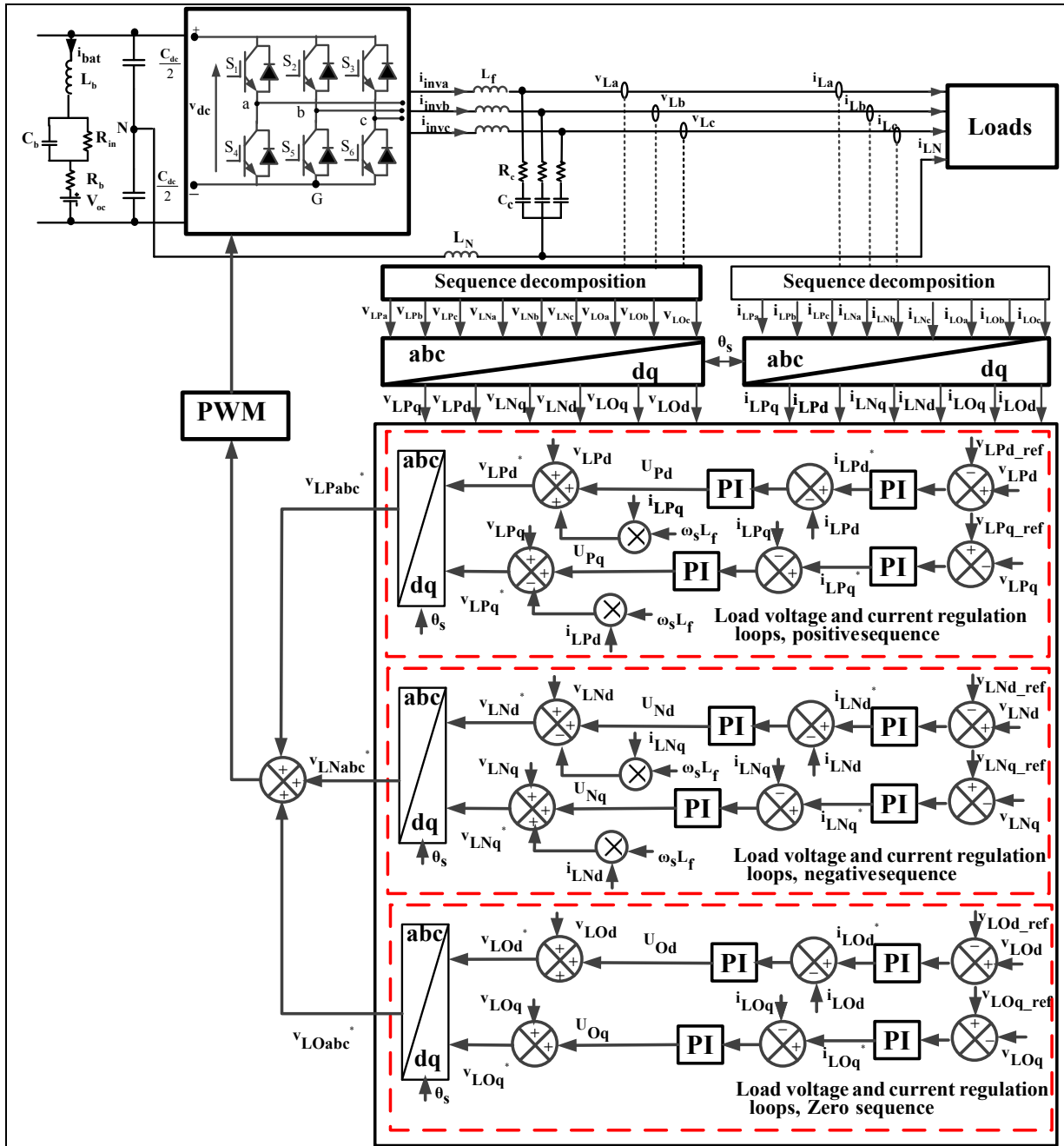


Figure 7.10 Control of the DC/AC inverter

## 7.4 Simulation results and discussion

### 7.4.1 Performance of the HSPGS based on DG and WT driven fixed speed SG and PMSG

Simulations are carried out using MATLAB/Simulink in order to test the performance of the proposed WT-DG HSPGS as shown in Fig.7.3, as well as the robustness of the proposed control algorithms for controlling the DC/DC boost converters and the DC/AC interfacing inverter. The system parameter is values given in Appendix Table A-9. Many scenarios, such as, sudden change of the wind speed, load variation, as well as, when the SOC% of BESS is greater or less than 50%, and when it becomes equal to 100%, are tested.

Fig.7.11 shows the waveforms of AC line voltage ( $v_L$ ), WT current ( $i_{WT}$ ), DG current ( $i_{DG}$ ), source current ( $i_s = i_{WT} + i_{DG}$ ), load current ( $i_L$ ), inverter current ( $i_{inv}$ ), DC voltage ( $V_{dc}$ ), state of charge of battery (SOC %), and the system frequency ( $f_s$ ).

In the first test, the SOC% of BESS is greater than 50%, and the wind speed and load are varying. It is observed that from  $t = 0.3$  s to 1.5 s, WT is able to satisfy the load power demand, and the extra power is sent to BESS, and that is why SOC% is increasing. Seeing that SOC% is greater than 50% and ( $i_{WT} > i_L$ ), DG is turned off and that is why  $i_{DG}$  is equal to 0. It is observed that from  $t=1.5$  s to  $t= 2.5$ s, wind speed is decreased but load is remaining constant, nevertheless  $i_{WT} < i_L$ , DG is still turned off, since the second condition is not fulfilling (SOC% < 50%). Therefore, to compensate deficit in power BESS is discharged. Therefore, SOC% and  $V_{dc}$  are decreased, and inverter current ( $i_{inv}$ ) is increased.

From  $t = 2.5$  s to  $t=3.5$  s WT-DG HSPGS is subjected to sudden load increase. Because of the SOC% is greater than 50%, BESS is discharged, therefore, SOC% and  $V_{dc}$  are decreased and  $i_{inv}$  is increased more. It is observed that throughout the simulation period, AC load voltage and system frequency are remaining constant, which confirms the smooth functioning of the proposed control algorithms for AC voltage and frequency regulation. In

addition, DG is turn OFF because of the SOC% of BESS is greater than 50%, which allows saving fuel and eliminating the multiple of on/off operations of DG.

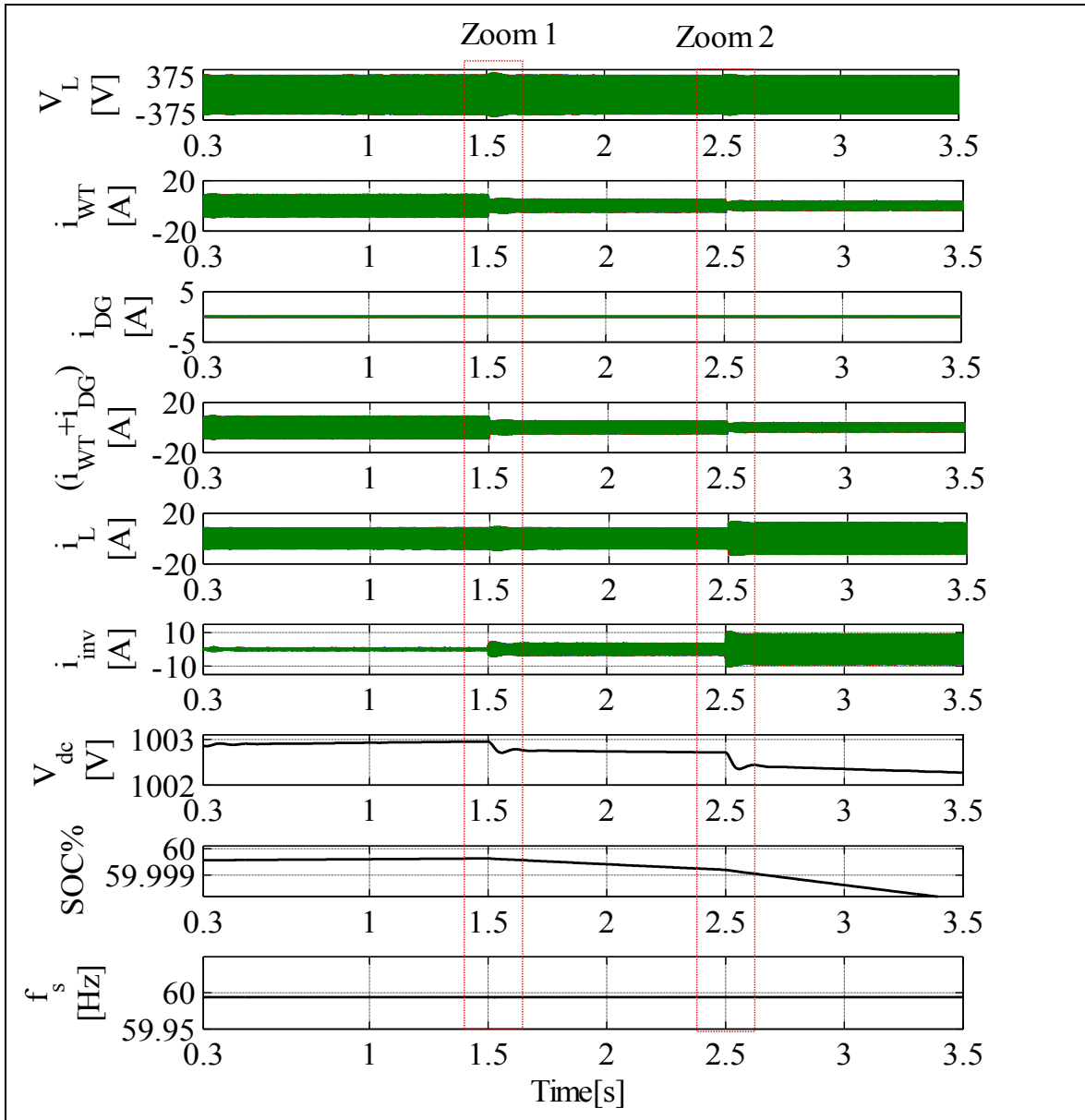


Figure 7.11 Dynamic performance of WT-DG HSPGS employing fixed speed generators under wind speed and loads change when the SOC% is greater than 50%

Fig.7.12 shows the zoomed waveforms of the simulation results shown in Fig.7.11, between  $t= 1.48$  s and  $t= 1.55$  s. One may see that the load current is equal to the output WT current, which represents the source current because in this test DG output current is equal to 0. At  $t= 1.5$  s, source current ( $i_s = i_{WT}$ ) is decreased and that is why inverter current ( $i_{inv}$ ) is increased in order to compensate the deficit. It is observed that the steady state error of the AC voltage is equal to zero and the system frequency is not affected during wind speed variation, which confirms the robustness of the proposed control approach for AC voltage and system frequency regulation.

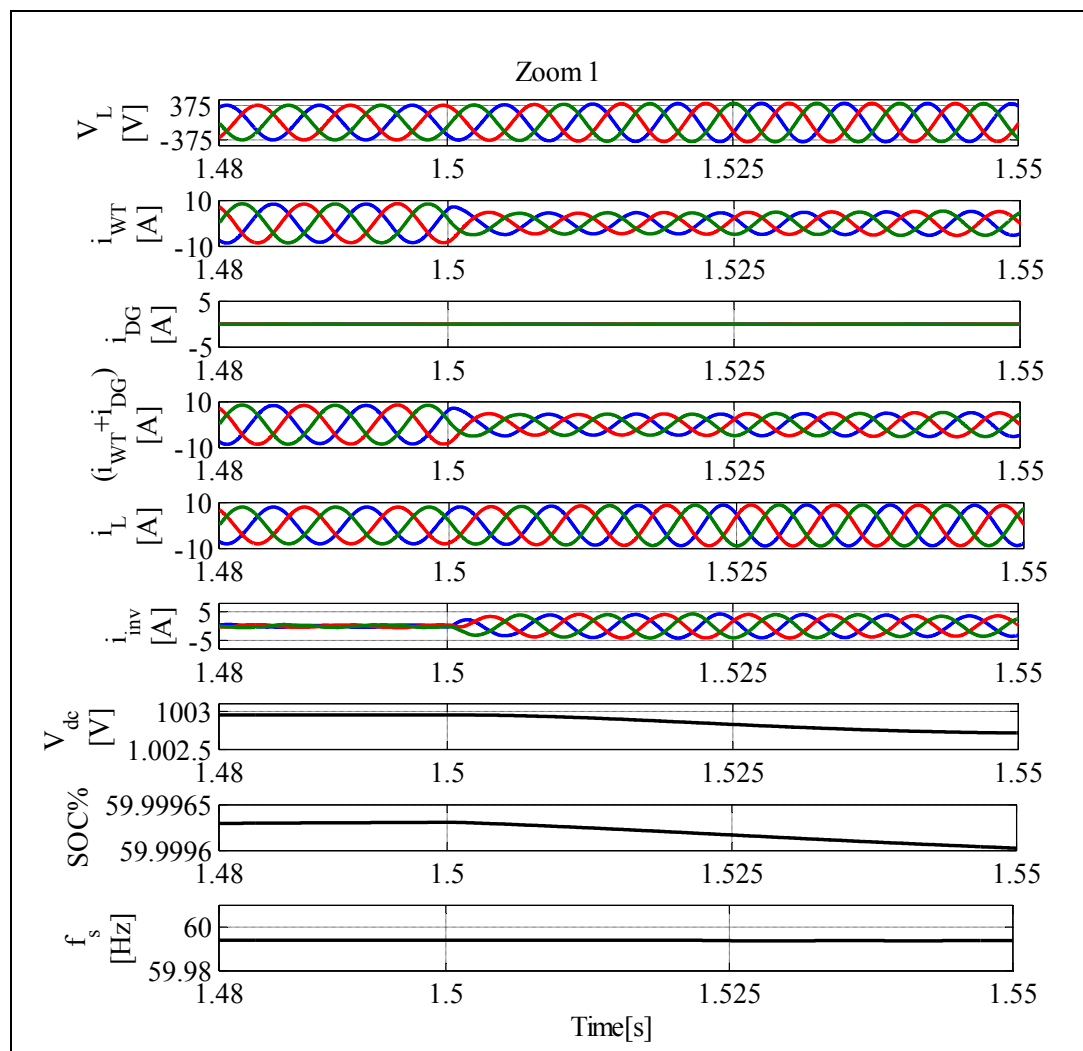


Figure 7.12 Zoom1 of the results shown in Fig.7.11 between  $t= 1.48$ s to  $t= 1.55$  s

Fig.7.13 shows the zoomed waveforms results shown in Fig.7.11, between  $t = 2.48$  s and  $t = 2.55$  s. It is observed that at  $t = 2.5$  s,  $i_{WT}$  is decreased more, and  $i_L$  is increased at the same time and therefore  $i_{inv}$  is increased more. It is observed that BESS has reacted immediately to balance the deficit in power in this transition period and the AC voltage, as well as, the system frequency are regulated at their rated values.

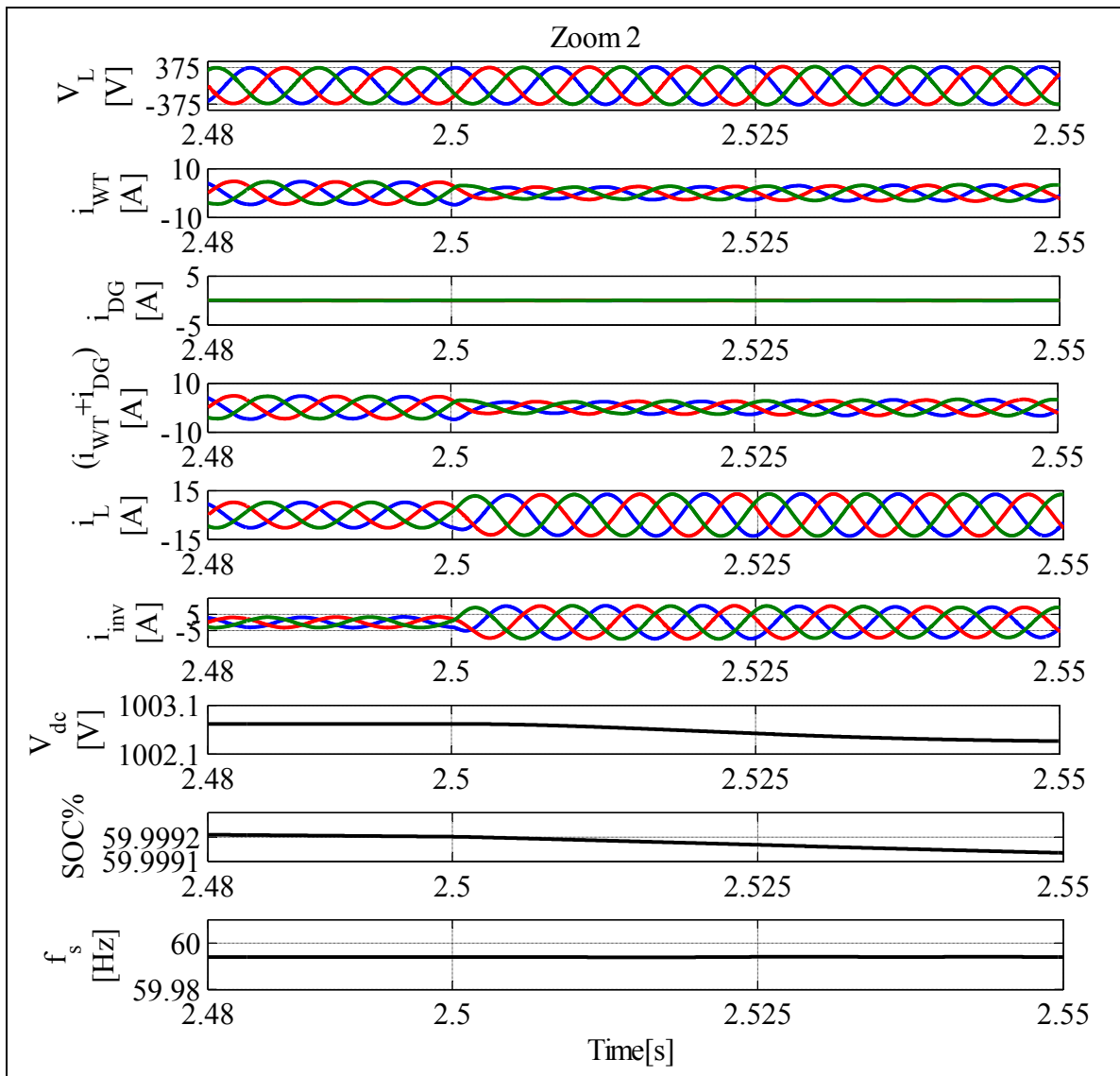


Figure 7.13 Zoom2 of the results shown in Fig.7.11 between  $t = 2.48$  s and  $t = 2.55$  s

### Performance analysis during wind speed and load changes and when the SOC% is less than 50%

Waveforms shown in Fig.7.14 represent the simulation results of the AC voltage ( $v_L$ ), WT current ( $i_{WT}$ ), output DG current ( $i_{DG}$ ), phase shift  $\theta_L$  of the AC voltage, phase shift  $\theta_{DG}$  of the terminal DG voltage, source current ( $i_s=i_{DG}+i_{WT}$ ), load current ( $i_L$ ), inverter current ( $i_{inv}$ ), DC voltage (Vdc), state of charge of battery (SOC%) and the system frequency (fs). To test the performance of the proposed WT-DG HSPGS, simulation is carried out using Matlab/Simulink.

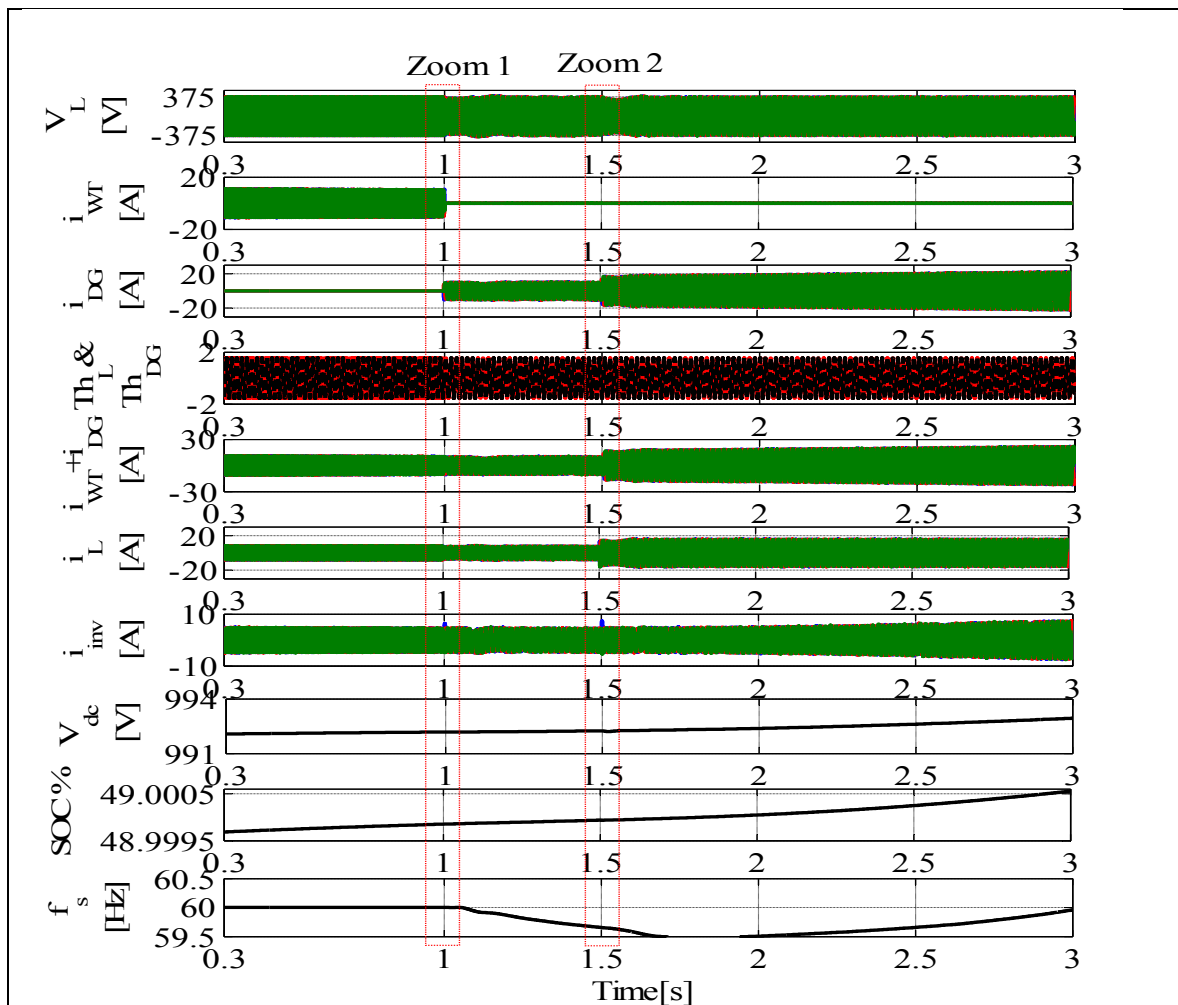


Figure 7.14 Dynamic performance of WT-DG HSPGS based on fixed speed generators when SOC% is less than 50%

The proposed WT-DG HSPGS employing fixed speed generators is subjected to the wind speed and load variation when the SOC% is less than 50%. It is observed that between  $t = 0.3$  s and  $t = 1$  s, the SOC% is less than 50% and  $i_{DG}$  is equal to 0. Seeing that the second condition ( $i_{WT} > i_L$ ) is not verified DG is still turn off. In this period of time the inverter current is increased ( $i_{inv}=i_s-i_L$ ), as well as, the SOC% and  $V_{dc}$  which means BESS is charging. At  $t = 1$  s, wind speed becomes equal to 0. Now, the second conditions to turn on DG is verified ( $i_L > i_{WT}$ ). Therefore, at  $t = 1$  s, the difference between  $\theta_L$  and  $\theta_{DG}$  is equal to 0, and that is why DG starts providing power to the load and charge the BESS simultaneously. It is observed that at  $t = 1.5$  s, the WT-DG HSPGS is subjected to a sudden load increase and at this time  $i_{WT} = 0$ , therefore,  $i_{DG}$  is increased. At the same time  $i_{inv}$ , SOC% and  $V_{dc}$  are increased signifying, BESS is charging. Using this new control it is observed that DG is used as an emergency ES, which allows increasing its life span and minimizing the use of the fuel.

Fig.7.15 shows zoomed waveforms of the results shown in Fig.7.14 between  $t = 0.98$  s and  $t = 1.05$  s. It is observed that from  $t = 0.9$  s to  $t = 1$  s, the SOC% is less to 50% and  $i_{WT}$  is greater to  $i_L$ . Therefore, DG is kept off ( $i_{DG} = 0$ ). WT provides extra power, which is not consumed by load, is absorbed by BESS. It is observed that at  $t = 1$  s,  $i_{WT}$  becomes equal to zero and the SOC% is less to 50%. Thus, conditions to start up DG are fulfilling from  $t = 1$  s,  $i_{DG} \neq 0$  and  $\theta_L = \theta_{DG}$ . It is observed that the synchronization between  $\theta_{DG}$  and  $\theta_L$ , is obtained at  $t = 1$  s, and DG starts working, but it achieves its rated speed within 0.01s due to slow dynamic of the DG. Thereby satisfying the requirement of CSA Z32 (Emergency electrical power supply for buildings), which requires less than 10 second.

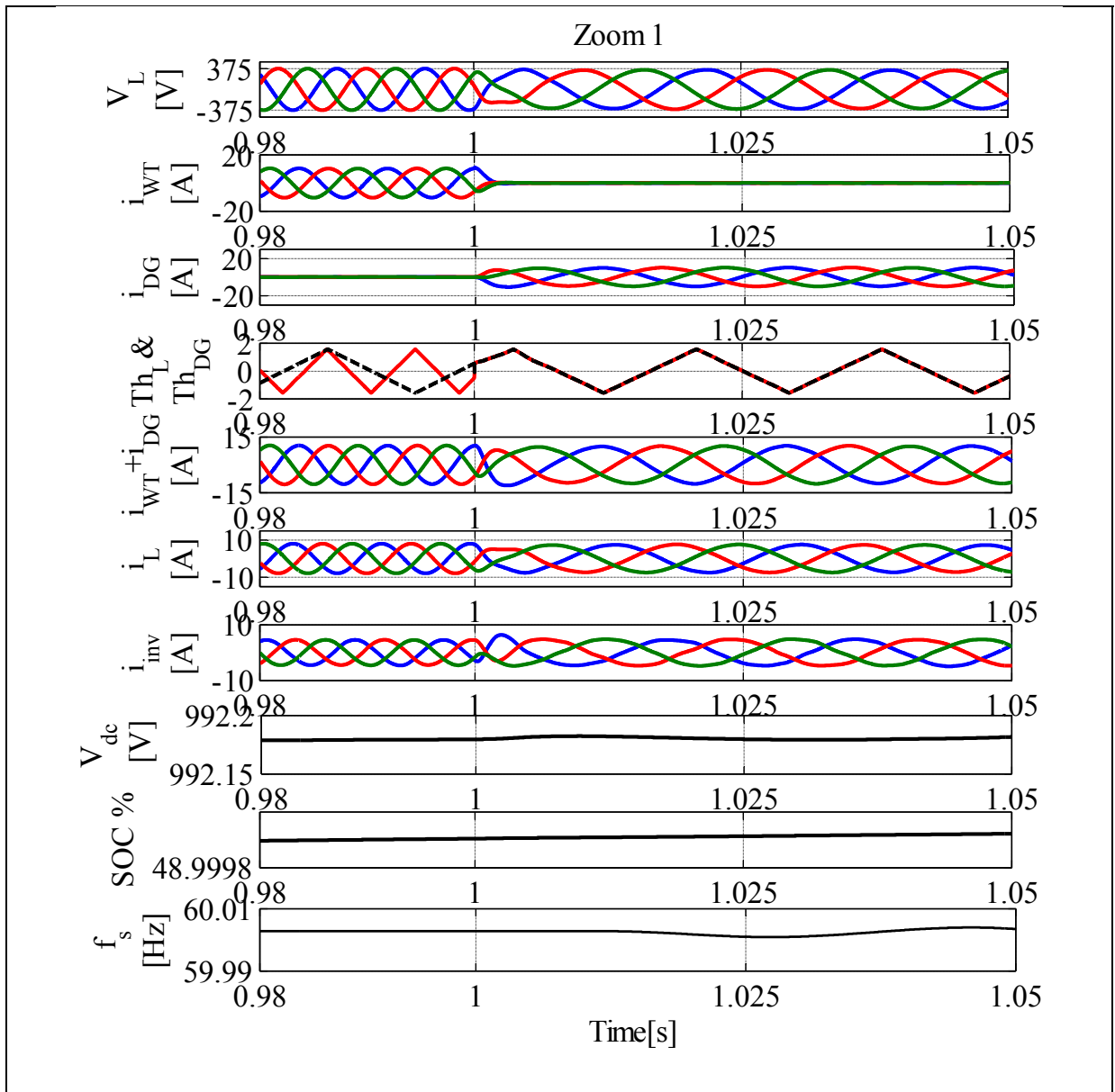


Figure 7.15 Zoom1 of the results shown in Fig.7.14 between  $t=0.98$  s and  $t=1.05$  s

Fig.7.16 shows zoomed waveforms of the results shown in Fig.7.14 between  $t= 1.48$  s and  $t= 1.55$  s. It is observed that  $i_{WT}$  is equal to 0 and load is supplied by only DG. Furthermore, DG in this operation mode is charging the BESS. It is observed that at  $t= 1.5$  s, load is increased, seeing that  $i_{WT}$  is equal to 0, DG supplies load and charges BESS, simultaneously.

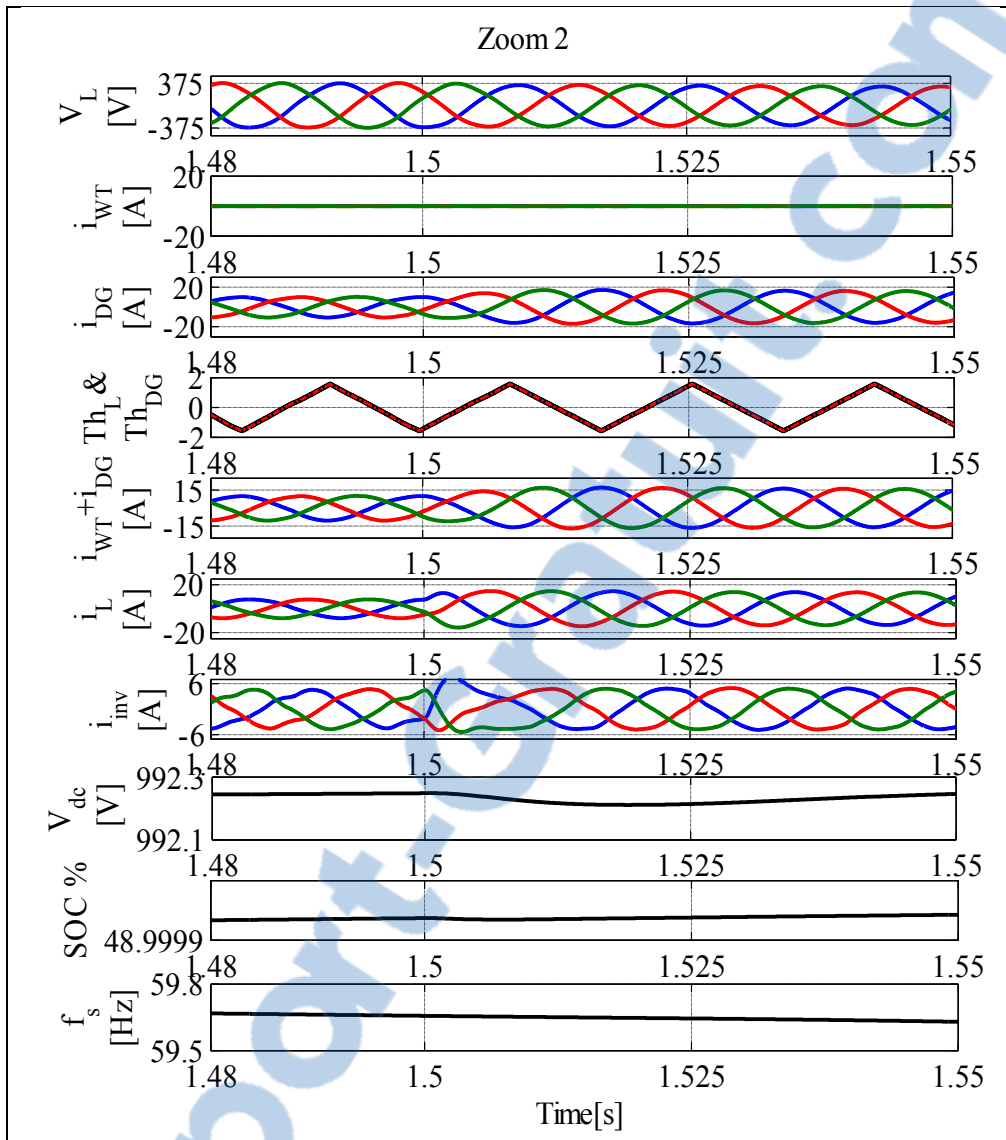


Figure 7.16 Zoom2 of simulation results shown in Fig.7.14 between  $t=1.48$  s and  $t=1.55$ s

### Performance analysis during presence of balanced and unbalanced nonlinear loads and when the SOC% is less than 50%

Figs. 7.17 and 18 shows the waveforms of the line voltage ( $v_L$ ), source current ( $i_s = i_{DG} + i_{WT}$ ), total load current ( $i_L + i_{NL}$ ), nonlinear load current ( $i_{NL}$ ), inverter current ( $i_{inv}$ ), DC voltage ( $V_{dc}$ ), state of charge battery (SOC %), and the system frequency ( $f_s$ ).

The performance of the system under balanced nonlinear loads is shown in Fig.6.17. The responses are observed when nonlinear is switched ON at  $t=1.5$  s. One may see that the magnitude of the source current, which represents the sum of the output currents of DG ( $i_{DG}$ ) and the WT ( $i_{WT}$ ) is increased at  $t=1.5$  s which denotes that DG provides more power in order to satisfy load power demand and charges the BESS simultaneously. Moreover, the AC voltage and the system frequency are well regulated and kept constant even in case of transition period at  $t=1.5$ s and during presence of balanced linear load from  $t=1.5$ s to  $t=1.55$ s. Here one may see that under balanced nonlinear load, the source current ( $i_s = i_{DG} + i_{WT}$ ), as well as, the AC voltage are balanced and sinusoidal with nearly unity power factor.

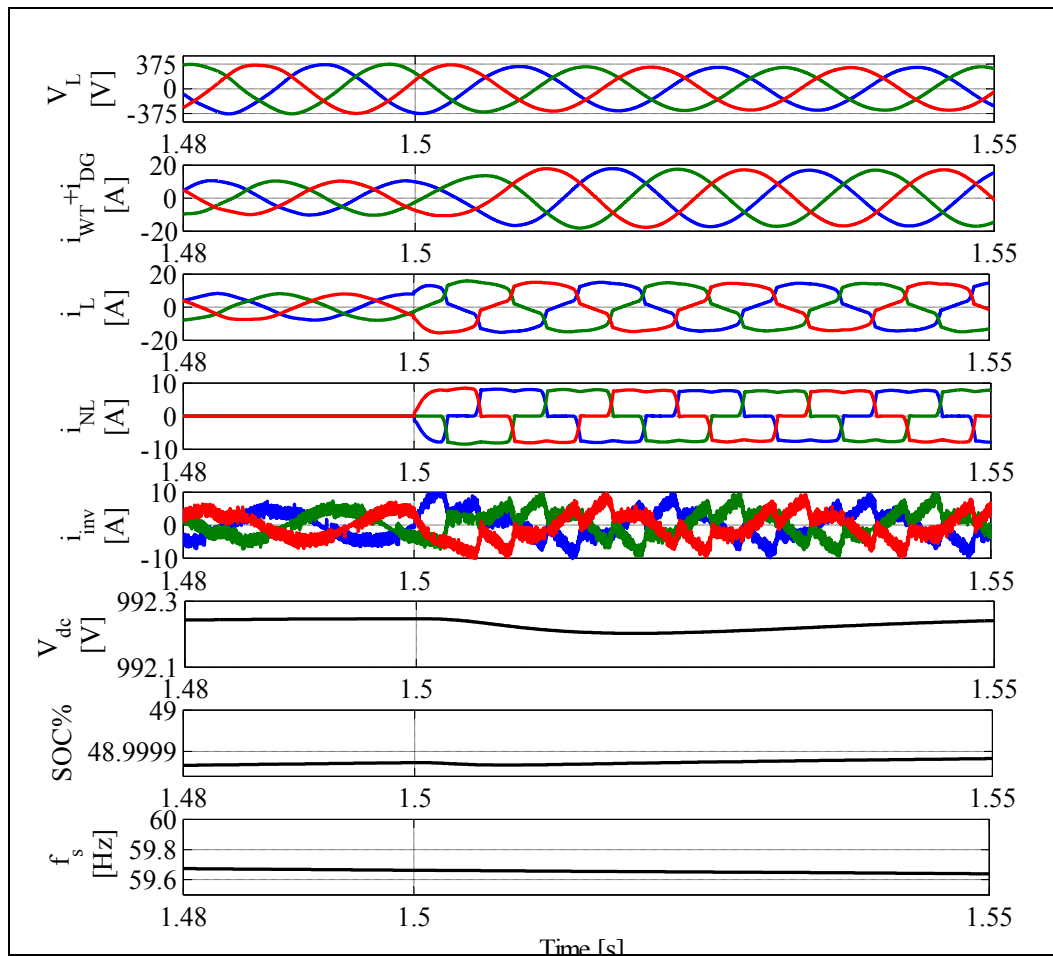


Figure 7.17 Dynamic performance of interfacing inverter under balanced nonlinear load

The dynamic performance of the proposed WT-DG HSPGS under unbalanced nonlinear loads is shown in Fig.6.18. The responses are observed when nonlinear is switched ON at  $t=2$  s. It is observed that the state of charge of BESS is increasing. One may see that the AC voltage and the system frequency at the PCC are regulated at their rated values during presence of balanced and unbalanced nonlinear load from  $t=1.98$  s to  $t=2$ s and from  $t=2$ s to  $t= 2.05$ s, respectively. Here one may see that the source current ( $i_s= i_{DG+} i_{WT}$ ), as well as, the AC voltage are balanced and sinusoidal with nearly unity power factor. It is observed that the interfacing DC/AC inverter acts as active filter to compensate load current harmonics and balance the source current and as battery charger.

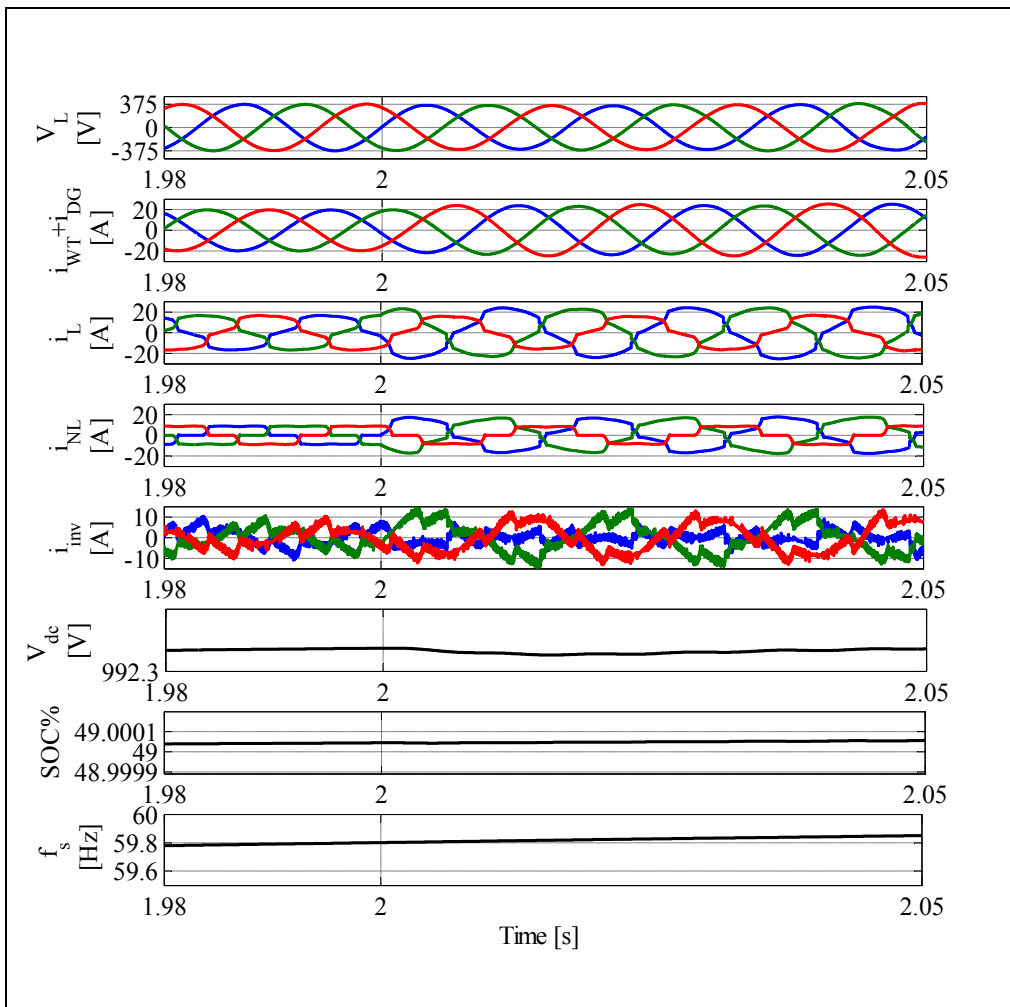


Figure 7.18 Dynamic performance of interfacing inverter under unbalanced nonlinear load

### Performance analysis when BESS becomes fully charged (SOC%=100%)

Fig. 7.19 shows the waveforms of the AC voltage ( $v_L$ ), system frequency ( $f_s$ ), DC-bus voltage ( $V_{dc}$ ), state of charge battery (SOC%), power provided by DG ( $P_{DG}$ ), power provided by WT ( $P_{WT}$ ), power consumed by load ( $P_L$ ) and that dissipated in dump load ( $P_d$ ) when the BESS becomes fully charged.

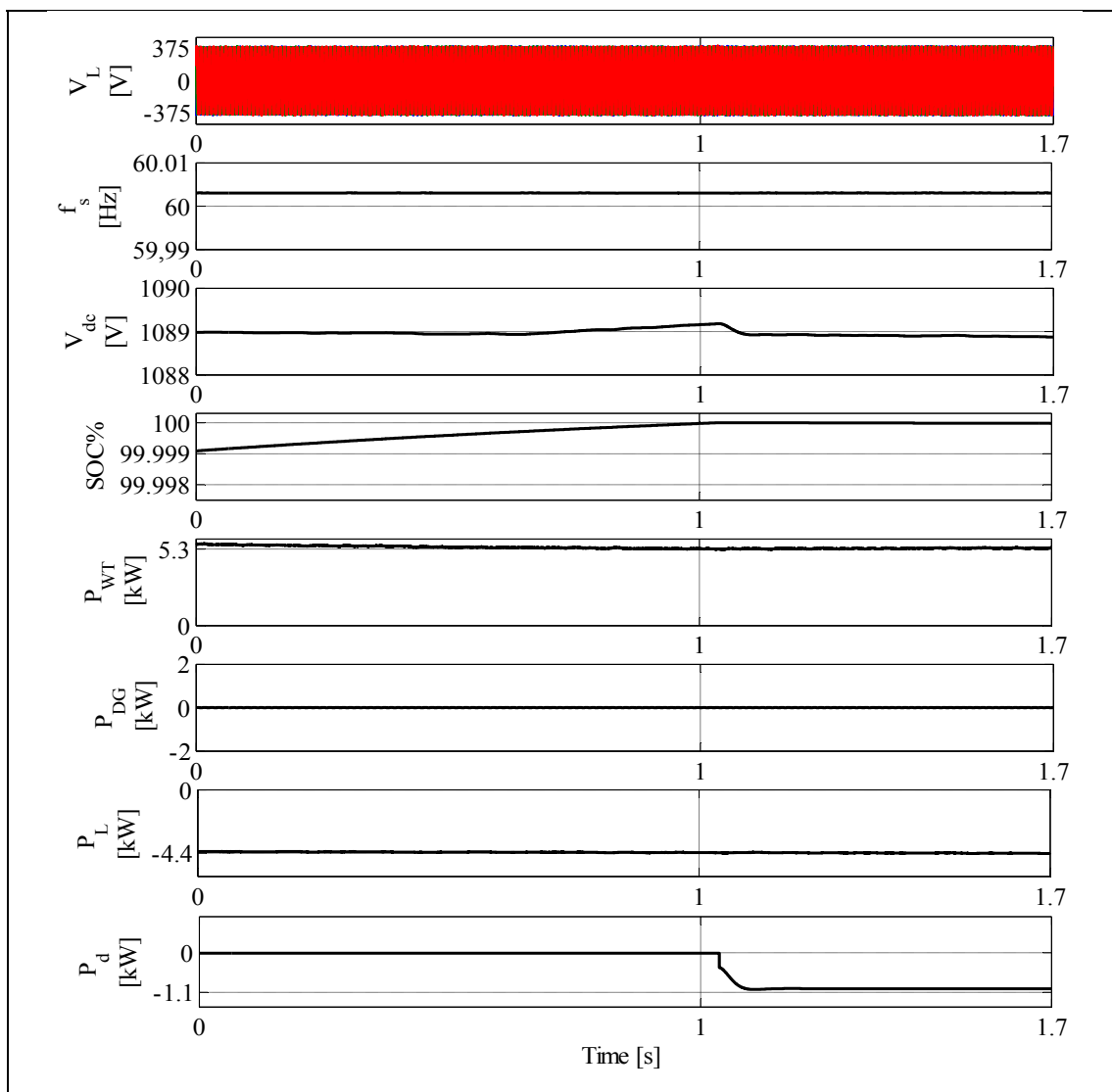


Figure 7.19 Dynamic performance of WT-DG HSPGS employing fixed speed generators when the SOC% of BESS is equal to 100%

One may see that DG is turn OFF ( $P_{DG}=0$ ) because of the SOC% is equal to 100%. Therefore, to ensure stable operating of the proposed WT-DG HSPGS and protect BESS from overcharging, dump load should be turned ON to dump the extra power provided by WT. At  $t=1$  s, this condition is fulfilling and that is why dump load power ( $P_d$ ) is equal to ( $P_d=(P_{WT}+P_{DG})-P_L$ ). It is observed that the DC link voltage, which represents the battery voltage, is kept constant and the AC voltage and the system frequency at the PCC are regulated at their rated values.

#### **7.4.2 Performance of the hybrid standalone power generation system based on DG and WT driven variable speed PMSG and PMBLDCG**

Simulations are carried out using MATLAB/Simulink to test the performance of the selected WT-DG HSPGS employing variable speed PMSG and PMBLDCG as shown in Fig.7.6, as well as, the robustness of the proposed control algorithms approach to get MPT from WT, to operate the DG at its maximum efficiency, as well as to regulate the AC voltage, system frequency and protect the BESS from overcharging. The system parameter values are given in Table A-10 in Appendix. Several scenarios, such as, a sudden change of the wind speed, load variation, as well as, when the SOC% of BESS becomes greater or less than 50%, and when it becomes equal to 100% are tested.

#### **Performance analysis under load and wind speed variation when the state of charge of battery is less than 100% but more than 50%**

Fig.7.20 shows the simulation results of the AC voltage ( $v_L$ ), load current ( $i_L$ ), system frequency ( $f_s$ ), wind speed, mechanical torque developed by WT ( $T_{mec}$ ), stator current of the PMBLDCG ( $i_{WT}$ ), WT current at the output of the diode bridge WT side ( $i_{dcWT}$ ), PMSG rotor speed ( $\omega_r$ ) and its reference ( $\omega_{rDGref}$ ), which represents the rotor speed of the DE, DG current at the output of the diode bridge DG side ( $i_{dcDG}$ ) DC voltage ( $V_{dc}$ ) and the state of charge of battery (SOC%).

It is observed that the stator current of PMBLDCG varies with this variation of the wind speed, it increases at  $t=0.3$  s and increases more at  $t=1.1$  s., which confirms the proposed

control approach based on P&O technique for MPT from WT. Because of the SOC% of BESS is greater than 50%, DG is turned OFF in this test. Therefore, only BESS and WT are supplying loads. It is observed that the use of BESS prevents DG to run at light load, which allows fuel savings. One may see that the AC voltage and the system frequency are maintaining constant, which confirms the robustness of the proposed control algorithm for the DC/AC interfacing inverter.

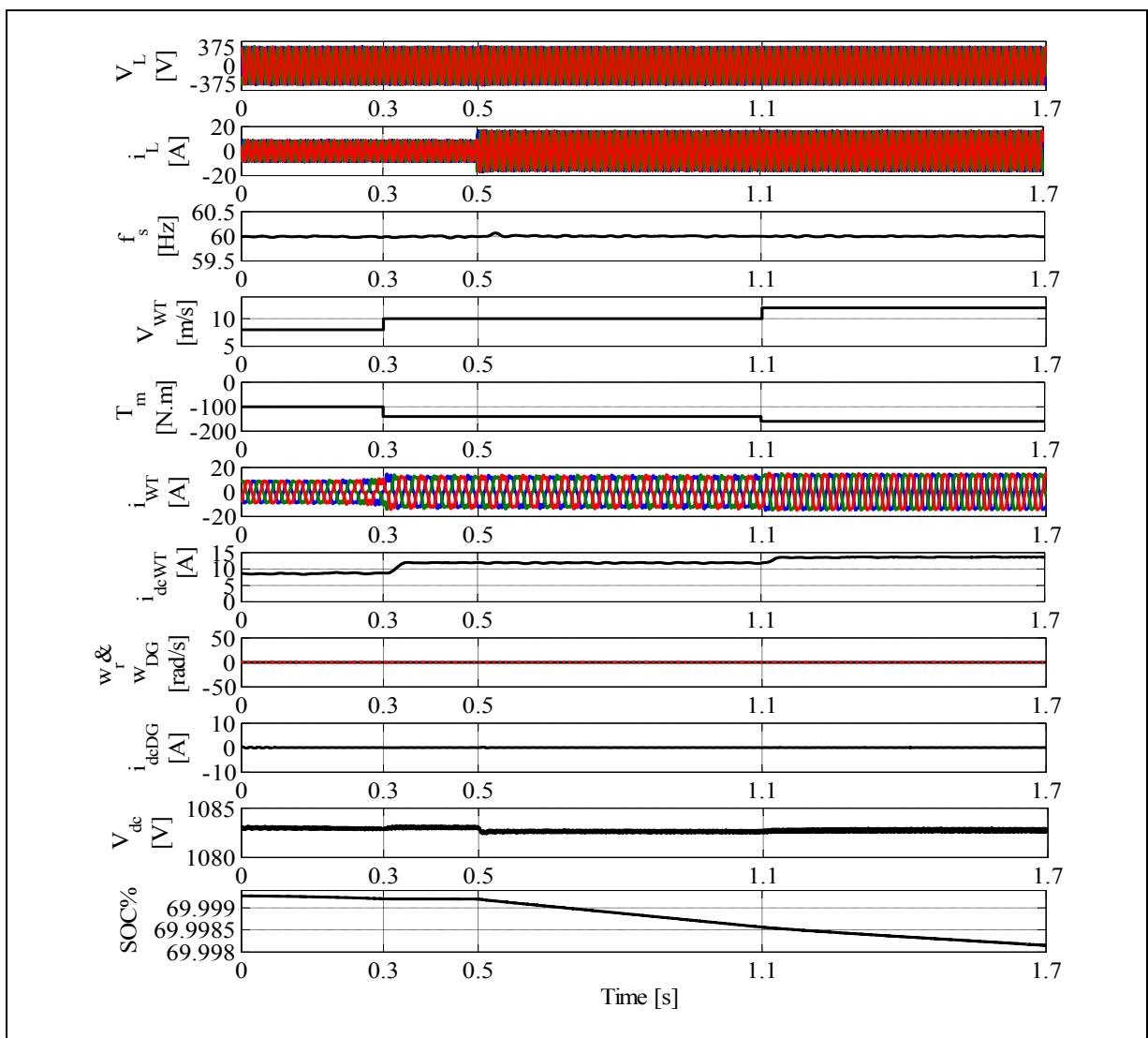


Figure 7.20 Dynamic response of WT-DG HSPGS based on variable speed generators when the SOC% of BESS is less than 100% and more than 50%

### Performance analysis under load and wind speed variation when the state of charge of battery is less than 50%

The dynamic response of the proposed WT-DG HSPGS when the state of charge of BESS is less than 50%, are shown in Fig.7.21. It is observed that DG is turn ON, it provides power to loads and charge the BESS simultaneously. It is observed that the output current of PMSG varies with variation of loads rotor speed of the PMSG ( $\omega_r$ ) follows its reference ( $\omega_{ref}$ ), which represents the DE speed. This confirms that the robustness of the proposed control for DC/DC boost converter WT side. The AC voltage and the system frequency are regulated at their rated values.

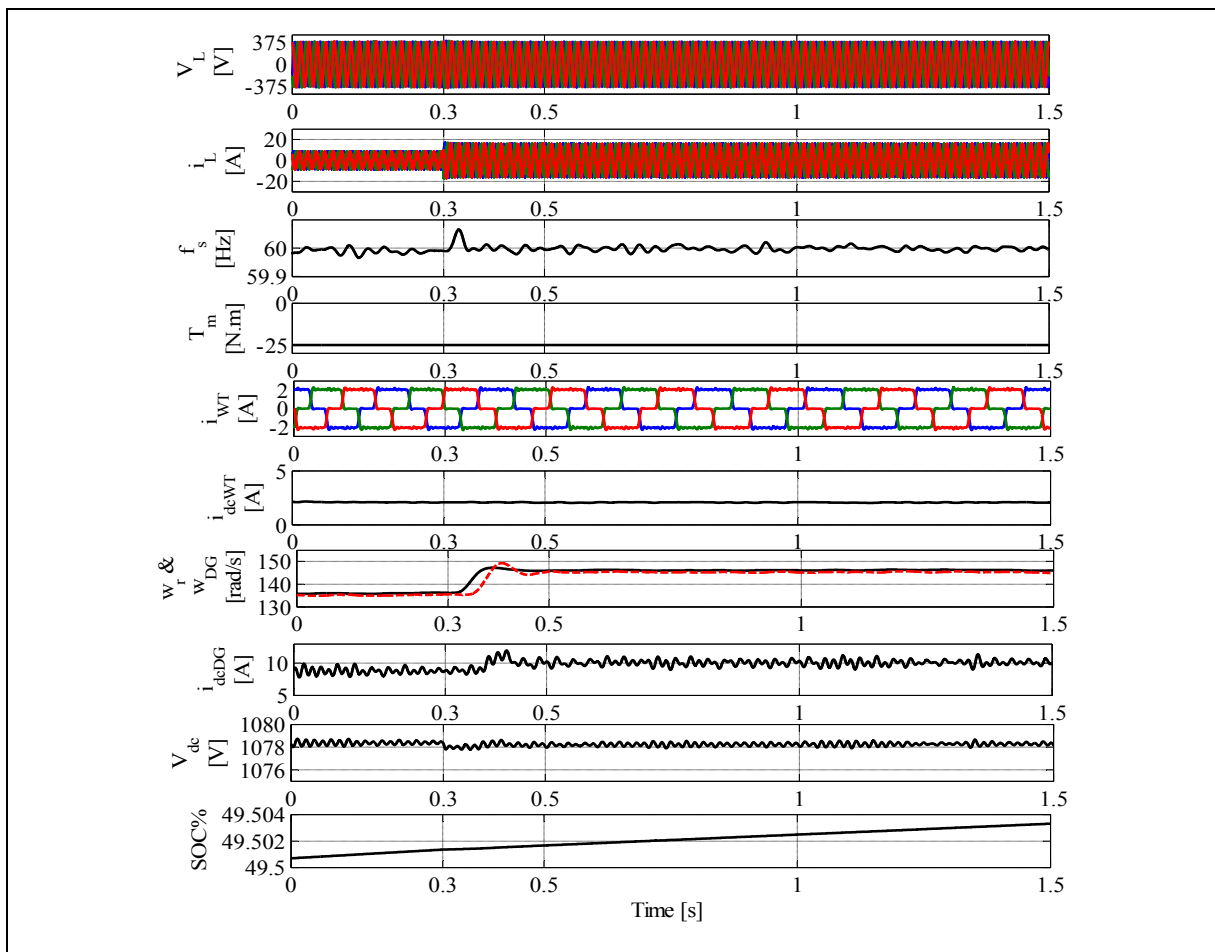


Figure 7.21 Dynamic response of WT-DG HSPGS based on variable speed generators when SOC% of BESS is less than 50%

### Performance analysis under unbalanced linear loads

Fig.7.23 presents the dynamic performance of the proposed topology under unbalanced linear load. AC voltage ( $v_L$ ), system frequency ( $f_s$ ), load current ( $i_L$ ), neutral current ( $i_n$ ), DC link voltage ( $v_{dc}$ ), and the state of charge of BESS are presented. The load is made unbalanced by opening the terminal of phase «a». It is observed that  $i_L$  is zero under unbalance condition and neutral current is not equal to zero in this period of time. The AC voltage in this transition period is kept constant and sinusoidal with zero steady-state error. Furthermore, the system frequency is regulated at their rated value.

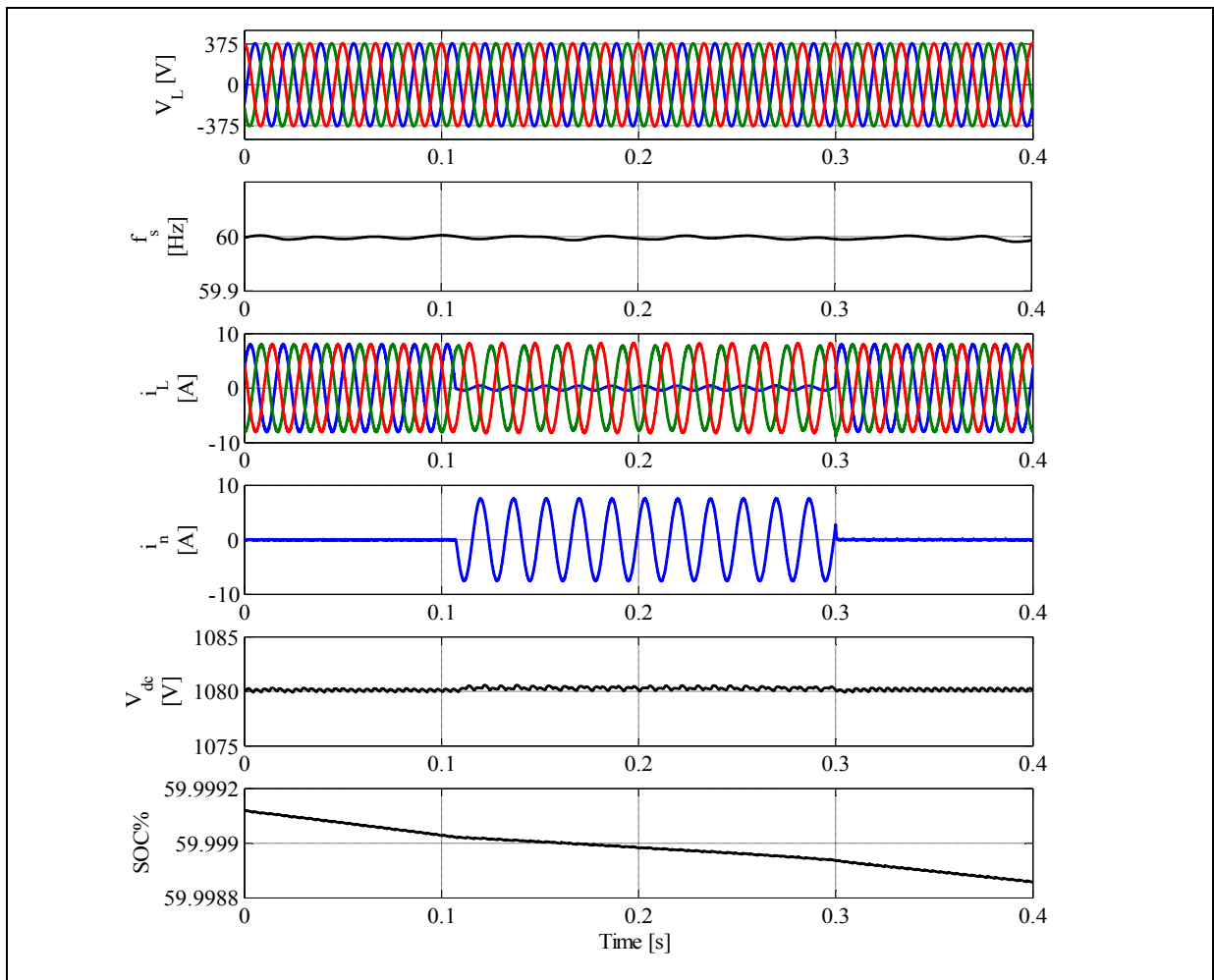


Figure 7.22 Dynamic performance of the of WT-DG HSPGS based on variable speed generators under unbalanced linear load

### Performance analysis under unbalanced nonlinear loads

Fig.7.24 presents the dynamic performance of the proposed topology under unbalanced nonlinear load. The load is made unbalanced by opening the terminal of phase «a». It is observed that  $i_L$  is zero under unbalance condition and neutral current is not equal to zero in this period of time. The AC voltage in this transition period is kept constant and sinusoidal with zero steady-state error. Furthermore, the system frequency is regulated at its rated value.

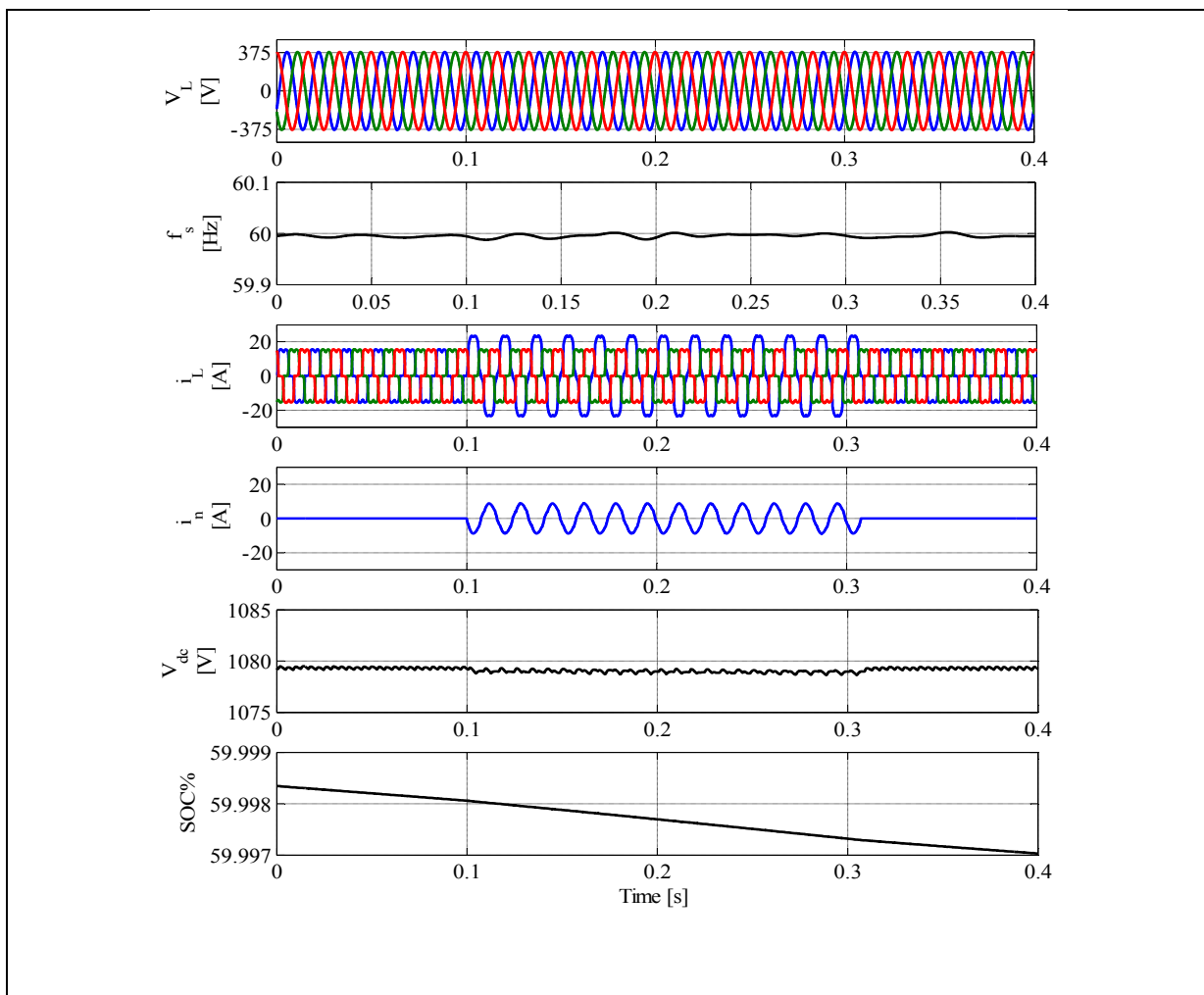


Figure 7.23 Dynamic performance of WT-DG HSPGS based on variable speed generators under unbalanced nonlinear load

### Performance analysis when the state of charge of battery is equal to 100%

Fig.7.24 presents the dynamic performance of the proposed control for dump load when the SOC% of BESS is equal to 100%. AC voltage ( $v_L$ ), system frequency ( $f_s$ ), state of charge of battery (SOC %), wind turbine power ( $P_{WT}$ ), diesel generator power ( $P_{DG}$ ), battery power ( $P_{bat}$ ), dump load power ( $P_{dL}$ ) and load power demand ( $P_L$ ) are presented.

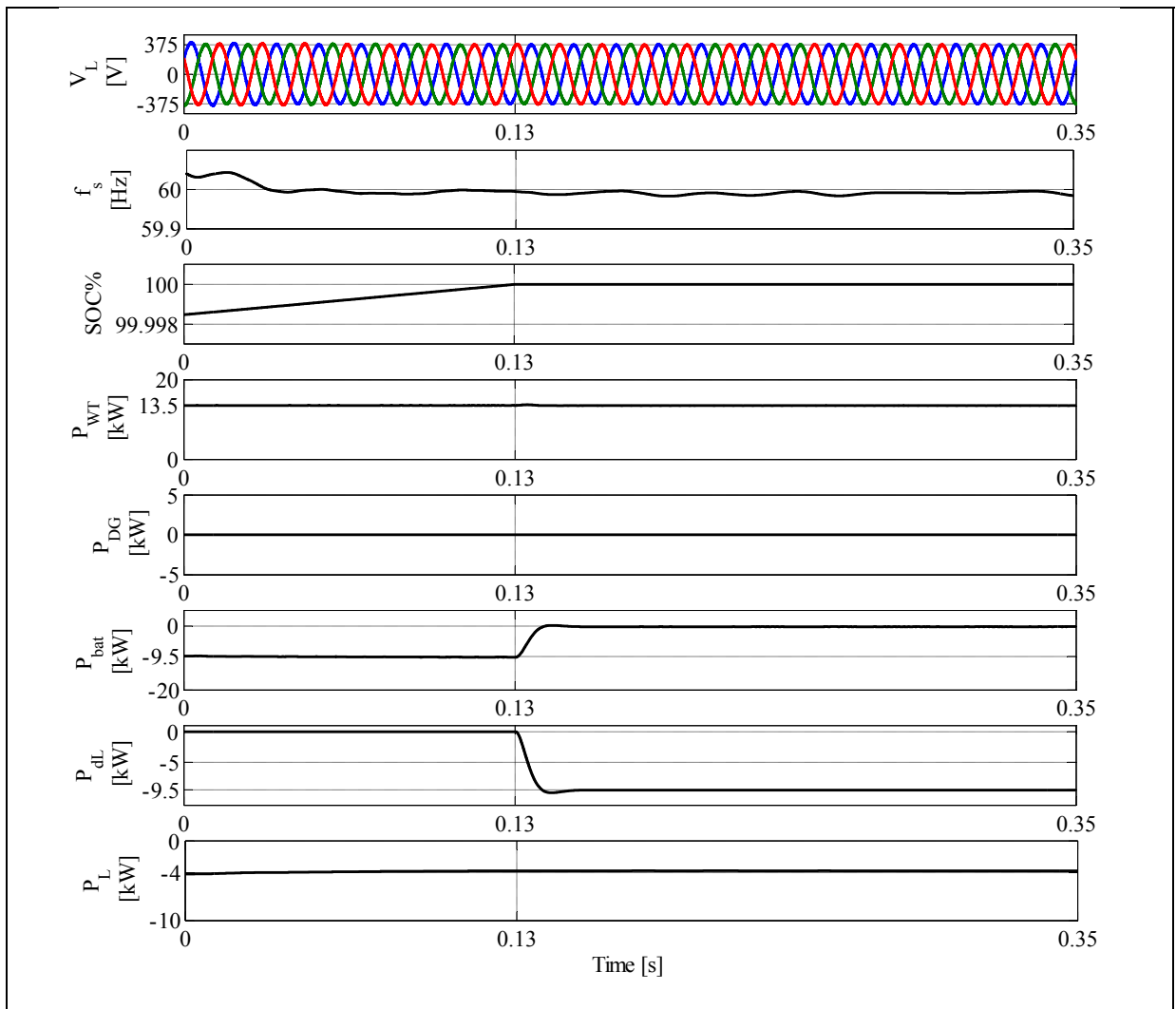


Figure 7.24 Dynamic performance of WT-DG HSPGS based on variable speed generators when the SOC% of BESS is equal to 100%

It is observed that between  $t=0.1$  s and  $t=0.13$ s, power provided by WT is greater than the load power demand, and that is why BESS is charging. At  $t=0.13$ s BESS reaches its maximum voltage (SOC%=100%). However, extra power ( $P_{WT} - P_L$ ) should be dissipated in dump load in order to protect BESS from overcharging. It is observed that dump load reacts instantaneously at  $t=0.13$  s. One may see that dump load power is 9.5kW, which represents the ( $P_{WT} - P_L$ ) and battery power is zero ( $P_{bat}=0$ ).

## 7.5 Conclusion

Several HSPGS which are based on WT and DG driven fixed and variable speed generators are discussed. Two different topologies are selected for study in detail. In the first HSPGS, SG and PMSG are used as generator for DG and WT, respectively. To regulate the AC voltage and the system frequency, as well as, to improve the power quality at the PCC, modified SRF approach control is used. The obtained results in the presence of different conditions, such as load and wind speed variations, as well as, when BESS becomes fully charged, show satisfactory performance. Based on this proposed design, DG becomes as backup ES, which leads minimizing of the use of the fuel. The second topology which is based on variable speed PMSG and PMBLDCG, P&O technique is used to get MPPT from the WT without sensing rotor speed. For controlling the rotor speed of PMSG, optimal rotational speed versus load curve is used to estimate PMSG rotor speed. For the AC voltage and the system frequency, control approach based on decomposition on symmetrical components of the load voltage and current is used. The obtained results in different conditions show satisfactory performances.

## CONCLUSION

In this thesis, many topologies designs and control algorithms for SPGS and HSPGS are discussed. In these topologies, different energy sources, such as solar PV array, MHP, WT and DG, as well as, various electrical machine types (e.g., PMSG, SG, PMBLDCG, SCIG, DFIG, SyRG) are used. In addition, fixed and variable speed generators technologies are tested. Extensive simulation tests and experimental results, for selected topologies, are provided.

Some of the major achievements of the thesis work are summarized as follows:

For SPGS based on solar PV array, new control algorithm designs using sliding mode approach for MPPT, AC voltage and system frequency regulation are proposed. This topology operates without dump load and offers protection of the BESS from overcharging using new current feedback control by forcing solar PV array to deliver exactly the required power load demands. This new proposed technique makes the SPGS based on solar PV array more effective, less expensive and stable. The performance of the proposed control approaches have been validate through simulation and experimental investigation.

Optimal design of PV-DG HSPGSs employing fixed and variable speed generators topologies have been proposed. To isolate DG from PCC, controlled switch is integrated in PV-DG HSPGSs employing fixed speed generators. To connect DG from the PCC without disrupting the local grid, new control algorithm has been developed. To regulate the AC voltage and the system frequency, as well as, to improve the power quality at the PCC, p-q theory control algorithm has been extended. Indirect stator flux oriented control has been proposed to control the rotor speed of DFIG. The obtained results for PV-DG HSPGSs employing fixed speed SG and variable speed DFIG show satisfactory performance during load and solar irradiation change and when the BESS becomes fully charged. DG in the proposed topology becomes as backup ES instead of principal ES. It is turned on only if the

provided power from solar PV array is less than the load power demand and when the SOC% is less than 50%, which leads to saving fuel and increasing DE span life.

In PV-MHP HSPGS only a fixed speed generator technology has been considered. Anti-Hebbian control approach and instantaneous p-q theory control have been extended to incorporate the AC voltage and system frequency regulation, as well as, MPPT from solar PV array for the topology that uses single-stage inverter. Dynamic performance under different conditions of PV-MHP HSPGSs employing SyRG and SCIG show satisfactory. To achieve frequency regulation in PV-MHP HSPGS that uses single-stage inverter, Buck-Boost DC converter is proposed. Using this converter as BESS charger, the rating of BESS is reduced and hence the overall cost of the proposed topology.

Design and control of PV-WT HSPGSs employing fixed and variable speed generators have been presented. Control algorithms, such as, indirect control and d-q control have been extended to achieve the AC voltage and system frequency regulation. To get MPPT from solar PV array and WT, P&O technique and rotor oriented control have been proposed. The obtained results during presence of different conditions, such as, wind speed and solar irradiances change, as well as, during load variation and when BESS becomes fully charged show satisfactory. New small-scale PV-WT HSPGSs employing variable speed PMBLDCG without dump load has also been proposed. To achieve MPPT from WT and PV array, SMC approach has been used. For AC voltage and system frequency at the PCC new control approach has been proposed. The performance of the newly introduced topology has been successfully validated through simulation, as well as, experimental results.

An innovative WT-DG HSPGSs employing fixed and variable speed generators have been presented. A special attention has been given to the fuel saving from DG side and power quality improvement at the PCC in the proposed WT-DG HSPGSs employing fixed speed generators. Three-phase inverter and BESS, and controlled switch have been added in the proposed topologies. SRF control has been extended to regulate the AC voltage and the system frequency, as well as, to control the power flow between BESS and the PCC.

An advanced WT-DG HSPGS employing variable speed generators has also been presented. In this topology, two-level neutral point clamped (NPC) has been proposed to connect the load neutral current. To achieve MPPT from WT and DG, P&O and optimal rotational speed vs load curve characteristic have been used. Control approach based on decomposition into symmetrical sequences of sensing AC voltage and load current has been proposed for AC voltage, and system frequency regulation, as well as, for power quality improvement at the PCC. The proposed WT-DG HSPGS employing variable speed generators and their developed control approaches have been successfully validate through simulation.

In summary, this thesis work puts forward new design topologies for SPGSs and HSPGSs employing fixed and variable speed generators, as well as, new control philosophy, which not only improves these types of installation but also reduces the overall system cost. Furthermore, it also proves that with these proposed topologies, can ensure a clean and interruptible power supply with reduced cost in the isolated areas. The work reported in this thesis with extensive experimental validation would certainly be considered as a remarkable development in the field of design and control of SPGSs and HSPGSs.



## RECOMMENDATIONS

Although the simulation and the experimental validation of the control schemes in this research show satisfactory performance, some recommendations for future research work can be considered and are as follows:

In this thesis some of the proposed topologies and control algorithms were only simulated because of non-availability of the equipment and the lack of space in the hardware Lab. It will be interesting to implement and validate them in real time.

In the proposed topologies most of the energy sources and their connected converters are tied to the DC bus. Therefore, presence of ripple current and voltage due to the high switching frequency at the DC bus increases BESS temperature. Elevated BESS temperature reduces its lifespan. Therefore, additional elements, such as LC filter is recommended. To determine the required values of the proposed LC filter, accurate design is recommended.

Desired BESS voltage which represents the DC link voltage is obtained using series-parallel connections of several batteries. Therefore, additional circuits are required to balance the series-parallel connection, in order to increase safety, and extended the BESS lifespan.

Mostly, the dynamic responses of existing battery technologies, such as, lead acid battery of Ni-Cd battery have slow dynamic response. However, to compensate instantaneously the fluctuation of generated power from renewable energy sources, additional storage elements which are characterized by fast dynamic response and high density, such as supercapacitor is required for SPGS and HSPGS. With help of supercapacitor, one can compensate short fluctuation instantaneously. However, one ensures stable power supply to the connected loads and extended the lifespan of the existing BESS.

For the proposed SPGS and HSPGS, energy management control is recommended to ensure stable and effective operation of different elements of system.

Most of existing HSPGSs use decentralized control. Each element of the system possesses its own control algorithm. To increase the profitability of these proposed topologies, centralized control is recommended. In addition, remotely diagnostics of installation in real time using digital communication networks to transmit the collect data to data center is suggested in order to minimize the additional costs of minor system maintenance and displacement of technician to these remote areas.

## APPENDIX I

### Systems Parameters

Table-A I-1 System parameters of PV array

Elements	Parameters and values
<b>PV array and DC/DC boost converter</b>	$i_{rr}=5.981 \cdot 10^{-8}$ A, $i_{scr}=3.81$ A, $k_i=0.0024$ , $T_r=298$ K, $q=1.6 \cdot 10^{-19}$ C, $K_b=1.38 \cdot 10^{-23}$ J/K, $E_g=1.12$ V, $A=1.2$ , $L=1.5$ mH, $C_{out}=200\mu$ F
<b>Battery Energy storage</b>	$V_{batmax}=V_{ocmax}=78.5$ V, $V_{ocmin}=68.5$ V, $V_{bat}=72$ V, $C_b=7346$ F, $N_b$ of batteries=12, (2string connected in parallel and each string possess 6 batteries connected in series)
<b>CC-VSC and load</b>	$L_f=5$ mH, $C_f=10$ $\mu$ F, $f_s=2$ kHz, $R_L=8\Omega$ , $k=0.1$ , $k_1=0.01$ , $k_2=0.01$ , $k_p=5$ , $k_i=10$ , $C_{pv}=100$ $\mu$ F, $f=60$ Hz, $v_{Lmax}=30$ V,

Table-A I-2 System parameters of Hybrid PV-DG based on fixed speed SG

Elements	Parameters and values
<b>PV array and DC/DC boost converter</b>	$i_{rr}=5.981 \cdot 10^{-8}$ A, $i_{scr}=3.81$ A, $K_i=0.0024$ , $T_r=298$ K, $q=1.6 \cdot 10^{-19}$ $E_g=1.12$ V, $A=1.2$ , $L=1.5$ mH, $C_{out}=200\mu$ F, $V_{out}=1000$ V
<b>DG</b>	<b>DE model</b> $K_i=1$ , $k_p=5$ , $k_I=1$ , $k_2=1$ , $\tau_1=0.4$ , $\tau_2=0.011$
	<b>AVR</b> $a=0.046$ , $b=4.8$ , $c=0.345$ , $d=0.0067$ , $e=13$ , $k_1=5.1$ , $k_2=-5.1$ , $k_3=5.1$ $V_{ref}=460$ V
	<b>SG</b> $S_n=10.2$ kVA, $V_{LL}=460$ V, $f_s=60$ Hz, $r_f=1.163\Omega$ , $L_f=0.01143$ H, $r_{Dd}=3.66$ $\Omega$ , $L_{Dd}=0.009167$ H, $r_{Dq}=4.752$ $\Omega$ , $L_{Dq}=0.01006$ H, $J=0.0923$ kg.m <sup>2</sup> , $2P=4$ , $F=0.0152$ N.m.s
<b>BESS and dump load</b>	$V_{bat}=1000$ V, $V_{ocmin}=980$ V, $V_{ocmax}=1088$ V, $C_b=6963$ F, $R_s=0.01$ $\Omega$ , $R_b=10$ k $\Omega$ , $C_{dc}=5000\mu$ F, $L_b=1$ mH, $R_d=142.85$ $\Omega$
<b>AC bus and Loads</b>	$V_{LL}=460$ V, $f_s=60$ Hz, $R=5$ $\Omega$ , nonlinear load (Diode bridge), $R_L=60$ $\Omega$ , $L_L=10e-3$ mH

Table-A I-3 System parameters of Hybrid PV-DG based on variable speed DFIG

Elements		Parameters and values
<b>PV array and DC/DC boost converter</b>		$i_{rr}= 5.981 \cdot 10^{-8}$ A, $i_{scr}=3.81A$ , $K_i=0.0024$ , $T_r=298K$ , $q=1.6 \cdot 10^{-19}$ $E_g=1.12V$ , $A=1.2$ , $L=1.5mH$ , $C_{out}=200\mu F$ , $V_{out}=1000V$
<b>DG</b>	<b>DE model</b>	$K_i=120$ , $k_p=10$ , $k_I=1$ , $k_2=1$ , $\tau_1=0.4$ , $\tau_2=0.011$
	<b>DFIG and Capacitor bank</b>	$S_n=14$ kVA, $\omega_r=184rad/s$ , $V_{LL}=460V$ , $f_s=60Hz$ , $r_s=0.2761\Omega$ , $L_s=0.002191H$ , $r_r=0.1645\Omega$ , $L_r=0.002191H$ , $L_m=0.07614\Omega$ , , $J=0.1kg.m^2$ , $2P=4$ , $F=0.01771N.m.s$ , $C_{cap}=320\mu F$
<b>BESS and dump load</b>		$V_{bat}=1000V$ , $V_{ocmin}=980V$ , $V_{ocmax}=1088V$ , $C_b=4560F$ , $R_s=0.01\Omega$ , $R_b=10k\Omega$ , $R_d=97.08\Omega$
<b>AC bus and Loads</b>		$V_{LL}=460V$ , $f_s=60Hz$ , $R=10\Omega$ , <i>nonlinear load (Diode bridge)</i> , $R_L=50\Omega$ , $L_L=60e^{-3}mH$

Table-A I-4 System parameters of Hybrid PV-MHP based on fixed speed SyRG

Elements		Parameters and values
<b>PV array and DC/DC boost converter</b>		$i_{rr}= 5.981 \cdot 10^{-8}$ A, $i_{scr}=3.81A$ , $K_i=0.0024$ , $T_r=298K$ , $q=1.6 \cdot 10^{-19}$ $E_g=1.12V$ , $A=1.2$ , $L=1.5mH$ , $C_{out}=200\mu F$ , $V_{out}=1000V$
<b>MHP</b>	<b>MHP model</b>	$T_0=19.89N.m$ , $m=0.1069$
	<b>SyRG and Capacitor bank</b>	$S_n=3.7$ kVA, $V_{LL}=460V$ , $f_s=60Hz$ , $L_{Dd}=0.009167H$ , $L_{Dq}=0.01006$ $C_{cap}=270\mu F$
<b>BESS and dump load</b>		$V_{bat}=1000V$ , $V_{ocmin}=980V$ , $V_{ocmax}=1088V$ , $C_b=4560F$ , $R_s=0.01\Omega$ , $R_b=10k\Omega$ , $R_d=97.08\Omega$
<b>AC bus and Loads</b>		$V_{LL}=460V$ , $f_s=60Hz$ , $R=10\Omega$ , <i>nonlinear load (Diode bridge)</i> , $R_L=50\Omega$ , $L_L=60e^{-3}mH$

Table-A I-5 System parameters of HSPGS based on PV array and MHP driven fixed speed SCIG

Elements	Parameters and values
<b>MHP and SCIG</b>	$T_0=39.7849\text{N.m}$ , $m=0.09$ , $P_n=3.7\text{kW}$ , $V_L=460\text{V}$ , $f_s=60\text{Hz}$ , $R_s=1.115\Omega$ , $L_{ls}=0.005974$ , $L_m=0.2037\text{H}$ , $2P=4$ , $J=0.02 \text{ kg.m}^2$ , $F=0.006\text{N.m.s}$ , $C_c=270 \mu\text{F}$
<b>Photovoltaic (PV) panel</b>	$P_{PV}= 5\text{kW}$ , $i_{rr}=5.981. 10^{-8} \text{ A}$ , $i_{scr}=3.81 \text{ A}$ , $T_r=298 \text{ K}$ , $q=1.6. 10^{-19}$ $C$ , $k_i=0.0024$ , $K_b=1.38. 10^{-23} \text{ J/K}$ , $E_g=1.12 \text{ V}$ , $C_{out}=200\mu\text{F}$
<b>Battery Energy Storage System</b>	$V_{ocmax}=450\text{V}$ , $V_{ocmin}=350\text{V}$ , $C_b=1080 \text{ F}$ , $R_b=10\text{k} \Omega$ , $R_s=0.01 \Omega$
<b>VSC and loads</b>	$L_f=5\text{mH}$ , $C_{dc}=2500 \mu\text{F}$ , $V_{dc}=750\text{V}$ , $P_L=5\text{kW}$ , NL (Three phase diode bridge) $R_L=10\Omega$ , $L_L= 20\text{mH}$

Table-A I-6 System parameters of Hybrid PV-WT based on fixed speed SCIG

Elements	Parameters and values
<b>PV array and DC/DC boost converter</b>	$i_{rr}= 5.981. 10^{-8} \text{ A}$ , $i_{scr}=3.81\text{A}$ , $K_i=0.0024$ , $T_r=298\text{K}$ , $q=1.6.10^{-19}$ $E_g=1.12\text{V}$ , $A=1.2$ , $L=1.5\text{mH}$ , $C_{out}=200\mu\text{F}$ , $V_{out}=1000\text{V}$
<b>WT</b>	<b>WT model</b> $P_{mec} = 14 \text{ kW}$ , $R = 5.7 \text{ m}$ , $C_1=0.5176$ , $C_2=116$ , $C_3=0.4$ , $C_4=5$ , $C_5=21$ , $C_6=0.0068$ , $\beta=0$ .
	<b>SCIG and Capacitor bank</b> $S_n=14 \text{ kVA}$ , $\omega_r=184\text{rad/s}$ , $V_{LL}=460\text{V}$ , $f_s=60\text{Hz}$ , $r_s=0.2761\Omega$ , $L_s=0.002191\text{H}$ , $r_r=0.1645 \Omega$ , $L_r=0.002191 \text{ H}$ , $L_m=0.07614 \Omega$ , , $J=0.1\text{kg.m}^2$ , $2P=4$ , $F=0.01771\text{N.m.s}$ , $C_{cap}=320 \mu\text{F}$
<b>BESS and dump load</b>	$V_{bat}=1000\text{V}$ , $V_{ocmin}=980\text{V}$ , $V_{ocmax}=1088\text{V}$ , $C_b=4560\text{F}$ , $R_s=0.01 \Omega$ , $R_b=10\text{k} \Omega$ , $C_{dc}=8000\mu\text{F}$ , $L_b=1\text{mH}$ , $R_d=38.46 \Omega$
<b>AC bus and Loads</b>	$V_{LL}=460\text{V}$ , $f_s=60\text{Hz}$ , $R=5 \Omega$ , nonlinear load (Diode bridge), $R_L=50 \Omega$ , $L_L=60e-3\text{mH}$

Table-A I-7 System parameters of Hybrid PV-WT based on variable speed SyRG

Elements	Parameters and values
<b>PV array and DC/DC boost converter</b>	$i_{rr}= 5.981. 10^{-8} \text{ A}$ , $i_{scr}=3.81\text{A}$ , $K_i=0.0024$ , $T_r=298\text{K}$ , $q=1.6.10^{-19}$ $E_g=1.12\text{V}$ , $A=1.2$ , $L=1.5\text{mH}$ , $C_{out}=200\mu\text{F}$ , $V_{out}=1000\text{V}$
<b>SyRG and Capacitor bank</b>	$S_n=10.2\text{kVA}$ , $\omega_r=1800\text{RPM}$ , $V_{LL}=460\text{V}$ , $f_s=60\text{Hz}$ , $r_s=162\Omega$ , $L_m=0.000451\text{H}$ , $J=0.0923\text{kg.m}^2$ , $2P=4$ , $F=0.0125\text{N.m.s}$ , $C_{cap}=5 \text{ kVar}$
<b>BESS and dump load</b>	$V_{bat}=1000\text{V}$ , $V_{ocmin}=980\text{V}$ , $V_{ocmax}=1088\text{V}$ , $C_b=4560\text{F}$ , $R_s=0.01 \Omega$ , $R_b=10\text{k} \Omega$ , $R_d=97.08 \Omega$
<b>AC bus and Loads</b>	$V_{LL}=460\text{V}$ , $f_s=60\text{Hz}$ , $R=10 \Omega$ , <i>nonlinear load (Diode bridge)</i> , $R_L=50 \Omega$ , $L_L=60e^{-3}\text{mH}$

Table-A I-8 System parameters of HSPGS based on PV array and WT driven variable speed PMBLDCG

Elements	Parameters and values
<b>PV array and DC/DC boost converter</b>	$i_{rr}=5.981. 10^{-8} \text{ A}$ , $i_{scr}=6 \text{ A}$ , $ki=0.0024$ , $Tr=298 \text{ K}$ , $q=1.6. 10^{-19}$ $C$ , $Kb=1.38. 10^{-23} \text{ J/K}$ , $Eg=1.12 \text{ V}$ , $A=1.2$ , $Cout1=200\mu\text{F}$ , $C1=100 \mu\text{F}$ , $L=1.5 \text{ mH}$ ,
<b>WT</b>	$C_{pmax}=0.48$ , $\lambda_{opt}=8.1$ , $C_1=0.5176$ , $C_2=116$ , $C_3=0.4$ , $C_4=5$ , $C_5=21$ , $C_6=0.0068$
<b>PMBLDCG And dc-dc Boost2</b>	$R_s=0.808 \Omega$ , $L_s=5.44 \text{ mH}$ , $V_s=208 \text{ V}$ , $\omega_r= 1800 \text{ RPM}$ , $J=0.01859 \text{ kg.cm}^2$ , $K_m=80 \text{ V/tr/min}$ , $C_{out2}=200\mu\text{F}$ , $C_2=100$ $\mu\text{F}$ , $L_{WT}=1.5 \text{ mH}$ . $2P=4$
<b>Bus DC</b>	$C_{dc}=500 \mu\text{F}$ , $V_{dc}=105 \text{ V}$ , AGM batteries for $9*(12\text{V}/12)\text{Ah}$ .
<b>AC local grid</b>	$f_s=60 \text{ Hz}$ , $V_{Lmax}=50\text{V}$ , linear load ( $R_L=8 \Omega$ ), nonlinear load (3 phase diode bridge $R_L=8 \Omega$ , $L_L=20 \text{ mH}$ ).

Table-A I-9 System parameters of Hybrid WT-DG based on fixed speed PMSG and SG

Elements		Parameters and values
WT	WT model	$P_{mec} = 8.5 \text{ kW}$ , $R = 4.2 \text{ m}$ , $C_1=0.5176$ , $C_2=116$ , $C_3=0.4$ , $C_4=5$ , $C_5=21$ , $C_6=0.0068$ , $\beta=0$ .
	PMSG	$P_n=8.5\text{kW}$ , $\omega_r=155\text{rad/s}$ $P=8$ , $V_{LL}=460\text{V}$ , $R_s=0.425 \Omega$ , $J=0.01197 \text{ kg.m}^2$ , $f=0.001189 \text{ N.m.s}$ , $L_d=L_q=0.835\text{mH}$ , $\lambda=0.14 \text{ Wb}$ .
DG	DE model	$K_f=120$ , $k_p=10$ , $k_I=1$ , $k_2=1$ , $\tau_1=0.4$ , $\tau_2=0.011$
	AVR	$a = 0.046$ , $b=4.8$ $c=0.345$ , $d=0.0067$ , $e=13$ , $k_1=5.1$ , $k_2=-5.1$ , $k_3=5.1$ $V_{ref}=460\text{V}$
	SG	$S_n=10.2 \text{ kVA}$ , $V_{LL}=460\text{V}$ , $f_s=60\text{Hz}$ , $r_f=1.163\Omega$ , $L_f=0.01143\text{H}$ , $r_{Dd}=3.66 \Omega$ , $L_{Dd}=0.009167 \text{ H}$ , $r_{Dq}=4.752 \Omega$ , $L_{Dq}=0.01006 \text{ H}$ , $J=0.0923\text{kg.m}^2$ , $2P=4$ , $F=0.0152 \text{ N.m.s}$
BESS and dump load		$V_{bat}=1000\text{V}$ , $V_{ocmin}=980\text{V}$ , $V_{ocmax}=1088\text{V}$ , $C_b=4560\text{F}$ , $R_s=0.01 \Omega$ , $R_b=10\text{k} \Omega$ , $R_d=117.64 \Omega$
AC bus and Loads		$V_{LL}=460\text{V}$ , $f_s=60\text{Hz}$ , $R=10 \Omega$ , <i>nonlinear load (Diode bridge)</i> , $R_L=50 \Omega$ , $L_L=20e-3\text{mH}$

Table-A I-10 System parameters of Hybrid DG-WT based on variable speed PMBLDCG and PMSG

Elements	Parameters and values
PMSG	$R_s=0.005 \Omega$ , $L=0.000835\text{H}$ , <i>flux linkage</i> $=0.5\text{V.s}$ , $J=0.25\text{kg.m}^2$ , $F=0.005\text{N.m.s}$
PMBLDCG	$R_s=0.808 \Omega$ , $L=5.44\text{mH}$ , <i>flux linkage</i> $=1.0083\text{V.s}$ , $J=0.01859\text{kg.m}^2$ , $F=0.0002024\text{N.m.s}$
BESS and dump load	$V_{bat}=1000\text{V}$ , $V_{ocmin}=980\text{V}$ , $V_{ocmax}=1088\text{V}$ , $C_b=4560\text{F}$ , $R_s=0.01 \Omega$ , $R_b=10\text{k} \Omega$ , $R_d=97.08 \Omega$
AC bus and Loads	$V_{LL}=460\text{V}$ , $f_s=60\text{Hz}$ , $R=10 \Omega$ , <i>nonlinear load (Diode bridge)</i> , $R_L=50 \Omega$ , $L_L=60e-3\text{mH}$

## APPENDIX II

### LABORATORY SETUP DETAILS

In order to test the proposed topologies, as well as the developed control algorithms, experimental scaled hardware prototypes are developed in laboratory. The WT is emulated with the help of four-quadrant dynamometer, which rotates at variable speed or at fixed speed depending on the type of the application. A programmable DC source is used to emulate a solar PV array. The performances during both nominal and severe operating conditions are evaluated in real-time using DSP (dSPACE DS1104) controller, supported by Real-Time Workshop of Matlab/Simulink environment. Hardware for control and processing of signals consists of: Hall's Effect voltage sensors (LEMLV 25-P), Hall's Effect current sensors (LEM LA-55P), three-legs VSC, two DC-DC boost converters and a battery bank. Four voltages and four currents are sensed and converted into digital signals using ADC interfaces of DSP. The gating signals for power converters are taken from digital I/O of DSP and fed through the isolation card. The laboratory experimental setups photographs are shown in Figs. A1.1, A1.2 and A1.3

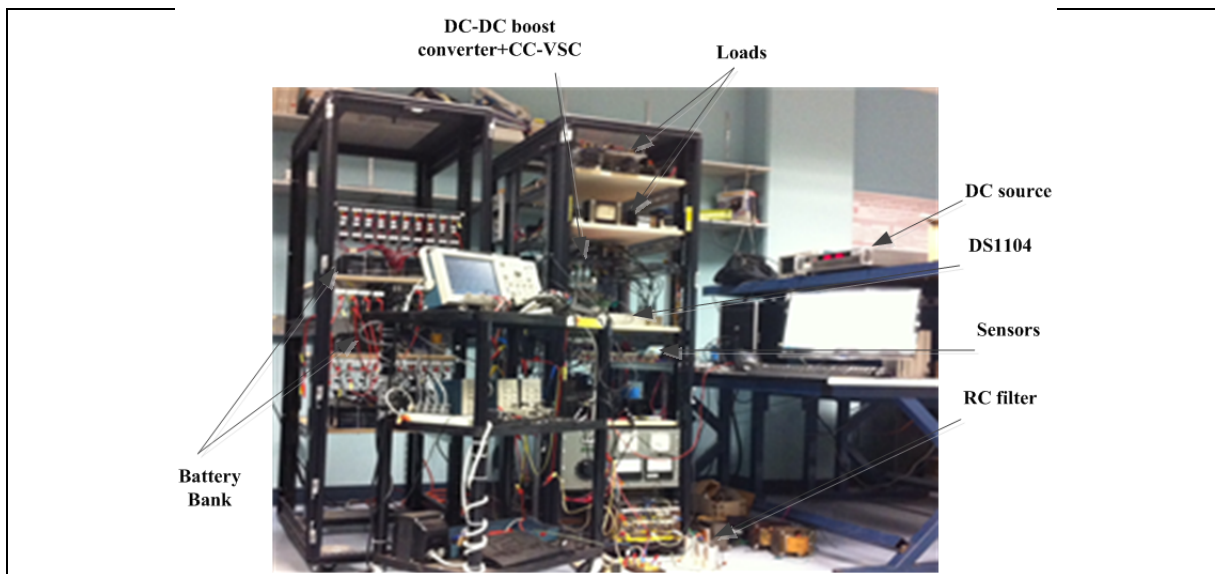


Figure A1.1 Experimental Setup for standalone system based on PV array

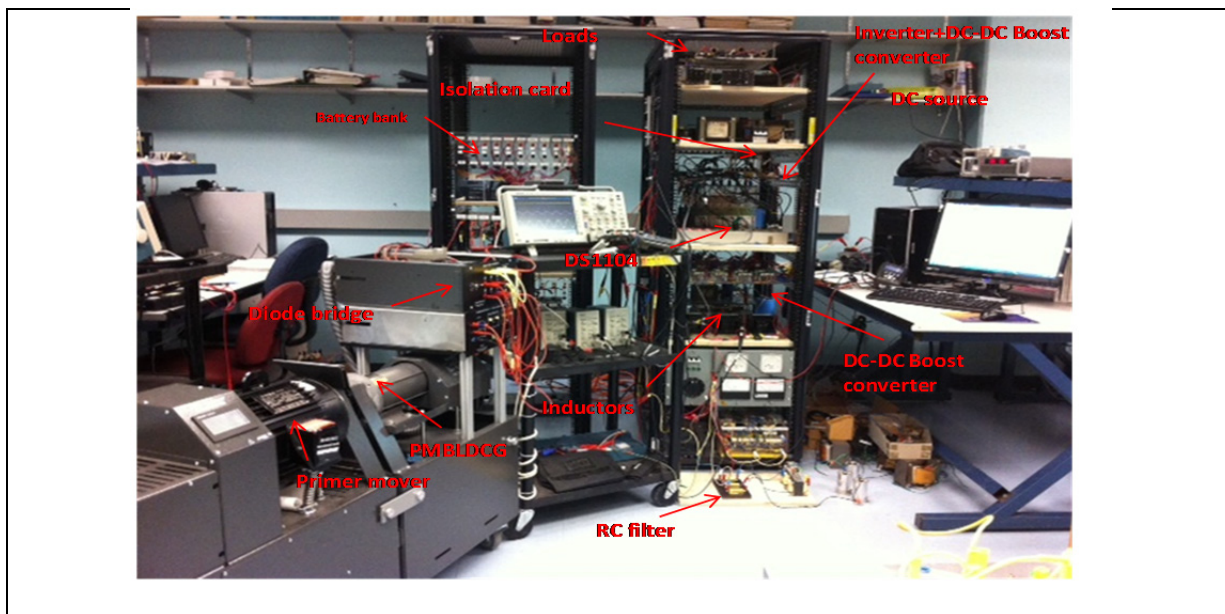


Figure A.1.2 Experimental Setup for hybrid standalone system based on PV array and WT driven variable speed PMLDCCG



Figure A.1.3 Experimental Setup for hybrid standalone system based on PV array and MHP driven fixed speed SCIG

## BIBLIOGRAPHY

- Abu-Elhaija, W. S., et A. Muetze. 2013. « Self-Excitation and Stability at Speed Transients of Self-Excited Single-Phase Reluctance Generators ». *Sustainable Energy, IEEE Transactions on*, vol. 4, n° 1, p. 136-144.
- Akagi, H., Yoshihira Kanazawa et A. Nabae. 1984. « Instantaneous Reactive Power Compensators Comprising Switching Devices without Energy Storage Components ». *Industry Applications, IEEE Transactions on*, vol. IA-20, n° 3, p. 625-630.
- Alepuz, S., S. Busquets-Monge, J. Bordonau, J. Gago, D. Gonzalez et J. Balcells. 2006. « Interfacing Renewable Energy Sources to the Utility Grid Using a Three-Level Inverter ». *Industrial Electronics, IEEE Transactions on*, vol. 53, n° 5, p. 1504-1511.
- Arya, S. R., B. Singh, A. Chandra et K. Al-Haddad. 2012. « Control of shunt custom power device based on Anti-Hebbian learning algorithm ». In *IECON 2012 - 38th Annual Conference on IEEE Industrial Electronics Society*. (25-28 Oct. 2012), p. 1246-1251.
- Arya, S. R., B. Singh, A. Chandra et K. Al-Haddad. 2014. « Learning-Based Anti-Hebbian Algorithm for Control of Distribution Static Compensator ». *Industrial Electronics, IEEE Transactions on*, vol. 61, n° 11, p. 6004-6012.
- Asiminoaei, L., F. Blaabjerg et S. Hansen. 2007. « Detection is key - Harmonic detection methods for active power filter applications ». *Industry Applications Magazine, IEEE*, vol. 13, n° 4, p. 22-33.
- Bhende, C. N., S. Mishra et S. G. Malla. 2011. « Permanent Magnet Synchronous Generator-Based Standalone Wind Energy Supply System ». *Sustainable Energy, IEEE Transactions on*, vol. 2, n° 4, p. 361-373.
- Blaabjerg, Frede, et Zhe Chen. 2006. *Power electronics for modern wind turbines*, 1st. [San Rafael, Calif.]: Morgan & Claypool Publishers, vii, 60 p. p.
- Bo, Zhao, Zhang Xuesong, Chen Jian, Wang Caisheng et Guo Li. 2013. « Operation Optimization of Standalone Microgrids Considering Lifetime Characteristics of Battery Energy Storage System ». *Sustainable Energy, IEEE Transactions on*, vol. 4, n° 4, p. 934-943.
- Boazzo, B., A. Vagati, G. Pellegrino, E. Armando et P. Guglielmi. 2015. « Multipolar Ferrite-Assisted Synchronous Reluctance Machines: A General Design Approach ». *Industrial Electronics, IEEE Transactions on*, vol. 62, n° 2, p. 832-845.
- Boldea, I. 2006. *Variable speed generators : the electric generators handbook*. Coll. « Electric power engineering series ». Boca Raton, FL: CRC/Taylor & Francis, 1 v.

- orkowski, D., et T. Wegiel. 2013. « Small Hydropower Plant With Integrated Turbine-Generators Working at Variable Speed ». *Energy Conversion, IEEE Transactions on*, vol. 28, n° 2, p. 452-459.
- Busca, Cristian, Ana-Irina Stan, Tiberiu Stanciu et Daniel Ioan Stroe. 2010. « Control of Permanent Magnet Synchronous generator for large wind turbines ». In *2010 IEEE International Symposium on Industrial Electronics, ISIE 2010, July 4, 2010 - July 7, 2010*. (Bari, Italy), p. 3871-3876. Institute of Electrical and Electronics Engineers Inc.
- Caisheng, Wang, et M. H. Nehrir. 2008. « Power Management of a Stand-Alone Wind/Photovoltaic/Fuel Cell Energy System ». *Energy Conversion, IEEE Transactions on*, vol. 23, n° 3, p. 957-967.
- Capecchi, E., P. Guglielmi, M. Pastorelli et A. Vagati. 2001. « Position-sensorless control of the transverse-laminated synchronous reluctance motor ». *Industry Applications, IEEE Transactions on*, vol. 37, n° 6, p. 1768-1776.
- Cardenas, R., R. Pena, M. Perez, J. Clare, G. Asher et F. Vargas. 2006. « Vector Control of Front-End Converters for Variable-Speed Wind-Diesel Systems ». *Industrial Electronics, IEEE Transactions on*, vol. 53, n° 4, p. 1127-1136.
- Cardenas, R., R. Pena, J. Proboste, G. Asher et J. Clare. 2005. « MRAS observer for sensorless control of standalone doubly fed induction generators ». *Energy Conversion, IEEE Transactions on*, vol. 20, n° 4, p. 710-718.
- Carrillo, C., A. E. Feijoo, Cidra, x, J. s et J. Gonzalez. 2004. « Power fluctuations in an isolated wind plant ». *Energy Conversion, IEEE Transactions on*, vol. 19, n° 1, p. 217-221.
- Chakraborty, S., B. Kramer et B. Kroposki. 2009. « A review of power electronics interfaces for distributed energy systems towards achieving low-cost modular design ». *Renewable and Sustainable Energy Reviews*, vol. 13, n° 9, p. 2323-35.
- Chan, Yea-Kuang, et Jyh-Cherng Gu. 2010. « Modeling and control of stand-alone photovoltaic generation system ». In *2010 International Conference on Power System Technology: Technological Innovations Making Power Grid Smarter, POWERCON2010*. (Hangzhou, China). IEEE Computer Society.
- Chatelain, Jean. 1983. *Machines électriques*. Coll. « Traité d'électricité », v 10. St-Saphorin: Editions Georgi, xii, 628 p. p.
- Chau, K. T., W. L. Li et C. H. T. Lee. 2012. « Challenges and opportunities of electric machines for renewable energy (invited paper) ». *Progress In Electromagnetics Research B*, vol. 42, p. 45-74.

- Chauhan, Anurag, et R. P. Saini. 2014. « A review on Integrated Renewable Energy System based power generation for stand-alone applications: Configurations, storage options, sizing methodologies and control ». *Renewable and Sustainable Energy Reviews*, vol. 38, p. 99-120.
- Chauhan, Y. K., S. K. Jain et B. Singh. 2010. « A Prospective on Voltage Regulation of Self-Excited Induction Generators for Industry Applications ». *IEEE Transactions on Industry Applications*, vol. 46, n° 2, p. 720-30.
- Chen-Chi, Chu, et Chen Chieh-Li. 2009. « Robust maximum power point tracking method for photovoltaic cells: a sliding mode control approach ». *Solar Energy*, vol. 83, n° 8, p. 1370-8.
- Chen, Haisheng, Thang Ngoc Cong, Wei Yang, Chunqing Tan, Yongliang Li et Yulong Ding. 2009. « Progress in electrical energy storage system: A critical review ». *Progress in Natural Science*, vol. 19, n° 3, p. 291-312.
- Chen, Y. M., Y. C. Liu, F. Y. Wu et Y. E. Wu. 2002. « Multi-input converter with power factor correction and maximum power point tracking features ». In *Applied Power Electronics Conference and Exposition, 2002. APEC 2002. Seventeenth Annual IEEE*. (2002) Vol. 1, p. 490-496 vol.1.
- Chilipi, R. R., B. Singh et S. S. Murthy. 2014. « Performance of a Self-Excited Induction Generator With DSTATCOM-DTC Drive-Based Voltage and Frequency Controller ». *Energy Conversion, IEEE Transactions on*, vol. 29, n° 3, p. 545-557.
- Chunting, Mi, M. Filippa, J. Shen et N. Natarajan. 2004. « Modeling and control of a variable-speed constant-frequency synchronous generator with brushless exciter ». *Industry Applications, IEEE Transactions on*, vol. 40, n° 2, p. 565-573.
- Cidras, J., et C. Carrillo. 2000. « Regulation of synchronous generators by means of hydrostatic transmissions ». *Power Systems, IEEE Transactions on*, vol. 15, n° 2, p. 771-778.
- Darabi, A., et C. E. Tindall. 2002. « Analogue AVR model for use in real time transient simulation of small salient pole alternators ». In *Power Electronics, Machines and Drives, 2002. International Conference on (Conf. Publ. No. 487)*. (4-7 June 2002), p. 451-455.
- Darabi, A., C. Tindall et S. Ferguson. 2004. « Finite-element time-step coupled Generator, Load, AVR, and brushless exciter modeling ». *Energy Conversion, IEEE Transactions on*, vol. 19, n° 2, p. 258-264.

- Datta, M., T. Senjyu, A. Yona, T. Funabashi et Kim Chul-Hwan. 2011. « A Frequency-Control Approach by Photovoltaic Generator in a PV&#x2013;Diesel Hybrid Power System ». *Energy Conversion, IEEE Transactions on*, vol. 26, n° 2, p. 559-571.
- Datta, R., et V. T. Ranganathan. 2002. « Variable-speed wind power generation using doubly fed wound rotor induction machine-a comparison with alternative schemes ». *Energy Conversion, IEEE Transactions on*, vol. 17, n° 3, p. 414-421.
- Dolara, A., R. Faranda et S. Leva. 2009. « Energy comparison of seven MPPT techniques for PV systems ». *Journal of Electromagnetic Analysis and Applications*, vol. 1, n° 3, p. 152-62.
- Dong-Jing, Lee, et Wang Li. 2008. « Small-Signal Stability Analysis of an Autonomous Hybrid Renewable Energy Power Generation/Energy Storage System Part I: Time-Domain Simulations ». *Energy Conversion, IEEE Transactions on*, vol. 23, n° 1, p. 311-320.
- Ekanayake, J. B. 2002. « Induction generators for small hydro schemes ». *Power Engineering Journal*, vol. 16, n° 2, p. 61-7.
- El Moursi, M. S., K. Goweily, J. L. Kirtley et M. Abdel-Rahman. 2014. « Application of Series Voltage Boosting Schemes for Enhanced Fault Ridethrough Performance of Fixed Speed Wind Turbines ». *Power Delivery, IEEE Transactions on*, vol. 29, n° 1, p. 61-71.
- Elgendy, M. A., B. Zahawi et D. J. Atkinson. 2014. « Operating Characteristics of the P&O Algorithm at High Perturbation Frequencies for Standalone PV Systems ». *Energy Conversion, IEEE Transactions on*, vol. PP, n° 99, p. 01-10.
- Fitzgerald, A. E., Charles Kingsley et Stephen D. Umans. 2003. *Electric machinery*, 6th. Coll. « McGraw-Hill series in electrical engineering. Power and energy ». Boston ; Montréal: McGraw-Hill, xv, 688 p. p.
- Fortmann, Jens,. *Modeling of Wind Turbines with Doubly Fed Generator System*. 1 ressource en ligne (XXIII, 183 p.) p.
- Goel, P. K., B. Singh, S. S. Murthy et N. Kishore. 2009. « Autonomous hybrid system using PMSGs for hydro and wind power generation ». In *Industrial Electronics, 2009. IECON '09. 35th Annual Conference of IEEE*. (3-5 Nov. 2009), p. 255-260.
- Goel, P. K., B. Singh, S. S. Murthy et N. Kishore. 2011. « Isolated Wind-Hydro Hybrid System Using Cage Generators and Battery Storage ». *Industrial Electronics, IEEE Transactions on*, vol. 58, n° 4, p. 1141-1153.

- Guha, S., et N. C. Kar. 2005. « Alinearized model of saturated self-excited synchronous reluctance generator ». In *Electrical and Computer Engineering, 2005. Canadian Conference on.* (1-4 May 2005), p. 633-636.
- Gulliver, John S., et Roger E. A. Arndt. 1991. *Hydropower engineering handbook*. New York, N.Y.: McGraw-Hill, 1 v. (pag. multiple) p.
- Hajizadeh, A., M. A. Golkar et A. Feliachi. 2010. « Voltage Control and Active Power Management of Hybrid Fuel-Cell/Energy-Storage Power Conversion System Under Unbalanced Voltage Sag Conditions ». *Energy Conversion, IEEE Transactions on*, vol. 25, n° 4, p. 1195-1208.
- Hasan, A. R., T. S. Martis et A. H. M. Sadrul Ula. 1994. « Design and implementation of a fuzzy controller based automatic voltage regulator for a synchronous generator ». *Energy Conversion, IEEE Transactions on*, vol. 9, n° 3, p. 550-557.
- Hee-Sang, Ko, et J. Jatskevich. 2007. « Power Quality Control of Wind-Hybrid Power Generation System Using Fuzzy-LQR Controller ». *Energy Conversion, IEEE Transactions on*, vol. 22, n° 2, p. 516-527.
- Hernandez-Aramburo, C. A., T. C. Green et N. Mugniot. 2005. « Fuel consumption minimization of a microgrid ». *Industry Applications, IEEE Transactions on*, vol. 41, n° 3, p. 673-681.
- Hidayat, N. M., M. N. Kari et M. J. Mohd Arif. 2014. « Storage capacity performance for hybrid PV/diesel system in Sabah Malaysia ». In *Power Electronics Conference (IPEC-Hiroshima 2014 - ECCE-ASIA), 2014 International.* (18-21 May 2014), p. 573-576.
- Hirose, T., et H. Matsuo. 2012. « Standalone Hybrid Wind-Solar Power Generation System Applying Dump Power Control Without Dump Load ». *Industrial Electronics, IEEE Transactions on*, vol. 59, n° 2, p. 988-997.
- Hofmann, H., et S. R. Sanders. 2000. « High-speed synchronous reluctance machine with minimized rotor losses ». *Industry Applications, IEEE Transactions on*, vol. 36, n° 2, p. 531-539.
- IEEE Guide for Design, Operation, and Integration of Distributed Resource Island Systems with Electric Power Systems. 2011. *IEEE Std 1547.4-2011*, p. 1-54.
- IEEE Guide for the Application of Turbine Governing Systems for Hydroelectric Generating Units. 2011. *IEEE Std 1207-2011 (Revision to IEEE Std 1207-2004)*, p. 1-131.
- IEEE Recommended Practices and Requirements for Harmonic Control in Electrical Power Systems. 1993. *IEEE Std 519-1992*, p. 1-112.

- Jae-Do, Park, C. Kalev et H. Hofmann. 2008. « Modeling and Control of Solid-Rotor Synchronous Reluctance Machines Based on Rotor Flux Dynamics ». *Magnetics, IEEE Transactions on*, vol. 44, n° 12, p. 4639-4647.
- Jaehong, Kim, J. M. Guerrero, P. Rodriguez, R. Teodorescu et Nam Kwanghee. 2011 . « Mode Adaptive Droop Control With Virtual Output Impedances for an Inverter-Based Flexible AC Microgrid ». *Power Electronics, IEEE Transactions on*, vol. 26, n° 3, p. 689-701.
- Jiang, J. 1994. « Optimal gain scheduling controller for a diesel engine ». *Control Systems, IEEE*, vol. 14, n° 4, p. 42-48.
- Jin, Lin, Sun Yuanzhang, Song Yonghua, Gao Wenzhong et P. Sorensen. 2013. « Wind Power Fluctuation Smoothing Controller Based on Risk Assessment of Grid Frequency Deviation in an Isolated System ». *Sustainable Energy, IEEE Transactions on*, vol. 4, n° 2, p. 379-392.
- Joon-Hwan, Lee, Lee Seung-Hwan et Sul Seung-Ki. 2009. « Variable-Speed Engine Generator With Supercapacitor: Isolated Power Generation System and Fuel Efficiency ». *Industry Applications, IEEE Transactions on*, vol. 45, n° 6, p. 2130-2135.
- Kakigano, H., Y. Miura et T. Ise. 2010. « Low-Voltage Bipolar-Type DC Microgrid for Super High Quality Distribution ». *Power Electronics, IEEE Transactions on*, vol. 25, n° 12, p. 3066-3075.
- Kasal, G. K., et B. Singh. 2011. « Voltage and Frequency Controllers for an Asynchronous Generator-Based Isolated Wind Energy Conversion System ». *Energy Conversion, IEEE Transactions on*, vol. 26, n° 2, p. 402-416.
- Kassem, A. M., et A. Y. Abdelaziz. 2014. « Reactive power control for voltage stability of standalone hybrid wind&#8211;diesel power system based on functional model predictive control ». *Renewable Power Generation, IET*, vol. 8, n° 8, p. 887-899.
- Kelemen, M., et D. Bensoussan. 2004. « On the design, robustness, implementation and use of quasi-linear feedback compensators ». *International Journal of Control*, vol. 77, n° 6, p. 527-45.
- Kim, K. A., Xu Chenyang, Jin Lei et P. T. Krein. 2013. « A Dynamic Photovoltaic Model Incorporating Capacitive and Reverse-Bias Characteristics ». *Photovoltaics, IEEE Journal of*, vol. 3, n° 4, p. 1334-1341.
- Kishor, N., R. P. Saini et S. P. Singh. 2007. « A review on hydropower plant models and control ». *Renewable & Sustainable Energy Reviews*, vol. 11, n° 5, p. 776-96.

- Krause, Paul C. 1986. *Analysis of electric machinery*. Coll. « McGraw-Hill series in electrical engineering. Power & energy. ». Toronto: McGraw-Hill, xvi, 564 p. p.
- Krause, Paul C., Oleg Wasynczuk et Scott D. Sudhoff. 2002a. *Analysis of electric machinery and drive systems*, 2nd. New York: IEEE Press, 1 texte électronique (xiv, 613 p.) p.
- Krause, Paul C., Oleg Wasynczuk et Scott D. Sudhoff. 2002b. *Analysis of electric machinery and drive systems*, 2nd. Coll. « IEEE Press series on power engineering ». IEEE Press, Wiley-Interscience, xiv, 613 p. p.
- Krause, Paul C., Oleg Wasynczuk, Scott D. Sudhoff, Steven Pekarek et Institute of Electrical and Electronics Engineers. *Analysis of electric machinery and drive systems*, Third edition., 1 ressource en ligne (663 pages) p.
- Krishnan, R. 2010. *Permanent magnet synchronous and brushless DC motor drives*. Boca Raton: CRC Press/Taylor & Francis, 1 texte électronique (xxxv, 575 p.) p.
- Kundur, Prabha, Neal J. Balu et Mark G. Lauby. 1994. *Power system stability and control*. Coll. « The EPRI power system engineering series ». New York ; Montréal: McGraw-Hill, xxiii, 1176 p. p.
- Kyoung-Jun, Lee, Shin Dongsul, Yoo Dong-Wook, Choi Han-Kyu et Kim Hee-Je. 2013 . « Hybrid photovoltaic/diesel green ship operating in standalone and grid-connected mode - Experimental investigation ». *Energy*, vol. 49, p. 475-83.
- Lagorse, J., M. G. Simoes et A. Miraoui. 2009. « A Multiagent Fuzzy-Logic-Based Energy Management of Hybrid Systems ». *Industry Applications, IEEE Transactions on*, vol. 45, n° 6, p. 2123-2129.
- Leon, A. E., M. F. Farias, P. E. Battaiotto, J. A. Solsona et M. I. Valla. 2011. « Control Strategy of a DVR to Improve Stability in Wind Farms Using Squirrel-Cage Induction Generators ». *Power Systems, IEEE Transactions on*, vol. 26, n° 3, p. 1609-1617.
- Leuchter, J., P. Bauer, V. Rerucha et V. Hajek. 2009. « Dynamic Behavior Modeling and Verification of Advanced Electrical-Generator Set Concept ». *Industrial Electronics, IEEE Transactions on*, vol. 56, n° 1, p. 266-279.
- Leyva, R., C. Alonso, I. Queinnec, A. Cid-Pastor, D. Lagrange et L. Martinez-Salamero. 2006. « MPPT of photovoltaic systems using extremum - seeking control ». *IEEE Transactions on Aerospace and Electronic Systems*, vol. 42, n° 1, p. 249-58.

- Li, Guo, Liu Wenjian, Jiao Bingqi, Hong Bowen et Wang Chengshan. 2014. « Multi-objective stochastic optimal planning method for stand-alone microgrid system ». *Generation, Transmission & Distribution, IET*, vol. 8, n° 7, p. 1263-1273.
- Li, Wang, Chen Su-Jen, Jan Shen-Ron et Li Hao-Wen. 2013. « Design and Implementation of a Prototype Underwater Turbine Generator System for Renewable Microhydro Power Energy ». *Industry Applications, IEEE Transactions on*, vol. 49, n° 6, p. 2753-2760.
- Logeswaran, T., et A. SenthilKumar. 2014. « A Review of Maximum Power Point Tracking Algorithms for Photovoltaic Systems under Uniform and Non-uniform Irradiances ». *Energy Procedia*, vol. 54, n° 0, p. 228-235.
- Lopes, V., et C. Borges. 2014. « Impact of the Combined Integration of Wind Generation and Small Hydropower Plants on the System Reliability ». *Sustainable Energy, IEEE Transactions on*, vol. PP, n° 99, p. 1-9.
- Madawala, U. K., T. Geyer, J. B. Bradshaw et D. M. Vilathgamuwa. 2012. « Modeling and Analysis of a Novel Variable-Speed Cage Induction Generator ». *Industrial Electronics, IEEE Transactions on*, vol. 59, n° 2, p. 1020-1028.
- Magureanu, R., M. Albu, V. Bostan, A. M. Dumitrescu, G. Dimu, F. Popa et M. Rotaru. 2008. « Smart AC grid integrating dispersed small hydropower sources ». In *Optimization of Electrical and Electronic Equipment, 2008. OPTIM 2008. 11th International Conference on*. (22-24 May 2008), p. 345-350.
- Mariam, L., M. Basu et M. F. Conlon. 2013. « A Review of Existing Microgrid Architectures ». *Journal of Engineering*, p. 937614 (8 pp.).
- Mendalek, Nassar Hanna. 2003. « Qualite de l'onde electrique et moyens de mitigation ». Ph.D., Ecole de Technologie Superieure (Canada), 221 p.
- Mendis, N., K. M. Muttaqi et S. Perera. 2014. « Management of Battery-Supercapacitor Hybrid Energy Storage and Synchronous Condenser for Isolated Operation of PMSG Based Variable-Speed Wind Turbine Generating Systems ». *Smart Grid, IEEE Transactions on*, vol. 5, n° 2, p. 944-953.
- Mendis, N., K. Muttaqi, S. Perera et S. Kamalasan. 2014. « An Effective Power Management Strategy for a Wind-Diesel-Hydrogen Based Remote Area Power Supply System to Meet Fluctuating Demands under Generation Uncertainty ». *Industry Applications, IEEE Transactions on*, vol. PP, n° 99, p. 1-1.
- Mipoung, O. D., L. A. C. Lopes et P. Pillay. 2014. « Potential of Type-1 Wind Turbines for Assisting With Frequency Support in Storage-Less Diesel Hybrid Mini-Grids ». *Industrial Electronics, IEEE Transactions on*, vol. 61, n° 5, p. 2297-2306.

- Muljadi, E., et C. P. Butterfield. 2001. « Pitch-controlled variable-speed wind turbine generation ». *Industry Applications, IEEE Transactions on*, vol. 37, n° 1, p. 240-246.
- Nehrir, M. H., C. Wang, K. Strunz, H. Aki, R. Ramakumar, J. Bing, Z. Miao et Z. Salameh. 2011. « A Review of Hybrid Renewable/Alternative Energy Systems for Electric Power Generation: Configurations, Control, and Applications ». *Sustainable Energy, IEEE Transactions on*, vol. 2, n° 4, p. 392-403.
- Nikkhajoie, H., et R. H. Lasseter. 2009. « Distributed Generation Interface to the CERTS Microgrid ». *Power Delivery, IEEE Transactions on*, vol. 24, n° 3, p. 1598-1608.
- Orlando, N. A., M. Liserre, R. A. Mastromauro et A. Dell'Aquila. 2013. « A Survey of Control Issues in PMSG-Based Small Wind-Turbine Systems ». *Industrial Informatics, IEEE Transactions on*, vol. 9, n° 3, p. 1211-1221.
- Papathanassiou, S. A., et M. P. Papadopoulos. 2001. « Mechanical stresses in fixed-speed wind turbines due to network disturbances ». *Energy Conversion, IEEE Transactions on*, vol. 16, n° 4, p. 361-367.
- Pathak, G., B. Singh et B. K. Panigrahi. 2014. « Isolated microgrid employing PMBLDCG for wind power generation and synchronous reluctance generator for DG system ». In *Power Electronics (IICPE), 2014 IEEE 6th India International Conference on*. (8-10 Dec. 2014), p. 1-6.
- Pena, R., R. Cardenas, J. Proboste, J. Clare et G. Asher. 2008. « Wind&#x2013;Diesel Generation Using Doubly Fed Induction Machines ». *Energy Conversion, IEEE Transactions on*, vol. 23, n° 1, p. 202-214.
- Pena, R., J. C. Clare et G. M. Asher. 1996. « A doubly fed induction generator using back-to-back PWM converters supplying an isolated load from a variable speed wind turbine ». *Electric Power Applications, IEE Proceedings -*, vol. 143, n° 5, p. 380-387.
- Peng, Wang, Liu Xiong, Jin Chi, Loh Pohchiang et Choo Fookhoong. 2011. « A hybrid AC/DC micro-grid architecture, operation and control ». In *Power and Energy Society General Meeting, 2011 IEEE*. (24-29 July 2011), p. 1-8.
- Priolkar, J. G., et S. Doolla. 2013. « Analysis of PV-hydro isolated power systems ». In *India Conference (INDICON), 2013 Annual IEEE*. (13-15 Dec. 2013), p. 1-6.
- Quincy, Wang, et Chang Liuchen. 2004. « An intelligent maximum power extraction algorithm for inverter-based variable speed wind turbine systems ». *Power Electronics, IEEE Transactions on*, vol. 19, n° 5, p. 1242-1249.

- Rahim, Y. H. A., et M. A. A. S. Alyan. 1991. « Effect of excitation capacitors on transient performance of reluctance generators ». *Energy Conversion, IEEE Transactions on*, vol. 6, n° 4, p. 714-720.
- Rahman, M. A., A. M. Osheiba, T. S. Radwan et E. S. Abdin. 1996. « Modelling and controller design of an isolated diesel engine permanent magnet synchronous generator ». *Energy Conversion, IEEE Transactions on*, vol. 11, n° 2, p. 324-330.
- Reis, F., C. Guerreiro, F. Batista, T. Pimentel, M. Pravettoni, J. Wemans, G. Sorasio et M. C. Brito. 2015. « Modeling the Effects of Inhomogeneous Irradiation and Temperature Profile on CPV Solar Cell Behavior ». *Photovoltaics, IEEE Journal of*, vol. 5, n° 1, p. 112-122.
- Rekioua, Djamila, Ernest Matagne et SpringerLink. 2012. *Optimization of Photovoltaic Power Systems: Modelization, Simulation and Control*, 2012. London: Springer London.
- Rezkallah, M., et A. Chandra. 2009. « Control of wind-diesel isolated system with power quality improvement ». In *Electrical Power & Energy Conference (EPEC), 2009 IEEE*. (22-23 Oct. 2009), p. 1-6.
- Rezkallah, M., A. Chandra et B. Singh. 2013. « Three-leg four-wire voltage source inverters for hybrid standalone system feeding unbalanced load ». In *Industrial Electronics Society, IECON 2013 - 39th Annual Conference of the IEEE*. (10-13 Nov. 2013), p. 1916-1921.
- Rezkallah, M., A. Chandra, B. Singh et R. Niwas. 2012. « Modified PQ control for power quality improvement of standalone hybrid wind diesel battery system ». In *Power India Conference, 2012 IEEE Fifth*. (19-22 Dec. 2012), p. 1-6.
- Rezkallah, M., A. Hamadi, A. Chandra et B. Singh. 2015a. « Real-Time HIL Implementation of Sliding Mode Control for Standalone System Based on PV Array Without Using Dumpload ». *IEEE Transactions on Sustainable Energy*, vol. 6, n° 4, p. 1389-1398.
- Rezkallah, M., Ab. Hamadi, A. Chandra et B. Singh. 2014. « Hybrid AC-DC standalone system based on PV array and wind turbine ». In *Industrial Electronics Society, IECON 2014 - 40th Annual Conference of the IEEE*. (Oct. 29 2014-Nov. 1 2014), p. 5533-5539.
- Rezkallah, M., Shailendra Sharma, A. Chandra et Bhim Singh. 2015b. « Hybrid standalone power generation system using hydro-PV-battery for residential green buildings ». In *Industrial Electronics Society, IECON 2015 - 41st Annual Conference of the IEEE*. (9-12 Nov. 2015), p. 003708-003713.

- Romeral Martinez, J. L., R. S. Arashloo, M. Salehifar et J. M. Moreno. 2015. « Predictive current control of outer-rotor five-phase BLDC generators applicable for off-shore wind power plants ». *Electric Power Systems Research*, vol. 121, p. 260-9.
- Roy, S., O. P. Malik et G. S. Hope. 1991. « A step predictive scheme for speed control of diesel driven power-plants ». In *Industrial and Commercial Power Systems Technical Conference, 1991*. (6-9 May 1991), p. 63-69.
- Scherer, L. G., et R. F. de Camargo. 2011. « Frequency and voltage control of micro hydro power stations based on hydraulic turbine's linear model applied on induction generators ». In *Power Electronics Conference (COBEP), 2011 Brazilian*. (11-15 Sept. 2011), p. 546-552.
- Schinas, N. A., N. A. Vovos et G. B. Giannakopoulos. 2007. « An Autonomous System Supplied Only by a Pitch-Controlled Variable-Speed Wind Turbine ». *Energy Conversion, IEEE Transactions on*, vol. 22, n° 2, p. 325-331.
- Sekhar, P. C., S. Mishra et R. Sharma. 2015. « Data analytics based neuro-fuzzy controller for diesel-photovoltaic hybrid AC microgrid ». *Generation, Transmission & Distribution, IET*, vol. 9, n° 2, p. 193-207.
- Senjyu, Tomonobu, Satoshi Tamaki, Endusa Muhando, Naomitsu Urasaki, Hiroshi Kinjo, Toshihisa Funabashi, Hideki Fujita et Hideomi Sekine. 2006. « Wind velocity and rotor position sensorless maximum power point tracking control for wind generation system ». *Renewable Energy*, vol. 31, n° 11, p. 1764-1775.
- Sharaf-Eldin, T., M. W. Dunnigan, J. E. Fletcher et B. W. Williams. 1999. « Nonlinear robust control of a vector-controlled synchronous reluctance machine ». *Power Electronics, IEEE Transactions on*, vol. 14, n° 6, p. 1111-1121.
- Sharma, S., et B. Singh. 2013. « Permanent magnet brushless DC generator based stand-alone wind energy conversion system ». In *Power Electronics for Distributed Generation Systems (PEDG), 2013 4th IEEE International Symposium on*. (8-11 July 2013), p. 1-6.
- Sharma, S., et B. Singh. 2014. « Asynchronous Generator With Battery Storage for Standalone Wind Energy Conversion System ». *Industry Applications, IEEE Transactions on*, vol. 50, n° 4, p. 2760-2767.
- Singh, B., et V. Bist. 2015. « A BL-CSC Converter-Fed BLDC Motor Drive With Power Factor Correction ». *IEEE Transactions on Industrial Electronics*, vol. 62, n° 1, p. 172-83.

- Singh, B., V. Bist, A. Chandra et K. Al Haddad. 2014a. « Power Factor Correction in Bridgeless-Luo Converter Fed BLDC Motor Drive ». *Industry Applications, IEEE Transactions on*, vol. PP, n° 99, p. 1-1.
- Singh, B., G. K. Kasal et S. Gairola. 2008. « Power Quality Improvement in Conventional Electronic Load Controller for an Isolated Power Generation ». *Energy Conversion, IEEE Transactions on*, vol. 23, n° 3, p. 764-773.
- Singh, B., S. S. Murthy et S. Gupta. 2005. « An Electronic Voltage and Frequency Controller for Single-Phase Self-Excited Induction Generators for Pico Hydro Applications ». In *Power Electronics and Drives Systems, 2005. PEDS 2005. International Conference on*. (0-0 0) Vol. 1, p. 240-245.
- Singh, B., S. S. Murthy et S. Gupta. 2006. « Analysis and design of electronic load controller for self-excited induction Generators ». *Energy Conversion, IEEE Transactions on*, vol. 21, n° 1, p. 285-293.
- Singh, B., et R. Niwas. 2014. « Single-Phase Power Generation Using Three-Phase Self-Excited Synchronous Reluctance Generator ». *International Journal of Emerging Electric Power Systems*, vol. 15, n° 4, p. 377-88.
- Singh, B., R. Niwas et S. Kumar Dube. 2014. « Load Leveling and Voltage Control of Permanent Magnet Synchronous Generator-Based DG Set for Standalone Supply System ». *Industrial Informatics, IEEE Transactions on*, vol. 10, n° 4, p. 2034-2043.
- Singh, B., et V. Verma. 2008. « Selective Compensation of Power-Quality Problems Through Active Power Filter by Current Decomposition ». *Power Delivery, IEEE Transactions on*, vol. 23, n° 2, p. 792-799.
- Singh, Bhim, Ambrish Chandra et Kamal Al-Haddad. 2015. *Power quality problems and mitigation techniques*. John Wiley and Sons Ltd, xiii, 582 pages p.
- Singh, Bhim, Ram Niwas, Ambrish Chandra et Rezkallah Miloud. 2014b. « Voltage control and load leveling of synchronous reluctance generator based DG set ». In *Power India International Conference (PIICON), 2014 6th IEEE*. (5-7 Dec. 2014), p. 1-6.
- Singh, Bhim, B. N. Singh, A. Chandra, K. Al-Haddad, A. Pandey et D. P. Kothari. 2004. « A review of three-phase improved power quality AC-DC converters ». *Industrial Electronics, IEEE Transactions on*, vol. 51, n° 3, p. 641-660.
- Singh, M., et A. Chandra. 2011. « Application of Adaptive Network-Based Fuzzy Inference System for Sensorless Control of PMSG-Based Wind Turbine With Nonlinear-Load-Compensation Capabilities ». *Power Electronics, IEEE Transactions on*, vol. 26, n° 1, p. 165-175.

- Singh, Mukhtiar. 2010. *Adaptive network-based fuzzy inference systems for sensorless control of PMSG based wind turbine with power quality improvement features*. Montréal: École de technologie supérieure, xviii, 220 f. p.
- Skvarenina, Timothy L. 2002. *The power electronics handbook*. Coll. « Industrial electronics series ». Boca Raton, Flor.: CRC Press, 1 v. (pag. multiple) p.
- Subudhi, B., et R. Pradhan. 2013. « A Comparative Study on Maximum Power Point Tracking Techniques for Photovoltaic Power Systems ». *Sustainable Energy, IEEE Transactions on*, vol. 4, n° 1, p. 89-98.
- Tokunaga, S., et K. Kesamaru. 2011. « FEM simulation of novel small wind turbine generation system with synchronous reluctance generator ». In *Electrical Machines and Systems (ICEMS), 2011 International Conference on*. (20-23 Aug. 2011), p. 1-6.
- Tremblay, E., S. Atayde et A. Chandra. 2011. « Comparative Study of Control Strategies for the Doubly Fed Induction Generator in Wind Energy Conversion Systems: A DSP-Based Implementation Approach ». *Sustainable Energy, IEEE Transactions on*, vol. 2, n° 3, p. 288-299.
- Vagati, A., M. Pastorelli, G. Franceschini et V. Drogoreanu. 1999. « Flux-observer-based high-performance control of synchronous reluctance motors by including cross saturation ». *Industry Applications, IEEE Transactions on*, vol. 35, n° 3, p. 597-605.
- Valenciaga, F., et P. F. Puleston. 2005. « Supervisor control for a stand-alone hybrid generation system using wind and photovoltaic energy ». *Energy Conversion, IEEE Transactions on*, vol. 20, n° 2, p. 398-405.
- Villalva, M. G., J. R. Gazoli et E. R. Filho. 2009. « Comprehensive Approach to Modeling and Simulation of Photovoltaic Arrays ». *Power Electronics, IEEE Transactions on*, vol. 24, n° 5, p. 1198-1208.
- Wang, D. H., C. V. Nayar et C. Wang. 2010. « Modeling of stand-alone variable speed diesel generator using doubly-fed induction generator ». In *Power Electronics for Distributed Generation Systems (PEDG), 2010 2nd IEEE International Symposium on*. (16-18 June 2010), p. 1-6.
- Waris, T., et C. V. Nayar. 2008. « Variable speed constant frequency diesel power conversion system using doubly fed induction generator (DFIG) ». In *Power Electronics Specialists Conference, 2008. PESC 2008. IEEE*. (15-19 June 2008), p. 2728-2734.
- Wei, Li, G. Joos et J. Belanger. 2010. « Real-Time Simulation of a Wind Turbine Generator Coupled With a Battery Supercapacitor Energy Storage System ». *Industrial Electronics, IEEE Transactions on*, vol. 57, n° 4, p. 1137-1145.

- Wei, Qiao. 2012. « Intelligent mechanical sensorless MPPT control for wind energy systems ». In *Power and Energy Society General Meeting, 2012 IEEE*. (22-26 July 2012), p. 1-8.
- Wen-Bin, Lin, Chiang Huann-Keng et Yeh Chen-Hsiang. 2013. « Sensorless vector control of synchronous reluctance motor with extended kalman filter ». *ICIC Express Letters*, vol. 7, n° 1-6, p. 1773-9.
- Whei-Min, Lin, Hong Chih-Ming et Chen Chiung-Hsing. 2011. « Neural-Network-Based MPPT Control of a Stand-Alone Hybrid Power Generation System ». *Power Electronics, IEEE Transactions on*, vol. 26, n° 12, p. 3571-3581.
- Xia, Chen, Hou Yunhe, Tan Siew-Chong, Lee Chi-Kwan et Hui Shu Yuen Ron. 2015. « Mitigating Voltage and Frequency Fluctuation in Microgrids Using Electric Springs ». *Smart Grid, IEEE Transactions on*, vol. 6, n° 2, p. 508-515.
- Xia, Y., K. H. Ahmed et B. W. Williams. 2011. « A New Maximum Power Point Tracking Technique for Permanent Magnet Synchronous Generator Based Wind Energy Conversion System ». *Power Electronics, IEEE Transactions on*, vol. 26, n° 12, p. 3609-3620.
- Xiong, Liu, Wang Peng et Loh Poh Chiang. 2011. « A Hybrid AC/DC Microgrid and Its Coordination Control ». *Smart Grid, IEEE Transactions on*, vol. 2, n° 2, p. 278-286.
- Yang, Du, D. D. C. Lu, G. M. L. Chu et Xiao Weidong. 2015. « Closed-Form Solution of Time-Varying Model and Its Applications for Output Current Harmonics in Two-Stage PV Inverter ». *Sustainable Energy, IEEE Transactions on*, vol. 6, n° 1, p. 142-150.
- Yang, Y., Kwan-Tat Mok, Siew-Chong Tan et S. Y. R. Hui. 2014. « Nonlinear Dynamic Power Tracking of Low-Power Wind Energy Conversion System ». *Power Electronics, IEEE Transactions on*, vol. PP, n° 99, p. 1-1.
- Yeager, K. E., et J. R. Willis. 1993. « Modeling of emergency diesel generators in an 800 megawatt nuclear power plant ». *Energy Conversion, IEEE Transactions on*, vol. 8, n° 3, p. 433-441.
- Yue, Zhao, Wei Chun, Zhang Zhe et Qiao Wei. 2013. « A Review on Position/Speed Sensorless Control for Permanent-Magnet Synchronous Machine-Based Wind Energy Conversion Systems ». *Emerging and Selected Topics in Power Electronics, IEEE Journal of*, vol. 1, n° 4, p. 203-216.

- Zhu, B., H. Tazvinga et X. Xia. 2014. « Switched Model Predictive Control for Energy Dispatching of a Photovoltaic-Diesel-Battery Hybrid Power System ». *Control Systems Technology, IEEE Transactions on*, vol. PP, n° 99, p. 1-1.
- Zhu, Yongli, Jianguo Yao et Di Wu. 2011. « Comparative study of two stages and single stage topologies for grid-tie photovoltaic generation by PSCAD/EMTDC ». In *Advanced Power System Automation and Protection (APAP), 2011 International Conference on*. (16-20 Oct. 2011) Vol. 2, p. 1304-1309.